Development of High Temperature Superconductors Coated Conductors for Resistive Fault Current Limiters with the Current Flow Diverter Architecture

Pedro Barusco

Development of High Temperature Superconductors Coated Conductors for Resistive Fault Current Limiters with the Current Flow Diverter Architecture

A dissertation submitted for the degree of
DOCTOR OF PHILOSOPHY IN MATERIAL SCIENCE
by

Pedro Barusco

Supervisors:
Prof. Xavier Obradors i Berenguer
Dr. Xavier Granados García

Superconducting Materials and Large Scale Nanostructures
Institut de Ciència de Materials de Barcelona (ICMAB-CSIC)

Tutor: Prof. Joan Francesc Piniella Febrer

Doctorat en Ciència de Materials
Departament de Física - Facultat de Ciències
Universitat Autònoma de Barcelona

October 2021

“The devil is in the details”

- Friedrich Wilhelm Nietzsche

Abstract

The primary benefit of a metallic stabilization/shunt in 2nd Generation (2G) High Temperature Superconductors (HTS) coated conductors (CC) is to prevent damage during quench by providing an alternative path for the current flow. On the downside, the increase in thermal capacity of a thick shunt makes the CCs prone to heat amassing due to hot-spots coming from variations in the critical current distribution of the HTS layer. This thermal issue makes the classical HTS tape design extremely vulnerable for operating in superconducting devices like high-field magnets and Superconducting fault Current Limiters SFCL. In SFCL, a prospective fault current level close to these tape's average critical current (I_c) can lead to destructive hot-spots in a matter of milliseconds. The Current Flow Diverter (CFD) is a promising multilayer architecture concept that has proven to increase the conductor's robustness against the inevitable hot-spot regime by inserting a high resistive layer partially covering the interface between the metallic silver shunt and the (Re)BCO film, thus alleviating shunt compromise. This relatively simple change creates a boost in the so-called Normal Zone Propagation Velocity (NZPV) and avoids the destructive heat amassing of hot-spots. However, since 2014 there has been a struggle in finding a practical manufacturing method compatible with the coating steps of reel-to-reel systems used by companies. In the framework of the H2020 project *FASTGRID*, this thesis reports on the technical journey of trying to achieve a feasible cost-effective method for implementing the CFD architecture in 12 mm wide 2G HTS tapes. Using chemical solution deposition (CSD) and chemical vapor deposition (CVD) methods, four materials, i.e epoxy, graphite, yttria and silver sulfide, led to four different manufacturing routes that helped identify the main practical constrains of the CFD fabrication and, for the first time, two viable CFD fabrication routes were found with yttria nanolayers and silver sulfidation reactions. Furthermore, for tapes with and without CFD, the I_c and NZPV, together with the maximum fault limitation conditions, electric field and fault time, were measured and compared using transport current in DC and AC respectively to confirm the advantages of the new proposed architectures.

Acknowledgments

I want to give a special thanks to my thesis supervisor Prof. Xavier Obradors for the consistent support, advices and valuable discussions throughout my PhD; Dr. Xavier Granados for his constructive questioning, indispensable technical knowledge and hands-on assistance during critical experimental points of my research; and the head of the Superconductivity group (SUMAN) at the Institute of Materials Science of Barcelona (ICMAB) prof. Teresa Puig, for providing me with the freedom and resources necessary to expand my range of knowledge and explore the new ideas that led to conclusive results in this thesis.

In ICMAB I extend my gratitude to all for creating a knowledgeable and friendly environment to help me advance with my PhD research. Nevertheless, I would like to highlight: Mar Tristany for relentlessly putting in order the bureaucracy of my PhD experience at ICMAB; Mariona de Palau and Joshua Balio for kindly maintaining my overall unorthodox experimental methods organized and efficient; Albert Queraltó and Diana García for always being up for quick discussions and precise SEM procedures; Roxana Vlad and Cornelia Pop for the solid work partnership in the FASTGRID project and personal carrying; Alexander Stangl for constantly opening my eyes to the intricate details of oxygen incorporation in HTS materials; Max Sieger and Guilherme Telles for the fun HTS knowledge exchange and good friendship; Pamela Machado for showing me the Sun furnace in a dark lab; Adrià Pacheco for sharing profilometry tips and remarkable conference memories; Francesco Silvestri for his AFM expertise and delightful positive behavior towards scientific research; Camilla Dore for helping me remember mind & body balance and teaching me the art of sharp lithography; Martì Gibert for always being interested in discussing and helping with innovative ideas; and Lavinia Saltarelli for lending me some of her experimental passion, high standards and daily dedication.

To my collaborators Christian Lacroix, Frédéric Sirois and Jean-Hughes Lupien at *Ecole Polytechnique Montréal* in Canada I must acknowledge the exceptional partnership revolving every aspect of my work during and after the FASTGRID project. Your continuous support with insightful discussions, quench simulations and experimental current transport measurements was undoubtedly paramount for the completion of this thesis. Thank you for all. Moreover, I would like to thank Roland Gyuráki from KIT and Alexandre Zampa from Université Grenoble Alpes for the opportunity to collaborate in experiments using slow-motion recordings for the quench propagation of HTS tapes.

And finally, I am thankful to my partner Karoline Hellmold for the unconditional care and for helping me overcome mind barriers throughout my last PhD year, as well as my family and close friends for their encouragement and unconditional support throughout my thesis.

Author Contributions

P. Barusco, X. Granados, L. Saltarelli, J. Fournier Lupien, C. Lacroix, H. Saad, F. Sirois, R. V. Vlad, A. Calleja, V. Grosse, T. Puig, X. Obradors. Chemical Solution Deposition of insulating Yttria nanolayers as Current Flow Diverters in superconducting $GdBa_2Cu_3O_{7-\delta}$ Coated Conductor, (2021) [Manuscript submitted for publication]

C. Lacroix, F. Sirois, A. Calleja, R. V. Vlad, J. P. Paricio X. Obradors, X. Granados, T. Puig, P. Barusco. "SUPERCONDUCTOR MATERIAL AND PROCESS FOR PRODUCING THE SAME", European Patent Office, N/Ref.: 2018/142640

P. Barusco, X. Granados, J. Fournier Lupien, C. Lacroix, F. Sirois, T. Puig and X. Obradors. Increasing the Normal Zone Propagation Velocity of 2G HTS tapes via Shunt Sulfidation. Coated Conductor, [unpublished manuscript] (2021)

Table of Content

1 A Brief Review of Superconductivity

This chapter briefly reviews the overall superconductivity theory in its historical context, focusing on the properties of High Temperature Superconductors (HTS) and their manufacturing details. Currently, HTS materials present the highest potential for being used as practical electric wires, also known as 2G HTS coated conductors (CC) or HTS "tapes". Improving the thermal performance of these tapes was the main focus of this work and it will be discussed in detail in chapter 2.

1.1 Basic Properties

In this section, the most basic properties of a superconducting material are presented; Zero resistivity and the Meissner-effect. Moreover, the critical parameters defining the superconducting state of a material are also defined.

1.1.1 Zero Resistivity

In general, the electrical resistivity ρ of metallic alloys decreases when cooled down. As temperature T decreases, the thermal effects coming from the atomic vibrations also decrease, creating less interference for the conduction of electrons through the material. For pure metals, interference in the movement of electrons should only occur due to thermal latent vibrations [1]. Therefore, the resistance of a pure metal should also approach zero as temperature decreases to 0 K. However, inevitable impurities and imperfections in the crystal structure of a metal [1] result in a residual resistance that should remain present even at cryogenic temperatures with a dependence $\rho \propto T^5$ according to the Bloch-Gruniensen formula.

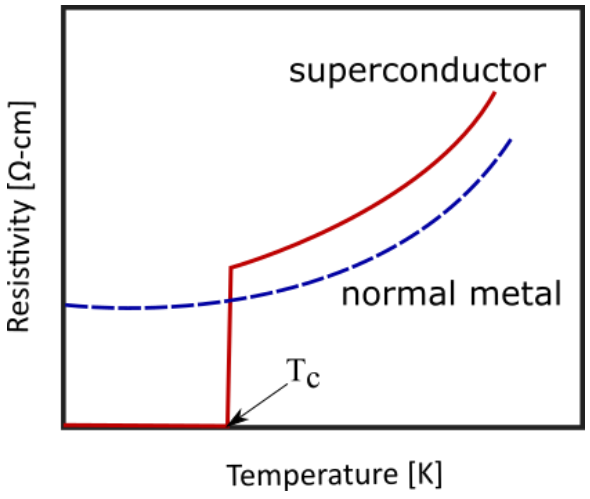

Figure 1.1: Resistivity vs. Temperature curves of a superconductor (red curve) and a normal metal (blue curve). For the superconductor the resistivity suddenly becomes zero at T_c, whereas for a normal metal it smoothly decays to a residual value at 0 K.

Nevertheless, in 1911 Kamerlingh Onnes discovered that certain metals, even in the presence of impurities, presented a different resistive behavior. For temperatures approaching 0 K, the resistivity of these metals, instead of presenting a residue value, dropped to neglectable levels that were practically non-existent (Figure 1.1) [2]. These first metals, presenting the zero resistivity phenomena, inaugurated a whole new class of materials known as superconductors.

1.1.2 The Critical Parameters

When a superconductor is cooled, the temperature threshold for the material to make the transition from the Normal Resistive State to a state presenting a neglectable resistance, is referred to as the transition temperature or critical temperature and is denoted by T_c (in Kelvin K). Moreover, up until 1914 with the continuation of Onnes's research, he observed that the superconducting metals, even below the transition temperature T_c, could lose the superconducting properties when induced with magnetic flux B_c (in Tesla T or W/m^2) by being exposed to a certain intensity of an external magnetic field force H_c (in A/m). The same would happen for a superconductor conducting a certain value of current density J_c (A/m^2), thus concluding that three parameters defined the superconducting state: the critical temperature T_c, the critical magnetic field H_c and the critical current density J_c. In other words, the superconducting state can only be sustained if the values of temperature, magnetic field and current density are maintained below their respective critical values (Figure 1.2).

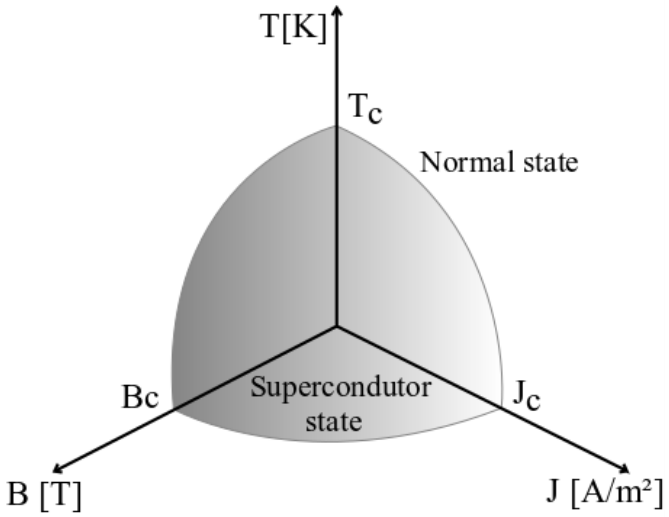

Figure 1.2: Superconducting state limited by three critical parameters: critical temperature T_c, critical field B_c and critical current density J_c

1.1.3 The Meissner-Ochsenfeld Effect and Perfect Diamagnetism

For 22 years after the first superconductor material was discovered, superconductors were thought to be "perfect conductors" due to the absence of resistance in the superconducting state. However, superconductors present a different magnetic behavior from what is expected from a theoretical "perfect conductor". If we consider a "perfect conductor" material, the resistance across any closed

path inside the material should be zero. Therefore, as long as the magnetic density inside the material does not change in time $dB/dt = 0$, the magnetic flux elapsed by any closed path of current should also not change. Consequently, the distribution of flux should not be alternated due to the transition from the normal state to the superconducting state.

Let us assume that a material is cooled down to the superconducting state and an external magnetic field H_a is applied afterwards (Figure 1.3 (A) (a) –(d)). Since the magnetic flux cannot change, the field density inside the material B should remain the same (zero) even after the field is applied. Induced currents inside the material will appear to create a magnetic flux of same intensity in opposition to the external field H_a. Since the material has zero resistivity, the induced currents do not decay and the resulting field density inside the material remains zero.

Now we consider a scenario in which the external magnetic field H_a is applied to the material before the transition to the "perfect conductor" state (Figure 1.3 (A) (e) –(g)). Once the body is cooled down below T_c, no magnetization should occur and the flux distribution should not change. Since the flux density inside the material cannot change, if the external field H_a is removed, induced currents should appear to maintain the internal flux resulting in a permanent magnetization of the body.

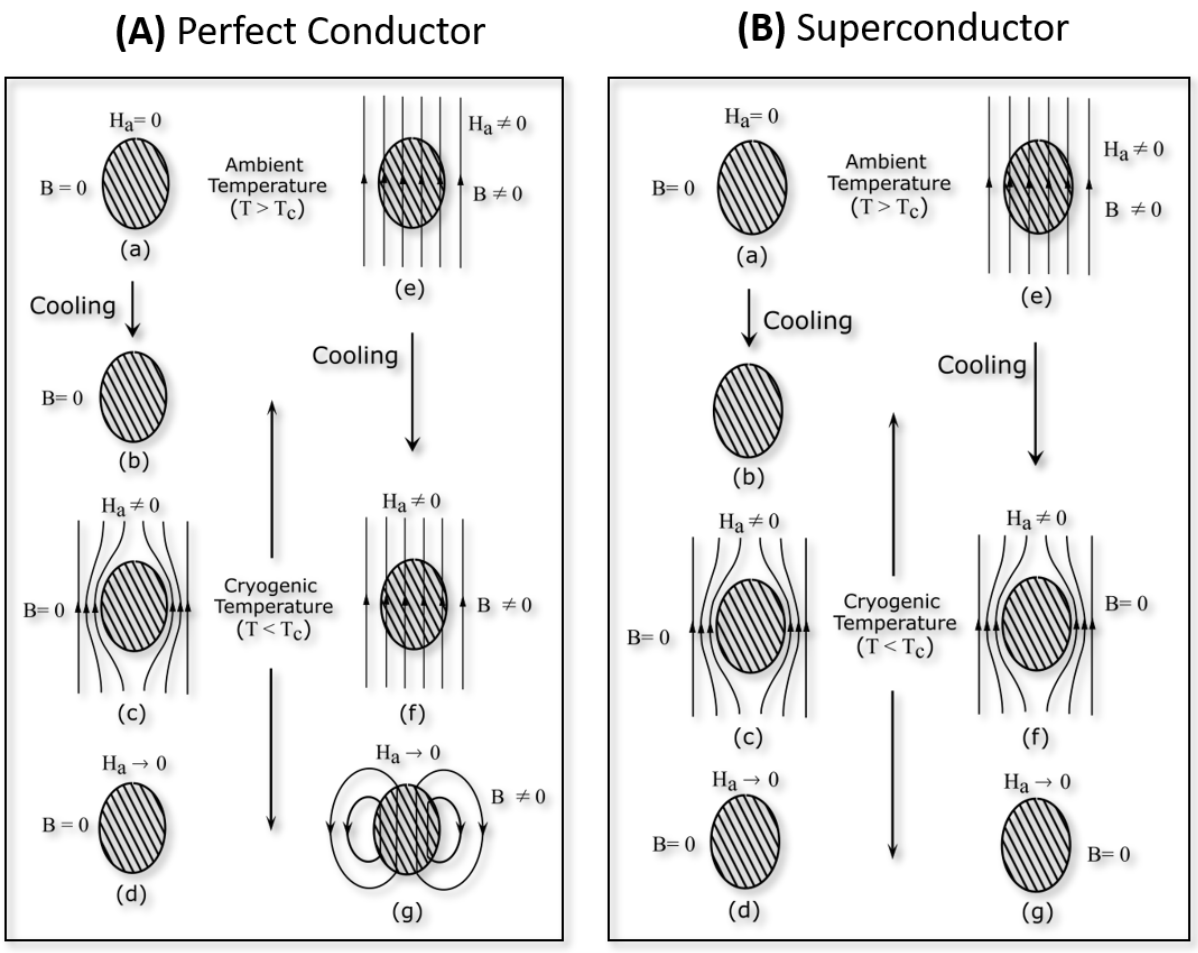

Figure 1.3: ***(A)*** *Behavior of a perfect conductor: (a)-(b) The conductor is cooled down to the superconducting state in the absence of a magnetic field. (c) A magnetic field is applied to the conductor. (d) The magnetic field is removed. (e)-(f) The conductor is cooled down to the superconductor state in the presence of a magnetic field. (g) The field is removed. Figure adapted from* [3].

(B) *Magnetization behavior of a superconducting material: (a)-(b) The conductor is cooled down to the superconducting state in the absence of a magnetic field. (c) A magnetic field is applied to the conductor. (d) The magnetic field is removed. (e)-(f) The conductor is cooled down to the superconductor state in the presence of a magnetic field. (g) The field is removed. Figure adapted from* [3].

Nonetheless, in 1933 Meissner and Ochsenfeld measured the magnetic flux distribution on the surface of Sn and Pb samples [4]. Samples were cooled down below T_c in the presence of a magnetic field and the result was not the same as expected from a theoretical "perfect conductor". Below T_c, the samples spontaneously presented a perfect diamagnetism cancelling all magnetic flux inside the material (Figure 1.3 (B) (e) –(g)).

It was concluded that a superconducting material cooled below T_c, in the presence of a magnetic flux, still induces superficial circulating currents to shield itself from being penetrated by an external magnetic field, i.e always $\boldsymbol{B} = \mathbf{0}$. This phenomenon was named the ***Meissner-Ochsenfeld*** effect. Differently from a "perfect conductor", the magnetization state of a superconductor is independent of how the final conditions of temperature and magnetic field were achieved.

1.1.4 London's Penetration Depth

In 1933, the brothers Heinz and Fritz London [5] suggested that the magnetic flux density $\vec{B}$ inside a superconductor could be descried by the equation (1.1). Utilizing this equation, they described the magnetic flux when a uniform magnetic field intensity is applied parallel to the superconductor's surface.

$$\nabla^2 \vec{B} = \frac{1}{\alpha} \dot{\vec{B}} \tag{1.1}$$

Rewriting equation (1.1) for a simplified unidimensional case we have:

$$\frac{\partial^2 B(x)}{\partial x^2} = \frac{1}{\alpha} B(x) \tag{1.2}$$

Being $B(x)$ the flux density at a certain distance x inside the superconductor from the surface. The solution for the simplified equation (1.2) is given by equation (1.3), where B_a is the external flux density applied to the material in the superconducting state.

$$B(x) = B_a e^{(-x/\sqrt{\alpha})} \tag{1.3}$$

In equation (1.3) the flux density $B(x)$ decreases exponentially inside the superconductor, decaying to $1/e$ of the initial B_a value for a distance $x = \sqrt{\alpha}$ from the surface. This distance is named *London's penetration depth* ($\lambda_L = \sqrt{\alpha}$). Where $\alpha = m\mu_0 n_s e^2$ and e is the electron charge, μ_0 is the magnetic permissivity in vacuum, m is the electron mass and n_s is the density of super electrons.

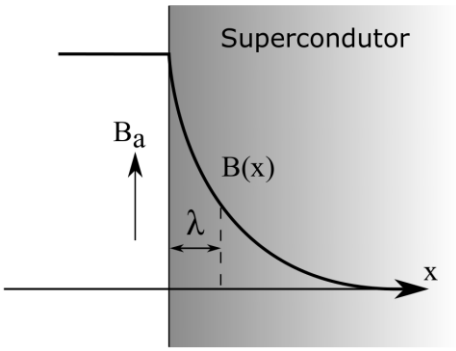

Figure 1.4: Variation of magnetic field density on the boundary of a superconductor material.

As a benchmark, using the usual values $e = 1.6 \times 10^{-19}$ C, m= 9.11 × 10^{-31} kg, μ_0= 4π × 10^{-7} H/m and a $n_s = 4 \times 10^{28}$ we find a penetration depth λ_L of 1 μm approximately. In summary, the field inside a superconductor, although zero inside, is still present in a thin layer of thickness λ_L close to the surface of the body.

1.2 Surface Energy of a Superconductor

In the previous section, we discussed how the magnetization state of a superconductor depends only on the final values of temperature and magnetic field. From a thermodynamic point of view, this implies that the transition from the normal state to the superconducting state is a reversible process. In this section, a simplified thermodynamic analysis of the superconducting state is used to explain the possibility of two different magnetic behaviors.

1.2.1 Free Energy

In any system, the equilibrium state is defined by the condition of minimum free energy (Gibbs free energy). If a material makes the transition from the normal state to the superconducting state below the T_c, this means that the free energy of the superconducting state is lower than the normal state. For a temperature T in the absence of a magnetic field ($H_a = 0$) let us define the free energy in the superconducting state as $g_s(T, 0)$ and the normal $g_n(T, 0)$.

If a magnetic field $H_a < H_c$ is applied to the superconductor, the material should acquire a magnetization M, thus changing the total free energy of the body according to:

$$\Delta g(H_a) = -\mu_0 \int_0^{H_a} M \, dH \tag{1.4}$$

If the field H_a would produce a magnetization in the same direction, the free energy would be reduced. As discussed before, the magnetization in the case of a superconductor is created in opposition to the applied field ($M = -H$) to shield the material. And so, the free energy increases:

$$g_s(T, H_a) = g_s(T, 0) + \mu_0 \int_0^{H_a} M \, dH$$

$$g_s(T, H_a) = g_s(T, 0) + \frac{1}{2}\mu_0 {H_a}^2 \quad (1.5)$$

Compared to the superconducting state, the magnetization acquired in the normal state is insignificant and so the presence of a field H_a creates no change in the free energy $g_n(T, 0) = g_n(T, H_a)$. If the applied field is equal or greater than the critical field $H_a \geq H_c$ the increase in the free energy will drive the material out of the superconducting state into the normal state. In this case $g_s(T, H_a) > g_n(T, 0)$, hence:

$$\frac{1}{2}\mu_0 {H_a}^2 > [g_n(T, 0) - g_s(T, 0)]$$

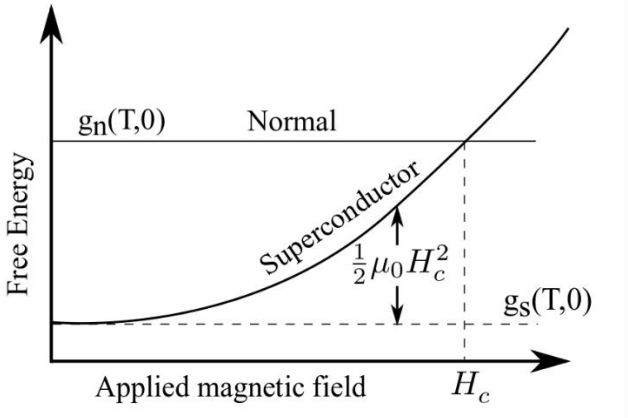

Figure 1.5: Effect of the magnetic field in the Gibbs free energy of a superconductor

In summary, when a magnetic field intensity H_a is applied to a material in the superconducting state, $\frac{1}{2}\mu_0 {H_a}^2$ is added to the free energy (Figure 1.5). The critical field H_c is simply the intensity that increases the free energy $g_s(T, 0)$ to $g_n(T, 0)$. And so, the difference in free energy for a superconducting material at a fixed temperature below T_c is:

$$g_n - g_s = \frac{1}{2}\mu_0({H_c}^2 - {H_a}^2) \quad (1.6)$$

1.2.2 The Coherence Length and Surface Energy

In 1953, *Brian Pippard* introduced the coherence length concept [6]. Pippard concluded that the density of super electrons n_s responsible for defining the superconductivity region could not change abruptly inside the material. It could only considerably vary across a certain distance that he named the coherence length ξ. In other words, ξ is the mean distance between the normal and the superconducting state inside the material. At the time, this was a vague concept created to simply describe the superconductor behavior, however it would later align with the predictions of the Ginzburg-Landau theory [7]. One of the main arguments in favor of the coherence length is the fact that it provides a simple explanation for the surface energy in the superconductor.

Considering a superconductor below T_c in the presence of a critical magnetic field H_c, the field should penetrate a distance λ and the number of super electrons n_s should increase gradually inside the material across the coherence length ξ. In order for stability to exist, the free energy of the

superconducting region and the normal region should be the same in the interface normal region/superconductor region. In this situation, there are two contributions that change the free energy from the superconducting state to the normal state. First the presence of super electrons, reducing the energy of the superconducting state in $g_n - g_s$, and the second contribution, the acquired magnetic energy $\frac{1}{2}\mu_0 H_c^2$ cancelling the field inside the superconductor. Therefore, $g_n - g_s = \frac{1}{2}\mu_0 H_c^2$ so that the two contributions balance the energy in the normal/superconductor interface.

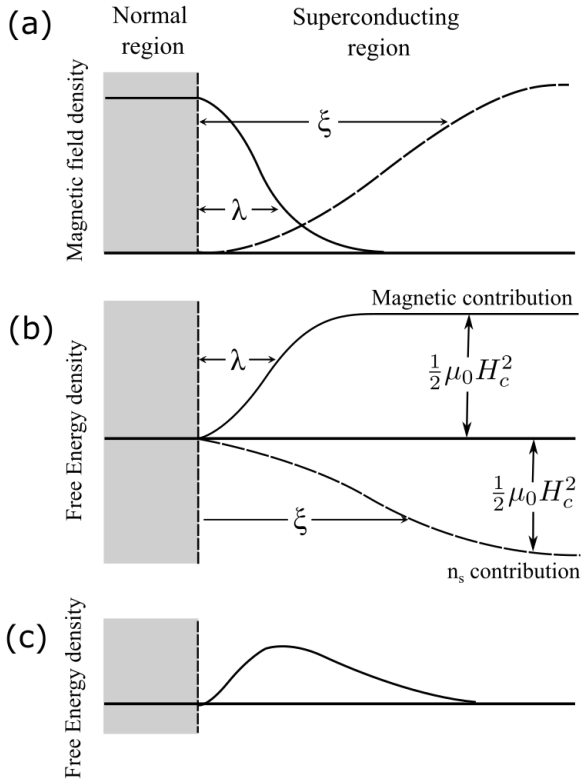

Figure 1.6: Positive surface energy on a superconductor. (a) penetration depth and coherence length on the surface of a superconductor. (b) magnetic and n_s contribution to the free energy. (c) total free energy in the surface.

In Figure 1.6, one can notice that if ξ is bigger than λ_L the total free energy increases near the interface, thus creating a positive surface energy. Substituting the n_s and H curves in Figure 1.6(b) for rectangular steps happening at distances ξ and λ_L, a rough approximation of the surface energy could be described as $\frac{1}{2}\mu_0 H_c^2(\lambda_L - \xi)$.

1.2.3 Negative Surface Energy

In the majority of metals ξ is bigger than λ_L and the total free energy in the normal state frontier increases creating a positive surface energy. However, the values of ξ and λ_L may change for some materials in a way that ξ is smaller than λ_L. This would create a negative surface energy in the normal state frontier as illustrated in Figure 1.7.

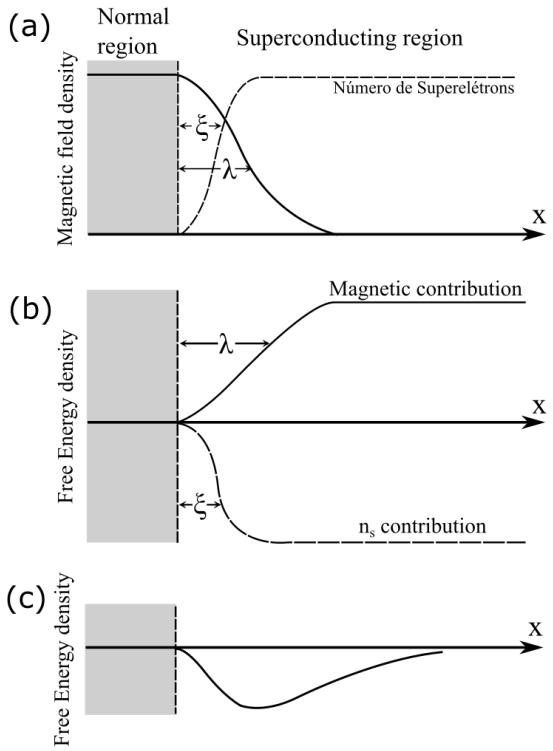

Figure 1.7: Negative surface energy on a superconductor. (a) penetration depth and coherence length on the surface of a superconductor. (b) magnetic and n_s contribution to the free energy. (c) total free energy in the surface.

The existence of a negative surface energy implies that energy is released in the normal/superconductor interface. The presence of an interface should reduce the total free energy and since any system always tends to the state of minimum free energy, if a magnetic field would be gradually applied to the superconductor with a negative surface energy, the body should favor the occurrence of a larger normal/superconductor interface.

1.3 The Mixed State

For many years it was thought that all superconductors would magnetically behave the same and that some anomalous behavior observed in superconductors with negative surface energy was due to "impurities". Only in 1957 Alexei Abbrikosov noticed that the anomalies were inherent properties of a new class of superconducting materials.

1.3.1 Vortex and Fluxoids

For a superconductor body with negative surface energy, Abbrikosov concluded that the only way for a large interface normal/superconductor to arise would be the spontaneous creation of normal zones in the superconducting material [8]. However, for such state to exist, the disposition of these zones inside the superconductor should maximize the normal zone volume/surface ratio. The configuration for this condition, occurs in the shape of narrow normal zone cylinders, organized in a stable hexagonal

grid as shown in Figure 1.8. These cylindrical regions, also known as fluxoids or vortexes [8], were later confirmed in experiments of magnetic decoration [9,10].

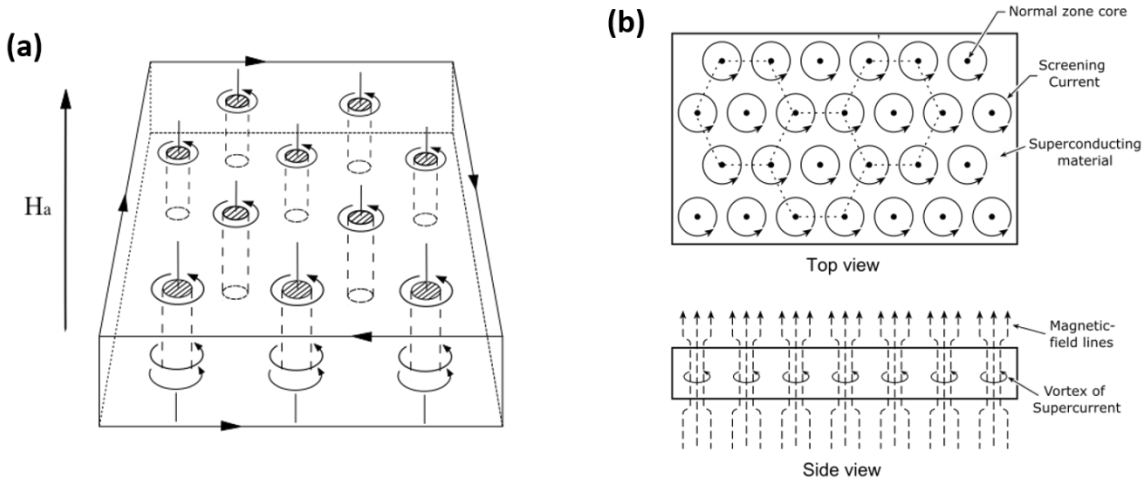

Figure 1.8: Mix state of a superconductor. (a) Isometric view of the fluxoid formation across the superconducting body in the presence of a magnetic field H_a. (g) Top view of the hexagonal lattice arrangement of the fluxoid formation.

The presence of this vortex lattice is also referred to as the Mixed State. The superconducting region is diamagnetic and it does not allow the presence of a magnetic field, but the normal zones are magnetically permeable. Each fluxoid traps a quantized amount of magnetic flux $\phi_0 = \hbar/2e$, regulated by a vortex of supercurrent around the region. The presence of such mixed state creates the division of two types of superconductors: type-I and type-II.

1.3.2 Type- I and Type-II Superconductor

Experimentally, the type-II superconductors where discovered in 1935 by Lev Shubnikov and Rjabinin [11] and in 1950, the possibility to divide superconductors into two types was suggested for the first time analyzing the theoretical implications of the constant $k = \lambda_L/\xi$ in the Ginzburg-Landau theory [7]. However, the new classification did not happen due to the scant experimental observations combined with the lack of a solid physical theory to describe the type-II behavior. It was only in 1957, with the Mixed State theory of Alexei Abrikosv [8], that the type-I and II division was truly introduced in the scientific community.

Type-I superconductors are characterized for having positive surface energy due to a small penetration length in comparison to the coherence length ($k > 0.707$). These materials present a pure Meissner effect. Any external magnetic field is completely expelled from the material until the intensity reaches the critical value H_c. Practically all the first chemical elements discovered as superconductors are classified as type-I (also known as soft superconductors).

In the case of type-II superconductors the penetration depth is considerably larger and creates the condition $k < 0.707$. Consequently, the surface energy becomes negative and minimization of the free energy is achieved by maximizing the area of the interface between the superconducting state

and normal state. In this case, it becomes energetically favorable for the superconductor to create normal zones allowing field penetration, thus entering the mixed state.

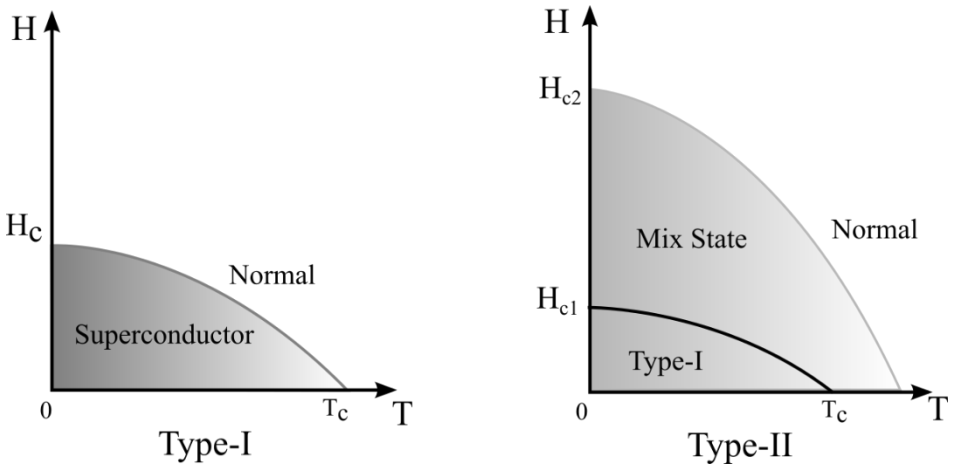

Figure 1.9: Different magnetic behaviors between type-I and II superconductors.

Nevertheless, there is a minimum magnetic field for the superconductor type-II to enter the mix state. This lower limit is shown in Figure 1.9 and is denoted by H_{c1}. For field values below H_{c1} the material behaves like a type-I superconductor presenting a pure Meissner effect. Above H_{c1} and below an upper limit H_{c2}, the superconductor allows a partial penetration of the field, thus entering the mix state. For field values above H_{c2} the material goes to the normal state.

1.3.3 Transport Current in Type-II Superconductors

Let us now consider a current I crossing a type-II superconducting body of length l, cross section area A, below T_c and in the presence of field a H between H_{c1} and H_{c2} ($H_{c1} < H < H_{c2}$). Since the superconductor is in the mixed state, the body is permeated by vortex regions of quantized magnetic flux. Therefore, a Lorentz force f_L should arise from each vortex region due to the interaction between flux and the transported electrons.

If the total magnetic flux density B created by the vortexes has an angle θ with the current I, then the Lorentz force is given by $F_L = IBsin(\theta)$. If every vortex imprisons a flux ϕ_0, then the magnetic flux density in the material can be describe as $B = n\phi_0$, where n is the number of vortexes per unit area. Finally, considering the total length of all the vortex along l as nlA, the mean force per unit length of vortex will be given by $F_L = (I/A)\phi_0 sin(\theta)$. Even if the current density varies, the mean current density will be $J = I/A$. Therefore, the Lorentz force can be rewritten as $F_L = J\phi_0 sin(\theta)$. Simplifying the case for a perpendicular field $\theta = 90°$ the Lorentz force in the wire is simply described by:

$$F_L = J\phi_0 \tag{1.7}$$

This simple equation shows that if there was no other force opposite to the Lorentz force the type-II superconductors would have no practical application. The vortex grid would move freely and induce an electrical field E_L as response to J, thus creating work and dissipation of energy. This energy would

increase the temperature of the body above T_c, thus killing the superconducting state. The description of this theoretical restriction was first suggested by J. Bardeen and M. J. Stephen [12] in 1965.

The force preventing the vortex grid from moving is called *pinning force* F_p. This force fixes the vortex in the so-called *pinning centers* located at the natural and/or artificial imperfections existing in the crystal structure of the material. The force F_p is limited by the amount of defects found in the material, but not all the vortexes are spatially fixed in pinning centers. Only a few pinned vortexes are needed to create a rigid Abbrikosov grid and prevent the other vortexes from moving.

As long as the existing current density J crossing the superconductor produces a force $F_L < F_p$, the Abbrikosov grid will not move. However, if J produces a force $F_L \gg F_p$, the vortexes will be dislocated and create a dissipative state of energy. In this scenario, the critical current density J_c is the threshold value to start moving the vortexes from the pinning centers. The vortexes motion regime in transport current is called *Flux Flow* and it is the source of resistance in type-II superconductors.

Furthermore, the vortexes motion in the mix state also defines two phases in the vortex grid depending on the intensity of an external magnetic field $H_{c1} < H < H_{c2}$: the vortex solid phase and the vortex liquid phase [13,14]. For low temperatures T and low magnetic fields H, $J_c > 0$ as long as $F_L < F_p$ for any current density $J < J_c$, thus defining the vortex solid phase. However, even in the absence of a transport current density $J = 0$, a certain value of field $H_{c1} < H < H_{c2}$ can create the condition $F_L \gg F_p$ for any practical value of current density $J > 0$, thus defining the vortex liquid phase where the unavoidable motion leads to the absence of critical current $J_c = 0$. In other words, in the liquid phase "… the influence of thermal fluctuations on the flux lines becomes so strong that currents cannot flow without losses although the superconductor is not yet in the normal state" [15]. This H value is known as the *irreversible field* H_{irr} and defines the *irreversibility line* (IL) in the T-H diagram of a type-II superconductor (Figure 1.10).

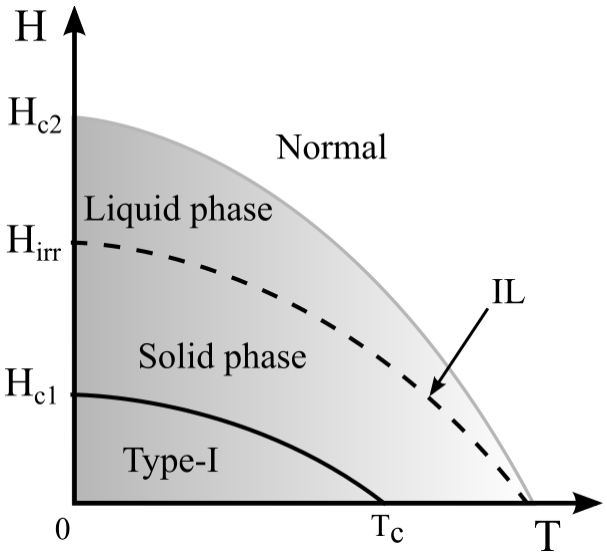

Figure 1.10: Magnetic phase T-H diagram for type-II superconductors with different vortex phases defined by the irreversibility line (IL) $H_{irr}(T)$.

1.3.4 Critical Current Density in HTS

In 1964, Anderson and Kim created the flux-creep concept to try to explain the exponential correlation between electric field and current density in type-II low temperature superconductors (LTS) [16,17]. However, at the time, the models from Warners and Larbalestier [18] and Plummer and Evetts [19] were also successful in describing the exponential behavior based on the non-uniformities of J_c across superconductors. But with the discovery of the high temperature superconductor (HTS) materials, these models started lacking explanations. It was only in 1996, that the flux creep concept from Anderson-Kim was completely re-introduced by Brandt [20] to explain the exponential E-J behavior of the HTS materials.

Anderson-Kim establishes an exponential relation between the electric field and current density inside the HTS material depending on the temperature. This relation is analog to the *Arrhenius Law* where the velocity of a chemical reaction v is a function of temperature T and an activation energy E_a:

$$v = Ce^{\left(\frac{-E_a}{RT}\right)} \quad \Leftrightarrow \quad E(U) = E_c e^{\left(\frac{-U(J)}{RT}\right)}$$

Being C a constant related to the chemical reaction and R the ideal gas constant. In this analogy, the electric field E created by the vortex motion of a transport current in the HTS material is also described as a function of T and an activation energy U. Where E_c is the critical electric field leading to the motion of the vortex lattice, and *U* arises as function of the applied current density J, as described by Zeldov et al. in [21]:

$$U(J) = U_c \cdot \ln\left(\frac{J_c}{J}\right) \tag{1.8}$$

U_c is a constant representing the critical activation energy and J_c is the critical current density threshold responsible for the appearance of E_c in the HTS. Finally, E is re-written as a function of J leading to the *Power Law* [22,23]:

$$E(J) = E_c\left(\frac{J}{J_c}\right)^n \tag{1.9}$$

Where $n = U_c/RT$ is known as the n-value. In this equation, the transport characteristics of the superconductor are described by J_c and the n-value. J_c indicates the maximum current transport capacity and the n-value the shape of the E-J curve. Moreover, the n-value also describes different regimes for the E-J curve as J increases.

- Zero resistance ($n \to \infty$): No vortexes motion and insignificant electric field values. This behavior is also described by Beans critical state model [24], not discussed in this thesis.
- Flux creep ($25 < n < 50$): Minor vortexes motion due to J inducing Lorentz forces with magnitude close to the pinning forces.
- Flux flow ($2 < n < 5$): Considerable motion of the vortexes due to J inducing Lorentz forces slightly above the pinning forces.
- Normal ($n = 1$): Complete transition from the superconducting state to the normal ohmic state. The Power Law becomes *Ohm's Law.*

1.4 Superconductor REBCO Oxides

In 1986, inside IBM's research facility, George Bednorz and Alex Müller, while experimenting with LaBaCuO systems, found a class of superconducting cuprates at a T_c of 35 K [25]. This discovery gave birth to a new classification in superconductors: The High Temperature Superconductors (HTS) and the Low Temperature Superconductors (LTS). In the following year, Ching-Wu Chu performed tests changing the lanthanum for yttrium in the cuprate system and observed the superconducting phenomena at 92 K [26]. This discovery had a great impact in the practical large-scale applications of superconductors. Differently from the previous Low Temperature Superconductors (LTS), that had to be cooled with liquid helium, the HTS materials could operate in a liquid nitrogen environment, thus substantially reducing operational costs.

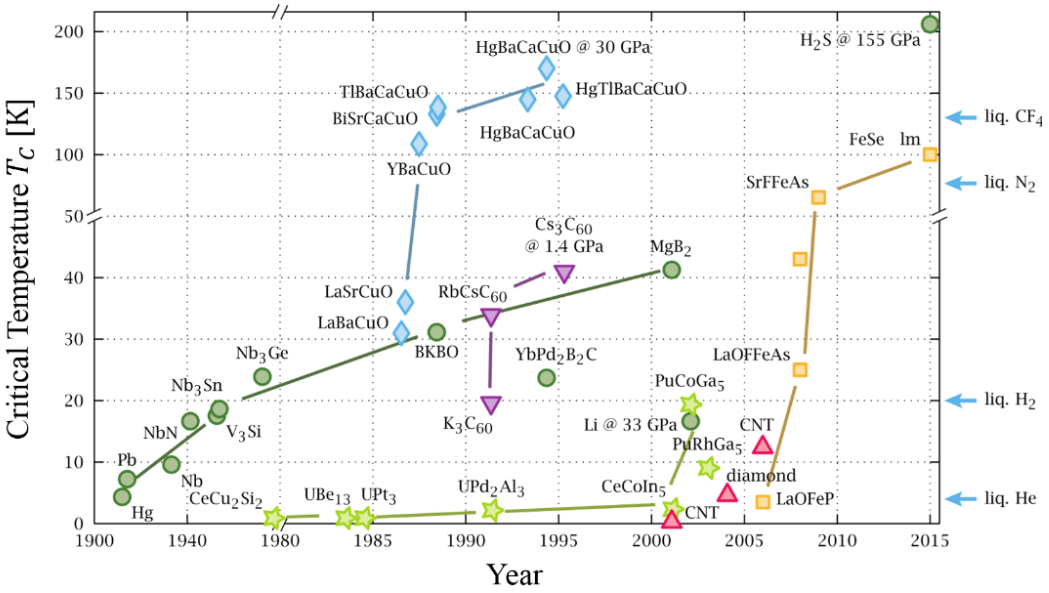

Figure 1.11: Chronological discovery of superconducting materials throughput the years. Three superconducting families are shown: The green circles representing the superconductors explained by the BCS theory; the blue diamonds for the REBCO cuprates and the yellow squares for the iron-based superconductors.

Figure 1.11 shows the discovery of superconductor materials throughout the years since 1911 and their respective critical temperatures. Since the discovery of the REBCO family, the HTS cuprates have shown to be the most promising compound for large-scale applications. Besides operating above 77 K, in general, these materials are capable of maintaining high values of J_c in the presence of high magnetic fields.

1.4.1 The REBCO Structure

The REBCO structure is composed of BaCuO3 and RECuO2 forming a triple perovskite compound shown in Figure 1.12. The sequence of planes in the REBCO structure is Re-CuO2-BaO-CuOx-BaO-CuO2-Re, with the two CuO2 planes and one single CuOx chain lying parallel to the a-b plane of the crystal.

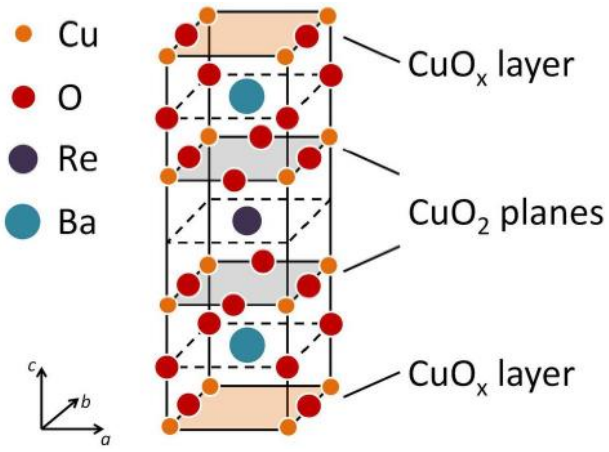

Figure 1.12: Unit cell of ReBCO compounds. This unit cell can change from a tetragonal to an orthorhombic structure.

The CuO_2 planes are present in all superconducting cuprates and are considered to be the main source for the superconducting behavior of the REBCO materials. The CuO_2 planes are known to be the conductive planes that transport the charge carriers [27]. Meanwhile the CuO_x chains are meant to be the charge reservoirs for the CuO_2 planes with the charge transfer happening via the apical oxygen between the plane and the chain [27]. This explanation is considered valid for the vast majority of REBCO materials with the expectation of some cases like the $PrBa_2Cu_3O_7$ described in [28].

The structural phase of the unit cell $REBa_2Cu_3O_y$ is directly tied to the presence of the superconducting properties in the material and it changes according to the oxygen content existing in the vacancies of the CuO_x chain. The final stoichiometry is defined by the oxygen deficiency $y = 7 - \delta$ indicating an empty chain at O_6 and a fully filled chain at O_7 [29]. At y = 6 the crystal has a tetragonal phase and behaves as an insulator. But as oxygen adds to the Cu-O chains and $y \to 7$, the phase changes to an orthorhombic structure where the periodical arrangement of the Cu-O chains forms the superstructures responsible for the superconducting properties [30].

Since the current flows only along the CuO_2 planes, the conductivity is confined in the ab-planes of the crystal and a large anisotropy in transport properties is observed. It becomes compulsory that all the grains present a perfect orientation of the c-axis to allow the current to flow freely in the CuO_2 planes. Small c-axis misalignments between the grains can lead to substantial decrease in the current capability (J_c) of the material as a whole [31]. For this reason, a perfect biaxial texture is required for the REBCO compound to achieve optimum superconducting properties.

Furthermore, the anisotropy also appears in the formation of the vortexes of the mixed state. The values of λ and ξ defining the fluxoids regions in the material depend on the orientation of the magnetic field with respect to the crystallographic ab and c-axis. This anisotropy is quantified in the Ginzburg-Landau theory as [32]:

$$\gamma = \frac{\lambda_c}{\lambda_{ab}} = \frac{\xi_c}{\xi_{ab}}$$

Another class of HTS materials discovered in 1988 that is worth mentioning is the BSCCO. This class was the first HTS family without a rare-earth element in the cuprate structure and has a general chemical formula $Bi_2Sr_2Ca_{n-1}Cu_nO_{2n+4+x}$, with n = 2 being the most commonly studied [33,34]. Like all

HTS cuprates, the superconductivity in BSCCO also relies on the orientation of the CuO_2 planes and, since it's grains could be more easily aligned by a simple melting process and/or by mechanical deformation [35], BSCCO was the first material to make use of the HTS properties in practical superconducting wires. However, due to the high value of anisotropy γ, its operational performance in high magnetic fields became compromised due to the irreversibility line (IL).

1.4.2 Operational Advantages of YBCO and GdBCO

YBCO is the HTS compound with the longest track of studies regarding physical properties. Besides being the first HTS operational above the temperature of liquid nitrogen ($T_c = 92$ K), it also presents incredible high values of critical current density in self-field; 2-3 MA/cm^2 at 77 K [36]. Moreover the anisotropy of YBCO is one of the lowest among HTS materials ($5 < \gamma < 7$) [37], especially when compared with BSCCO ($25 < \gamma < 30$) [38] and other type-II materials (Figure 1.13). This low anisotropy leads to a substantial shift in the *IL* towards H_{c2} and for that, YBCO was considered a better HTS candidate with high potential for power applications at self-field and in conditions of high magnetic fields (Figure 1.13).

However, in recent years, substituting the Y^{3+} for other RE ions such as Nd^{3+}, Sm^{3+}, Eu^{3+} or Gd^{3+}, became an attractive alternative due to improvements in certain operational aspects when compared to YBCO. For instance, La^{3+} and Eu^{3+} present a critical temperate of 93 K, higher than YBCO, but still their critical current densities range around 1 MA/cm^2 [39,40]. These differences in J_c and T_c among different RE compounds arise mostly due to the ionic radius of the rare earth atom [41]. If the ion is too small, it is no longer possible to achieve a single crystal phase throughout the material during synthesis, because of the tendency of RE ions to exit the RE vacancies. Whereas if the ions are too big, there is a greater tendency for it to substitute the Ba^{2+} and, once again, prevent a stable single-phase formation [42]. Nevertheless, in general, RE ions with bigger radiuses seems to yield higher T_c for the REBCO compound.

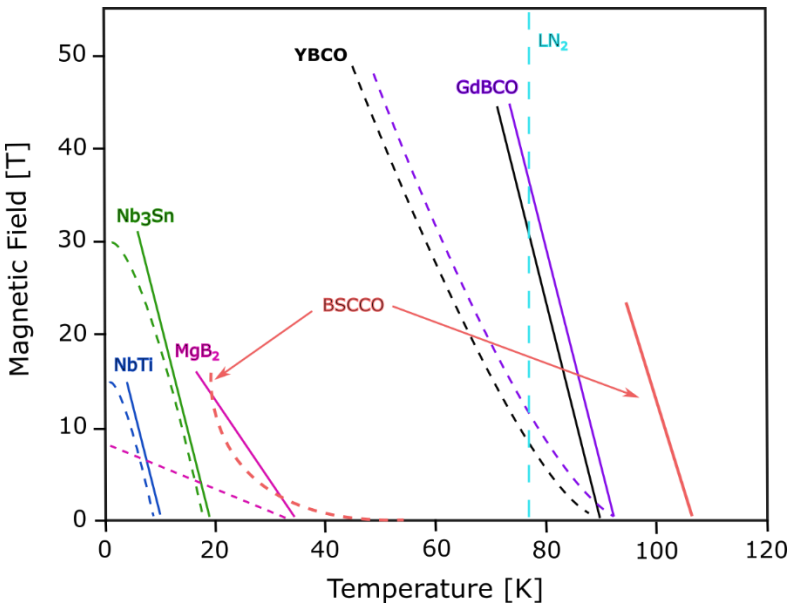

Figure 1.13: Irreversibility lines for the most used type-II superconducting materials.

In comparison with Y^{3+}, Gd^{3+} is the first bigger RE ion with lowest tendency to substitute the Ba^{2+} in the REBCO crystal. The GdBCO compound has a T_c of 94 K, therefore increasing H_{c2} and shifting the IL slightly above YBCO's IL. In addition, GdBCO's critical current density sits around 3-4 MA/cm^2 at 77 K in self-field, thus representing a clear advantage over the classic YBCO (2-3 MA/cm^2) for operating at higher currents and magnetic fields.

1.4.3 The Influence of the Oxygen Content

As mentioned in the previous section, the amount of oxygen in the crystal structure of the unit cell plays a crucial role in the final superconducting properties of the REBCO compound. As an example, Figure 1.14 shows the T_c dependency on the y in the $YBa_2Cu_3O_y$ compound [43]. Starting at $y = 6$, as oxygen start randomly filling the CuO chains, the non-superconducting tetragonal structure of the crystal is maintained up until $y \sim 6.35$ and so, for $6 < y < 6.35$ there is an absence of the critical temperature ($T_c = 0$). However, for $y > 6.35$, oxygen starts to periodically fill the vacancies, the a-parameter of the unit cell gets compressed and the b-parameter expands, leading to an orthorhombic phase ($T_c \neq 0$). As oxygen continues to dope the crystal, T_c starts to increase reaching its maximum of 94.3 K at $y = 6.92$. For $y > 6.92$, the crystal starts to become over-doped and T_c decreases reaching a minimum around 89 K.

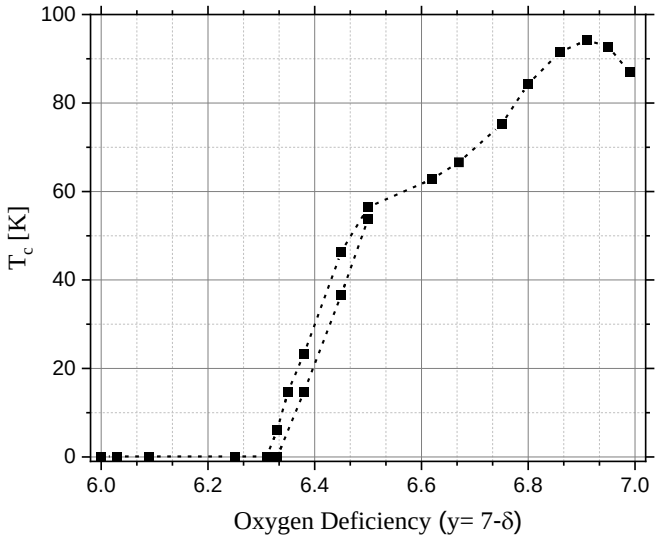

Figure 1.14: Critical temperature (T_c) evolution in YBCO as a function of oxygen content in the $YBa_2Cu_3O_y$ crystal. Figure taken from [43].

A reduced T_c in the final REBCO material leads to a series of disadvantages. First, evidently, if T_c goes below 77 K, the superconducting behavior cannot be reached in liquid nitrogen and cooling costs increase. In addition, if T_c is closer to 77 K the operational temperature margin with liquid nitrogen becomes narrower, making the superconducting behavior unstable due to small temperature variations. Furthermore, H_{c2} is also reduced, thus preventing an operation in high field. But, more importantly, due to the universal Ginzburg–Laudau behavior $J_c \propto (T_c - T)^{3/2}$ in REBCO films [44], J_c is also substantially reduced with T_c. Therefore, maintaining a reasonably high value for T_c is indispensable for any practical use of the superconducting properties of the REBCO materials.

1.5 Superconducting Wires

The incorporation of superconducting properties in wires for practical use in electric devices is probably one the main goals in the research field of superconductors. The first well established superconducting wires were LTS metallic alloys of NbTi and Nb_3Sn. Due to the malleability of the Nb alloy, these wires can be easily produced in large scale with relatively inexpensive mechanical techniques like co-extrusion [45]. However, the low performance of the LTS at high-fields (> 10 T) combined with the need for liquid helium as coolant, held back their implementation in many applications.

With the discovery of the HTS materials, the hope for a more practical superconducting wire was rekindled. The possibility of using liquid nitrogen as coolant finally created an optimistic scenario for making more versatile conductors in electric devices. The first generation (1G) of HTS wires, were produced in a Powder-In-Tube (PIT) process using the BSCCO ceramic compound [46,47]. These wires presented relatively high T_c (~ 96 K) and a reasonable J_c (10^4 – 10^5 A/cm^2) in self-field at 77 K, but an IL far below H_{c2} due to high anisotropy of the BSCCO crystal. Consequently, the 1G HTS wire performance at high-fields (> 10 T) became compromised [35,48] (Figure 1.13).

The second generation (2G) of HTS wires resolve the low high-field performance of the 1G architecture by substituting the BSCCO for REBCO compounds. In this 2G version, due to the biaxial texture requirement for the REBCO, the wire is built in a flat tape shape following a specific sequence of coating techniques to create a multilayer architecture. The first version of the wire was accomplished in 1991 by Y. Iijima et al. using a polycrystalline Ni-Alloy substrate coated with a biaxial oriented film of yttrium-stabilized ZrO_2 to grow an oriented YBCO film [49]. Since then, the architecture substrate-buffer-REBCO-stabilizer (Figure 1.15) has remained basically the same and the focus of research groups and manufactures worldwide has revolved around the optimization of the deposition methods used for the construction of these multilayers [50].

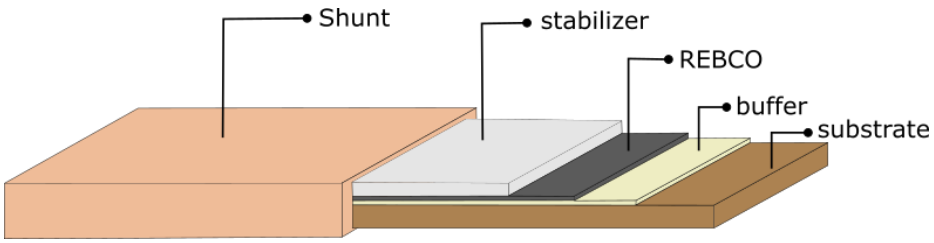

Figure 1.15: Classic multilayer structure of a 2G HTS coated conductor.

The following subsections, discuss the purpose of each layer in the 2G HTS architecture in the actual sequence of production steps. Moreover, a brief description of the most recent deposition techniques for each layer is provided highlighting the advantages, disadvantages and pending optimizations.

1.5.1 Substrate and Buffer

In the 2G HTS coated conductor (CC) architecture, the substrate usually consists of a thick (30 -100 μm) flexible metallic, nonmagnetic Stainless Steel (SS) or Ni-alloy, usually Hastelloy c-276. The substrate is the foundation to initiate the tape's construction, therefore it is the thickest layer in the architecture and is responsible for the thermal and mechanical properties of the conductor. The REBCO cannot be deposited directly on the substrate alloy due to metallic ion diffusion from the alloy causing reactivity in the REBCO. For this purpose, the substrate is coated with a thin buffer layer to provide a smooth chemically inert surface for the deposition of the REBCO material. The most common materials for the buffer layers are CeO_2, MgO, $Y:ZrO_2$, $SrTiO_3$, $La_2Zr_2O_7$ and $LaMnO_3$. Still, the most important requirement for the wire performance is the biaxial texture of the REBCO film. In the current industrial know-how, there are three major techniques capable of creating this texture in a continuous through put: Ion Beam Assisted Deposition (IBAD), Rolling-Assisted Biaxial Texture Substrate (RABiTS) and the Inclined Substrate Deposition (ISD).

In the IBAD process the buffer layer is deposited onto the substrate with the appropriate texture to grow the REBCO crystal. A high-power electron beam evaporates a chosen ceramic material and the vapor molecules condense on the metallic substrate forming the buffer coating. Simultaneously, a high energy ion beam treats the surface of the evaporated coating, improving adhesion and creating the right texture for the REBCO layer. Nevertheless, in the majority of cases, the texture of the initial buffer is not properly tuned for the REBCO epitaxial growth and subsequent layers may be added to finish the texture [51] leading to a complex buffer multilayer.

In the RABiTS process the biaxial texture is created directly onto the substrate instead of the buffer. The untextured metallic substrate goes through a sequence of rolling and annealing steps to produce the desired texture. The deposition of the buffer layer(s) becomes more simple afterwards; it merely mimics and transfers the underlying texture of the substrate to the upcoming REBCO film [52].

In the case of the ISD, a well-aligned MgO-buffer layer is deposited on a pre-cleaned metallic substrate by Physical Vapor Deposition (PVD) using an electron beam and a turntable feeding stage [53]. The alignment of the MgO develops naturally on the substrate due to the inclined angle of 25 - 30 ° towards the vapor source. Due to the growth selection by shadowing and the high deposition rate of the vapor, only the MgO grains with good alignment with the surface tilt become dominant [54]. The alignment improves with increasing deposition rate and film thickness, reaching an optimum reasonable texture at a thickness of about 2.5 - 3.0 μm. The result is a highly oriented film composed of a tilted columnar MgO structure. Finally, on top of the thick ISD-MgO layer, a thin MgO cap layer (∼200 nm) is grown homo-epitaxially at perpendicular incidence angle with the vapor. This final cap layer closes the gap between the large MgO columns and creates a continuous surface for the subsequent REBCO coating. The critical current density of the REBCO film in this case gains an extra degree of anisotropy, becoming maximal at the direction perpendicular to the projection of the vapor direction [55]. This approach has shown excellent quality and homogeneity for growing REBCO films with high critical current densities (> 2.5 MA/cm^2) on flexible substrates and is currently exclusively implemented by THEVA GmbH [56].

1.5.2 REBCO Coating

The coating of the REBCO film on the texturized substrate-buffer template is the most challenging part of the wire construction. The methods for depositing and growing c-axis oriented epitaxial REBCO grains can be classified as: *in-situ* and *ex-situ* growth techniques.

In the in-situ techniques, the deposition of the chemical elements and the growth of REBCO phase material happens simultaneously. Layer-by-layer the REBCO is deposited and grown whereby each new layer grows and reproduces the texture of the previous one. Common *in-situ* growth techniques include: Pulsed Laser Deposition (PLD), Pulsed Electron Deposition (PED), Chemical Vapor Deposition (CVD), Physical Vapor Deposition (PVD) and Sputtering. All of these techniques require a high vacuum environment, thus making the continuous production of long length REBCO CCs technically complicated. However, this issue did not stop CC manufacturers from creating dedicated complex high vacuum systems to incorporate a reel-to-reel REBCO in-situ growth system (usually PLD or MOCVD) [50,57,58] for producing meters of high quality 2G HTS tapes.

In the ex-situ growth techniques, the REBCO phase is not formed during the deposition of the precursor chemical elements. A separate thermal treatment at high temperatures is required to form the superconducting REBCO phase. This sequential process of REBCO deposition-growth is often used in solution-based techniques like Metal Organic Deposition (MOD) [59] and Sol-gel [60] where no vacuum is required for both steps. In addition, Chemical Solution Deposition (CSD) methods, like ink jet printing (IJP) [61,62] or slot-dye coating [63], can be used to deposit the metal precursors continuously over large substrate areas in ambient atmosphere, thus avoiding costly vacuum equipment. This is a low-cost operation that has been shown possible at an industrial level by D-nano [61] and Oxolutia [64].

The most recent deposition technique promising to fulfil the market needs of low-cost, performance and scalability, was develop by the SUNAM in a novel two-step [65] reactive co-evaporation by cyclic deposition and reaction (RCE-DR) process [66]. The two-step consists of fast co-evaporation of the precursor films at low temperature under low oxygen pressure (PO_2) and subsequent annealing at high temperature under high PO_2 to produce a quality epitaxial GdBCO CC at speeds up to 360 m/h.

There are many defects that can arise naturally in the REBCO film during the growth step; oxygen vacancies, in-plane dislocations, twin boundaries, antiphase boundaries, stacking faults, intergrowths, etc [67]. Discussing all of these different kind of defects during the REBCO synthesis is beyond the scope of this thesis. The bottom line is that the majority of these defects can create current percolation issues in the film that drastically reduces J_c [68]. For instance, in polycrystalline REBCO films, the grains boundaries act as current barriers reducing J_c to 10^4 - 10^5 A/cm^2 [69]. Nevertheless, is important to highlight that some of these defects can act as pinning centers and actually improve the pinning forces against *flux creep*, thus reducing the decay of J_c with an applied magnetic field H_a. This phenomena lead to intense research revolving the intentional creation of artificial pinning centers in REBCO layer during the CC manufacturing [70].

1.5.3 The Stabilizer/Shunt and Interfacial Resistance

The stabilizer is the last layer in the 2G HTS architecture and its primary objective is to protect the final epitaxial REBCO layer from corrosion with the atmospheric environment. In ambient atmospheric conditions, a slow irreversible chemical decomposition degrades the REBCO material into non-superconducting phases as described in equation [71]:

$$YBa_2Cu_3O_7 + 1.5H_2O \rightarrow 2.5CuO + 1.5Ba(OH)_2 + 0.5Y_2BaCuO_5 + 0.5O_2 \qquad (1.10)$$

Furthermore, apart from the obvious gradual destruction of the REBCO material, the formation of copper oxide and secondary phases creates an additional technical issue for the tape. The degraded layer forms a highly resistive barrier on the surface of the REBCO film, thus making the injection of high currents into the actual superconducting REBCO film practically impossible. Any physical current contact attached to such oxidized surface, would create an unacceptable joule heating loss in the interface. Therefore, in order to provide protection from atmospheric corrosion and a low resistance path for practical current contacts, the REBCO film is coated with a stabilizer metallic layer.

Knowing the contact resistance is crucial for estimating the minimum contact area needed to avoid excessive joule heating in the connection of the REBCO conductor with the current leads. A helpful way to describe this resistance independently of the contact area is to use a quantity known as "*specific contact resistivity*" (or *interfacial resistance)* ρ_c*:*

$$\rho_c = A_c R_c \ [\Omega\text{-}m^2] \qquad (1.11)$$

Where R_c is the contact resistance in Ω and A_c is the contact area in m^2. This quantity is used for practical application purposes since the thickness of the metal/REBCO interface cannot be properly defined.

Nevertheless, depending on the fabrication technique, the contact resistance of the stabilizer metal on top of the REBCO can change considerably. Depositing metals like indium, lead, tin, chromium, aluminum, nickel and copper, all lead to oxygen reactions in the REBCO/stabilizer interface causing two problems [72]:

- the surface of the REBCO film is depleted of its oxygen, thus losing the orthorhombic phase and destroying part of the superconducting property;
- the oxygen from the REBCO crystal can bound to an element of the metal and form an oxide resistive barrier at the interface ($> 10^{-3}\ \Omega\text{-}cm^2$).

Low values of interfacial resistance ($< 10^{-5}\ \Omega\text{-}cm^2$) are only achieved by using materials with a low affinity for oxygen like noble metals such as silver, gold and platinum. The vast majority of CC manufacturers chose silver for the stabilizer material due to the low price in comparison with other noble metals. The metal coating can be accomplished *ex-situ* or *in-situ* via magnetron sputtering or physical vapor deposition (PVD) after the REBCO growth. In comparison to PVD, sputtering provides a better adhesion of the silver onto the REBCO due to the extra kinetic energy of the silver particles created in the bombardment of the electron gun. However, PVD is a much simpler technique that provides the same (if not better) low interfacial resistance silver/REBCO by simply post-treating the coating in an annealing process. The *in-situ* deposition of silver yields the lowest interfacial resistance

values in the $10^{-9} - 10^{-7}\ \Omega\text{-}cm^2$ range since the REBCO is not exposed to air degradation [72]. Still, this approach is considerably more expensive due to the need for a multi-deposition vacuum chamber capable of: depositing/growing the REBCO, and sputtering the silver. The additional surface resistance of $10^{-5} - 10^{-2}\ \Omega\text{-}cm^2$ caused by air exposure while opting for an *ex-situ* deposition can be easily reduced to $10^{-9} - 10^{-6}\ \Omega\text{-}cm^2$ by cleaning the REBCO surface before coating and annealing the metal afterwards [73]. The effect of annealing the stabilizer in oxygen atmosphere is illustrated in Figure 1.16 for samples of YBCO coated with silver and gold contacts.

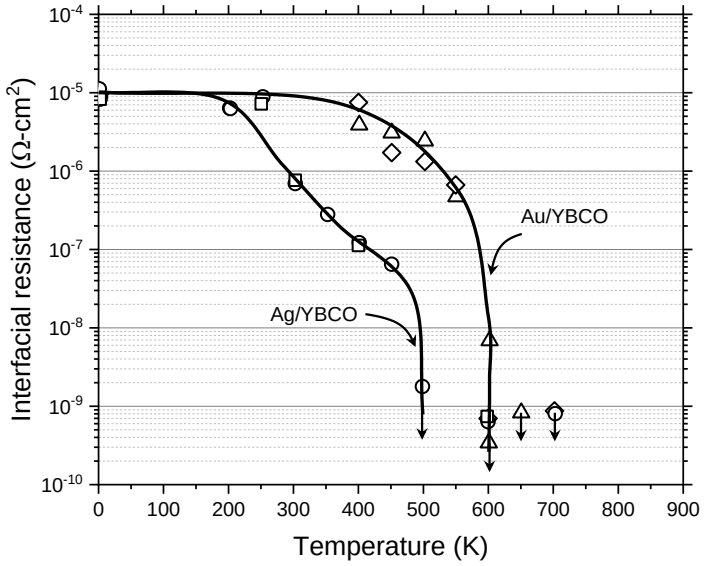

Figure 1.16: Interfacial resistance of silver and gold contacts on sintered bulk YBCO after oxygen annealing at different temperatures; annealing time was 1 h and oxygen was supplied at atmospheric pressure, flowing at a rate of about 2 m³/s. The arrows pointing downwards represent data obtained from measurements in the limit of the measurement equipment. Figure adapted from J. Ekin et al. [74].

The tuning of the interfacial resistance stabilizer-REBCO for the creation of new features in the 2G HTS tapes is the main topic of this thesis. More information on the practical limitations revolving the values of contact resistance $\Omega\text{-}cm^2$ will be discussed later in section 2.4.

1.6 The Oxygen Annealing of REBCO

During the growth process of the REBCO material, the final crystal structure arises naturally in the tetragonal phase, and so the oxygen deficiency must be compensated to achieve the orthorhombic phase. The standard technique for increasing the oxygen content in the $REBa_2Cu_3O_y$ film is called oxygenation and involves the annealing process of the whole substrate-buffer-REBCO-stabilizer structure in oxygen atmosphere. In many manufacturing systems, this is the same annealing process responsible for decreasing the interfacial resistance silver/REBCO.

This section discusses the variables influencing the final oxygen grating of the REBCO films, the oxygen path for it to be incorporated in the REBCO crystal, a basic introduction to diffusion theory and the considerations for performing the oxygenation process in a viable manufacturing time.

1.6.1 Oxygen Partial Pressure and Temperature Influence in $REBa_2Cu_3O_y$

In the oxygen-annealing treatment, temperature and oxygen pressure have a great influence in the equilibrium state of the oxygen content of the REBCO crystal [75–77]. In the detailed study performed by Jun-Ichi Shimoyama et al. [76], the oxygen nonstoichiometry behaviors for different $REBa_2Cu_3O_y$ compounds (e.g RE= Nd, Sm, Eu, Gd and Y) were precisely determined by thermogravimetric measurements for different temperature and pressure conditions. The dependency of oxygen content on temperature and oxygen partial pressure were found to be only slightly dependent on the RE element [76]. Moreover, the range of oxygen content in YBCO was found to be the largest among the RE elements, therefore, as a general example, the oxygen nonstoichiometric behavior for $YBa_2Cu_3O_y$ is shown in Figure 1.17.

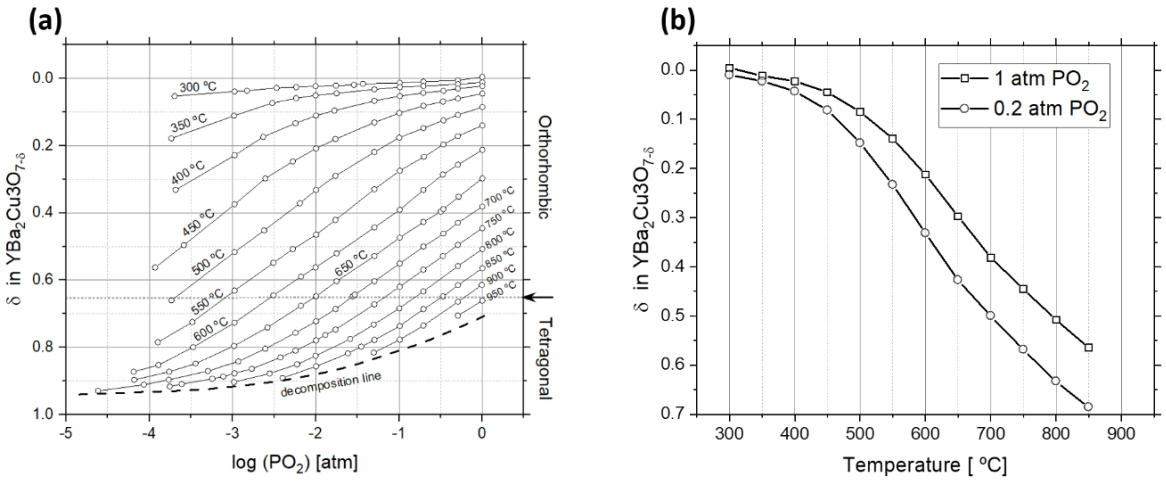

Figure 1.17: (a) Equilibrium Oxygen concentration δ in $YBa_2Cu_3O_{7-\delta}$ as a function of oxygen partial pressure environment PO_2 for different temperatures. (b) Oxygen concentration δ in $YBa_2Cu_3O_{7-\delta}$ as a function of annealing temperature for 1 atm of PO_2. Figures adapted from [76].

Looking at Figure 1.17(a), it is evident that - regardless of temperature - higher oxygen content is achieved at higher PO_2 values, yet no concrete advantage is yet known by annealing above 1 atm of PO_2 [78]. Moreover, for any arbitrary constant partial pressure of O_2, the oxygen content in $YBa_2Cu_3O_y$ increases as temperature decreases (Figure 1.17(b)). For 1 atm of PO_2, the maximum concentration for δ is achieved around 300 °C, still, as partial pressure drops to ambient partial pressure (0.2 atm), so does δ and consequently the superconducting properties of the material. Any heating of a REBCO material above 300 °C for long periods of time in ambient air can end-up removing oxygen from the orthorhombic structure, thus compromising T_c.

1.6.2 Basic Theory of Diffusion

For each pressure and temperature condition shown in Figure 1.17, a certain amount of time is required for the oxygen environment to reach the equilibrium stoichiometry in the $REBa_2Cu_3O_y$. This time is crucial for producing the REBCO CCs in an industrial scalable timeframe. Therefore, the

characteristic timescale of oxygen diffusion must be known for the calculation of an optimal temperature profile for continuous and optimum oxygen doping during the CC production.

The diffusion of one substance into another is described using Fick's first and second laws. The first law, assumes that the rate of mass transfer (flux) of a substance per unit area J_i is proportional to the species perpendicular concentration c gradient and the diffusion coefficient D of the media.

$$J_i = -D\frac{\partial \mathrm{c}}{\partial \mathrm{x}} \tag{1.12}$$

If the diffusion constant D is assumed to be the same over the spatial coordinates (isotropic media), the specimen concentration for the three-dimensional case is described by the second law in equation (1.13). The second law simply describes how the diffusion of the substance through the media causes a change of the species concentration in time.

$$\frac{\partial c}{\partial t} = D\left(\frac{\partial^2 c}{\partial x^2} + \frac{\partial^2 c}{\partial y^2} + \frac{\partial^2 c}{\partial z^2}\right) \tag{1.13}$$

Taking the one-dimensional case, the solution for equation (1.13) is given by [79,80]:

$$\frac{c(t) - c_\infty}{c_0 - c_\infty} \cong ke^{-\left(\frac{t}{\tau}\right)} \tag{1.14}$$

where c_0 is the initial concentration, c_∞ is the final concentration $c(t \to \infty)$, $k = 8/\pi^2$ is the exponential pre-factor and τ is saturation/relaxation time. Considering a purely limited bulk diffusion process, τ is defined by equation (1.15) where l is the thickness of the media. The relaxation time represents the time needed for the concentration to reach 1/e of the final value.

$$\tau = \frac{l^2}{2\pi^2 D} \tag{1.15}$$

These equations are fundamental for modeling and evaluating the bulk oxygen diffusion in the REBCO material. The exact analytical solution for anisotropic materials ($D_x \neq D_y \neq D_z$) in three dimensions can only be achieved in certain cases, which is why numerical methods are often used [79].

1.6.3 Oxygen Diffusion in the REBCO

For many cases, the assumption that diffusion takes place in a direction perpendicular to the surface with a spatially constant diffusion is a sufficient approximation of reality. However, as mentioned in subsection 1.4.1, the REBCO materials are strongly anisotropic in their physical properties. This anisotropy extends to the coefficient D where diffusion occurs primarily through the oxygen vacancies of the CuO chains along the ab-planes and so, the lack of vacancies along the c-axis makes its diffusion significantly slower when compared to the ab-planes ($D_{ab} > 10^4 - 10^6 D_c$) [81–83]. In this scenario, solving Fick's laws analytically starts to become more challenging.

One approach to simplify the diffusion modeling in an anisotropic media is to consider D a diffusion tensor [79]. The diffusion behavior is described with three independent diffusion constants D_a, D_b

and D_c along the three main crystal axes where Θ_i are the angles between the direction of diffusion and the crystal axes.

$$D = D_a cos^2(\Theta_a) + D_b cos^2(\Theta_b) + D_c cos^2(\Theta_c) \quad (1.16)$$

The diffusion D between a-axis and the b-axis can vary but the difference is relatively small [82], and so equation (1.16) can be rewritten as:

$$D = D_{ab} sin^2(\Theta) + D_c cos^2(\Theta) \quad (1.17)$$

Where Θ is the angle shift between the normal ab-plane and the *c-axis.* Modeling the diffusion with equation (1.17) implies that for a perfect *c-axis* oriented REBCO film $(\Theta = 0°)$ the diffusion across the thickness takes place predominantly via the *c-axis*. However, due to the large difference in diffusion between the *c* and *ab* directions (D_{ab}>$10^4 - 10^6 D_c$), even a slight one-degree tilt in Θ can make the diffusion contribution in both directions equivalent.

Equation (1.17) illustrates how measuring the experimental D_c and D_{ab} in oriented films can only be precisely done if it is ensured that the film was not grown at an angle. Otherwise there is always some contribution of fast loading along the ab levels, which leads to incorrect experimental values. Furthermore, the different experimental methods used to determine the diffusion D can also produce some differences in the measured values. These methods measure parameters that change proportionally to the oxygen concentration: conductivity σ [Ω-m] in *in-situ* resistivity measurements [84–86], mass swift in thermogravimetry [87] and distribution of oxygen tracer atoms (^{18}O isotope) in oxygen tracing [81,82,88].

Despite minor swifts in the orientation of the crystal for different samples (Θ) and the different experimental methods, the experimental data from different authors is coherent with the fact that the temperature dependence of the diffusion coefficient in REBCO follows an Arrhenius law as shown in Figure 1.18. Moreover, the comparison among different REBCO single crystals reveals that the diffusion coefficients of all crystals are in the same range. No dependence of the diffusion coefficient from the rare earth atom has been found [89]. Therefore, the data collection of Figure 1.18 for YBCO samples can be used to roughly estimate the time needed for oxygen loading generic REBCO films.

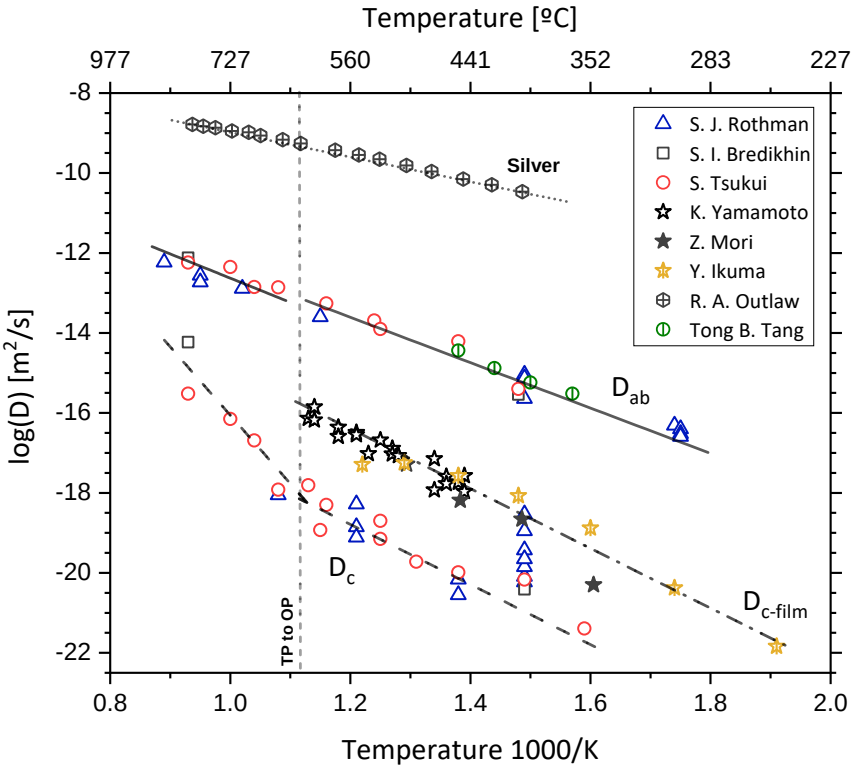

Figure 1.18: Arrhenius plot of chemical diffusion coefficients of oxygen in YBCO from different authors: oxygen tracer study from S. J. Rothman (blue triangles); oxygen tracer study from S. I. Bredikhin (black squares); oxygen tracer study from S. Tsukui (red circles) ; in-situ resistivity measurements from K. Yamamoto (black starts); an XRD study from Z. Mori (black filled start); oxygen tracer study from Y. Ikuma (yellow cut starts); For comparison, the oxygen diffusion in silver (crossed black hexagons) is also plotted from R. A. Outlaw.

The loading time is estimated here by considering a linear fit in the reciprocal temperature range from 1.1 to 1.8 K^{-1} for D_c (dashed solid line) and D_{ab} (black solid line) in the cluster of data of Figure 1.18. These fits can be considered the upper (D_{ab}) and bottom (D_c) diffusion limits in the REBCO crystal for the two orientations of the lattice. Using the D_c and D_{ab} fits in equation (1.17) and applying $D(\Theta)$ to equation (1.15), the relaxation time τ is estimated as a function of temperature in Figure 1.19 considering an arbitrary 3.0 µm thick REBCO film with initial oxygenation grating δ=0 and with different orientation angles for Θ. Figure 1.19 illustrates how impractical a perfect c-axis oriented REBCO film would be if diffusion took place only in the c direction. For instance, oxygen annealing at 350 °C to achieve $\delta \sim 0.2$ in $YBa_2Cu_3O_{7-\delta}$ and obtain optimum values of $T_c \sim 92$ K, would take more than 1 year. Small tilts in the orientation of the c-axis have a great influence in the oxygen loading time at different temperatures. This behavior is observed especially in THEVA-CC where the GdBCO superconductor grows with a tilt of approximately 22-24 ° due to the implementation of the ISD method [54].

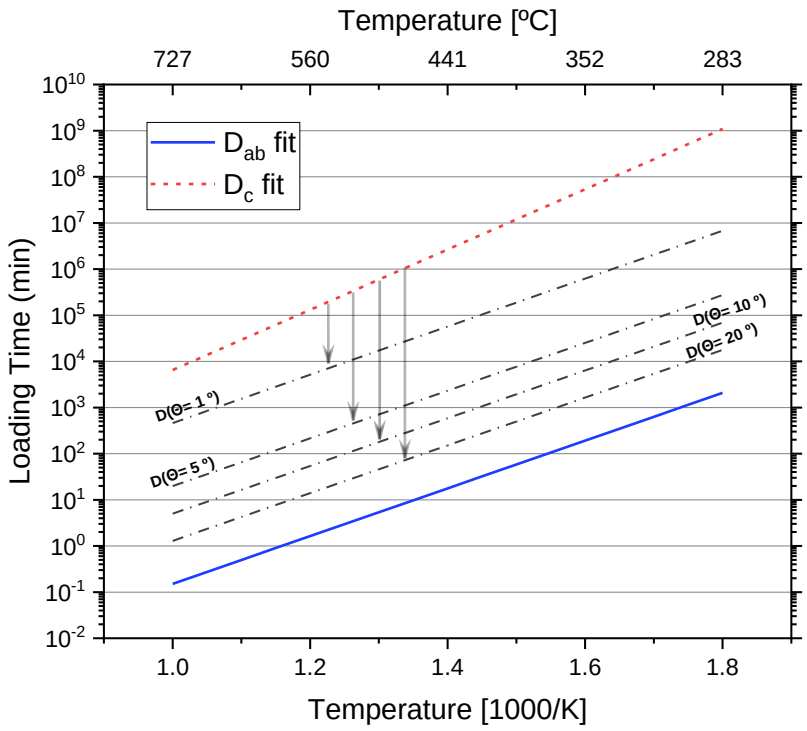

Figure 1.19: Estimation of diffusion relaxation times for 3 µm generic REBCO film considering the diffusion D a tensor following equation (1.17). The coefficients D_{ab} and D_c were taken from the fits of the gathered data from Figure 1.18.

A pure bulk diffusion assisted by the ab-planes is only part of the whole oxygen exchange mechanism. The presence of cracks, crystal defects and grain boundaries can also contribute to the diffusion across the thickness of the REBCO film [82,85,88]. More specifically, according to the mathematical model of Fisher, grain boundaries can be considered as regions with high diffusion D_{gb} capable of completely bypassing the diffusion along the c-axis ($D_{gb} > D_{ab} \gg D_c$) [90]. It is assumed that the diffusing substance can move along grain boundaries ($\sim$ 1 nm) into the depth of the film and then exit into the grains parallel to the surface at the volume diffusion rate D_{ab} [91]. Adding the grain boundary presence to the bulk diffusion process makes the overall oxygen diffusion in the REBCO film mainly limited by the diffusion D_{ab} along the ab planes (blue line in Figure 1.19).

In summary, due to the general low values for oxygen diffusion of D_{ab} ($\sim 10^{-10}$ - 10^{-12} cm^2/s) in the REBCO crystal at low annealing temperatures (400 – 350 °C), annealing solely at low temperatures to properly load oxygen becomes impractical for an industrial process. The standard annealing temperature profile for manufacturing CCs consists of speeding up the oxygen diffusion in the REBCO film by heating the material up to 500-600 °C and slowly cooling it down to ambient temperature [92–94].

1.6.4 The Influence of Surface Reactions

Bulk diffusion is indeed the main mechanism for oxygen to travel towards the vacancies existing in the CuO chains of the REBCO structure. Still, even before diffusing, the oxygen molecule must first pass through a series of reactions on the REBCO surface for it to acquire the proper atomic state required for initiating the bulk diffusion [95]. Depending on the state of the REBCO surface, the time required

for the completion of these reactions may or may not substantially increase the overall time for oxygen loading. Therefore, the possibility of surface reactions must be taken into consideration when analyzing the time for the diffusion process in the REBCO film of the CC.

According to [95], before diffusing, the oxygen molecule must first pass through 5 main reactions as illustrated in Figure 1.20. In the first step, the oxygen must suffer physi- and chemisorption for the rupture of the covalent bond and creation of an ionic bond (1). In the second step, the oxygen molecule suffers ionization (2), thus becoming a O_2^{2-} molecule by borrowing 2 electrons leaving a hole in the REBCO surface. In theory, since Cu ions can exist as Cu^{+}, Cu^{2+} or Cu^{3+} in the REBCO structure, they are considered the electron donors [96,97]. In the third step, the O_2^{2-} molecule is dissociated into charged ions O^{-} (3) and in the fourth, the ions diffuse across the surface to find an oxygen vacancy (4). Finally, in the fifth step, the O^{-} ion is incorporated in the vacancy of the surface layer by borrowing an extra electron thus entering the bulk oxidation state of O^{2-} (5) and hence starting bulk diffusion (6).

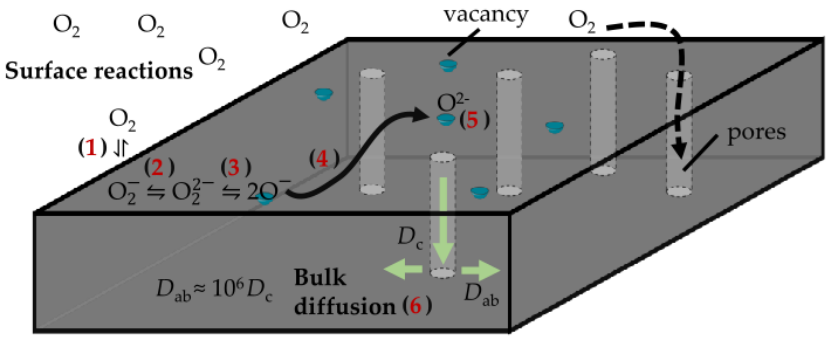

Figure 1.20: Schematic drawing of the oxygen surface reactions before bulk diffusion. The relevant steps are (1) chemisorption, (2) ionization, (3) dissociation (4) surface diffusion, (5) incorporation and (6) bulk diffusion. This Figure was taken from [80].

For the scenario where surface reactions limit the whole diffusion process, the saturation time $\boldsymbol{\tau}$ correlates to a reaction rate linked to the oxygen exchange at the surface and the thickness of the film. A parameter defined as *surface exchange coefficient* $\boldsymbol{k_{chem}}$ (cm/s) overwhelms the diffusion $\boldsymbol{D}$ (cm^2/s) and relates to $\boldsymbol{\tau}$ in equation (1.16) to define the rate of surface reactions as:

$$k_{chem} = l/\tau \tag{1.18}$$

Similar to the diffusion D, the reaction rate $\boldsymbol{k_{chem}}$ follows an Arrhenius law with a temperature dependency described by equation (1.19):

$$k_{chem} = k_0 e^{\left(-\frac{E_a}{k_B T}\right)} \tag{1.19}$$

Where k_B is the Boltzmann constant, E_a the activation energy in eV and k_0 is a pre-exponential factor in m/s. E_a represents the minimum kinetic energy required for the reaction to occur; the Boltzmann factor k_B gives the probability of the reaction to occur; k_0 is considered the total rate of collisions independent of temperature and k_{chem} is the number of collisions per time leading to a reaction [98,99].

From step 1 to 6 in Figure 1.20, a typical assumption is that one single process limits the overall exchange rate of oxygen between the surrounding atmosphere and the bulk material. This process is

referred to as the rate determining step (RDS). For REBCO single crystals with low defect density, bulk diffusion is indeed the main RDS [85,100] and for many years the majority of the superconductivity community extended this conclusion for the realm of thin films, even though in the presence of strong evidence pointing towards a surface limiting exchange process in other thin oxide films [101]. In the early years of manufacturing REBCO films for CC, some authors suggested that the surface reactions had to be considered for the oxygenation process [102,103], but it is only in the past decade that the importance of the surface exchange mechanism became clear to be the RDS [80,99].

One major indication of surface reactions controlling the oxygen exchange process in the REBCO film, is the presence of experimental measurements showing asymmetric rates for the in- and out-diffusion (τ_{in} and τ_{out}). Such asymmetry is not expected from a purely bulk diffusion process. Furthermore, in previous studies of the SUNAM group, it has been shown via Electrical conductivity relaxation (ECR) measurements that the silver coating has a significant influence on the oxygen exchange kinetics of YBCO films. Films coated with silver have faster exchange rates for both, oxidation and reduction processes (τ_{in} and τ_{out}) and lower activation energies compared to non-silver coated samples [80,99]. This enhancement of the ex-change kinetics due to the presence of silver is another evidence that oxygen exchange in YBCO is limited by surface reactions. Yet, the asymmetry between τ_{in} and τ_{out} was kept in the presence of a silver coating leading to the conclusion that bulk diffusion is still much faster compared to surface exchange kinetics enhanced by silver.

Identifying precisely the RDS among the surface reactions was beyond the practical scope of this thesis and so, from a practical perspective the overall exchange mechanism is simply divided here into surface exchange and bulk diffusion processes. More details about the analysis of these mechanisms will be discussed in subsection 3.3.2 of the methodology chapter 3.

2 The FASTGRID Project

Among all the different applications revolving 2G HTS REBCO tapes, the Superconducting Fault Current Limiter (SFCL) is possibly the one with highest potential of fully being accepted as a commercial device for the protection of the power grid. For many years now, different designs of SFCL demonstrators were built and successfully tested for low and medium voltages using commercially available HTS tapes. However, advocating in favor of all the operational advantages brought by the SFCL has been challenging due to the elevated costs associated with the HTS coated conductor itself and the cryogenic equipment required for operating the device. Finding the right scenario for justifying the need for an SFCL has been a patient journey for the superconducting R&D community.

For the past 20 years, power electronic circuits using solid state switches have gradually integrated the operational landscape of power grids forcing the integration of DC systems in the traditional AC operation. And now in Europe, the potential need for meshing these DC systems in high-voltage has led to a crucial re-evaluation of the safety protocol of the grid, especially regarding current faults. This is a major opportunity to insert SFCLs in the power grid and ensure its safety, but before reaching this reality there is still a demand for increasing the maximum electric field that REBCO tapes can withstand during fault current limitation in order to implement more compact/cost-effective SFCLs specially for HVDC grids.

In this scenario, the H2020 European project *FASTGRID* was conceived as a partnership between different companies and research centers in Europe and Canada aiming to fabricate the ideal coated conductor capable of fulfilling the HVDC requirements for a viable SFCL. In a general manner the four main objectives of the project were:

- Increase the electrical field that these conductors can withstand under limitation without any degradation of properties;
- Improve the value and homogeneity of the critical current I_c of the conductors;
- Raise the robustness of the tapes against all kinds of operational conditions using a novel approach to boost the so-called Normal Zone Propagation Velocity (NZPV);
- Functionalize its surface to increase the thermal exchanges with the coolant.

The majority of the objectives were accomplished and the project ended in July of 2020 with the successful test of two pancake coils based 2G HTS tapes from *THEVA GmbH* soldered with a metallic Hastelloy shunt. However, the results presented and discussed in this thesis are solely focused on the boost of the NZPV. This chapter will explain the context of the EU power grid regarding the existence of the *FASTGRID* project and the need for a SFCL. Furthermore, the work principle of a resistive SFCL will be discussed as well as the technical and theoretical limitations revolving the use of the 2G HTS architecture in the device and how boosting the so-called *Normal Zone Propagation* Velocity (NZPV) can lead to a significant superior, safer and cheaper SFCL performance.

2.1 The Power Grid

In this section, the basic definition of a current fault happening in the grid is presented together with a brief description of the classic devices used for suppressing the fault phenomena. Moreover, we discussed how the desire for a broader integration of renewable energy sources in the EU power grid makes the traditional AC fault protection obsolete and calls for new devices capable of dealing with high-voltage DC systems.

2.1.1 The Current Fault and Protection

Among all the expected and unexpected operational events happening in the electrical grid, current faults are considered one of the most destructive ones. A fault can be defined as an unwanted short circuit connection between one phase wire and another, or between a phase wire and the electric ground. As a result, the current flowing increases suddenly and damage is caused by the extra heat produced in the circuit. The term prospective fault current in this case refers to the highest electric current that can exist in a particular electrical system under short-circuit conditions.

For domestic house circuits the prospective current is low. In case of two phases touching each other, a simple fuse melts or a circuit breaker opens to safely suppress the surge of current. However, in the case of a transmission line operating at high voltages, two conductors too close to each other is already enough to cause the dielectric breakdown of air and create an arc. If the conditions of humidity and air pressure are right for the air to be ionized, the arc is persistent and can only be extinguished if the voltage is reduced. Even if the phases are securely spaced at all times, a lightning strike to the transmission line can increase the voltage for the time needed to once again create a persistent fault arc. Faults in transmission lines can also appear due to physical objects such as tree branches, animals, operating cranes, and so own.

Faults must be suppressed as fast as possible to avoid damages to the equipment connected to the grid, to secure the stable operation of power flow in the grid and to reduce potential danger to people. Like in a domestic household, the classical approach to eliminate faults in the power grid is to suppress the current surge by opening the circuit containing the short-circuit. As mentioned before, this is widely done by utilizing two devices.

- A fuse: a device regulated to self-destruct upon reaching a threshold of current. Once the device is blown, the current is suppressed and the fuse must be replaced. This solution is only applied to low voltage grids or as the last back-up plan in high voltage grids.

- A circuit breaker (CB): an automatic switch, triggered by a relay, capable of interrupting the passage of current without being destroyed.

Differently from a household, different switching responses are considered depending of the fault location in the grid. In distribution grids, line feeders usually have only one circuit breaker. Therefore, topological considerations must be rapidly made to isolate the faulty section and later on safely reconnect the loads. In the case of transmission grids, due to the meshed connections, power can flow from both sides of a transmission line and so one faulty line must be isolated by the action of two circuit breakers at each end of the line. Moreover, the grid must be prepared to operate in the N-1

state, meaning that it is compulsory to trip (open the line) the faulty line and continue to operate. Overall speaking, the action of fuses and circuit breakers must follow a protection plan to avoid inconvenient tripping, but also be fast enough to protect the other elements of the grid.

For a CB to actuate, first the fault's presence is detected by relays using an overcurrent criterion, directional criteria or measuring the zero-sequence voltage between the phases. Moreover, protection algorithms can be implemented utilizing different kinds of relays such as over current relays [104], differential relays and distance relays [105]. However, for the past decade, electrical grids have been expanding and incorporating new technologies that challenge the classical way these systems are operated, especially in a fault event.

2.1.2 The Challenge of Meshed HVDC Network

By lowering the carbon footprint from all economic sectors in the EU, the European Green Deal, expects the EU to reach climate neutrality by 2050. Since more than 75% of the greenhouse emissions correspond to the energy sector, the EU Renewable Energy Directive requires that 32% of the energy consumption comes from renewable sources by 2030.

Coincidently to the public opinion regarding the visual impact of wind farms and solar panels, the regions with higher potential for renewable energy production are indeed far from the consumption centers. For instance, wind velocity is considerably higher and more constant offshore than onshore, thus making offshore wind energy more efficient [106]. In addition, in the case of solar energy, the highest suitability range for photovoltaic cells is also in non-urban areas [107]. Moreover, thanks to the advances in power electronics converters over the past decade, the use of DC cables for energy transmission can now outperform the classical AC solution in the case of intercontinental transmission [108].

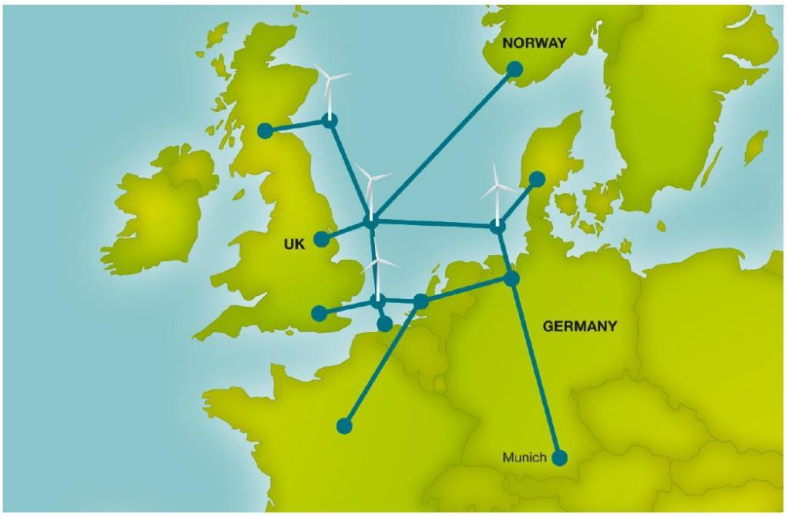

Figure 2.1: Estimated structure of the HVDC super grid in Europe by 2050.

In this scenario, projects like the *EC Project Twenties* [109] and *Best Paths* [110–112] have studied and confirmed the advantages of integrating large-scale solar and off-shore wind power farms in Europe

with a meshed/multi-terminal High Voltage Direct Current (HVDC) supergrid. The point-to-point HVDC links used nowadays do not present any topological requirements meaning that the current fault can be suppressed by the AC/DC converter control actions on either end of the DC side or by traditional AC breakers on the AC side. However, meshing the HVDC lines in a multi-terminal grid like shown in Figure 2.1, implies having to suppress faults on the DC side of the grid [113].

When operating at high voltages, protecting the grid in case of a DC fault becomes a critical issue for the overall safety of the network. Switching times longer than 5 ms will cause significant rise in the offshore grid frequency, which could cause the turbines to trip [112]. Moreover, the HVDC links increase drastically the prospective current fault due to the extra current stored in the capacitors of the AC/DC converters. When a fault occurs, besides having to deal with the N-1 protocol, a faulty HVDC line must be isolated as soon as possible to avoid destruction of the converters. As explained in [114], a prospective DC fault current of 3.5 kA will lead to the destruction of the antiparallel diodes of a converter in less than 5 ms if it is not suppressed in time.

In addition, the theory behind breaking the flow of a direct current is not as simple as opening a circuit breaker like in the AC case. For clarification, the circuit of Figure 2.2 exemplifies the basic principle of all DC breakers with equation (2.1) describing the circuit behavior.

$$U_G = L\frac{di}{dt} + Ri + u_{CB} \quad \rightarrow \quad \frac{di}{dt} = U_G - (R_G i + u_{CB})\frac{1}{L} \tag{2.1}$$

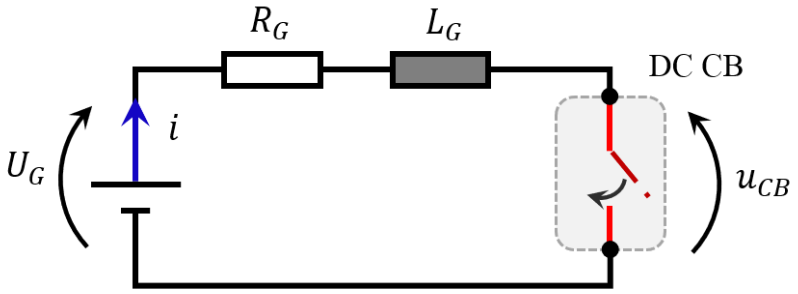

Figure 2.2: Basic conceptual circuit for illustrating the conditions of a Direct Current (DC) Circuit Breaker (CB).

Where i is the current, L is the grid inductance, R_G is the grid resistance, U_G is the power grid voltage and u_{CB} is the voltage across the DC circuit breaker. This equation bluntly shows that if R_G is small and constant, the fault current will only decrease (di/dt <0) if the voltage across the circuit breaker, namely the counter voltage, exceeds the voltage of the grid ($u_{CB} > U_G$). A counter voltage u_{CB} superior to U_G must be generated for a sufficient amount of time for the fault current to be suppressed to zero within the fault current suppression time. For this reason, differently from an AC interruption the HVDC interruption presents some major challenges [115]:

- DC systems do not have a zero-crossing point of the current like in AC, meaning there is no moment where the magnetic energy of the system ($Li^2/2$) is zero. For AC systems, the zero crossing provides an opportunity to interrupt the current when there is no magnetic energy thus alleviating the AC breakers from absorbing the fault's energy whereas in HVDC, the breaker must be prepared to absorb mega joules of the energy. An example to illustrate the magnitude of such energy is given by [115], where a HVDC circuit breaker should be tough enough to absorb at least 11 MJ of energy when interrupting 15 kA fault current flowing in a

100 km suspended transmission line. Such energy is equivalent to absorbing and stopping a 30-ton train running at 100 km/h in a few milliseconds.

- The fault in a DC system is only limited by the resistance R in the path of the current whereas in AC the peak value is also limited partially by the inductance of the circuit. This means that in HVDC the fault reaches the peak current much faster than AC. Considering a DC current rate-of-rise in the range of a few kA/ms [116], in order to be able to handle a manageable value of peak current, the actuation time of the HVDC breaker cannot exceed 8–10 ms. The HVDC breaker must be somewhat 10 times faster than a standard AC breaker (20 ms) [114] to clear the fault during the rise before reaching the theoretical peak. The HVDC fault current might not be as high as the AC breaker rated short-circuit breaking current (63-80 kA), but as mentioned before, the challenge is to act fast enough to prevent undesirable consequences to elements of the DC system like the converters. According to [117] relay times of 1-3 ms for the fault detection are considered tolerable.

- In a HVDC system, the breaker must have a robust and reliable electronic circuit capable of detecting the fault and quickly producing (within a few milliseconds) a sufficiently high counter voltage u_{CB} to be able to start suppressing the current. Contrarily, in an AC system, the breaker passively withstands the transient recovery voltage imposed by the system after the mechanical interruption of the current.

Even with all the R&D of high-voltage DC circuit breakers in the last 20 years [118], the breakthrough of hybrid HVDC breakers [119] and the creation of a dedicated HVDC prototype [120] for the project *Twenties*, the DC fault remains an issue. According to the RC Twenties project, this technology remains expensive, bulky and unreliable due to the high complexity of the active electronic control circuit [121]. Furthermore, it was concluded that the cost of the fault protection function should be less than 10 M€ per equipment in order to make the meshing of a HVDC network economically viable.

2.2 The Superconducting Fault Current Limiter

One technology brings a very attractive solution to the DC fault current problem: The Superconducting Fault Current Limiter or SFCL. Since the first SFCL concept in 1963 [122], different types of SFCLs have been proposed with different operational principles, many have been built and successfully tested [123,124]. In this section, we briefly discuss some of the SFCL designs and their classification giving focus exclusively to the resistive SFCL general design, it's work principle, the equivalent circuit, operational conditions and the optimizations needed for a reliable large-scale implementation.

2.2.1 A Brief Overview of SFCL Designs

In a broad classification, the SFCLs can be divided into two operational categories: the quench based and the none-quench based. The quench can be defined as the intrinsic transition from the superconducting state to the resistive normal state when the critical current I_c is surpassed in a superconductor element. This resistive switch happens fast and passively but it can lead to thermal

damage in the superconductor element if not well controlled. The non-quenched SFCLs, like the *DC biased iron core* type [81][82] and the *Bridge type* [127][128], use the DC zero-resistance feature of a superconductor to implement an elaborate isolated control circuit for limiting the fault. Therefore, quench related damages are avoided and recovery times for the SC element to resume operation become almost instantaneous. Still, apart from the *DC biased iron core*, these circuits are not completely fail-safe due to the complete reliance on the actuation of semiconductors. On the other spectrum, quench based SFCLs are considered fail-safe, but must be very well designed to avoid damaging the SC element. These SFCL can be subdivided into: inductive, resistive and hybrid types.

The premise of a resistive SFCL (or rSFCL) is adding an SC element in series with the power grid and let the non-linear current voltage behavior of superconductors limit the short-circuit current at the first current rise. This is a robust and simple implementation concept that requires no active control circuit, but exposes the superconductor to intense joule heating, thus requiring large recovery times that can go up to seconds. Furthermore, the device size and the amount of superconductor material needed for a resistive type SFCL scales considerably with the rated current and voltage. Nevertheless, given the simplicity and reliability of this design, many prototypes have been built and tested [129–135] with different designs for the SC element and some medium-voltage models were even considered for full commercial applications [136]. These designs for the resistive SC element will be discussed in subsection 2.2.3.

The inductive SFCL type is also referred to as the *shielded* type and its circuit design can be basically compared to a classic transformer with the primary winding connected in series with the grid and a secondary winding made of a perfect short-circuited superconductor [137]. In normal operation, the current induced in the secondary winding is below I_c and the superconductor shields the magnetic field inside, making the resulting impedance equal to the low stray inductance between windings. In the occurrence of a fault, the induced current surpasses I_c, the superconductor winding quenches and the magnetic shielding disappears, thus increasing the impedance in the primary winding and limiting the current. Differently from the resistive type, the inductive type does not present an invisible impedance to the grid in normal operation, but it can be designed to reach neglectable values. The key issue with this concept is maintaining a practical size and weight for the device while using an iron core for the windings of the magnetic circuit. Some designers have proposed removing the iron core [138], but the results of the air coil demonstrated a significant reduction of the impedance for limitation.

Observing the overall advantages and disadvantages of both resistive and inductive SFCLs, for the past two decades, R&D designers have come up with *hybrid* switching concepts trying to incorporate solid-state breakers and fast mechanical switches into the SFCL. Many arrangements have been proposed and successfully tested [139–142], but these systems tend to become complex as trying to scale to transmission level voltages [124].

Nevertheless, even in the presence of such variety of SFCL designs, none of the state-of-the-art models are yet fully commercially available for high voltage applications. However, it is reasonable to assume that the best design would emerge from fulfilling the majority of the requirements expected from an ideal fault current limiter. These requirements can be listed as [124]:

- Fast and effective current limitation
- Quick and automatic recovery time

- Fail-safe and reliable operation
- Low AC loss and low normal operation voltage drop
- Compact and light weight

All SFCLs can achieve fast and effective current limitation, the major differences appear in the recovery time, fail-safeness, normal operation loss and size/weight. That being the case, when comparing the SFCL types, the classic resistive concept remains as one of the most promising approaches since it checks the majority of the present bullet points.

2.2.2 Work Principle of a Resistive SFCL

The single-phase circuit for a purely resistive SFCL is shown in Figure 2.3. The SFCL module is represented by two resistances connected in parallel: the variable resistance of the superconductor material R_{SC} and another "fixed" resistance R_{shunt} representing all other conductive materials. Both, the SC element and the shunt resistance, remain cooled by the cryogenic environment (T_{op}) at all times. Figure 2.4 shows the three operation modes of the SFCL module.

For the grid operating in normal condition, the current flows with rated value ($I_{ac} = I_a$) smaller than the SC critical current ($I_a < I_c$), as a result $R_{SC} \approx 0$, thus making the SFCL impedance neglectable to the grid. In a fault condition, if the current I_{ac} surpasses I_c, the SC element will start dissipating energy and enter the normal state. Consequently, the resistance R_{SC} increases sharply following the Power Law (subsection 1.3.4). This resistive switch, from the SC state to the normal state, is also known as "quench". The sudden R_{SC} increase after the quench will limit the rise of I_{ac} to an acceptable operational level. Meanwhile, as R_{SC} increases, R_{shunt} starts sharing current to alleviate the joule heating created in the SC element before the opening of the CB. Without a CB, if the fault persists for too long, the joule heating could damage or even destroy the SC element. Once the CB is opened, the current is cut and the SFCL module enters the recovery process where the cryogenic environment will cool down SC material back to $R_{SC} \approx 0$.

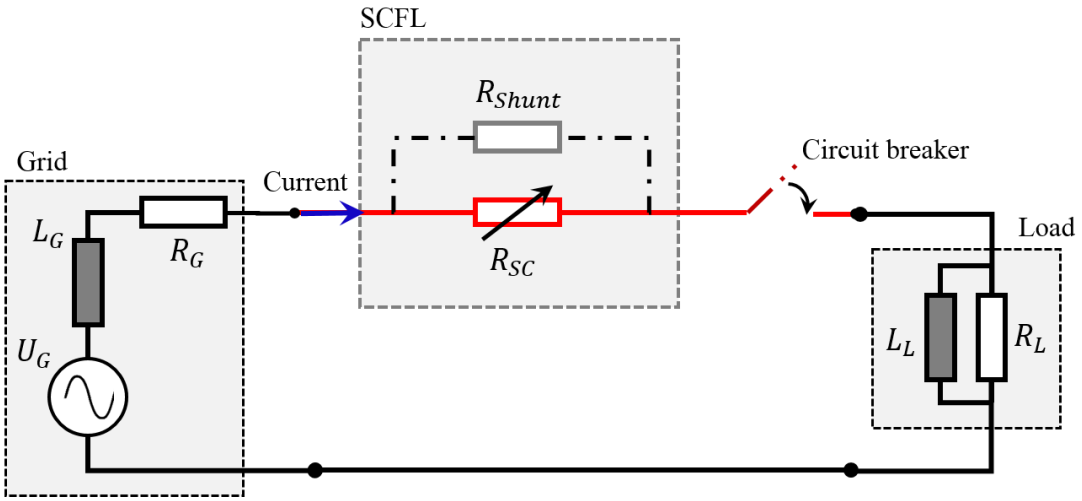

Figure 2.3: Equivalent electric circuit for pure resistive SFCL connected to the power grid.

After recovery, the circuit breaker closes and the SFCL goes back to “Normal Operation”. If the fault persists, this limitation cycle repeats until the fault is completely extinguished, or the circuit breaker is kept permanently open waiting for a contingency plan. Due to the fast and intrinsic switching behavior of the SC element, this type of SFCL is considered fail-safe and offers many technical and economic benefits to the power grid [143].

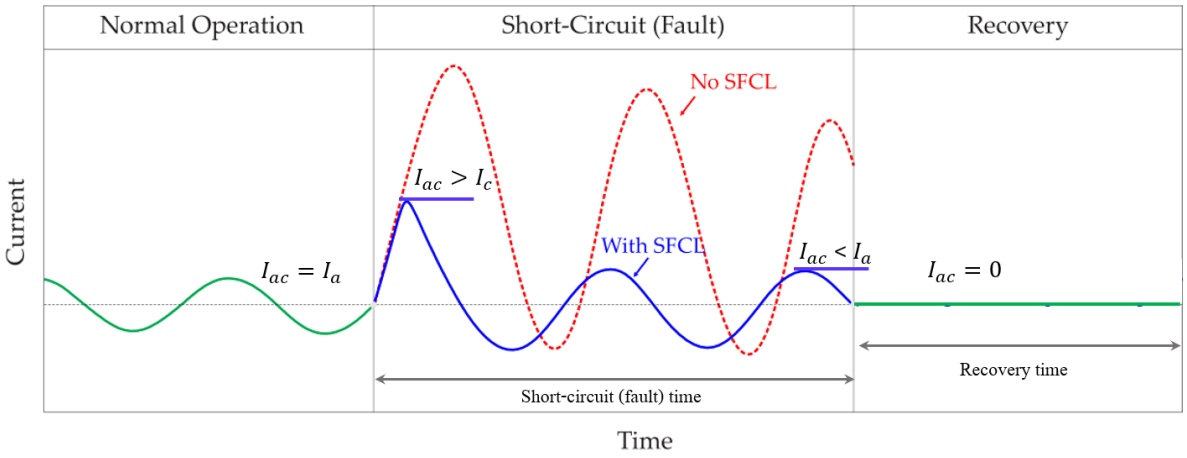

Figure 2.4: Operation modes of a resistive SFCL module.

2.2.3 The SC Element

All ceramic HTS superconductors that rely on the disposition of Cu-O planes to achieve the superconductor state, present lower J_c and H_c properties in the polycrystalline structure when compared to their respective crystal orientated phase. However, melted cast processed (MCP) BSCCO 2212 [144], even though poly-crystalline, has reasonable properties for practical applications. For instance, the critical current density has a moderate value of J_c~1000 A/cm^2 at 77 K, and the J_c reduction due to external magnetic fields is one order of magnitude lower than the polycrystalline YBCO [145], making the use of MCP-BSCCO 2212 manageable in self-field even in high current applications.

The first robust prototype of a resistive SFCL for medium-voltage-level was developed and manufactured by Nexans Superconductors using the MCP-BSCCO 2212 material to make tubes cut into bifilar coils [146]. The module (Figure 2.5) was built in 2003 and successfully tested in a three-phase 10 kV, 10 MVA demonstrator named CURL10 [147,148]. This design, although practical, presented difficulties with scaling up to higher voltages and Nexans changed the focus to the resistive type with magnetic field assisted quench [149].

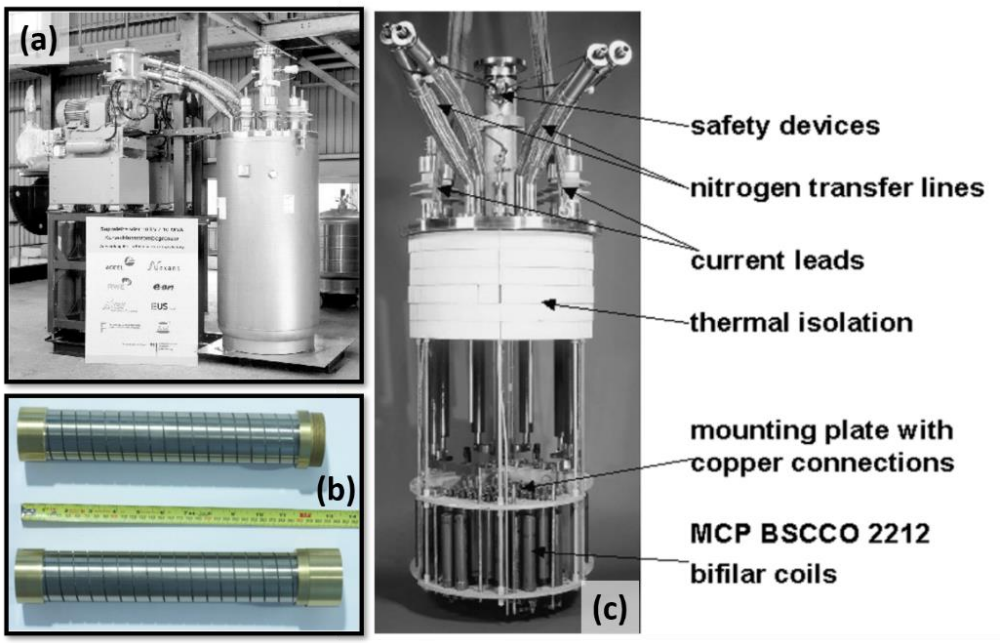

Figure 2.5: Pictures of the demonstrator CURL10, 10 kV, 10 MVA resistive SCFCL. (a) Fully assembled SFCL with cryostat and cryocoolers. (b) The bifilar MCP BSCCO 2122 tube used as the SC element. (c) The internal structure placed inside the cryostat with the MCP BSCCO 2122 coils.

The past 15 years of development of high performance textured REBCO materials on metallic substrates also played a role in over shadowing the use of MCP-BSCCO 2212. The potential of REBCO materials like YBCO only became noticeable once methods of preparing it in textured ways began to appear. In the 90's, melted textured bulk YBCO structures created from single domains, either by Bridgman [150] or top-seeding grown [151], provided the first opportunities to test the YBCO material for current limitation [152,153] and in several SFCL demonstrators [139,154]. In bulk YBCO, the lack of high angle grain boundaries (HAGB) yields J_c values up to 10^4 to 10^5 A/cm^2 and the characteristic n-value in the Power-law ($E(J) \propto (J/J_c)^n$) is higher than BSCCO, thus making a sharper transition to the normal state above J_c [155] . However, current limitation tests turn out to be destructive for the majority of bulk YBCO samples and not enough development was accomplished to scale it up to industrial SFCL devices. Nevertheless, these bulk YBCO structures remain valuable as "proof-of-concept" for resistive SFCL and other devices.

In parallel with the developments of bulk YBCO in the 90's, the improvements of physical vapor deposition (PVD) methods for thin films like IBAD also showed the potential for coating structures with YBCO for applications. But in the initial stages of this research, the levels of J_c at the time were not enough to justify the use in the resistive SFCL. The game changer for the RECBO materials only started becoming clear in the early 2000's when thin YBCO films grown on long lengths of metallic substrates started to presented consistent values of J_c in the MA/cm^2 range at 77 K. As discussed in section 1.5, the multilayer structure of these 2G HTS tapes, besides allowing high-values for J_c, offers many advantages for implementing the resistive switching behavior into the rSCFL. For instance, the recovery time depends very much of the geometry of the superconducting material. For a thin film superconductor, the recovery time ranges from a second to a few seconds whereas for a bulk the recovery time can take minutes [156,157]. Moreover, the asymmetric shape of the conductor reduces the AC losses [158] when compared to bulk materials and makes it technically easier to inject current into the REBCO layer.

After the first successful test of a rSFCL with YBCO coated conductors in the European Superpoli project [159], many follow-up theoretical analysis and prototypes have shown the great potential of these wires for current limitation [160] and other applications. Consequently, for the past 10 years, all major projects on resistive SFCLs have based their designs on REBCO tapes [136,161–166]. The traditional approach was to substitute the BSCCO 2212 tubes (Figure 2.5(b)) for bifilar coils of 2G HTS tapes (Figure 2.6) staked in series.

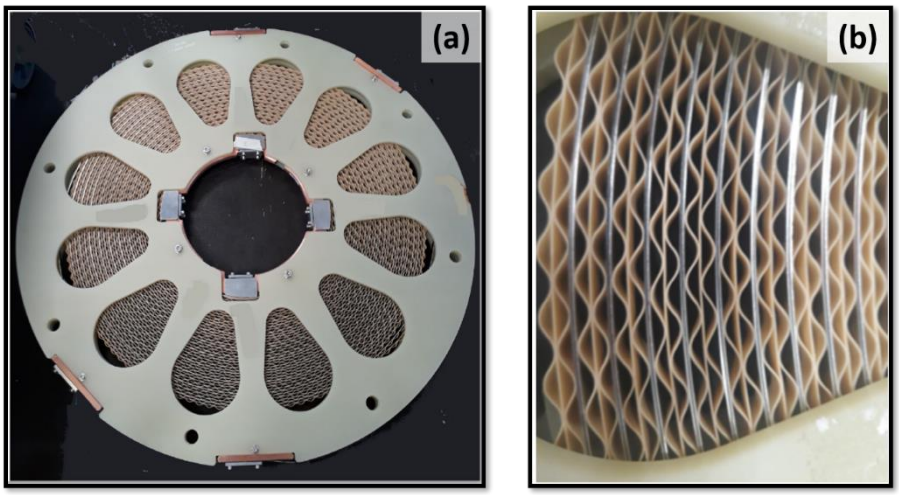

Figure 2.6: FASTGRID pancake bifilar coil prototype (5 kV/1.5 kA) sub-module. According to the FASTGRID specifications one module will consist of 10 sub-modules of coils connected in series. In the sub-module coil, two bare CCs are separated by two corrugated fibre glass tapes. This configuration provides the HV isolation and an efficient cooling. The critical current is about 2.6 kA. Figure taken from [164].

The idea of using a thin YBCO film grown on sapphire substrate [167,168] was also investigated for resistive SCFCLs. The first functional model was accomplished on epi-polished sapphire wafers by Siemens in 2000 [129] and led to a 100 kVA successful test following the manufacturing of a three phase 1 MVA demonstrator in 2001 [169] and a 1 kA DC prototype [170] in 2005. Although promising, a major issue for the commercialization of this SCFL with epi-polished sapphire wafers is the cost and the limited wafer size resulting in a large number of connections to reach the desired rated voltage and power [114,124]. One way to reduce the wafer cost is to increase the power-surface ratio YBCO/Sapphire to reduce the amount of sapphire needed. This concept is seen in the attempt of designing new meanders [171] and trying to coat both sides (top and bottom) of the sapphire with YBCO [172]. A second way is to use sapphire ribbons produced by the Edge defined, Film-fed Growth (EFG) process instead of wafers. The EFG process can continuously grow thick long length ribbons and assure the maximum surface utilization when depositing the YBCO. However, dealing with the roughness of the EFG sapphire is still a challenge for consistently growing thick high-quality epitaxial REBCO films with high values of critical current density above 1 MA/cm^2. Another indirect way to compensate the overall price is to grow the YBCO with cheaper techniques like CSD [50,61,173]. Still, the inherit costly manufacturing process of the sapphire currently remains the major barrier [174].

2.2.4 Operation in Liquid Nitrogen

The simplest way to cool down the SC element for operation in the SFCL (and other HTS devices) is to submerse it directly into the 77 K cryogenic environment of liquid nitrogen (LN_2). This method although efficient, has an inherent disadvantage regarding the heat transfer in the liquid/solid interface between the SC and the LN_2. Depending on the temperature difference between the liquid and the solid, the heat transfer decreases drastically due to film-boiling formation in the interface. Figure 2.7 shows the heat-flux in the liquid/solid interface as function of the temperature gradient between the domains at 1 atm.

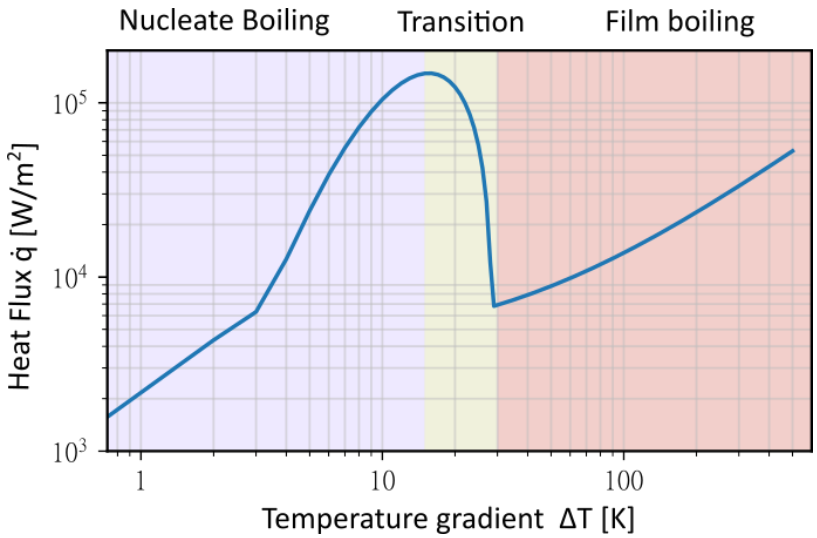

Figure 2.7: Heat transfer from a metal surface to liquid nitrogen, showing nucleate-boiling and film-boiling regimes. Figure adapted from [175].

For low temperature gradients $\Delta T \leq 10\ K$, the heat flux is low ($< 2 \times 10^5\ W/m^2$) and the liquid/solid interface is continuous. This regime is called *nucleate-boiling* and according to [72], the average heat-transfer in this condition can be approximated by the function:

$$\dot{q} \cong [5 \times 10^2]\Delta T^{2.5}\ [(W/m^2)(K^{-2.5})] \tag{2.2}$$

As ΔT increases beyond 10 K, at a critical heat flux of about $2 \times 10^5\ W/m^2$, nitrogen gas starts forming in the interface creating an insulating film that drastically reduces the heat transfer. In this "*film-boiling*" regime, if the heat source in the solid is not controlled to stay below $\dot{q}$, the temperature of the solid will increase rapidly. In the case of a REBCO conductor operating in an SFCL, the dissipated energy during the fault is orders of magnitude higher than $\dot{q}$, and so, almost all heat transfer happens via conduction along and in between the layers of the CC. For this reason, the overall thermal conductivity and heat capacity of the CC plays a vital role in limiting harmful temperatures in the REBCO film during quench.

For an SC element operating in a continuous superconducting state, equation (2.2) is a straightforward approach for the design of current contacts and other electric elements relying on the cooling mechanism of liquid nitrogen. This equation will be used later on to explain the operational limits of high interfacial resistance silver/REBCO.

2.2.5 The Hot-spot Regime

Because of the manufacturing techniques used to synthetize the REBCO material in the CC, the value of the critical current I_c is not completely homogenous across the whole length of the conductor. As an example, the I_c fluctuation along 12 meters of a GdBCO tape produced by THEVA GmbH is shown in Figure 2.8. This tape has a maximum I_c of 622.4 A with an average of 517.3 A and a standard deviation σ of 36.39 A (Appendix Figure D-2). The standard deviation here is less than 10%, meaning a fairly homogenous I_c distribution. Nevertheless, even with a higher homogeneity ($\sigma < 5\%$) it is almost impossible to avoid small region(s) with lower critical current.

During a short-circuit (Figure 2.4), depending on the level of the current fault, the SFCL can end-up operating in two different conditions: the *clear-fault* or the *hot-spot* regime. A dead short-circuit, means that no impedance is in the way of the current fault and so the prospective current I_p of a dead-short is usually much greater than the critical current I_c of the HTS conductor. This creates the ideal clear-fault scenario, where the I_c inhomogeneities become irrelevant and the conductor's length quenches homogeneously. However, dead shorts are rare events and more than 90% of short circuits happen through an impedance, thus making the prospective fault current range randomly from nominal values up to a clear-fault condition.

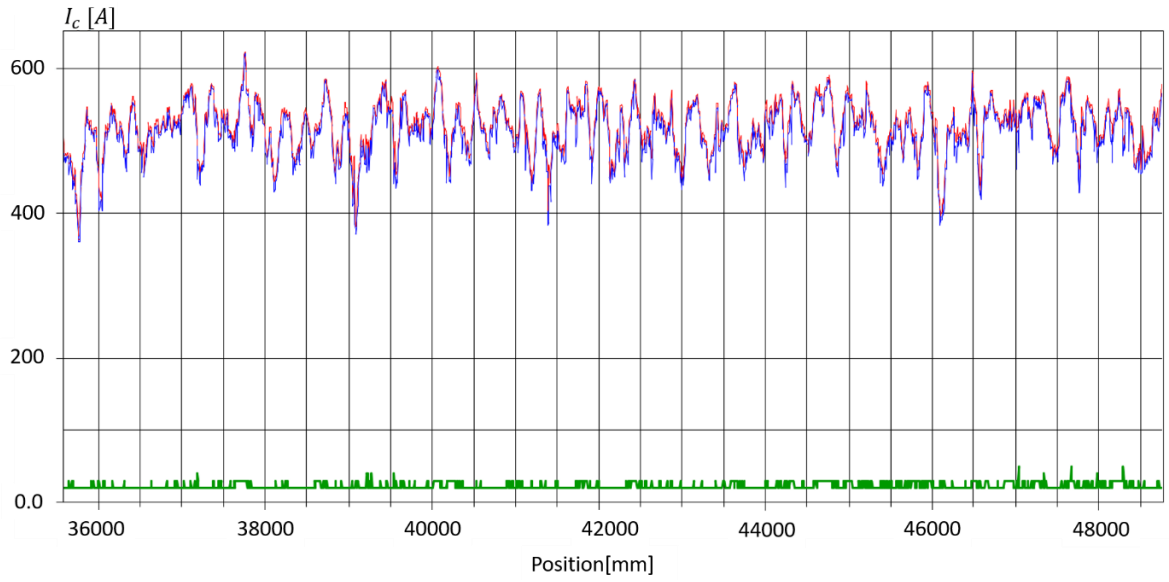

Figure 2.8: Tape star critical current scan for 12 meters of THEVA GmbH tape code FG-ICMAB-001. The official report of this scan can also be found in Appendix D of this thesis.

In case of a fault through an impedance creating the condition $I_p \approx I_c$, a lower I_c region in the conductor will locally dissipate energy in the form of heat, thus creating the commonly known "hot-spot". As long as the cooling rate of the cryogenic fluid (liquid nitrogen) plus the heat conduction along the wire balances the joule heating in this hot-spot zone, the superconductor will remain thermally stable and no resistive normal zone will appear. However, if the dissipated energy in the hot-spot surpasses a certain amount, the conductor will quench locally and expand in a thermal runway across the length. If the quenched zone does not spread fast enough, the heat accumulation in the initial hot-spot can damage the tape irreversibly. Assuming adiabatic conditions, the minimum

amount of energy required for initiating a quench is known as the minimum quench energy (MQE) and is described by [176]:

$$Q_{MQE} = \int_{T_{op}}^{T_l} c_p^{tot}(T)\, dT$$

Where T_{op} is the initial operating temperature of the wire and T_l is the temperate where current starts being diverted to the substrate and the other metallic coatings. The MQE is also referred to as the stability margin and depends solely on T_l and the total thermal capacity of the wire. The presence of metallic layers in the substrate and the stabilizer (Hastelloy, Ag, Cu, Ni, etc.) increases the thermal capacity $c_p^{tot}(T)$ setting a higher energy Q_{MQE} for the hot-spot to initiate quench.

2.3 The Design of the Resistive SFCL with 2G HTS Tapes

The dimensions of the metallic layers on a REBCO tape can have a significant impact in the cost/performance of the SFCL. These relevant dimensions are depicted in the simplified cross-section scheme of a HTS tape in Figure 2.9 [177]. Assuming that the electric and thermal behavior is completely homogenous throughout the cross-section of the wire, the total normal state resistivity and the volumetric heat capacity $J/(cm^3\text{-}K)$ of the conductor becomes a compound value of all materials involved in the construction following the formulas:

$$c_p^{tot} = \frac{1}{A_{total}} \sum_{m=1}^{M} c_p^m A_m \qquad and \qquad \frac{1}{\rho^{tot}} = \frac{1}{A_{total}} \sum_{m=1}^{M} \frac{A_m}{\rho_m} \tag{2.3}$$

Where M is the number of conductive and non-superconductive materials effectively changing the conductor's conductivity $1/\rho$ and thermal capacity c_p. The area A_m represents the cross-section area of the material m with resistivity ρ_m and specific heat c_p^m.

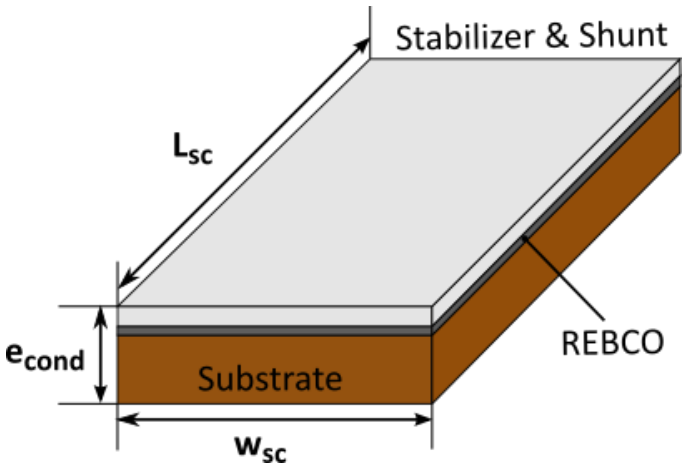

Figure 2.9: Simplified cross-section of a 2G HTS REBCO tape for calculating the compound parameters of thermal capacity c_p^{tot} (J/cm³-K) and electrical resistivity ρ^{tot} (Ω-m).

This simplification although not completely accurate, allows a thoughtful preliminary consideration of the ideal dimensions: Tape width w_{sc} , total thickness e_{cond} and total length L_{sc} required for an HTS tape to operate safely in an SFCL for all fault scenarios.

2.3.1 The Conductor's Width w_{SC}

In steady state conditions, the grid current has the rated current value I_a and expected current transients. These transients most commonly happen due to sudden load changes such as starting large induction motors and spikes in the consumption demand. To avoid the SFCL being triggered by such events, an over current margin $k_a I_a$ must be considered when choosing I_c for limiting the current. Hence, the optimum conductor's width can be estimated as [178]:

$$w_{sc} = \frac{k_a I_a}{I_{c-w}(T = T_{op})} \tag{2.4}$$

Where k_a is the overcurrent margin and I_{c-w} is the critical current per unit width, a convention unit used for REBCO conductors ($I_c(T_{op}) = I_{c-w}(T_{op}) w_{sc}$). From a cost point of view, I_{c-w} should be as high as possible to narrow the conductor's width and save material. For this reason, increasing I_{c-w} by reducing the nitrogen operational temperature from 77 K to 65 K has been a topic of interest in the SFCL community [179,180]. As a benchmark, the critical current of a commercial REBCO conductor is typically around 400 A/cm-w at 77 K and 800 A/cm-w at 65 K. Moreover, the current margin k_a should also be minimum to reduce cost. Nonetheless, it cannot be too low, otherwise it will trigger the current limitation under transient operation. Once the optimal w_{SC} width is set by the rated current, the actual tape width should be adjusted considering parallel paths and the available commercial tape widths (ranging from 4 to 12 mm).

2.3.2 The Conductor's Length L_{SC}

The minimum tape length L_{SC} required to operate an SFCL at a specific rated voltage is defined by the clear-fault condition. In principle, during the clear-fault ($I > I_c$), the temperature of the HTS material will rapidly increase homogeneously across the width and length due to joule heating. To avoid thermal damage to the HTS material, the CB must cut the current after a pre-determined time before the conductor reaches its maximum allowed temperature. As deduced in Appendix B and in [178], considering adiabatic conditions and a homogenous quench, the minimum length L_{SC} can be estimated as:

$$L_{SC} = V_{SC} \sqrt{\frac{\Delta t}{\int_{T_c}^{T_{max}} \rho(T) c_p(T) dT}} \tag{2.5}$$

Where T_{max} is the maximum allowed temperature in Kelvin before risking degrading the REBCO thermally; T_c is the critical temperature; Δt is the clearing time for the CB to open (limitation time) in seconds; and V_{SC} is the RMS value of the voltage across the SFCL module. An important parameter

derived from L_{SC} in equation (2.5) is the electric field under limitation $E_{lim} = V_{SC}/L_{SC}$. This electric field E_{lim} indicates how much voltage can be applied to 1 meter of conductor for a safe current limitation without overheating the tape.

$$E_{lim} = \sqrt{\frac{1}{\Delta t}\int_{T_c}^{T_{max}} \rho(T)c_p(T)dT} \tag{2.6}$$

In general, the clearing time for the CB should be as short as possible to suppress the temperature rise. However, to avoid a price compromise for the SFCL by implementing an expensive ultra-fast CB, a classical CB with 40-50 ms action time must be considered. Moreover, the REBCO structure itself does not suffer any significant degradation to brief temperature increases up to 720 K [181], but changes in the critical current can occur due to oxygen loss in the CuO chains for long periods of time at temperatures above 150 °C in ambient atmosphere. Therefore, for general safety reasons, the limit for T_{max} is considered 400 K to avoid possible I_c reduction after several current limitation cycles. In other words, the only way to safely adapt the length L_{SC} to a safe clear-fault scenario is to alter the conductor's total normal state resistivity ρ and/or the specific heat capacity c_p according to equation (2.5).

Nevertheless, increasing E_{lim} to reduce L_{SC} by focusing solely on tuning the thicknesses of the metallic layers has its theoretical limits. As an example, considering a generic commercial REBCO tape of 12-mm-width with silver stabilizer (top and bottom stabilizer) and Hastelloy substrate, equation (2.6) can be used to plot the surface E_{lim} for different thickness combinations as shown in Figure 2.10.

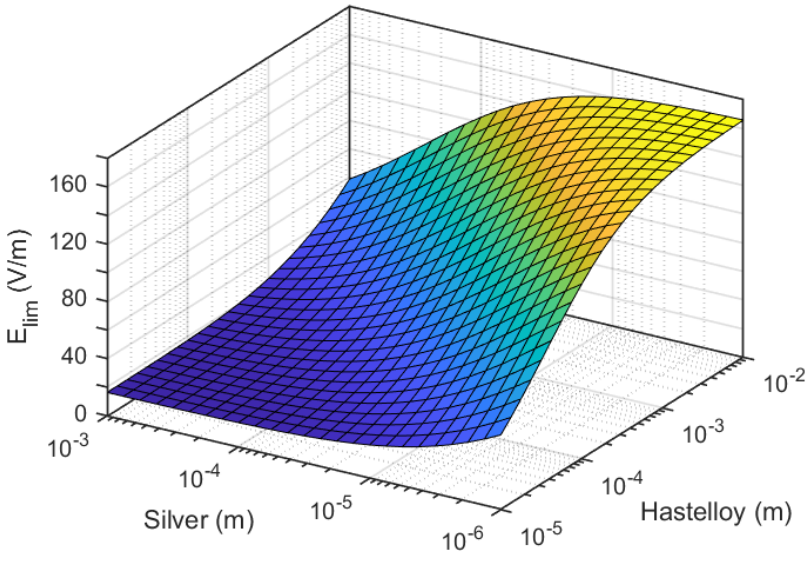

Figure 2.10: The maximum electric field under limitation E_{lim} for a standard 12-mm-wide HTS tape considering different thicknesses for the silver stabilizer and the Hastelloy shunt.

When analyzing the surface, it's easy to see how any small increase in the stabilizer thickness (micrometers) would represent a drastic decrease in E_{lim} due to the silver's low resistivity, but due to the Hastelloy high heat capacity [182] and high resistivity compared to silver, the increase of the substrate thickness increases E_{lim}. However, increasing the substrate thickness also reaches a theorical limit of about 160 V/m (for 400 K and 50 ms fault) because of the Hastelloy's considerable electrical conductivity as a metallic alloy. Moreover, the required Hastelloy thickness to reach the

160 V/m range becomes too large (~ 1 mm) leading to a very stiff conductor; not easy to wind. This practical restriction hinders the substrate thickness and E_{lim} to a maximum value around 150 V/m as shown in the contour lines of Figure 2.11.

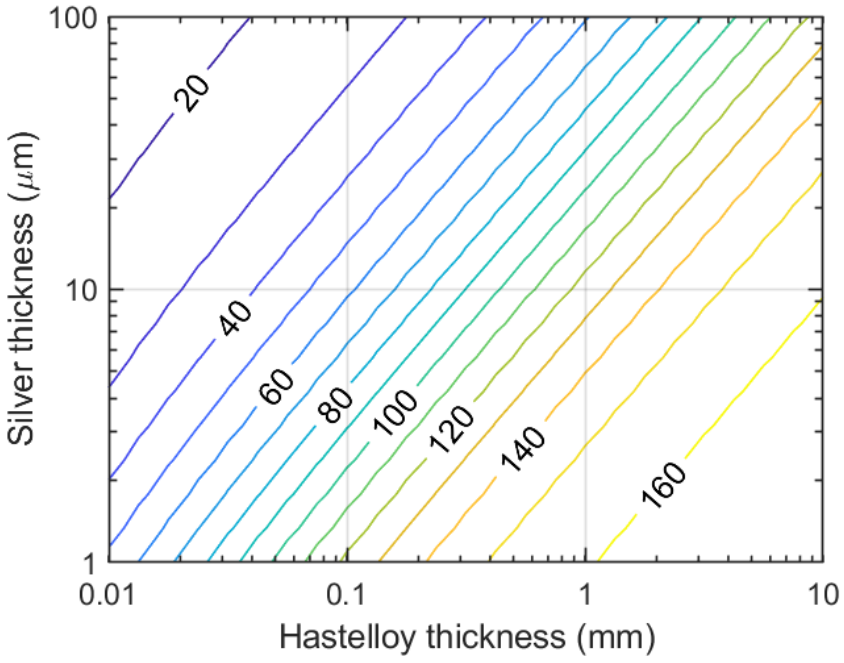

Figure 2.11: Contour lines of the maximum electric field under limitation E_{lim} (V/m) for a standard 12-mm-wide HTS tape considering different thicknesses of the silver stabilizer and the Hastelloy substrate.

2.3.3 The Conductor's Thickness e_{cond}

As explained before in subsection 2.2.5, hot-spots zones with intense heat dissipation can develop in the CC because of inhomogeneous I_c distribution in the REBCO film or due to secondary thermal perturbations that are promoting local quench. For the scenario of a prospective current fault equal to the minimum quench current, the hot-spot quenches, but the normal zone expands slowly (cm/s) due to the high thermal capacity of the tape (The velocity of the expansion of the normal zone will be addressed in more details in the final subsection of this section). As a matter of fact, the small quenched zone does not really expand in the millisecond timeframe of the CB action thus creating a low resistance in comparison to the original fault impedance. In this situation, differently from the clear-fault scenario, the current fault is not immediately limited and the grid behaves as a current source supplying a current with a value close to the CC's I_c. This is the worst-case scenario in the SFCL and the thermal equation described in Appendix B defines the minimum transversal area A_{cond} needed to withstand the hot-spot scenario as [178]:

$$A_{cond} = I_c \sqrt{\Delta t \left(\int_{T_c}^{T_{max}} \frac{c_p(T)}{\rho(T)} dT \right)^{-1}} \tag{2.7}$$

Dividing both sides of equation (2.8) by the width of the conductor we have:

$$e_{cond} = I_{c-w}\sqrt{\Delta t\left(\int_{T_c}^{T_{max}} \frac{c_p(T)}{\rho(T)}dT\right)^{-1}} \tag{2.8}$$

Where e_{cond} is the final CC thickness required to withstand the hot-spot scenario for a certain critical current per unit width I_{c-w} (subsection 2.3.1). However, this thickness e_{cond} is considering the compound values of $c_p(T)$ and $\rho(T)$ for the CC and these values are already a function of the combined thicknesses of the substrate and the stabilizer in equation (2.3). Therefore, the final thickness can actually be better evaluated by isolating the I_c term and rewriting equation (2.7) as:

$$I_{c-lim} = A_{cond}\sqrt{\frac{1}{\Delta t}\int_{T_c}^{T_{max}} \frac{c_p(T)}{\rho(T)}dT} \tag{2.9}$$

Equation (2.9) allows an evaluation of the maximum critical current I_{c-lim} permitted in a CC with a specific thickness e_{cond} (substrate + Hastelloy) to survive the hot-spot regime for a certain amount of time Δt before the opening of the CB. Considering the same generic commercial REBCO tape of 12-mm-width with silver stabilizer (top and bottom stabilizer) and Hastelloy substrate of the previous subsection, equation (2.9) can be used to plot the contour lines of I_{c-lim} for different thickness combinations as shown in Figure 2.12. As the thickness of the stabilizer and the substrate increases it is clear that the I_{c-lim} expands due to a direct mass bump up in the thermal capacity and the inherit electric conductivity of the materials involved. However, when increasing the silver stabilizer, a compromise is made between I_{c-lim} and E_{lim} (Figure 2.11.), thus making the Hastelloy the preferable material for tuning I_{c-lim}.

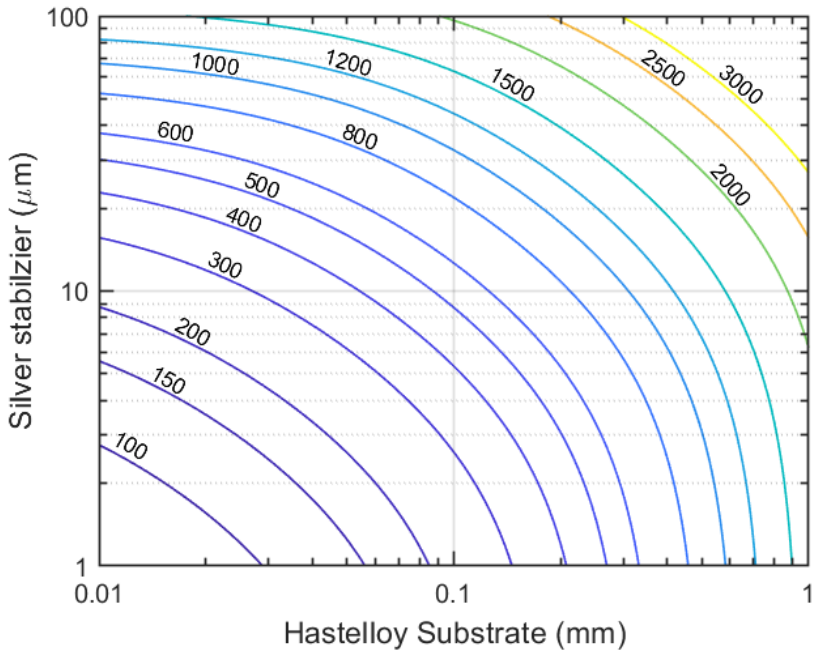

Figure 2.12: Contour lines of the maximum critical current I_{c-lim} (Ampere) in hot-spot regime for a standard 12-mm-wide HTS tape considering different thicknesses of silver stabilizer and the Hastelloy substrate. These curves were calculated with a limitation time of 50 ms and a maximum allowed temperature of 400 K.

As an example, in the case of a standard THEVA tape with 100 µm hastelloy substrate and 2 µm of silver stabilizer, $E_{lim} \approx 100$ V/m according to Figure 2.11 and $I_{c-lim} \approx 290$ A according to Figure 2.12.

Nowadays, THEVA's I_c is able to surpass 1000 A, meaning a massive vulnerability to the hot-spot scenario. If one would try to increase I_{c-lim} to 1000 A by depositing extra silver or copper to reach 40 µm of stabilizer, E_{lim} would be reduced below 30 V/m. On the other hand, increasing the hastelloy thickness from 100 µm to 600 µm also increases I_{c-lim} slightly beyond 1000 A, but also conveniently pushes E_{lim} beyond 150 V/m.

From the perspective of equation (2.6) and (2.9), the simplest solution to simultaneously maximize E_{lim} and I_{c-lim} for the resistive SFCL seems to be increasing the Hastelloy substrate to about 500 µm. However, in the quest of creating HTS tapes with high critical currents for overall applications using coils and cable-based devices (motor, generators, magnets, etc), the final performance of the tape is dependent on the whole-wire cross-section, i.e the engineering critical current density J_e (A/mm^2). For example, in the case of accelerator magnets, an engineering critical current density of at least 3 – 6 kA/cm^2 is required [183]. However, in typical commercial CC, since the thickness of the REBCO layer is around 1-3 µm while the entire conductor thickness is in the range of 50–120 µm, J_e values are significantly smaller ($\sim$ 3 kA/cm^2) than the REBCO's J_c (1 – 4 MA/cm^2). Increasing the thickness of the Hastelloy substrate would only aggravate the issue. Furthermore, attempts of growing thicker REBCO films above 3 µm face the problem of decreasing the average J_c due to the deterioration of the microstructure with increasing thickness [184].

With the focus on keeping-up with the needs of the market for the past years, CC manufacturers have opted to increase J_e by reducing the wire thickness targeting the thick Hastelloy substrate [185–188]. Therefore, for economic reasons, all manufactures start from a "standard" thicknesses of 100 µm or 50 µm thick substrate. Proposing a change from 50 or 100 µm to a thickness of 500 µm substrate just for the optimization of a tape for the resistive SFCL case is not an attractive solution for companies. More specifically, in the case of *THEVA GmbH*, the current reel-to-reel system is not compatible with the 500 µm thick Hastelloy tape. For this very reason, the solution proposed in the *FASTGRID* project was to solder the thick 500 µm Hastelloy tape on top of the silver stabilizer of a 12-mm-wide THEVA tape with 10 µm of tin solder. Besides being more convenient, this soldering method also protects the tape by keeping the REBCO layer closer to the neutral axis of the mechanical stress happening between layers. The results for the THEVA tape with 500 µm Hastelloy shunt were experimentally successful for samples with I_c = 720 A at 100 V/m for 50 ms [189].

2.3.4 The Cost of an SFCL

The constraints E_{lim} and I_{c-lim} mentioned previously are not only technically important, but they also help estimate the most crucial variable to be considered: the final cost of the total amount of HTS conductor in the SFCL. The final HTS tape cost can be approximated by:

$$Cost_{cond} = k_a S_a \frac{C_{SC}}{E_{lim}} \tag{2.10}$$

Where k_a is a coefficient considering the range of overcurrent during the grid normal operation, S_a is the rated power fixed by the grid, E_{lim} is the maximum electric field under limitation and C_{SC} the cost of the superconductor material. The cost C_{SC} is a quantity commonly expressed in €/kA/m and

represents the cost of one meter of SC tape with a critical current of 1 kA. The present C_{SC} for REBCO tapes ranges from 200 - 250 €/kA/m at 77 K.

Considering the installation of an SFCL into a HVDC grid operating at ± 320 kV/1.5 kA with the parameters $k_a = 1.5$ and $C_{SC} = 200$ €/kA/m. If one would use a standard HTS tape with 100 µm Hastelloy substrate, according to Figure 2.12, the amount of silver stabilizer required to safely operate for 50 ms at 1000 A in hot-spot regime above the I_{c-lim} curve would be approximately 40 µm. This thickness combination (substrate + stabilizer) would reduce E_{lim} to 40 V/m and, according to (2.10), lead to a total length of 8 km yielding a cost of 3.6 M€ just for the CC. This estimation shows how the cost of the SC conductor alone can correspond to more than 30% of the maximum 10 M€ budget stipulated by the EC project Twenties [109]. Adding the additional costs of the cryogenic equipment and the switching gear would make the SFCL too expensive for HVDC operation. Therefore, reducing the conductor cost becomes a critical requirement to implement the SFCL into a HVDC grid.

One way to artificially reduce the cost C_{SC} is to increase the tape's critical current by operating the SFCL in a pressurized liquid nitrogen environment at 65 K instead of 77 K. This approach doubles the critical current and should reduce the cost by half [179]. However, doubling the fault current increases drastically the amount of power that one single segment of tape should absorb during the quench. This makes the tape more sensitive to hot-spots for low prospective current faults. The tape should be very well designed to have a high thermal capacity to suppress hot-spots and be able to withstand the thermo-mechanical effects.

For direct commercial applications, the major expectation in the HTS community is the direct reduction of the manufacturing cost associated with C_{SC}. However, the price of the source materials utilized in the construction of the REBCO conductor is not the main culprit for the high C_{SC} value. The price is rather constrained by the different manufacturing processes requiring expensive machinery for preparing the different layers and synthesizing the REBCO material. From this perspective, increasing E_{lim} to reduce the length of tape needed in the SFCL becomes the preferable short-term solution to reduce the total SFCL cost.

In summary, equation (2.6) shows that in order to maximize E_{lim} and reduce cost, a high $c_p(T)$ and high $\rho(T)$ is required, but equation (2.9) indicates that a CC with high $c_p(T)$ and small $\rho(T)$ is preferable for a current fault in a hot-spot regime. A cost compromise is inevitable when trying to optimize E_{lim} and I_{c-lim} focusing only in the metallic layers of the substrate and stabilizer. Moreover, in the case of one opting for an increase of E_{lim} by removing some stabilizer/shunt material, the only alternative solution for I_{c-lim} would be reducing the limitation time for the switching of the CB, which cannot always be accomplished.

2.3.5 Alternative Solutions for Improving the CC Design

One way to maximize E_{lim}, I_{c-lim}, and reduce cost, is to increase the CC thermal capacity $c_p(T)$ without changing the electrical resistivity $\rho(T)$ by adding an extra non-conductive layer on top of the shunt stabilizer. In this scenario, the heat dissipated during the quench or hot-spot formation is not reduced and the non-conductive (high-ρ) layer should act as a thermal stabilizer suppressing the temperature. In the *FASTGRID* project, this kind of "insulated heat sink" was experimentally studied

by colleagues at the Slovak University of Technology in Bratislava using a commercially available Stycast resin filled with different high-c_p materials [190,191]. Some of the results were promising, but one major challenge of this approach is to match the thermal expansion of the resin-epoxy composited to the whole CC to avoid possible delamination and strain degradation of the REBCO during the quench [192].

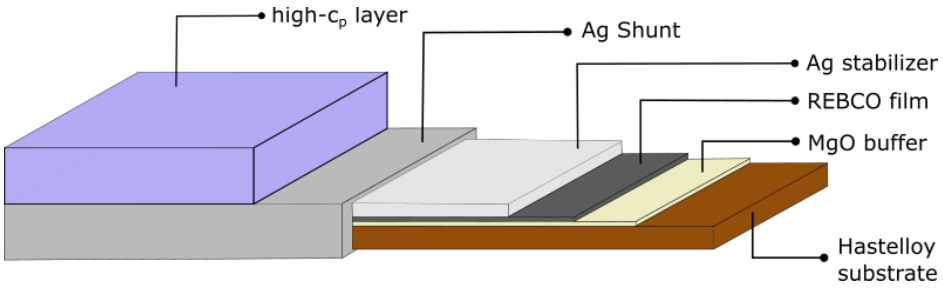

Figure 2.13: Classic multilayer structure of a 2G HTS tape coated with a silver shunt, plus an extra insulating layer of a material with high thermal capacity c_p.

Another approach, already mentioned in subsection 2.2.3, that can substantially increase the CC thermal capacity $c_p(T)$ and reduce $\rho(T)$ without compromising the tape's integrity in the hot-spot regime, is the sapphire substrate-based REBCO tapes. Besides being an insulator, sapphire has a thermal capacity significantly higher than Hastelloy for temperatures > 150 K (Appendix Figure A-1). This combination of properties theoretically pushes E_{lim} to the 1000 V/m range bringing very attractive economic advantages to the architecture [164,193]. Furthermore, sapphire possesses a thermal conductivity that is orders of magnitude higher than silver, copper and Hastelloy (Appendix Figure A-2), thus leading to a very high thermal diffusivity (Appendix Figure A-3) capable of suppressing the temperature rise of a hot-spot much more efficiently.

However, as mentioned in subsection 2.2.3, the technical difficulties of homogenously growing the thin REBCO film with J_c > 1 MA/cm^2 on top of a rough unpolished sapphire surface without crack formation [194], combined with the inherited costly manufacturing process of sapphire rods, remains as major barriers for the large-scale adoption of the sapphire tape designs [174].

2.3.6 The Normal Zone Propagation Velocity

As commented before, a hot-spot can intensively heat to the point of causing the rupture of the SC conductor if either not suppressed, or if the normal zone does not spread fast enough to homogenize the temperature of the quench. How fast the HTS material quenches along the conductor starting from an arbitrary position along the length can be described by the Normal Zone Propagation Velocity (NZPV). The simplest way to assess the NZPV of a conductor is by measuring it experimentally as described in section 3.4. Another less time-consuming method, is through numerical simulations. This is particularly useful in the case of systems with complex CC designs. Nevertheless, the most practical way to evaluate the NZPV is to use the formulas that result from the solution of the heat equation describing the quench process. In a theoretical analysis performed by M. Bonura and C. Senatore [195,196], the characteristic NZPV is described by:

$$v_{nzp} = \frac{I}{wd}\sqrt{\frac{k(T_t)\cdot\rho(T_t)}{c_p(T_t)\cdot\int_{T_{op}}^{T_t} c_p(T)dT}} = \sqrt{D_T\gamma} \tag{2.11}$$

Where $k(T)$ is the compound thermal conductivity (W/m-K) of all materials in the CC, c_p is the compound volumetric heat capacity (J/m^3-K) of the CC, $\rho(T)$ is the compound resistivity (Ω-m) of the CC conducting layers in parallel, d is the combined thickness (m) of all the metallic stabilizers sharing current with the HTS layer, w is the tape's width and I is the sheet current (A) in the CC. From this equation the primary parameters influencing the NZPV can be described as the thermal diffusivity $D_T = k/c_p$ (m^2/s) and the characteristic time $\gamma = \rho I^2/(c_p^{tot}\int_{T_{op}}^{T_t} c_p(T)dT)$ (s^{-1}) required for a segment of the conductor to heat up to T_t and start sharing current to the shunt layers. Although not precise, equation (2.11) gives a reasonable estimation of the NZPV for comparing different architectures with different shunt materials.

In the case of LTS wires operating in liquid helium, the small thermal capacity and high thermal conductivity of the metal alloys (Nb-Ti and Nb-Sn) makes the conductor more prone to quench (small Q_{MQE}) in the presence of a thermal disturbance like a hot-spot. On the flip side, their small thermal diffusivity and small temperature margin, leads to an NZPV of several meters per second (m/s) [197]. From a protection point of view, a high NZPV value allows a rapid detection of a quench and safe current mitigation. Contrary, the HTS REBCO tapes are naturally more stable in the presence of hot-spots due to the increased heat capacity of the Hastelloy substrate and higher temperature margins. On the down side, the NZPV becomes significantly slower (in the range of cm/s) [198,199], thus making the quench detection and protection more difficult.

Since the NZPV along the width of the tape is neglectable when compared to the longitudinal NZPV, many authors have used 1D numerical models to evaluate the influence of the NZPV in the performance of 2G HTS tapes [198,200]. In one 1D analysis performed by Daniele Colangelo and Bertrand Dutoit, the impact of the NZPV of a HTS-CC was evaluated for a resistive SFCL integrated in a AC MV power grid [200]. The parameters of the tape considered are shown in Table 2-1 and the NZPV was numerically varied from 20 cm/s up to 400 cm/s. This set of simulations demonstrate that only with an NZPV greater than 300 cm/s, it would be possible to achieve a satisfying local thermal stability in a relatively short CC of 8 m.

Table 2-1: Experimental parameters of the 2G HTS tape used by [200] *in the study of the NZPV impact of a resistive SFCL.*

Parameters	Value	Physical properties reference
Thickness of the silver stabilizer	4.8 µm	4-5 W/cm-K, 1.7 J/cm^3-K
Thickness of the Hastelloy® substrate	105 µm	70 mW/cm-K, 1.4 J/cm^3-K
Thickness of the HTS material	1 µm	
Width of the HTS-CC	12 mm	-
Length of the HTS-CC	8 m	-
Average critical current (I_c @ 77 K)	365 A	-
Standard deviation of I_c	10%	-

However, increasing the NZPV beyond 300 cm/s in a hastelloy-substrate HTS tape is basically impossible if one would simply try to decrease the compound heat capacity c_p. As an example,

applying the same parameters of the simulated tape from Table 2-1 to equation (2.11) with $T_t = 90\ K$, the normal zone propagation velocity is estimated to be 22.24 cm/s. This value agrees with the initial 20 cm/s considered as lower limit in the simulations performed for Table 2-1.

$$v_{nzpv} = \frac{365\ A}{12 \cdot 10^{-3}\ \times 110 \cdot 10^{-6}\ [m^2]} \sqrt{\frac{(16.73\ [W/m\text{-}K]) \times (18.15\ [\text{n}\Omega\text{-m}])}{(1.77 \cdot 10^{6}\ [\text{J/m}^3\text{-K}]) \int_{77}^{92} c_p(T) dT}} = 22{,}24\ cm/s$$

Even if some significant thermal stability was sacrificed by reducing the silver stabilizer to 1 µm and the Hastelloy substrate from 100 to 50 µm, the NZPV would only increase to 66.82 cm/s, far below the safe 300 cm/s range at 365 A. The heat capacity of the Hastelloy substrate dominates the structure of the HTS conductor [201] and suppress the NZPV to values below 100 cm/s thus making the hot-spot a critical issue.

2.4 Boosting the NZPV

When focusing solely on the interpretation of the NZPV via equation (2.11) it seems that thermal stability and high NZPV are two requirements that always compete. The NZPV seems to be rigidly constrained by the thermal properties of the materials used in the fabrication of the 2G HTS layers, thus making a CC with high-c_p the only viable way to suppress a hot-spot. However, as this section will show, equation (2.11) is an incomplete description of the NZPV process that does not account for the interfacial and geometrical properties of the stabilizer and substrate layers surrounding the HTS material. Tuning these properties is the key to significantly boost the NZPV of a 2G HTS coated conductor (CC) without having to alter the thermal capacity or the final resistivity of the tape. This approach was the major objective of the studies conducted in this thesis.

2.4.1 The Current Transfer Length (CTL)

The electrical path between the REBCO layer and the stabilizer metal coating, e.g. REBCO-silver, is not perfect. The existence of an interfacial resistance between the layers creates an imperfect parallel path for a current being injected (or ejected) into the HTS. As shown in Figure 2.14, a current in the silver metal (I_{Ag}) decays exponentially with the distance from the point $x = 0$ of injection in the form:

$$I_{Ag} = I_0 \exp(-x/\lambda) \tag{2.12}$$

Where I_0 is the injected current and λ is the characteristic Current Transfer Length (CTL). The CTL can be experimentally defined as the resistance ratio:

$$\lambda = \sqrt{\frac{R_t}{R_{Ag}}} \tag{2.13}$$

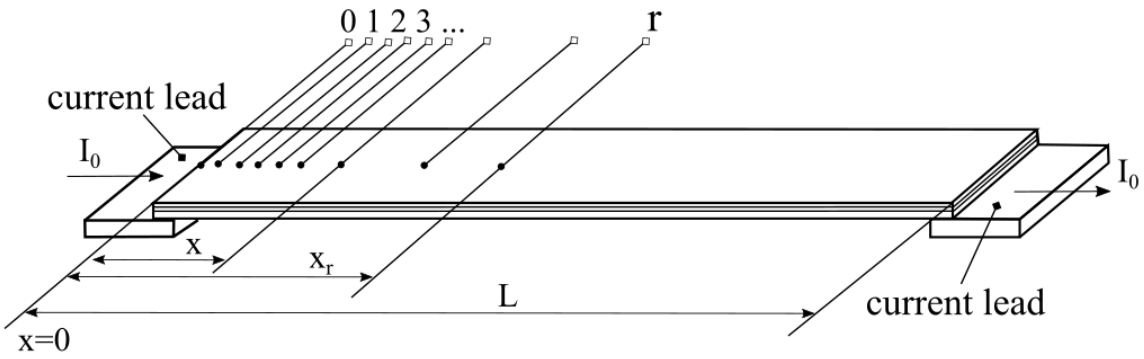

Figure 2.14: Schematic drawing of the Current transfer Length (CTL) of a 2G HTS CC leads transporting current with two current attached.

Where R_t is the transfer resistance per unit length ($\Omega \times m^2/m$) and R_{Ag} is the metal stabilizer resistance per unit length (Ω/m). The resistance R_t is simply described by the interfacial resistance and the contact area per unit length ($R_t = \rho_c/A_{c-lenth}$). As one can see, the interfacial resistance represents a direct increase in the CTL by creating an ohmic interface in the path of the current traveling from the HTS to the metallic stabilizer/shunt. As a result, a transfer voltage V_{ct} also develops along the conductor. The voltage between $x = 0$ and another point along the *x-axis* x_r ($x = r$) will be:

$$V_{ct} = \int_0^{x_r} I_{Ag}(x)\, R_{Ag}\, dx \tag{2.14}$$

Hence, the voltage also decays exponentially along the conductor away from the current contacts:

$$V_{ct} = I_0 R_{Ag} \exp(-x/\lambda) \tag{2.15}$$

In the experimental literature, estimating the CTL helps determining a safe distance to install voltage probes [72]. A sufficient distance is needed from the current contacts to avoid spurious voltage V_{ct} from interfering with the measurements. In addition, the CTL helps explain the unusual asymmetry in voltage/temperature distribution between the top and bottom metallic layers in CCs during the propagation of a normal zone [202]. The presence of an oxide buffer layer increases the interfacial resistance of the HTS with the metallic substrate and consequently produce a larger CTL in comparison with the top metallic stabilizer layer that maintains direct contact with the HTS and has a smaller CTL. This difference in the CTL provokes a voltage potential between the stabilizer and the substrate during quench [203].

Furthermore, the CTL explains the existence of a significant electric field outside of the thermally active normal zone: when a hot-spot creates the normal zone in the HTS, the transport current does not follow a perfect parallel path to the stabilizer, the current is shared across the CTL to reach the stabilizer and the substrate [203]. If the interfacial resistance is high enough, the CTL will create a voltage well beyond the normal zone adding to the normal zone expansion. In other words, the NZP velocity (NZPV) is not strictly defined by the intrinsic thermal/electrical properties of the substrate and the stabilizer, but it is also influenced by the CTL. In a numerical simulation study performed by George A. Levin and Paul N. Barnes [204], it was concluded that the NZPV could be significantly improved

beyond 100 cm/s if the interfacial resistance increased by at least two orders of magnitude in comparison to the commercial values 50 nΩ-cm^2 [205].

2.4.2 The Operational Limits of the Interfacial Resistance

In practice, increasing the interfacial resistance stabilizer-REBCO to create a bigger CTL is not a viable solution to boost the NZPV in the CC due to practical constrains revolving the use of current contacts. As an example, supposedly we wanted to determine the size of the current connections needed to test an HTS conductor immersed in liquid nitrogen. The critical current is assumed to be about 500 A and the total surface area of the contact and bus bar cooled in liquid nitrogen to be 10 cm^2. Stipulating a maximum 5% decrease in the critical current due to Joule heating, this corresponds to a 0.5 K temperature increase for YBCO at 77 K in self-field. This temperature increase of 0.5 K places a limit on the power generation, which is given by the solid/liquid heat-transfer rate for liquid nitrogen explained in section 2.2.4.

$$\dot{q} \cong [5 \times 10^2 * (0.5\ K)^2]\left[\left(\frac{W}{m^2}\right)(K^{-2.5})\right] * (10^{-4}\ m^2) = 88\ mW$$

Utilizing Ohm's law and 500 A current, the contact resistance is limited to about:

$$R_c \leq \dot{q} I^{-2} = (88\ mW) * (500\ A)^{-2} = 352\ n\Omega$$

Assuming, a uniform interface silver/HTS dominating the contact resistivity, we can take $\rho_c \cong 10^{-5}\ \ \Omega\text{-}cm^2$ and calculate A_c using R_c:

$$A_c \geq \frac{\rho_c}{R_c} = \frac{(10^{-5}\ \Omega\text{-}cm^2)}{352\ n\Omega} = 28.41\ cm^2$$

Finally, considering the 1.2 cm standard tape width, we would need at least 23 cm of tape just for the current contacts to prevent critical heating in the current connections. This example clearly illustrates how the current contact areas start becoming impractical as the operational current increases beyond 500 A for an interfacial resistance in the order of $10^{-5}\ \Omega\text{-}cm^2$. The contact area increases with the square of the current and for this very reason, the state of art REBCO conductors are manufactured with an interfacial resistance in the 10^{-8} - $10^{-7}\ \Omega\text{-}cm^2$ range as mentioned before [205].

2.4.3 The Current Flow Diverter

A deliberate increase of the interfacial resistance is not a viable way to improve the NZPV in 2G HTS conductors for practical applications. In this scenario, *FASTGRID* partners from Ecole Polytechnique Montréal (EPM) have proposed a simple alteration of the 2G HTS architecture in order to substantially increase the CTL while maintaining an overall low interfacial resistance. Instead of using a tape with uniform interfacial resistance (Figure 2.15 (a)), the tape should only have a section of the width presenting a high resistance interface (Figure 2.15 (b)) to create the so-called "Current Flow Diverter" (CFD) behavior [206].

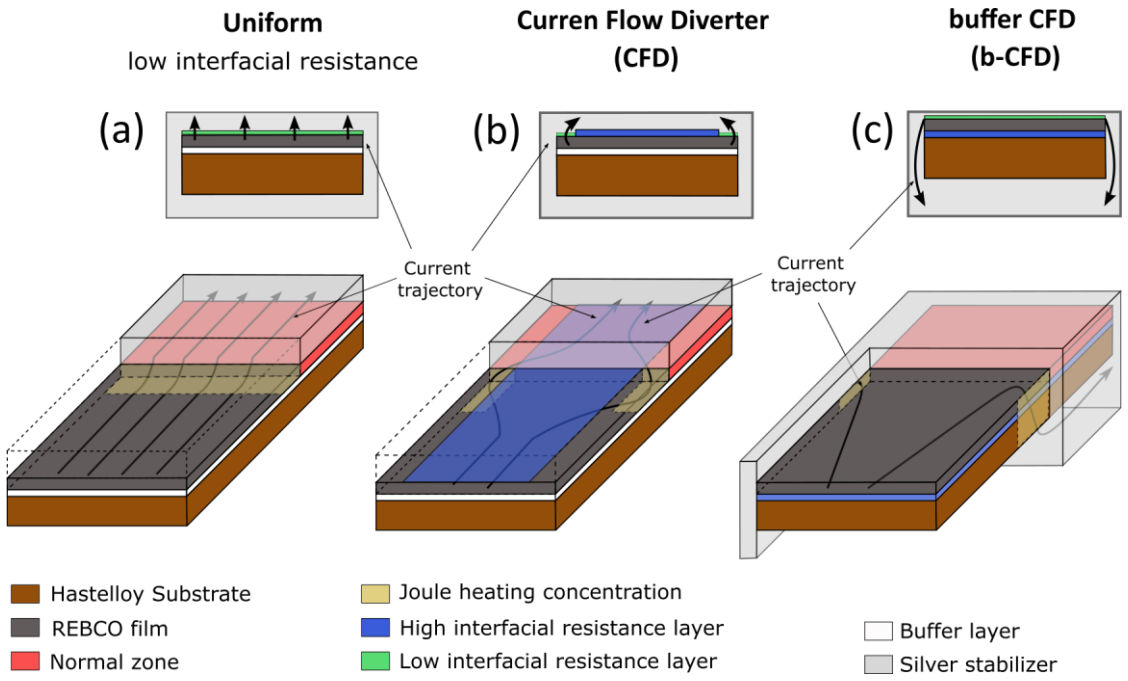

Figure 2.15: Schematic drawing (cross-section and isometric) showing the current transfer path from the HTS layer to the stabilizer in the presence of a normal zone for three tape architectures: (a) Uniform tape, (b) a CFD tape and (c) a b-CFD tape. For simplification purposes only, the top silver stabilizer is shown for the Uniform and CFD cases in the isometric view.

In the presence of a normal zone, the CFD interface forces a large portion of the current flowing in the HTS to pass through the narrow silver edges with low interfacial resistance to reach the stabilizer layer (Figure 2.15(b)). Consequently, this path artificially increases the CTL making the joule heating spread over a longer path along the CC's length away from the initial hot-spot zone, thus accelerating the NZPV. At the same time, the area corresponding to the silver edges in combination with the CFD area, maintain a reasonable low interfacial resistance for the current contacts. Considering a CFD tape with an intrinsic low interfacial resistance ρ_i^* and a CFD high interfacial resistance of ρ_f, if $\rho_f \gg \rho_i^*$, the global interfacial resistance ρ_i of a CFD tape can be approximated as [206]:

$$\rho_i \approx \frac{\rho_i^*}{(1-f)} \tag{2.16}$$

Where ρ_i^* ranges from 50 to 100 nΩ-cm^2 and f represents the fraction of the width covered by the CFD layer. Even if the low interfacial resistance was in the upper limit $\rho_i^* = 100$ nΩ-cm^2, and 90% of the width were to be covered by a highly resistive CFD, the global resistance would still be at an acceptable level of $1\ \mu\Omega\text{-}cm^2$. Nevertheless, the NZPV enhancement is still proportional to the high interfacial resistance ρ_f (Ω-cm^2) and to the CC's width fraction covered with the CFD. As an example, Figure 2.16 shows the dependence of the NZPV on ρ_f for a simulated HTS CC with $\rho_i^* = 100$ nΩ-cm^2 and 90% of the surface covered with the CFD ($f = 0.9$). In order to attain an NZPV increase of at least one order of magnitude, the CFD interfacial resistance ρ_f must be three orders of magnitude greater ($10^{-4}\ \Omega\text{-}cm^2$) than the low resistance edges ($10^{-7}\ \Omega\text{-}cm^2$) for an applied current of 250 A.

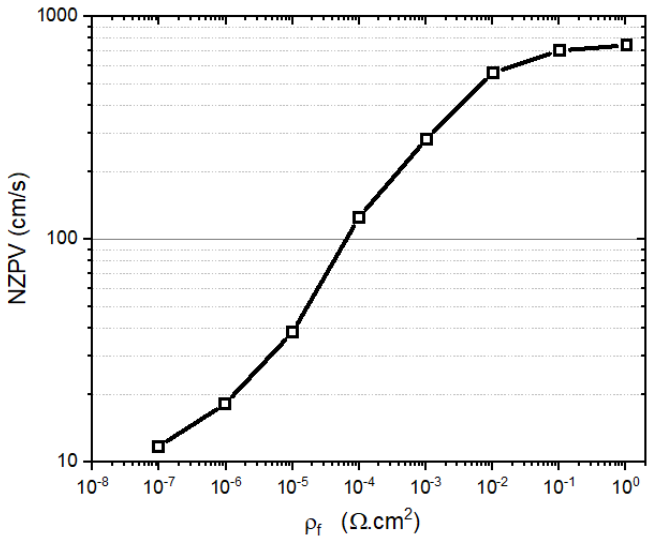

Figure 2.16: The NZPV as function of the interfacial resistance of the CFD (ρ_f) for the CFD region covering 90% of the superconductor–stabilizer interface (f = 0.9) with an applied current of 250 A. Figure adapted from [206]

This CFD concept was initially studied via 3D finite element simulations in COMSOL Multiphysics [206] and it revealed a 2x increase in the NZPV magnitude in comparison with tapes with low uniform interfacial resistance. The effect was confirmed experimentally [207] utilizing 4-mm-wide SuperPower tapes and a patent for this concept was launched [208] expecting industrial applications. Even though promising, the original experimental approach for creating the CFD interface is not compatible with the large-scale production of HTS CC tapes [207]. As shown in Figure 2.17, the approach starts with a commercial silver coated tape as template and consists of a partial etching process (section 3.1.3) of the silver layer in the middle of the width leaving both edges intact. The REBCO layer is exposed briefly to atmospheric degradation due to the air humidity and creates a highly resistive thin (~ 100 nm) oxide layer [209]. The tape is subsequently re-puttered with silver to complete the stabilizer/shunt material required for current contacts and thermal stability. This method is simple and efficient for creating small samples (10-15 cm) to be tested experimentally in the lab, but re-sputtering the silver layer coming from the factory for meters of CC would undoubtedly increase the price of such CFD-CC beyond the reasonable cost/benefit levels. The main challenge for the acceptance of the CFD in the industry now is to find an attractive low-cost manufacturing technique able to bypass the need to re-sputter silver and to easily incorporate it into the existing steps of the CC fabrication.

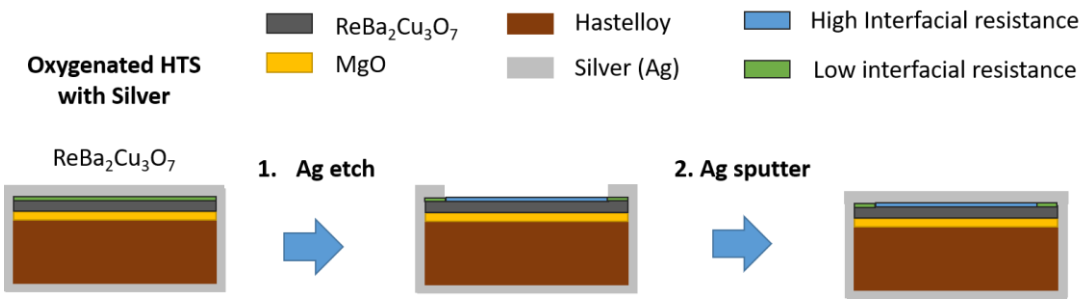

Figure 2.17: Experimental procedure utilized by EPM to locally increase the interfacial resistance of a commercial CC in order to create the CFD architecture. Silver etching is performed with a hydrogen peroxide solution and the silver coating via magnetron sputtering.

Another way to significantly increase the NZPV of a CC without having to manipulate the interfacial resistance silver-REBCO is to use the pre-existing buffer layer of the tape to create the CFD effect, thus the name b-CFD in Figure 2.15(c) [210]. In this approach, the thickness ratio between the top and the bottom shunt/stabilizer layer is adjusted so that, in the presence of a normal zone, the majority of the current is forced to flow in the bottom shunt layer. Since the buffer layer is usually a natural electric insulator, the current is diverted around the buffer to reach the bottom stabilizer thus creating a similar effect to that of the classic CFD. This b-CFD effect is present in all HTS tapes where the a top and bottom metallic shunt layer are well connected along the edges of tape and the thickness shunt ratio $r = h_{top}/h_{bot} \leq 1$. Besides not having to deal with the tuning of the interfacial resistance silver-REBCO, a second major advantage of the b-CFD architecture is that it allows the increase of the NZPV even in the presence of a thick shunt/stabilizer (20-40 µm), which is not the case for the classical CFD architecture [211]. This feature becomes extremely attractive for applications requiring a thick stabilizer such as HTS superconducting magnets [212].

The b-CFD concept is theoretically simpler than the CFD and its effectiveness has been proven experimentally [210]. The task now is to find a way to re-create the b-CFD conditions in an industrial process over hundreds of meters of HTS CC. In principle, such fabrication technique should incorporate a low-cost metal plating process (Cu or Ni) capable of ensuring the electrical connection between the top and the bottom stabilizer layers along the full length of the conductor. But more importantly, one must find a way to keep a continuous thin silver thickness (~20–100 nm) in the top stabilizer layer of the final CC. This detail is the main challenge for the b-CFD since silver layers (< 100 nm) are known to aggregate and form discontinuous silver islands (i.e. dewetting) during heat treatments [213], like the final oxygen annealing process required for lowering the interfacial resistance Ag/REBCO and loading oxygen into the $Re_1Ba_2Cu_3O_{7-\delta}$ structure (Figure 2.18). In one study of the SUNAM group it has been shown that a 20 nm thick silver layer on top of YBCO forms spherical islands and becomes electrically discontinuous when annealed at temperatures as low as 300 °C [72,99].

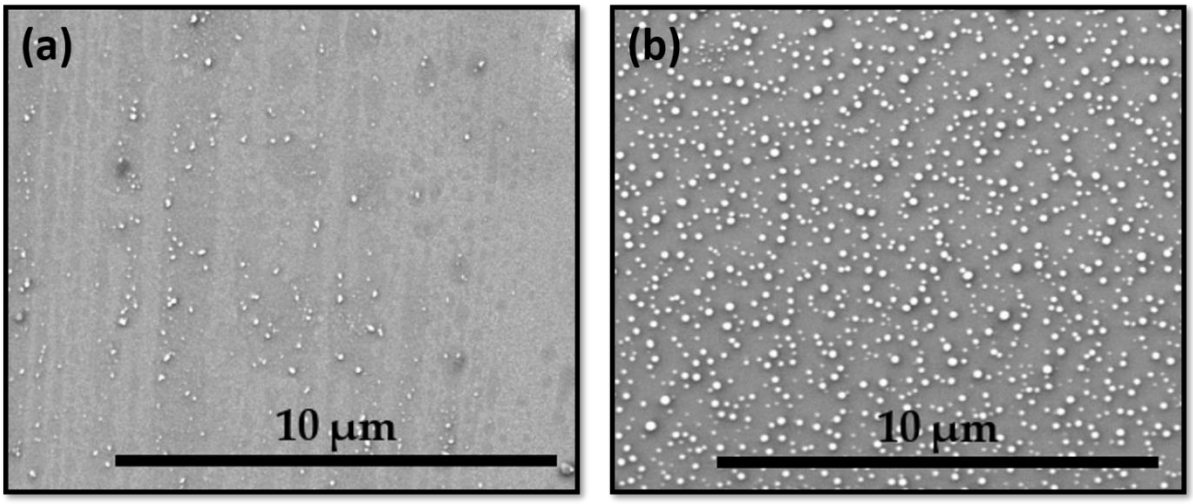

Figure 2.18: Dewetting process of a 20 nm thick silver layer on top of YBCO after being annealed in oxygen for 2 hours at 400 °C. (a) Silver coating before the annealing. (b) Silver coating after the annealing. Figures adapted from [99].

3 Simulation and Experimental Techniques

As explained in the previous chapter, implementing the CFD concept in an economically viable way for CC manufacturers was the main goal of this study. Accordingly, this chapter is dedicated to explain all the main experimental methods applied for creating the different CFD routes as well as the basic characterization techniques used to evaluate the presence and efficiency of the desired CFD behavior. Additionally, the end of the chapter presents the COMSOL Multiphysics simulation template used to study the constrains of the CFD behavior in THEVA tapes.

3.1 Preparation of CC Samples

3.1.1 Spin Coating Deposition

Spin coating is a common technique used to uniformly deposit a thin layer of material on a flat substrate. The technique starts by positioning the substrate onto a flat support inside a spinner device. A small amount of precursor solution of the chosen material is then deposited on the middle of the stationary substrate. Subsequently, the substrate is rotated inside a spinner at high speeds (up to 10000 rpm) creating a centrifugal force that spreads the material uniformly across the surface. The solvent in the precursor solution is usually volatile and naturally evaporates during the spinning session. However, the final step to achieve the desired structure usually involves a post thermal treatment to solidify the final material. All of these steps are illustrated in Figure 3.1.

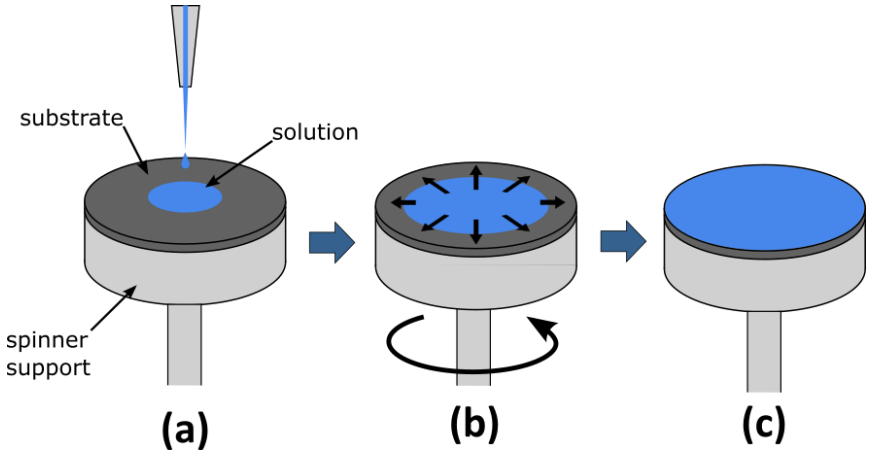

Figure 3.1: Step-by-step schematic of the spin-coating procedure. (a) Deposition of the liquid solution onto a substrate attached to the spinner support. (b) Rotation of the support to spread the solution across the whole substrate area. (c) Substrate coated with the solution ready for the thermal treatment to evaporate the solvent and solidify the coating.

The universal description of the thickness of a spin coated film involving these parameters was proposed by Danglad-Flores et al. [214]. Angular speed, acceleration, solution's viscosity and concentration, all of these parameters affect the final thickness. However, in this work, the majority of solutions at disposal had already been pre-tuned for the desired thicknesses in the SMA Spinner 6000 Pro installed at ICMAB.

Moreover, since the full surface of the sample is covered with the coating material in this method, in order to create coating patterns on the substrate, the surface must be masked beforehand. Therefore, the deposition of different materials to create the CFD pattern, was accomplished by masking the edges of the REBCO CC samples with a polyimide tape before spin coating.

3.1.2 Ink Jet Printing (IJP) the CFD

Even though practical, spin coating presents one major drawback, the method is not compatible with the standard reel-to-reel system commonly used by CC manufacturers. Consequently, ink jet printing (IJP) was envisioned as the final practical method to create the CFD pattern in reel-to-reel production [64]. This low cost technique uses a multi-nozzle printing head for continuous solution deposition [215] on a moving surface capable of creating personalized patterns for different applications such as electronics [62]. Moreover, the method is very versatile; either the surface or the print head can move.

The Drop on Demand (DoD) IJP technology has been successfully employed to promote the Solution Deposition Planarization (SDP) of substrates with nano-crystalline yttrium oxide films in the past [216]. Therefore, depositions of yttria films on long lengths (> 1 m) of bare CC were performed by *FASTGRID* patterns of the company *Oxolutia Ltda*.

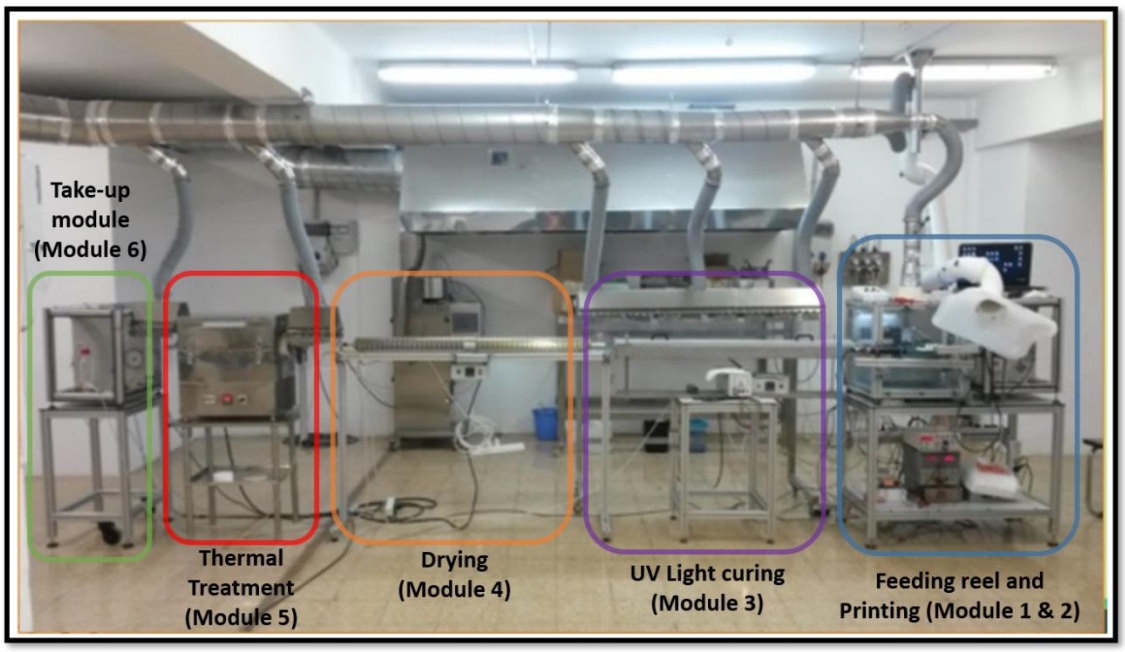

Figure 3.2: Reel-to-reel ink jet deposition system used by Oxolutia Ltda.

A picture of Oxolutia's reel-to-reel (R2R) IJP system for special oxides is shown in Figure 3.2. The system is arranged in 6 modules connected in series, each with a specific task.

- Module 1, the Feeding module: Is the feeding reel that delivers tape that is ready for the ink deposition.
- Module 2, the Printing module: A multi nozzle print head deposits the ink on the moving tape substrate. This IJP was performed using a piezoelectric 512 nozzle Konica Minolta head on

which the droplet density of the Y ink was modified near the edges to keep a uniform film thickness through the whole width of the yttria layer.

- Module 3, Curing module: The ink is cured under UV light with an array of 10 cm by 25 cm of LEDs with wavelengths between 275-295 nm.
- Module 4, Drying module: The ink is dried in a hot air tube with temperatures below 100 °C. The use of modules 3 and 4 depend on the type of ink deposited onto the substrate. Some precursor solutions do not require UV light treatment and so only module 4 is used.
- Module 5, Pyrolysis module: The substrate with the cured ink goes through a tubular furnace capable of achieving temperatures above 500 °C in order to decompose the organic compounds of the ink.
- Module 6, Take-up module: Contains the final reel that coils the inkjet coated substrate coming from the furnace.

Yttria nanolayers were deposited on top of the GdBCO layer of THEVA using propionate Yttrium solution precursors DoD IJP. Yttrium acetate ($Y(OAc)_3$) salts were dissolved in a mixture of 26% v/v propionic acid ($CH_3CH_2CO_2H$, Aldrich) and 74% v/v of n-butanol in concentrations ranging from 0.01 M and 2 M. The solution also included diethanolamine (DEA) in a [Y]/[DEA] molar ratio of 4.5. The objective was to coat about 85 - 90% of the 12 mm width along the surface of the GdBCO films with Y_2O_3. This work reports only on some of the optimizations coming from the ICMAB-Oxolutia partnership based on the morphological characterization of the final IJP-yttria layer and its effects on the HTS material.

3.1.3 Metal Etching

In many of the CC experiments performed in this work, the silver coating had to be removed to access the REBCO layer underneath. For this matter, a solution was used to safely etch the metallic silver without jeopardizing the superconducting properties of the REBCO. The silver etching solution was a mixture of ammonia and hydrogen peroxide diluted with methanol in the proportion H_2O_2 : NH_4OH : CH_3OH = 1 : 1 : X , where the amount of methanol X varies with the etching rate desired and the thickness of the silver layer [217].

In this reaction, the H_2O_2 oxidizes and dissolves the silver into ions, while the NH_3 combines with the ions to form Ag (NH_3) in accordance with the equation:

$$2\mathrm{Ag} + 4\mathrm{N}H_3 + H_2O_2 \longrightarrow 2\mathrm{Ag}\,(\mathrm{N}H_3)_2{}^{+} + 2OH^-$$

After submerging the CC sample into the solution and observing the complete etching of the silver, the exposed HTS surface is rinsed with pure methanol to prevent further etching.

3.1.4 Oxygenation and Annealing

As commented before, in this thesis, all CFD samples were created using THEVA's CC structure (GdBCO/MgO/Hastelloy) as template and so, to assure compatibility of the different theorized CFD

architectures with the standard manufacturing steps, the oxygen annealing steps utilized by THEVA had to be recreated at ICMAB's laboratory environment. The 30-meter-long furnace located at THEVA's facility has 7 isothermal regions (Figure 3.3 lower x-axis scale).

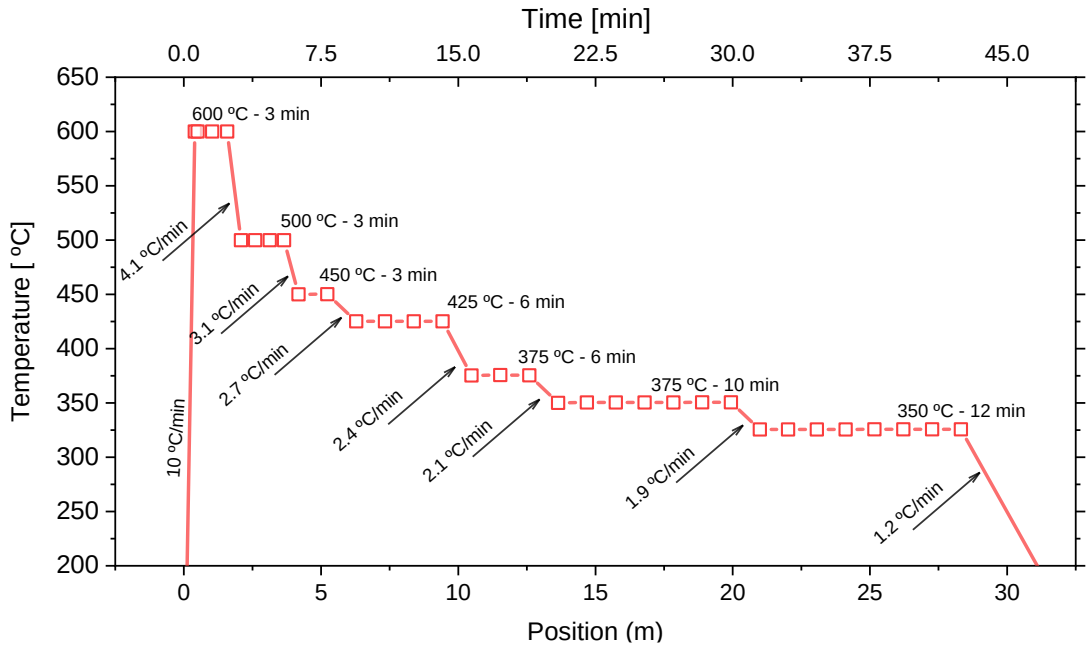

Figure 3.3: Temperature profile used for oxygen annealing the GdBCO film in THEVA's CC, also referred to as THEVA's temperature profile. This profile emulates the temperature gradient experience by tape moving in the 30 meters reel-to-reel furnace of THEVA.

Considering the tape traveling in a reel-to-reel process at a speed of 40 m/h inside the furnace from the hottest to the coolest end, the average exposure time at each isotherm was calculated by simply diving the length of the isotherm by the tape's travelling speed. Using this average dwell time, the equivalent temperature profile in a static furnace was created as shown in Figure 3.3 (upper x-axis scale).

3.1.5 Plasma Treatments

Plasma treatments are techniques commonly used for surface modification in order to achieve better acceptance of secondary manufacturing applications. The plasma is formed by using an electric potential at high frequencies (MHz) to charge a gas with moving electrons and ions in both the negative and positive state. When a particular surface is exposed to this partially ionized gas, the plasma treatment is initiated until the electric potential is ceased. The type of surface treatment always depends on the surface material and the type of gas used, but in general the gas types can be classified as [218]:

- Inert gas plasma: Argon is the most common because of its low cost, but helium, neon, and argon are also used in plasma technology;
- Oxygen plasma: Oxygen and oxygen-containing plasmas are most common for modifying surfaces and removing organic compounds. Especially in the case of polymers;

- Nitrogen plasma: Nitrogen-containing plasmas are widely used to improve wettability, printability and biocompatibility of polymer surfaces;
- Fluorine plasma: When a plasma gas contains fluorine gas, surface reactions, etching, and plasma polymerization may take place simultaneously;
- Hydrogen plasma: Hydrogen-containing plasmas are commonly used to promote chemical processes like reduction of metal oxides and other inorganic contaminants like sulfur and chlorine.

Another classification resides in the method for creating the plasma; it can be either low-pressure or atmospheric. Low-pressure plasma is also referred to as "cold plasma" and is the most common technique, usually performed in a chamber or enclosure where the air is evacuated prior to letting the gas in (Figure 3.4(a)). In atmospheric plasma, a plasma jet is ignited with an electric arc between two electrodes and a vortex of gas flowing between the electrodes. The compressed gas is ionized as it passes close to the arc and creates a plasma flame of highly reactive gas species that react with the top atomic layers of the target surface [219] (Figure 3.4(b)).

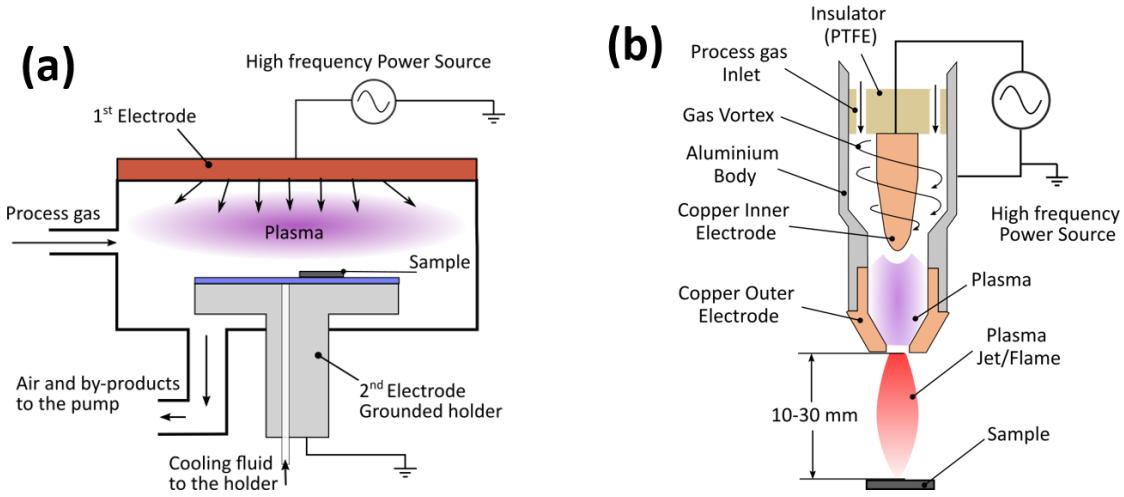

Figure 3.4: Schematic drawings of the two standard types of forming plasma for surface treatments. (a) Low-pressure plasma in a chamber; (b) Atmospheric pressure plasma jet.

In this thesis, both techniques were used with hydrogen gas to treat the silver coating on CC samples to achieve a special CFD design that is discussed in chapter 6. The low-pressure treatments were conducted in a commercial system (Femto Plasma-Surface-Technology) at the Universitat Politècnica de Catalunya (UPC), and the atmospheric plasma treatments were performed in the laboratories *of Relyon Plasma GmbH* for silver recovery tests with the atmospheric plasmabrush® PB3 system [220,221] (Figure 3.4(b)).

3.2 Structural Characterization Techniques

3.2.1 X-ray Diffraction (XRD)

The XRD technique is a practical method to characterize and identify the structure of crystalline materials. Given the periodicity of the crystal lattice, Bragg´s formulation assumes that a crystal structure could be decomposed into a well-defined arrangement of planes separated by a constant d spacing. Since the wavelength λ of an X-ray radiation is similar to the atomic distances in a crystal, the distance d between the planes can be inferred by analyzing the diffraction pattern originated from the elastic scattering of an incident X-ray radiation. According to Bragg's Law, the incident angles θ at which the diffraction presents a constructive interference is given by:

$$n\lambda = 2d\sin(\theta)$$

Where n is a positive integer. The classic Bragg-Brentano experimental setup used for XRD is illustrated in Figure 3.5. An X-ray source shoots the sample at an incident angle θ and the diffracted radiation is picked up by a detector positioned at the same angle θ. Both source and detector rotate simultaneously to scan the diffraction intensity for each angle. The diffraction "powder pattern", intensity as a function of 2θ , is then plotted and analysed following the constructive interference restriction given by Bragg's Law.

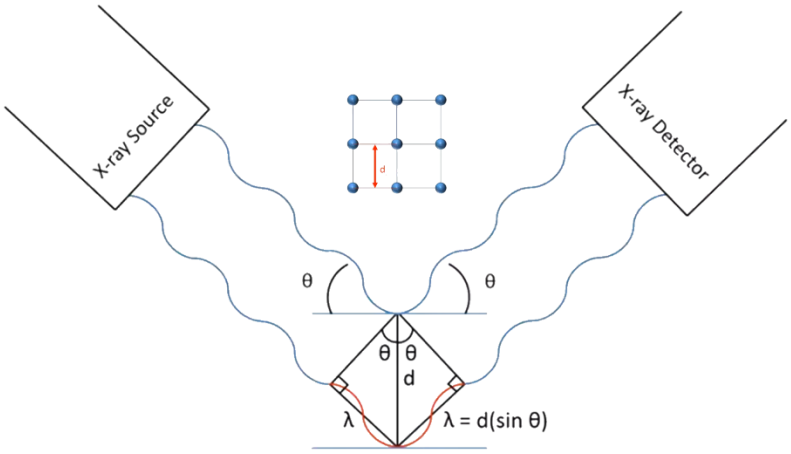

Figure 3.5: Bragg-Brentano configuration for XRD measurements.

In the case of well-prepared powder samples without partially oriented grains, i.e *preferred orientation* [222], the crystal domains are randomly orientated and the majority of the overserved 2θ peaks will follow Bragg's Law for any incident angle. In other words, diffraction peaks will happen in all the planes of the crystal described by the Miller indices (h k l). However, if the material is not in the powder form, texture effects can enhance or reduce the peaks intensity to the point of suppressing it completely. For instance, in epitaxial films like YBCO and GdBCO with the c-axis perpendicular to the substrate, diffraction peaks will only happen for the planes perpendicular to the substrate (001).

In this thesis, a General Detector Diffraction System (GADDS) with a Hi-Star Bruker-AXS detector was used with Cu-Kα radiation to characterize the REBCO films and other crystalline coatings. This system provides the rotation of the sample in three different directions θ, χ and ϕ (Figure 3.6) allowing a

broader analysis of oriented films. Moreover, the bidirectional detector of this machine allows the creation of a 2D diffraction pattern as shown in Figure 3.7. The 2D pattern data is treated with the GADDS software to create the classic "powder pattern" shown in Figure 3.7.

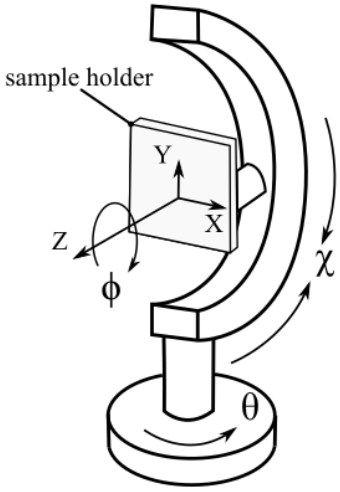

Figure 3.6: Degrees of freedom for Bruker diffractometer sample holder.

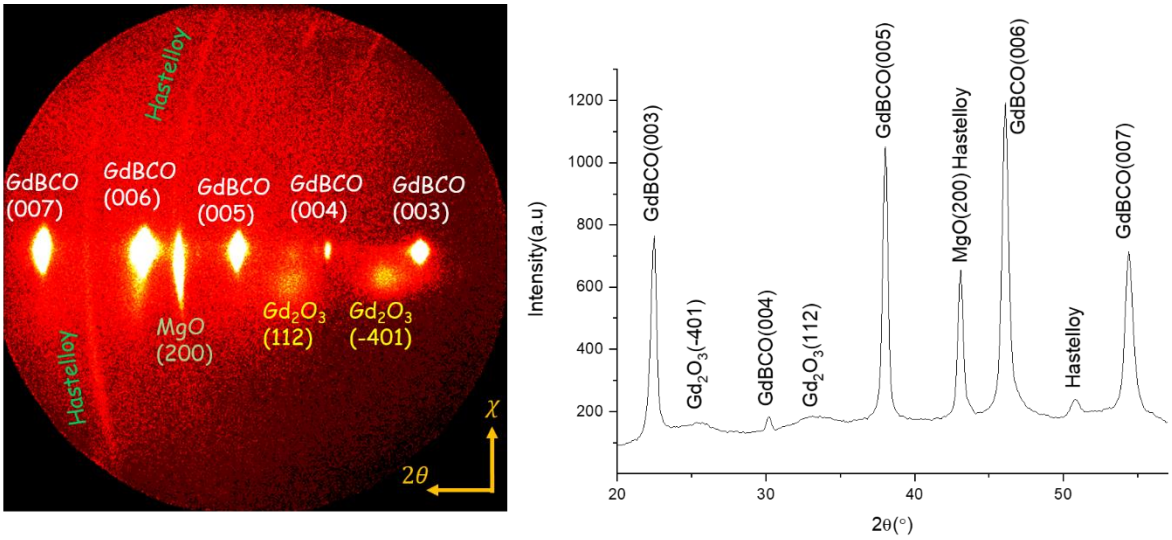

Figure 3.7: Diffraction pattern taken with GADDS for a GdBCO film grown on top of MgO and Hastelloy. (a) $\theta - 2\theta$ 2D Diffraction pattern. (b) 2θ peak intensity powder pattern.

3.2.2 Electron Microscopy – SEM and TEM

The resolution of any microscopy technique is limited by the wavelength of the type of beam used on the sample under study [223]. For instance, in optical instruments it is not possible to distinguish two objects separated by a lateral distance less than approximately half the wavelength of the light beam (400 - 750 nm for visible light) used to focus the image of the specimen under study. This physical restriction is also widely known as the *diffraction barrier* and it is well described by *Abbes Resolution*

theory [224]. In addition, different information can be extracted depending on how the light coming from the specimen is detected; If light is reflected (reflection mode) or transmitted (transmission mode). Electron microscopy follows the same principle using a beam of electrons coming from an electron-gun (e-gun) in vacuum environment. Due to the small wavelength (10^{-10} to 10^{-12} m) of a charged moving electron (Broglie wavelength [225]) the electron-matter interaction happens in the atomic scale providing a higher magnification and resolution.

Depending on the acceleration voltage (V_a) of the beam, analog to a photon, the electron can be scattered (reflected) or transmitted through the sample. However, the electron-matter interaction goes beyond just the transmission/reflection phenomena of a photon. All interactions with the electron beam are summarized in Figure 3.8.

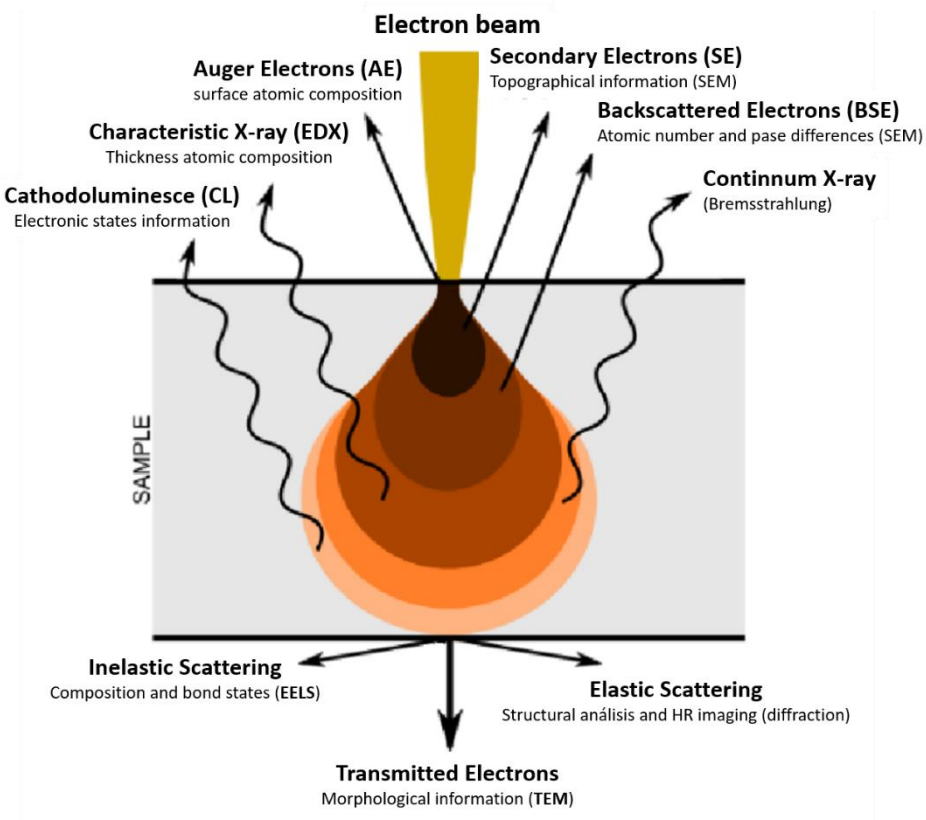

Figure 3.8: Schematic drawing of the Electron–matter interactions and the different types of generated signals.

Scanning Electron Microscopy (SEM), works with V_a~1–30 kV. At this level, the electrons do not acquire momentum for crossing the sample and so part is reflected by elastic atomic collisions creating the Back Scattered Electrons (BSE). Another part is absorbed by the sample in inelastic collisions exciting the atoms, leading to an emission of Secondary Electrons (SE), Auger electrons (Auger e^-) and X-rays.

The standard SEM use a specific set of coils to scan the beam in a raster-like pattern and collect the scattered electrons in two detection systems: one for the SE and another for the BSE. The SE originates from surface regions due to the low energy of the inelastic interactions of the beam with the sample's atoms. They provide only topological information while the beam is scanning a defined area. The contrast in SE images represent different heights between different regions on the sample. On the other hand, the BSE comes from deeper regions within sample as a result of higher energy in the

elastic collisions. These reveal differences in the atomic number and are used to simply identify (not define) regions with different phases and compositions on the sample. In the BSE images, the brighter the material appears, the higher is the atomic number, thus higher density. Overall, SEM provides information on the surface of a sample with magnifications up to ∼1–2 million times and a spatial resolution limited to ∼0.5 nm.

The SEM can also come with an Energy-Dispersive X-ray spectroscopy (EDX or EDS) detector to use the X-ray signals for both qualitative and quantitative analysis. This detector enables the identification of the type of elements that are present as well as the percentage of each element's concentration within a region of choice on the sample. In an EDX spectrum, the energy position of the peaks (keV) defines the element, whereas the intensity of the signal corresponds to the concentration of the element. In this thesis, a SEM device from Quanta FEG-200 located at ICMAB was used for evaluating the morphology of different materials deposited on fully-grown HTS REBCO films.

Transmission Electron Microscopy works with higher V_a ∼60–300 kV to transmit the electrons through the specimen. The portion of electrons that cross the sample can be classified as elastic scattered electrons, or inelastic scattered electrons. The elastic electrons are used in TEM and High-Resolution TEM (HRTEM) to extract the structural composition of samples. The inelastic electrons are used in techniques such as Electron Energy Loss Spectroscopy (EELS) or Energy Filtered Transmission Electron Microscopy (EFTEM) for compositional information. The information appears as 2D projections on a fluorescent screen or via a charge-coupled device (CCD) camera onto a PC screen. It provides information of the crystal structure of the sample with magnification > 50 million times and a resolution < 50 pm.

The TEM measurements presented in this thesis were performed in partnership with members of EPM in a TEM model JEOL 2100F equipped with an Oxford EDS detector using AZtec software from Oxford Instruments.

3.2.3 Focus Ion-Beam (FIB)

Focus Ion-Beam is another microscopy technique used to characterize samples down to the nm scale. The working principle is very similar to a SEM system described in the previous subsection. However, instead of using a focused beam of electrons to scan and image the sample, the FIB uses a focused beam of ions, usually gallium ions (Ga+). The ion-beam can be used at low or high currents depending on the objective of the measurement.

At lower beam currents, the FIB operates in two imaging modes: the secondary electrons and the secondary ions, both produced by the primary ion beam. The secondary electron images show intense grain orientation contrast, thus allowing morphology characterizations like in an SEM. In addition, the secondary ion imaging also reveals chemical differences. At higher beam currents, the high-energy gallium ions in collision with the sample, sputter atoms from the surface. Owing to this feature FIB systems are designed to etch and machine surfaces, especially for the manufacturing and study of semiconductors. Moreover, the ion-beam can precisely mill trenches (slits) through multilayer films, allowing a direct analysis of interfaces. In this thesis the FIB cross section images were acquired with a dual beam (SEM-FIB) Zeiss 1560 XB apparatus.

3.2.4 Atomic Force Microscopy (AFM)

The AFM is a technique capable of characterizing the topography of a sample's surface in the nm scale. The method relies on the atomic force interactions happening between the surface of a material and a nanoprobe sharp tip. Depending on the material and probing method, the atomic forces may come from different sources such as Van der Waals forces, mechanical contact, capillary force and others.

The four basic components of an AFM are shown in Figure 3.9, it consists of: a cantilever, composed of a sharp silicone tip attached to a flexible support acting like a spring; a four-quadrant position sensitive photodiode detector; a laser diode; and a piezoelectric plate scanner. The laser diode continuously shines light on the backside of the cantilever and the reflected light is picked-up by the photodiode detector. As the tip reaches the surface of the sample, the atomic force interaction deflects the whole cantilever, thus leading to a shift on the reflected light beam picked-up by the four-quadrant photodiode detector. The light's position shift allows the quantification of the cantilever's deflection, torsion force, normal force and friction between the tip and the surface. A 2D map of these forces is obtained by moving the sample in a scanning motion using a piezoelectric plate as holder. These maps are later processed in a dedicated software to translate the info to a topography study of the scanned area.

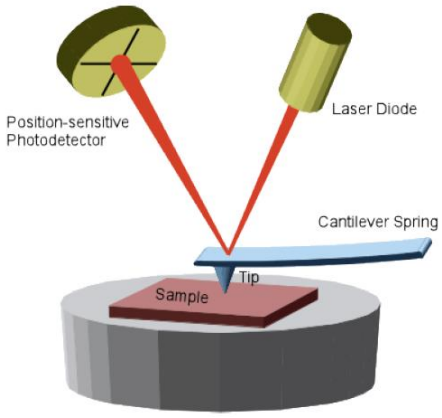

Figure 3.9: Drawing of the basic components of an Atomic Force Microscope: cantilever; a four quadrant position sensitive photodiode detector; a laser diode; and a piezoelectric plate scanner holding the sample.

The scanning tip of the AFM can operate in three different modes: Contact Mode, Non-Contact Mode and Tapping Mode. In this thesis, only Contact mode was used. In this mode, the tip practically touches the surface and scans a predetermined area with a control feedback for the normal force. Meaning, during the scan, whether the tip encounters a bump or valley, the feedback system will move the cantilever vertically in order to maintain a constant normal force.

Another additional feature of the AFM method used in this thesis is the conductive AFM (c-AFM). In this technique, the silicone tip is varnished with a thin metallic conductive film (Pt, Au, Ru, Ti and Cr, among others), the cantilever is charged with a constant voltage (bias-voltage) and the sample is grounded onto the sample holder. In Contact Mode, the electric current flows at the contact point of the tip with the surface of the sample simultaneously with the topography scan. All the AFM measurements presented here were performed at ICMAB with an Agilent 5100 AFM system and AFM images were processed with Mountains Map software from Digital Surf.

3.3 Characterization of the Superconducting Properties

3.3.1 Scanning Hall Probe Measurements (SHPM)

The scanning hall probe microscopy (SHPM), or Hall-scan, was by far the most reliable technique used throughout the experimental work of this thesis. In this method, the superconducting properties are evaluated by analyzing the state of magnetization M on the HTS conductor after field-cooling the CC to 77 K. A scanning probe containing a small Hall sensor at the tip measures the perpendicular trapped magnetic field B_z across the surface (x, y) of a HTS sample [226]. Later on, the mapped $B_z(x, y)$ data, besides providing an overall view of the HTS condition, can be used to calculate the magnetization M and estimate the critical current density distribution $J_c(x, y)$. ICMAB's homemade Hall-scan experimental setup is detailed in [227].

In this procedure, the tape sample is first positioned on a 200x60x2 mm flat Aluminum slab with GE cryogenic varnish on the backside to hold the tape flat onto the Al surface. Afterwards, the sample is covered with a 16 µm thick Al-foil to avoid scratches coming from the moving Hall-probe during the scan. The Al-slab holding the sample is then laid down to rest on the flat bottom of a cryogenic vessel and an origin point $(x = 0, y = 0)$ is set for the Hall-probe. Once the origin is set, a large flat rectangular NdFeB magnet is placed on top of the sample covering the whole CC surface and liquid nitrogen is added to the vessel to start the field cooling process. After the cryogenic thermal equilibrium is reached, the magnet is vertically removed out of the vessel leaving the tape sample magnetized inside. Finally, the LabView routine is initiated to move the Hall-probe and acquire the $B_z(x, y)$ data. An example of the data acquired after the Hall scan is shown in Figure 3.11.

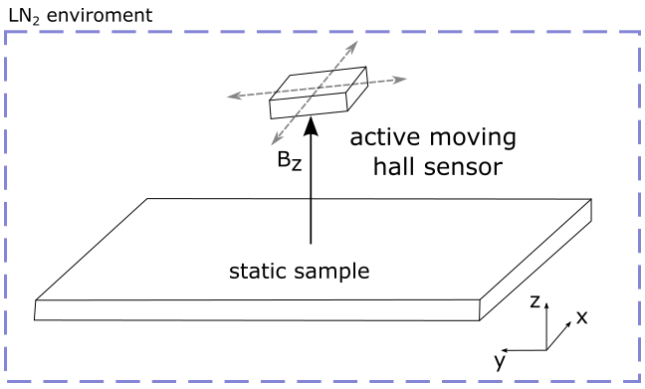

Figure 3.10: Schematic drawing of the CC sample being scanned for the perpendicular magnetic field B_z .

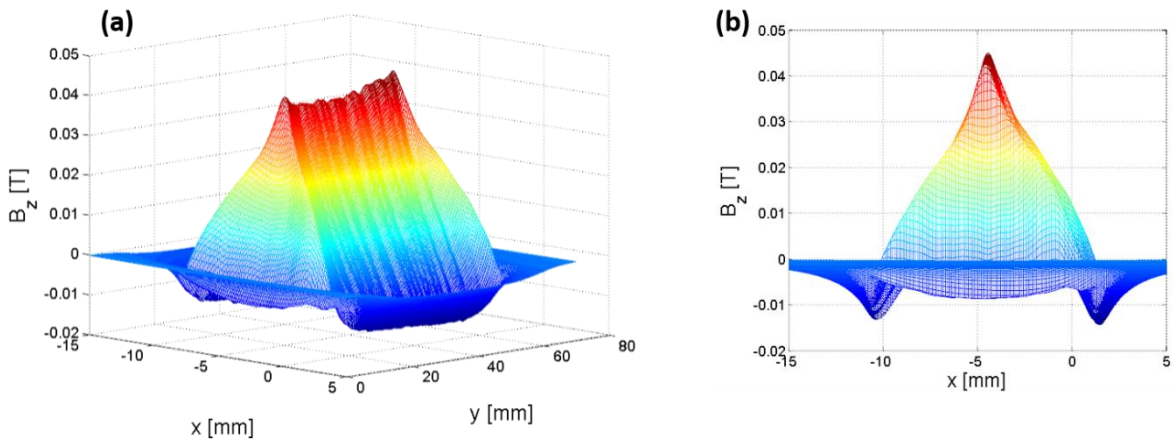

Figure 3.11: B_z distribution acquired with SHPM for a 50x12 mm GdBCO tape sample from THEVA GmbH at 77 K. (a) Isometric view of the B_z (x,y) distribution; (b) frontal view of B_z across the 12 mm width (x-axis); (c) lateral view of B_z .

Before applying the mathematical *MATLAB* routine to calculate the magnetization M and the $J_c(x,y)$ distribution, the initial homogeneity of the REBCO superconductor can be verified by simply analyzing the variation of the maximum field along the tape's length (y-axis). As shown in Figure 3.12(a), the mean field along the length is calculated as an arithmetic average of the plateau region (y from 15 to 54 mm) with an associated standard deviation. The overall continuity of the superconducting state across CC surface can also be qualitatively evaluated with the top view of the B_z (Figure 3.12(b)).

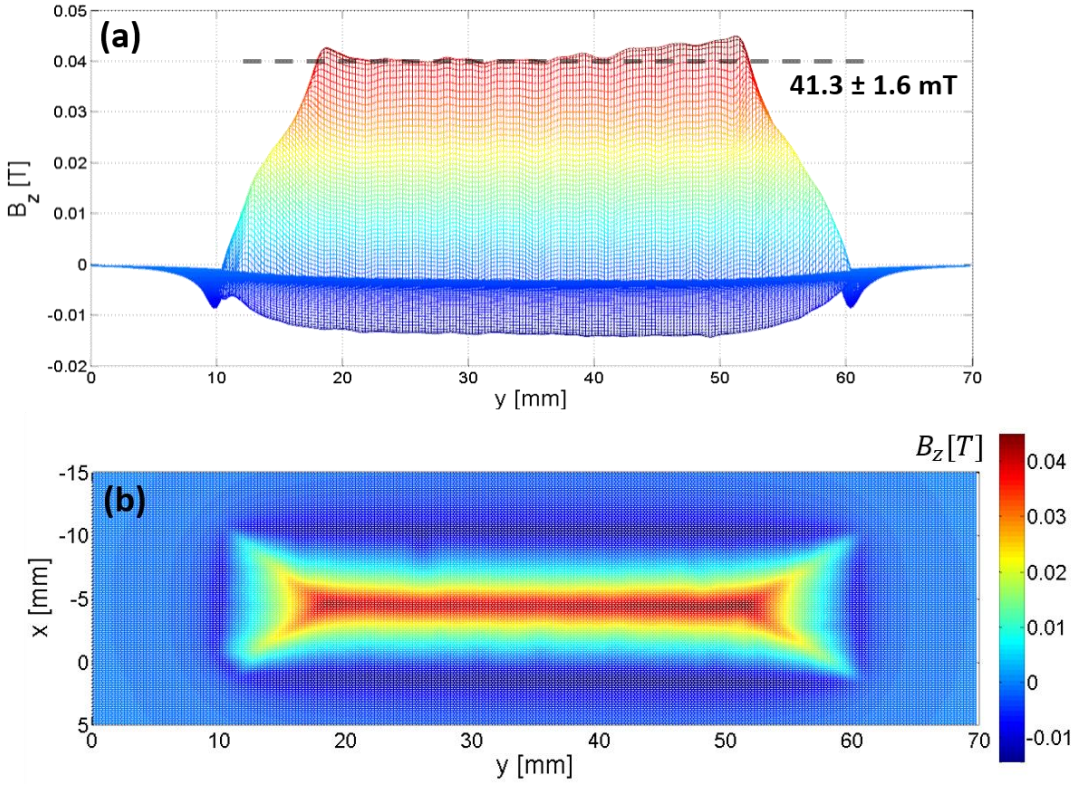

Figure 3.12: B_z distribution acquired with SHPM for a 50x12 mm GdBCO tape sample from THEVA GmbH at 77 K. (a) Longitudinal view of the B_z (x,y) distribution; (b) Top view of B_z across the whole surface of the tape.

From the $B_z(x,y)$ data acquired after the scan, the planar distribution of the critical current density $J = (J_x(x,y), J_y(x,y), 0)$ is directly calculated by the expression:

$$J = rot\ M = \left(\frac{\partial M}{\partial y}, -\frac{\partial M}{\partial x}\right) \tag{3.1}$$

Therefore, the objective is to find M solving the inverse Biot-Savart problem. The Biot-Savart equation analytically describes the magnetic field distribution in the vicinity of a wire transporting a current:

$$B = \frac{\mu_0 I}{4\pi} \int \frac{dl \times \vec{r}}{r^3} \tag{3.2}$$

Where I is the current passing through the wire and r in the spatial position vector for a segment dl of a wire. Theoretically, finding the inverse solution for this equation cannot be done analytically for the $B_z(x,y)$ map shown in Figure 3.12. However, given the discrete nature of the $B_z(x,y)$ measurements, the inverse Biot-Savart problem is tackled by creating a rectangular discrete grid for the sample where the magnetization M is assumed to be constant $M(i,j)$ for each Δij square element. Above this magnetization grid, a second rectangular grid containing the $B_z(x,y)$ measurements is also considered at a fix arbitrary distance $z = h$ from the sample.

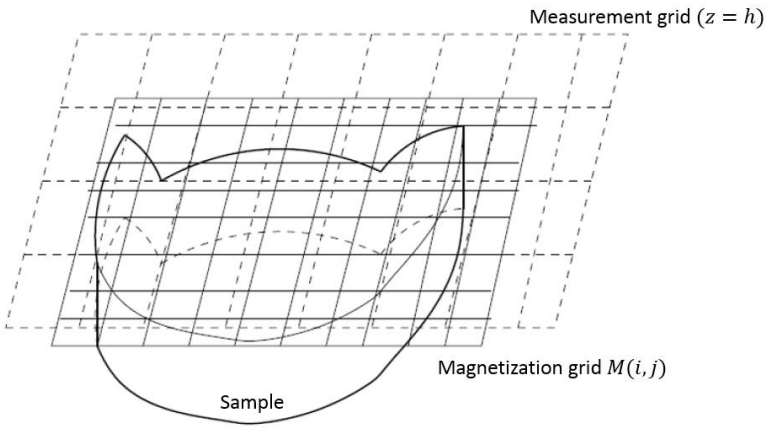

Figure 3.13: Schematic drawing of the theoretical magnetization grid $M(i,j)$ and the measurement grid containing the $B_z(x,y)$ data at $z = h$ for estimating the critical current density distribution $J_c(x,y)$.

Utilizing these two grids, according to [228], the Biot-Savart law for each point (x_m, y_m, h) in the B_z measurement grid can be described by the expression:

$$B_z(x_m, y_m, h) = \sum_{ij} M(i,j) \frac{\mu_0}{4\pi} \int \frac{3z^2 - r^2}{r^5} dvol_{\Delta ij} \tag{3.3}$$

Where $r = |(x_m, y_m, h) - (x, y, z)|$ for all the points in the discrete grid. Simplifying the above equation with the coefficient:

$$G(m,n,i,j) = \frac{\mu_0}{4\pi} \int \frac{3z^2 - r^2}{r^5} dvol_{\Delta ij}$$

The term $B_z(x_m, y_m, h)$ can be rewritten as a linear equation as a function of $M(i,j)$ and $G(m,n,i,j)$:

$$B_z(x_m, y_m, h) = \sum_{ij} M(i,j)\, G(m,n,i,j)$$

Where G is a 4 dimensional Toeplitz matrix [229] that can be written as:

$$G(m,n,i,j) \coloneqq g(m-i,n-j)$$

Therefore:

$$B_z(m,n) = \sum_{ij} M(i,j)\, g(m-i,n-j) = (M * g)(m,n)$$

Applying the convolution properties of a Fast Fourier Transformation (FFT) and using the Inverse Fast Fourier Transformation (IFFT) we have:

$$FFT(B_z) = FFT(M * g) = FFT(M) \cdot FFT(g)$$

And finally,

$$FFT(M) = \frac{FFT(B_z)}{FFT(g)} \Rightarrow M = IFFT\left[\frac{FFT(B_z)}{FFT(g)}\right]$$

After calculating the $M(x,y)$ data, the $J_c(x,y)$ distribution (Figure 3.14) is easily obtained by applying equation (3.1) to M. The final I_c and J_c at 77 K is calculated by integrating $J_c(x,y)$ over a virtual close path inside the tape. The I_c found using this method is not the exact same one found using the critical current transport measurements due to magnetic relaxation in the material after the field cooling procedure [230], but it can be safely estimated with a 15-20% compensation in the final calculated value. For instance, I_c= 432 A according to the integration of $J_c(x,y)$ in Figure 3.14, but according to direct I_c measurements, I_c~517 A which corresponds to a 20% difference.

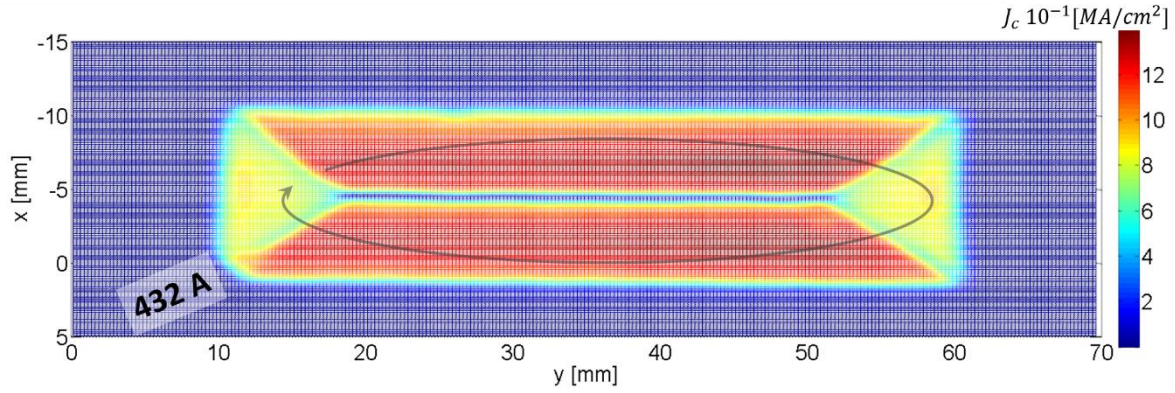

Figure 3.14: J_c distribution calculated with the magnetic flux density B_z data shown in Figure 3.12.

3.3.2 *In-situ* Electrical Conductivity Relaxation (ECR) Measurements

As discussed in section 1.6, the superconducting properties of the $RE_1Ba_2Cu_3O_y$ material is greatly influenced by the oxygen content $y = 7 - \delta$ and so, an oxygen annealing is required to properly dope the material and create practical critical current values. For the standard manufacturing of REBCO tapes, the oxygenation process is usually performed with a temperature profile like the one shown in subsection 3.1.4. However, for one of the diferent manufacturing CFD routes of this thesis, the conditions for oxygenation had to be re-evaluated in the presence of the CFD architecture in order to complete the final CC. For this matter, the oxygen exchange mechanism between the REBCO and the atmosphere was evaluated via Electrical Conductivity Relaxation (ECR) measurements.

In this method, the evolution of the sample's resistance (or conductance) is continuously recorded *in-situ* over time during the oxygenation process. Considering the oxygen in- and out-diffusion following Fick´s 2nd law in equation (1.13), and not too large changes in oxygen partial pressure (PO_2), the proportionality between oxygen concentration and resistivity can be described by the normalized equation (3.4):

$$\frac{\rho(t) - \rho_\infty}{\rho_0 - \rho_\infty} \propto e^{-\left(\frac{t}{\tau}\right)} \tag{3.4}$$

Where $\rho(t)$ is the resistivity in time, ρ_0 is the initial resistivity, ρ_∞ is the final resistivity for $t \to \infty$ and τ is the relaxation time. This equation implies that the resistance is directly linked to the oxygen concentration of the film and it increases and decreases exponentially with a rate described by τ. The bigger τ the slower is the oxygen incorporation process and vice versa.

If the oxygen transfer is dominated by the bulk diffusion in the REBCO, τ represents the diffusion along the ab-planes D_{ab} and $\tau \equiv \tau_{ab}$. However, it is possible that bulk diffusion is not the only mechanism in the overall oxygen loading process and so, one single linear fit is not enough to describe the $\rho(t)$ curve. This scenario is predicted by considering two exponential terms as shown in equation (3.5).

$$\frac{\rho(t) - \rho_\infty}{\rho_0 - \rho_\infty} \propto e^{-\left(\frac{t}{\tau_1}\right)} + e^{-\left(\frac{t}{\tau_2}\right)} \tag{3.5}$$

Samples tested in the ECR set-up were prepared by cutting 12x12 mm specimens from a reel of "naked" (no silver stabilizer) commercial 2G HTS tape. Figure 3.15 shows an example of a 12x12 mm tape specimen GdBCO/MgO/Hastelloy mounted onto the sample holder with four silver wires electrically contacting the four corners of the surface of the HTS material (3 µm thick GdBCO in this case). The wires are bonded to the surface using a high temperature silver ink (Laque Argent L-200N from *CDS Electronique*) and the edges of the specimen were milled with sand paper Struer grit 1000 to avoid short-circuits with the metallic Hastelloy substrate. After bonding the wires, the sample is inserted and sealed hermetically inside a tubular furnace where resistance is recorded whilst temperature and the PO_2 are controlled with a LabView routine.

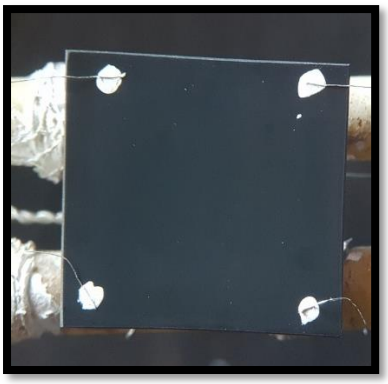

Figure 3.15: Picture of a 12x12 mm piece of GdBCO/MgO/Hastelloy tape sample mounted onto the in-situ ERC measurement system with four silver wires (0.1 mm diameter) bonded to the surface of the GdBCO layer.

Based on the assumptions used for the formulation of equation (3.4), ideally, the sample's resistivity (Ω-cm) should be measured. This could be achieved by using the Van der Pauw [72,231] configuration, but due to logistic and technical difficulties in the ICMAB ERC system this feature was not implemented. Instead, a direct proportionality between resistance (Ω) and resistivity (Ω-cm) is assumed in the film.

A typical temperature profile used to study the kinetics of oxygen diffusion is shown by the red line in Figure 3.16. The measurement starts at 500 °C and cools in steps of 50 °C. A rate of 10 °C/min is used for the initial heating ramp and 5 °C/min for the subsequent cooling steps. At every temperature dwell, the oxygen partial pressure alters from 1 bar to 5 mbar and reverse to observe the in- and out diffusion process respectively. The change in atmosphere is indicated by the colored rectangles in the background. Red and blue represent low (5 mbar) and high (1 bar) oxygen partial pressures respectively. The resistance evolution of the sample in time is depicted by the black curve in Figure 3.16. For temperatures above 400 °C in a 1 bar oxygen atmosphere, the equilibrium resistance can be achieved in less than 1 hour. However, for temperatures below 400 °C, even after long annealing times, the equilibrium resistance cannot be reached in a reasonable period.

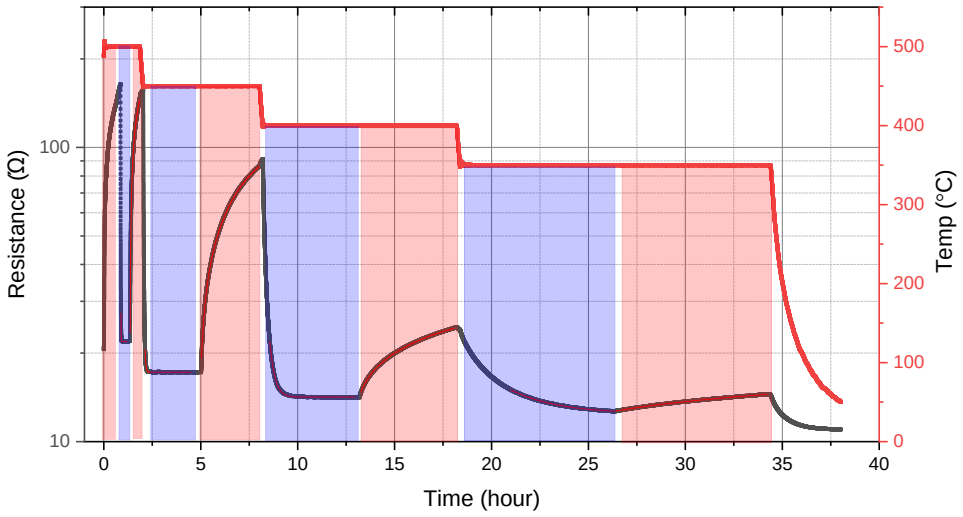

Figure 3.16: Time evolution of the resistance of 12x12 mm GdBCO tape sample from THEVA without silver coating. The temperature decrease following steps of 50 °C starting at 500 °C (500 °C, 450 °C, 400 °C and 350 °C). The resistance curve for

temperature dwells at 475 °C, 425 °C and 375 °C was also taken, but it is not shown here. Oxygen kinetics present a much faster response to changes in pressure at temperatures above 400 °C.

For every section of an atmosphere change at constant temperature, the resistance segment is analyzed individually. The curve segment is fitted to the solution of the diffusion equation described previously using two exponentials as:

$$R(t) = R_\infty + \left[ae^{t/\tau_1} + (a-1)e^{t/\tau_2}\right] \times (R_0 - R_\infty) \tag{3.6}$$

Where $R(t)$ is the resistance in time, R_0 the initial resistance, R_∞ the final stabilized resistance corresponding to $R(t \to \infty)$, τ_1 and τ_2 are the relaxation times and a is a weight factor. In many cases, the oxygen out-diffusion is not well described by a single process and using a two τ constants model results in higher fit accuracy and accurate saturation values for $R(t)$. A single saturation time is sufficient only if the difference of the two saturation times, τ_1 and τ_2, is smaller than the fitting error or if the weight factor a approaches unity ($a \to 1$).

The saturation time dependence on the temperature, extracted from Figure 3.16 using equation (3.6), is shown as an example in Figure 3.17. As expected for a thermally activated process, the time to stabilize the resistance value increases exponentially with decreasing temperature, in both in- and out processes. As shown in Figure 3.17(a), in the range of 350 - 500 °C for oxygen incorporation, one single saturation time linked to a single process is only valid for 500 °C, whereas for oxygen excorporation (out-diffusion Figure 3.17) a double process is required for the entire temperature range. As temperature decreases, there is a shift from one fast exchange mechanism (τ_1) to a second slower parallel mechanism (τ_2). In order to facilitate the analysis of the overall time for oxygen loading between different samples, a weighted arithmetic mean value called effective saturation time τ_{eff} is introduced:

$$\tau_{eff} = a \cdot \tau_1 + (1-a) \cdot \tau_2 \tag{3.7}$$

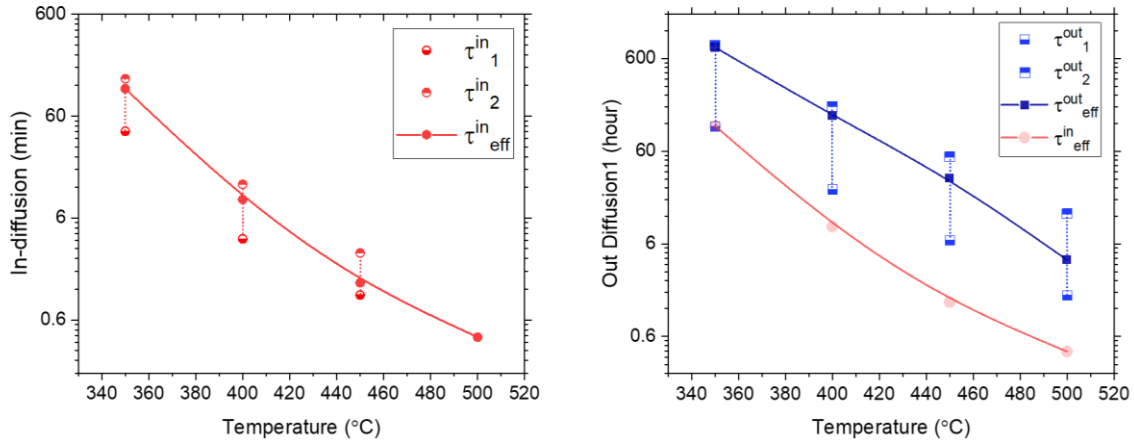

Figure 3.17: Analysis of the relaxation times τ_1, τ_2 and τ_{eff} for a GdBCO/MgO (ISD)/Hastelloy tape sample (Figure 3.16) without silver: (a) Temperature dependence of τ for in-diffusion using 2 exponential constants; (b) Temperature dependence of τ for out-diffusion using 2 τ model and comparing to the τ_{eff} of in-diffusion.

Considering a pure bulk diffusion process (section 1.6.2), the relaxation times as a function of temperature for the in- and out diffusion process should be the same. However, when comparing τ_{eff}^{in} and τ_{eff}^{out} in Figure 3.17(b), it's clear that the effective in-diffusion relaxation times are shorter than

the effective out-diffusion over 1 order of magnitude. This asymmetry has been reported in previous works from the SUMAN-ICMAB group [80,99] and is a strong indication that surface exchange reactions play a crucial role in REBCO thin films.

Therefore, considering the overall process controlled by the surface exchange rate k_{chem} (cm/s), using the data from Figure 3.17 and equation (1.18), the Arrhenius plot of k_{chem} versus the reciprocal temperature $1000/T$ can be used to extract the activation energies of the in- and out- diffusion using equations (1.18) and (1.19) as shown Figure 3.18.

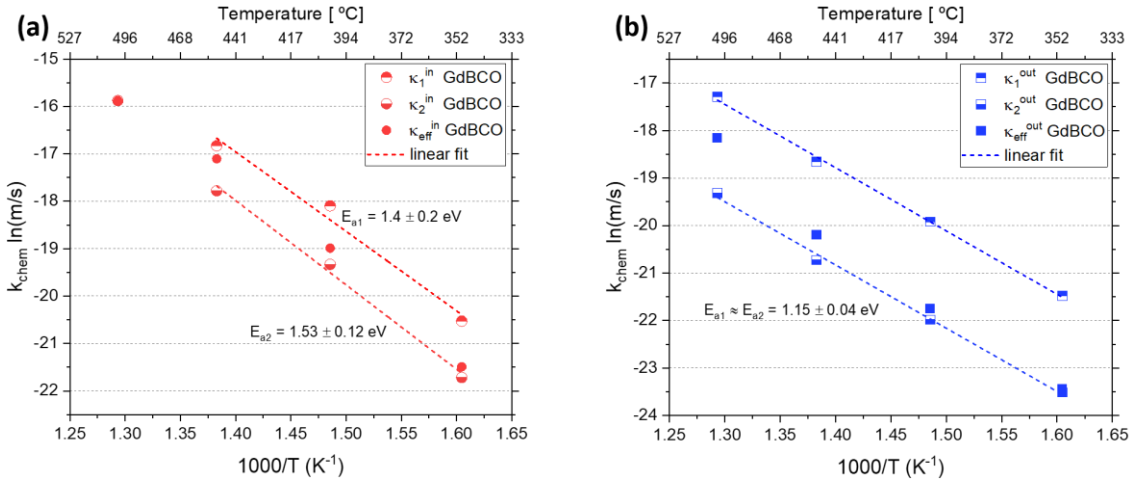

Figure 3.18: Calculation of the activation energies E_a from the Arrhenius plot k_{chem} versus 1000/T for the in- (a) and out- (b) diffusion of oxygen in GdBCO/MgO (ISD)/Hastelloy tape sample (Figure 3.16) without silver.

The extracted activation energy in the temperature range of 350 – 500 °C for oxygen incorporation is 1.44 eV for the faster process link to τ_1^{in} and 1.53 eV for the slowest τ_2^{in}, which is slightly higher than for the reverse process of oxygen excorporation (out-diffusion), with an activation energy of 1.15 eV for both of the two parallel mechanisms (τ_1^{out} and τ_2^{out}, Figure 3.18(b)). These values are slightly higher than the usual reported activation energies around 1 eV, but again seem to agree with previous studies from the ICMAB-SUMAN group for YBCO thin films (200-1000 nm) [99].

3.4 Electric Transport Measurements

Transport measurement is a general term used to describe any type of electric test where a current is transported from end-to-end by physically applying a voltage potential in a HTS sample like the 2G HTS tape. Depending of the objective of the measurement, the voltage/current profile applied may change. In this thesis, four types of transport measurements were performed: critical current tests (to determine I_c in A), AC/DC limitation tests (to determine E_{lim} in V/m and fault time in ms), Current Transfer Length (CLT) tests (to determine the presence of the CFD architecture) and the Normal Zone Propagation Velocity (NZPV) measurements (to determine the NZPV in m/s).

3.4.1 Critical Current Test

A typical sample holder used for measuring a CC sample in transport current is shown in Figure 3.19. This basic configuration is also used with minor alterations to perform current limitation tests and measure the NZPV behavior of the tape.

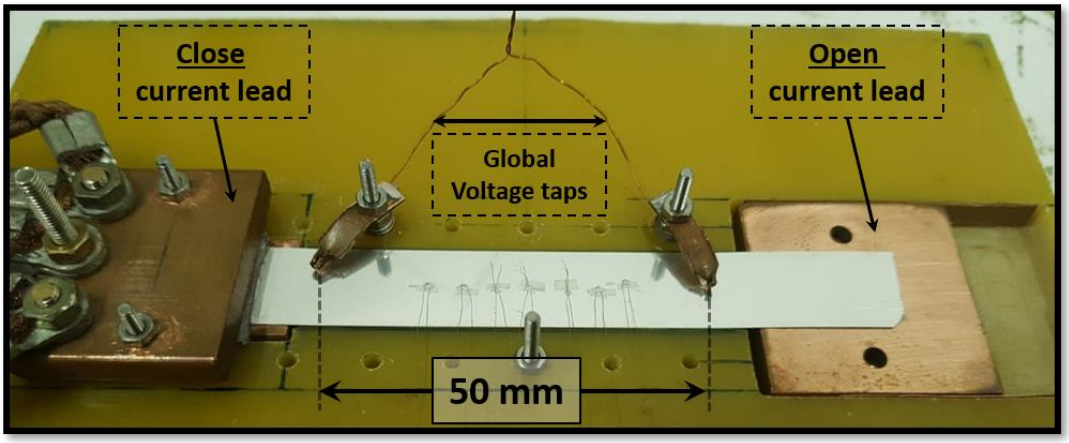

Figure 3.19: Picture of ICMAB's sample holder used for critical current measurements and other transport current tests in 2G HTS tapes. The sample in the picture is a 10 cm piece of commercial THEVA tape with silver stabilizer. The sample was mounted with only one pair of voltage taps.

The sample's I_c is extracted by applying consecutive square pulses of transport current with a gradual increase of amplitude (Figure 3.20(a)). For each pulse, the voltage across a certain known fixed distance L is measured before (M_1), during (M_2) and after (M_3) the current plateaus to calculate precisely the voltage drop during each current pulse as $V_{drop} = (2M_2 - M_1 - M_3)/2$. The result is a non-linear I-V curve where I_c is interpolated for the correspondent value of critical voltage V_c defined by the critical electric field E_c (Figure 3.20(b)). Conventionally, E_c is defined as $1\ \mu V/cm$ and $V_c = L \times E_c$. The amplitude of the current pulses is increased usually beyond V_c to provide a good range for the interpolation of I_c, but it should stop before surpassing the electric field threshold (E_{stop}) to avoid quenching the sample and possible damage.

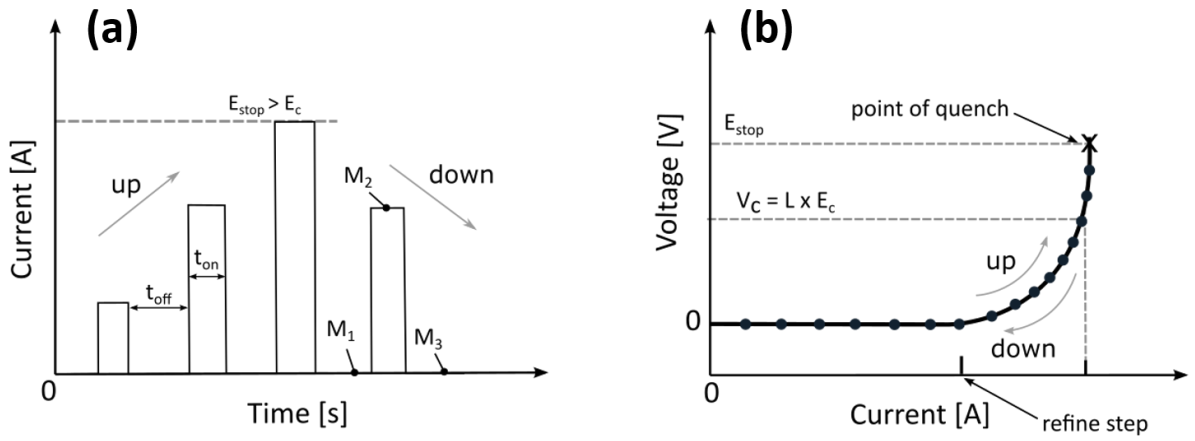

Figure 3.20: Experimental procedure for critical current analysis of CC samples. (a) Sequence of current pulses used for creating the intrinsic I-V curve of the sample. The voltage measurement for each pulse is usually compensated for off-sets with three measurement M_1, M_2 and M_3 and current amplitude of the pulse can be gradually increased or decreased if needed. (b) Analysis of the I-V curve for the extraction of I_c using the critical electric field criteria E_c.

In the I-V curve, the values of applied current below 70% of I_c represent the *transport region* of the curve where no voltage is detected due to the zero-resistance state of the superconductor, and the region corresponding to the voltage rise around I_c, is the *intrinsic region*. The transition behavior between these two regions can be well-described by the *Power Law* (section 1.3.4) written in the I-V form:

$$V(I) = I_c \left(\frac{I}{I_c}\right)^n \tag{3.8}$$

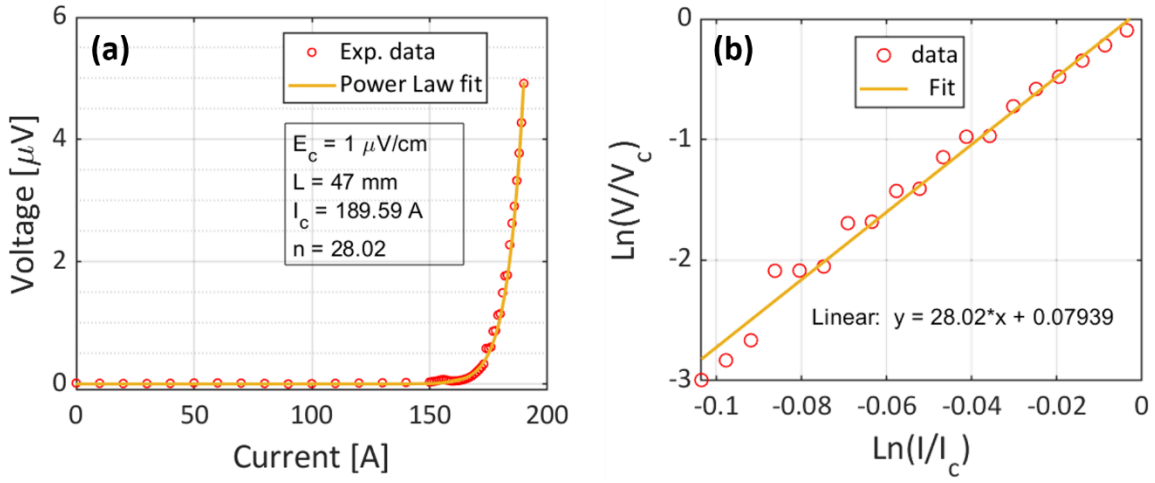

Figure 3.21: Example of a fitting procedure for critical current analysis of CC samples. (a) Fitting of the transport and intrinsic regions of the I-V curve is done with the Power Law to determine I_c based on E_c criteria (usually 1 μV/cm). (b) Normalized I-V data using I_c in Ln scale for the linear fit of the n-value

Using equation (3.8) to fit the I-V data, the exponential n-value term can be determined with a linear fit of the normalized curve in log scale (Figure 3.21(b)). As mentioned in subsection 1.3.4, this value is a crucial input parameter for numeric simulations of devices utilizing superconducting wires [232]. But it can also be used for evaluating the sensitivity of the CC to a quench due to thermal disturbances [233], thus potentially revealing possible defects in the REBCO material causing a premature quench process. Nonetheless, most of the times the direct inspection of I_c before and after an experiment is a faster approach to spot the degradation of the HTS film.

3.4.2 Current Transfer Length Measurements

The Current Transfer Length (CTL) test is a relative new technique in the experimental realm of REBCO CCs and it was developed by *FASTGRID* partners at EPM to specifically evaluate the CTL of a CC for the CFD architecture. Since the increase in the CTL is directly related to the NZPV increase (subsection 2.4.1), this technique can be used to make a pre-evaluation of the current crowding effect created by the presence of the CFD architecture. The method basically consists of mapping and analyzing the voltage distribution across the flat surface of a small (3-5 cm) REBCO CC in low transport current (< 1 A) after performing a special etching procedure of the REBCO layer.

As shown in Figure 3.22, the CC sample is modified by chemically etching away the REBCO-stabilizer layers locally to form a groove/trench along the width of the tape (y-axis) at a position half-way across

the length (x-axis). After the etching, the sample is silver sputtered to fill the groove and close an electrical path with the overall silver stabilizer. In the presence of a low-level transport current at 77 K, the groove forces the current to transfer from the REBCO to the silver. Using arrays of pogo-pins, the surface potential in the region of the groove is measured and the data is fitted to a semi-analytical (SA) model to calculate the CTL. The detailed development of the SA model can be found in [234]. Here, only a conceptual summary is presented to illustrate the usefulness of the technique.

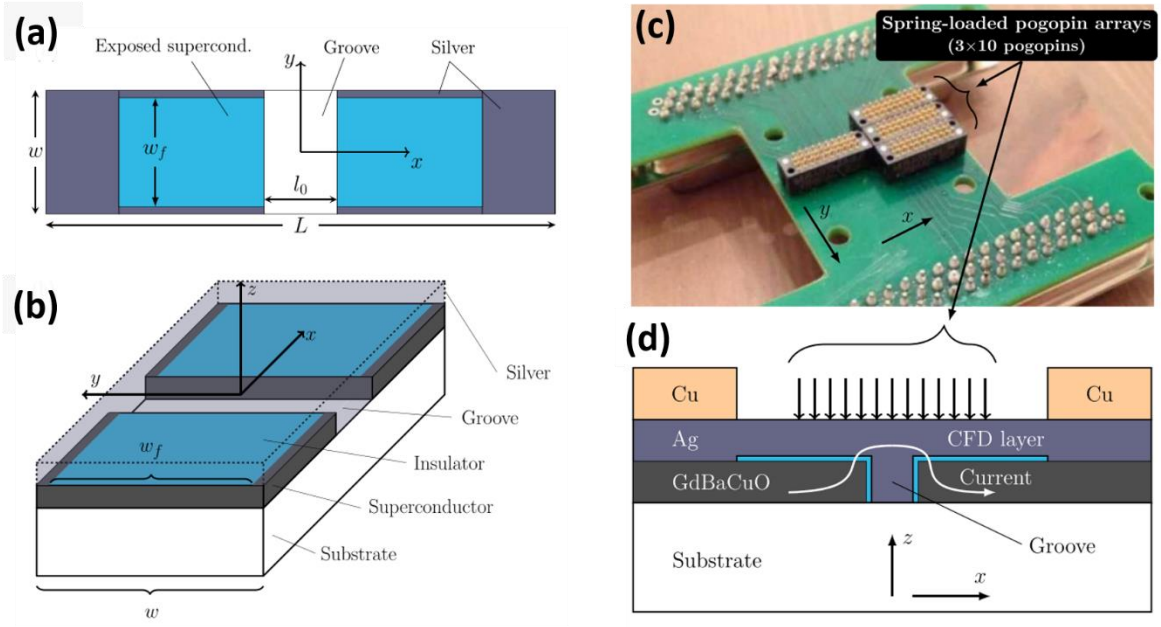

Figure 3.22: (a) Spring-loaded pogo pin arrays soldered to a PCB. The PCB piece is positioned on top of the HTS CC for the CTL measurements. (b) Schematic drawing of the sample's cross-section with the etched groove. The groove diverts the current path in transport current between the Cu pads (pogo pins represented by the black arrows on the groove region). Figures taken from [235] *with permission.*

Assuming small potential fluctuations due to neglectable thickness variation (z-axis) of the thin silver stabilizer and the REBCO layer, the voltage distribution can be described by a planar Helmholtz equation:

$$\nabla^2\big(V_{Ag}(x,y)\big) - k^2(y)\Big(\big(V_{Ag}(x,y)\big)\big) - \big(V_{RE}(x,y)\big)\Big) \tag{3.9}$$

Where $V_{Ag}(x,y)$ is the surface potential of the silver, $V_{RE}(x,y)$ is the potential in the REBCO layer and $k(y) = \sqrt{\rho_{Ag}/R(y)}d_{Ag}$ with ρ_{Ag} being the silver resistivity, d_{Ag} silver thickness and $R(y)$ the local interfacial resistance function across the width described as:

$$R(y) = \begin{cases} R_f, & if \ \ -w_f/2 < y < w_f/2 \\ R_0\,, & if \ \ -w_f/2 < y < w/2 \end{cases} \tag{3.10}$$

Working in equation (3.9), a differential Laplace operator $D \equiv \nabla^2 - k^2(y)$ can be used to rewrite the equation as:

$$DV_{Ag}(x,y) = -k^2(y)V_{RE}(x,y) \tag{3.11}$$

In the equation (3.11) format, $V_{Ag}(x,y)$ can be decomposed into a linear combination of eigenfunctions ψ_{ij} of the operator D. Consequently, this allows $V_{Ag}(x,y)$ to be rewritten as $V_{SA}(x,y)$

(semi-analytical SA) a double infinite sum of analytical eigenfunctions $\psi_{ij}(x,y)$ and coefficients c_{ij} as follows:

$$V_{SA}(x,y) = \sum_{i=1}^{\infty}\sum_{j=1}^{\infty} c_{ij}\,\psi_{ij}(x,y) \tag{3.12}$$

The fitting procedure of the experimental data using equation (3.12) includes seven input parameters: the total width of the CC tape (w), the width of the CFD region (w_f), the thickness of the silver shunt (d), the width of the groove (l_0), the high interfacial resistance of the CFD region (R_f), the low interfacial resistance of the CFD-free edges (R_0) and the total voltage drop ΔV resulting from the etched groove path.

Table 3-1: Example of the parameters used to fit the CTL experimental data with the semi analytical model described in [234]. *The experimental data was taken for a THEVA CC altered by EPM's silver re-sputtering technique.*

Parameters	Value
w	12 m
w_f	11.28 mm
d	1 µm
l_0	2 mm
R_f	1 mΩ-cm^2
R_0	100 nΩ-cm^2
ΔV	335 µV

Figure 3.23(a) shows an example of a surface $V_{Ag}(x,y)$ fitted with the parameters of Table 3-1 on to the experimental data of a CFD sample done by the classic technique described in subsection 2.4.3. The parabolic distribution of the voltage potential along the width (y-axis) in Figure 3.23(b) is considered the "signature" behavior of the CFD. If the interfacial resistance were uniform ($R_0 = R_f$) the voltage distribution would be constant (flat shape across the y-axis).

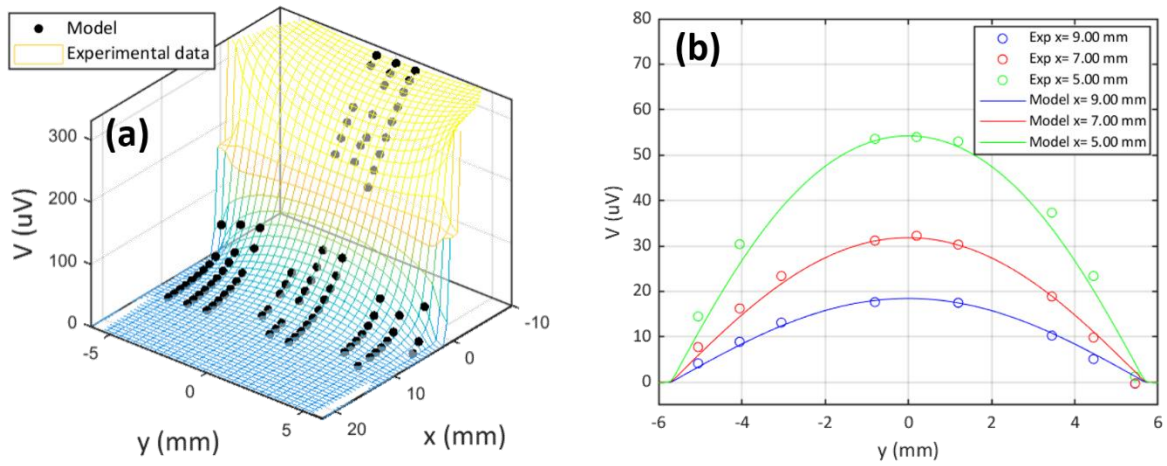

Figure 3.23: Current Transfer Length (CTL) measurements for a typical CFD sample at 77 K. (a) Experimental data (black dots) fitted to the model for potential distribution on the silver surface of sample. (b) Parabolic potential distribution along the width (y-axis) of sample.

The direct inspection of the presence of the CFD effect can be spotted by analyzing the profile of the potential across the width (y-axis) of the tape (Figure 3.23(b)). The "bell shape" of the curves indicates a non-uniform interfacial resistance creating the expected current crowding effect.

Furthermore, knowing $V_{SA}(x,y)$, the current density along the length $J_x(x,y)$ can be calculated as:

$$J_x(x,y) = -\rho_{Ag}^{-1}\frac{\partial V_{SA}(x,y)}{\partial x} \tag{3.13}$$

And the net current $I(x)$ flowing through the silver determined as:

$$I(x) = d_{Ag}\int_{-w/2}^{w/2} J_x(x,y)\,dy \tag{3.14}$$

Finally, with $I(x)$ the CTL can be calculated using the definition for the CTL given in section 2.4.1 with equation (2.12).

3.4.3 Electric NZPV Measurements

In the NZPV tests, the NZPV of the tape is evaluated by applying a single current pulse of constant amplitude. The voltage evolution is recorded across the length of the tape with multiple voltage probes touching the metallic stabilizer/shunt of the tape as illustrated in Figure 3.24 and detailed in Appendix C. However, previous to the pulse, an artificial hot-spot is created on the middle of the tape by positioning an NdFeB magnet close to its surface. The magnet's field induces a substantial local decrease in critical current ($I_c(x=0) = I_c^* < I_c$) and serves as a consistent point of origin for the quench propagation in repetitive tests. Therefore, the amplitude of the pulse I_p is chosen in the range $I_c^* < I_p < I_c$ and the current is held constant as a way to minimize changes in input power to acquire an average value of the NZPV.

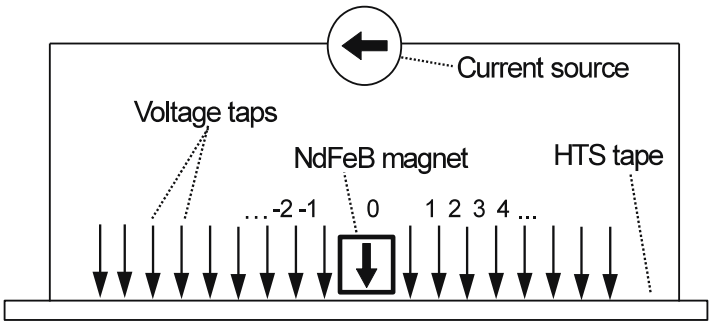

Figure 3.24: Schematic drawing of the experimental set-up used to measure the NZPV of 2G HTS CC tapes. Figure taken from [207] *with permission.*

One example of the data acquired with the array of probes after a 120 A current pulse, is shown in Figure 3.25. Dividing the voltage data by the known distances between the probes, the y-axis is plotted as the electric field V/m. The NZPV is extracted by initially finding the time intervals between curves required for the E-field to reach an established, arbitrary fixed value above the critical electrical ($E_c =$

$1\ \mu V/cm$). Finally, the NZPV is calculated using these time intervals and the distances between the voltage probes to obtain an average value of the quench velocity.

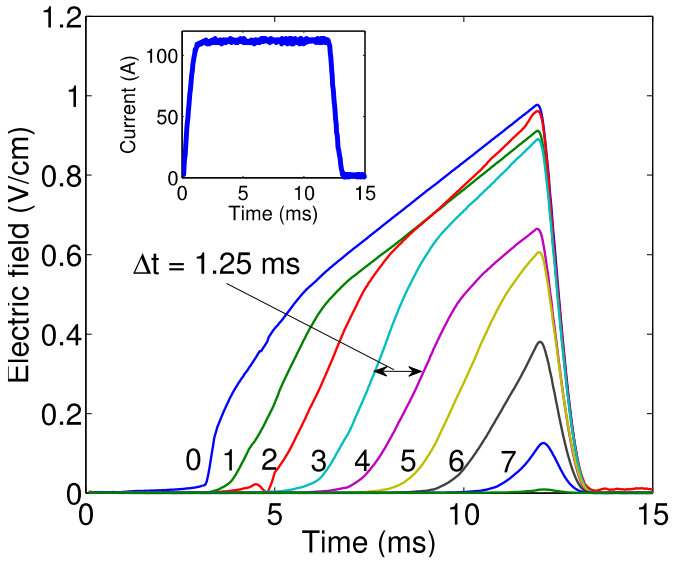

Figure 3.25: Example of the experimental data acquired after the NZPV test. One single current pulse was applied and held constant for a short time (10 ms). Meanwhile the evenly distributed probes record the voltage evolution in time.

The measurement of Figure 3.25 is repeated multiple times for different amplitudes of current to determine the NZPV (cm/s) as a function of the current amplitude (A). As a benchmark, Figure 3.26 shows the NZPV curves for the commercial THEVA tapes with the uniform interfacial resistance and the CFD tape created with THEVA's CC following EPM's silver re-sputtering technique. These curves represent crucial information for comparing the experimental and simulated NZPV data between different CC architectures. This graph will reappear many times throughout this thesis.

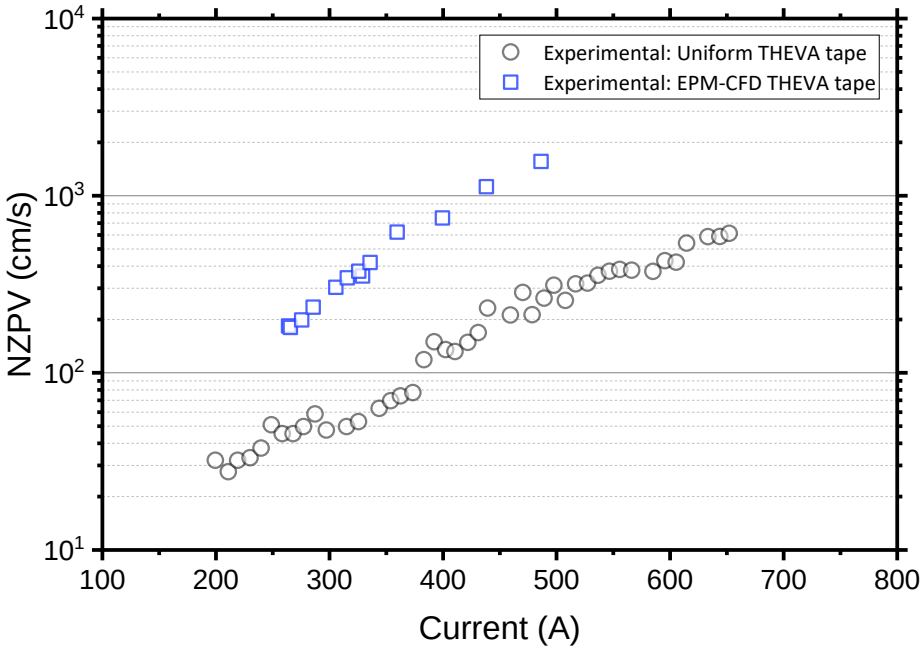

Figure 3.26: NZPV versus current for experimental data measured by EPM of a classic THEVA tape with uniform low interfacial resistance.

3.4.4 Fluorescent Thermal Imaging

Developed by *FASTGRID* partners in Karlsruhe Institute of Technology (KIT), the Fluorescent Thermal Imaging was another technique used to characterize the quench propagation for the 2G HTS CCs studied in this thesis. This approach uses a fluorescent micro-thermographic imaging technique at high speeds for measuring the normal zone propagation [236,237].

In this method, the CC sample is initially coated with a thin layer of a fluorescence material (EuTFC or EuTTA) via droplet deposition. Once the fluoresce coating is established, the CC is mounted on a holder with current leads, two voltage probes at the ends and an NdFeB magnet positioned behind the CC as shown in Figure 3.27. For the measurements, the holder is vertically inserted inside a double-walled glass cryostat and filled with liquid nitrogen. As described in subsection 3.4.3, a current pulse of amplitude in the range $I_c^* < I_p < I_c$ is applied to ignite the quench. Outside of the cryostat, an array of UV LEDs excites the fluorescence coating and a high-speed camera records the fluorescent light emission reflected from a mirror directly positioned in front of the CC.

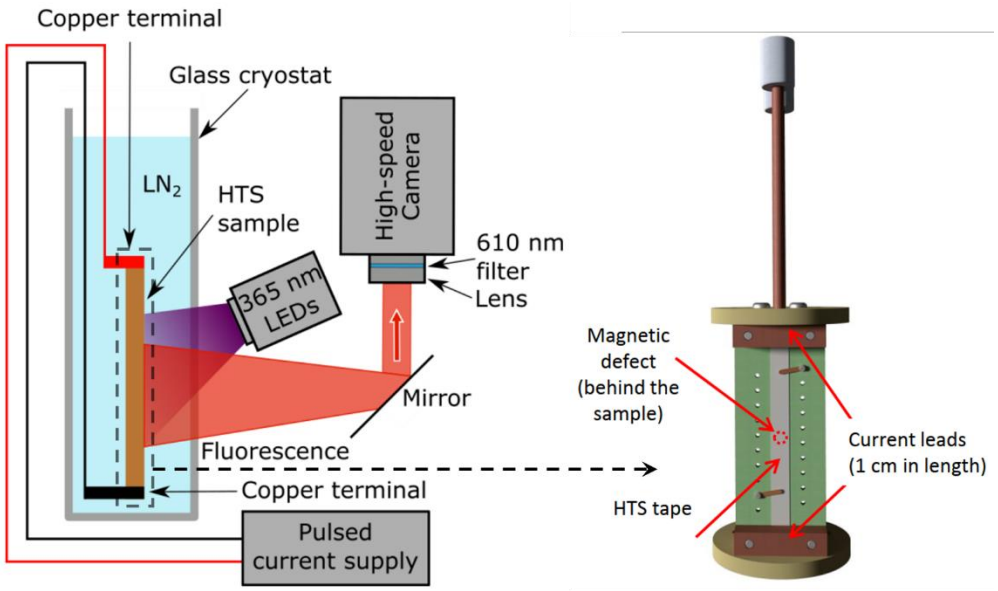

Figure 3.27: Schematic view of the fluorescent thermal imaging experimental setup. The sample is placed in a double-walled glass cryostat and submerged in liquid nitrogen. The UV LED array excites the sample at an oblique angle and the high-speed camera records the fluorescent light emission through a mirror due to the experimental arrangement.

The NZPV (subsection 2.3.6) is evaluated by post-processing the recordings of the high-speed camera after the pulse(s) of current. The temperature evolution on the 2D surface of the CC is extracted by correlating the intensity (Figure 3.28(a)) of the fluorescent emission with temperature (Figure 3.28(b)) in a linear calibration done prior to the experiment. The speed of the *thermal* wave front is determined by using an overlay grid to measure the distances (Figure 3.28(b)) frame by frame considering the following arbitrary time and distance criterion:

Definition of quenched region: Any region where the temperature is at or above 93 K.

Definition of starting time: The quench start time is chosen as the first-time instance where a quench is visible. The NZPV is measured from this point onwards.

Definition of distance travelled: The distance travelled is defined as the furthest point of the quench zone, along any position of the tape's width.

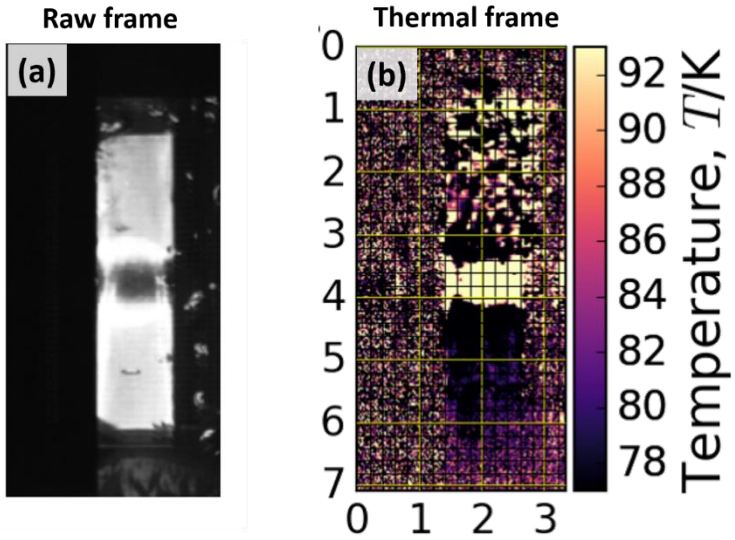

Figure 3.28: Example of Fluorescent Thermal analysis for a frame of a CC sample during quench at 680 A pulse. (a) Frame of the raw footage taken with the high-speed camera. (b) Thermal analysis of the frame with a mm-scale grid used solely for measuring the propagation of the normal zone. The temperature scale is set to 77-93 K.

3.4.5 DC Limitation Tests

In DC limitation tests, a current fault condition is emulated by applying a single rectangular voltage pulse of fixed amplitude. Since the voltage is held constant for a certain time, the value of the current in the circuit is solely defined by the resistance of the HTS tape. During the fault, the local and global electrical field (E-field) across the tape's length is measured using multiple voltage probes as illustrated in Figure 3.24. The array of voltage probes is the same used in the NZPV system shown in Appendix C.

A schematic drawing of the fault limitation circuit used by *FASTGRID* patterns in EPM is shown in Figure 3.29. A more detailed description of the system can be found in [189]. The circuit consists of two set-ups operating separately: the "Limitation setup" containing a voltage source in series with the sample, and the "I_c setup" containing a current source to determine the critical current. The circuit alters between the two setups using knife switches at the leads of the sample. With this circuit, the robustness of the sample in different fault conditions is evaluated by measuring the I_c before and after each limitation test.

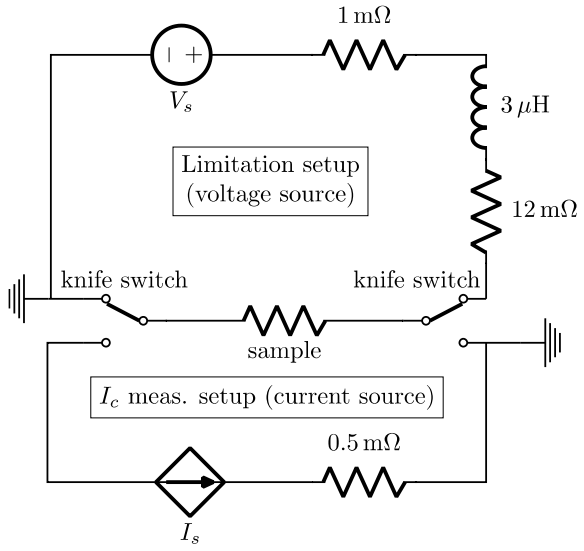

Figure 3.29: Schematic drawing of the experimental setup used for performing limitation tests and critical current measurements.

3.4.6 AC Limitation Tests

The AC limitation tests were performed with collaborators of the Université Grenoble Alpes with the system shown in the diagram of Figure 3.30. In this system, the current fault condition is created by applying a single voltage pulse in AC (50 Hz or 60 Hz). The voltage source V_{source} is an autotransformer capable of delivering $0 - 380\ V$ and a second transformer with a ratio $m = 30/380$ controls the high current levels needed to quench the samples. The overall circuit impedance is represented by $R_{circuit}$ and $L_{circuit}$. The remote-controlled switch S1 connects and disconnects the SFCL element (2G HTS CC tape sample) to the voltage source V_{source} and the switch S2 by-passes the resistor R_f to create the short-circuit fault. The prospective fault current in the circuit is adjusted changing the value of the resistance R_f and V_{source}.

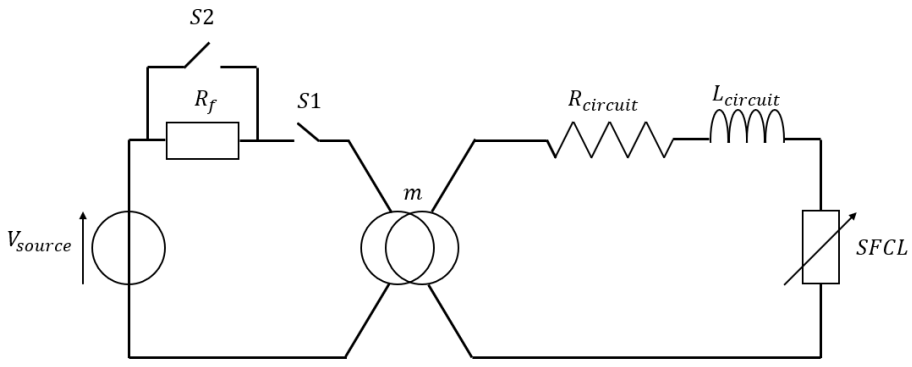

Figure 3.30: Simplified schematic drawing of the experimental setup used for performing AC limitation tests in Université Grenoble Alpes.

Figure 3.31 shows an example of the data collected during one AC limitation test for a clear-fault scenario of ~50 ms with the autotransformer set to 200 V_{rms}/m. The SFCL element in this case was a 15 cm CFD tape sample created with EPM's method using a 12 mm wide THEVA tape (subsection

2.4.3). The current fault (yellow line in Figure 3.31) of ~750 A was created at t = 10 ms closing the switch S2. The tape quenched immediately in the first AC cycle sustaining a E_{lim} of approximately 200 V_{rms}/m for ~50 ms (red line in Figure 3.31) and S1 disconnected V_{source} in the zero-crossing point t = 57 ms.

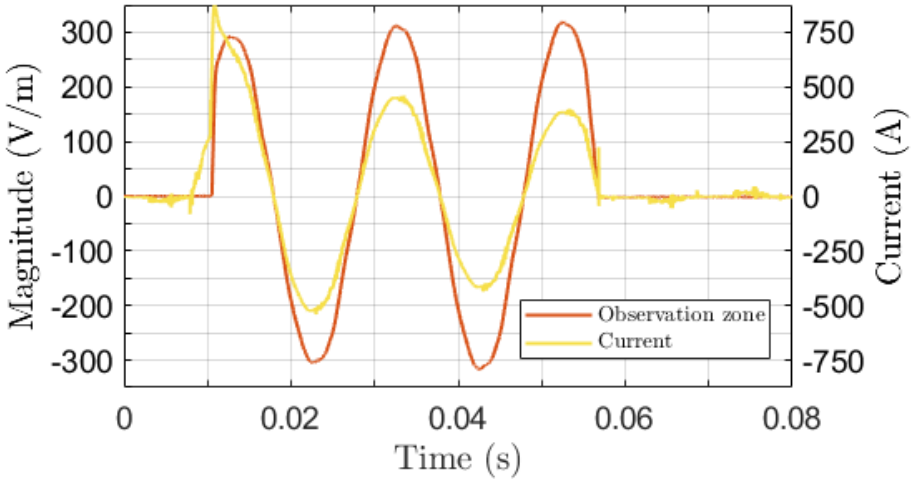

Figure 3.31: EPM-CFD test in AC Limitation at 200 V_{rms}/m for 50 ms fault duration to achieve the clear-fault regime.

The possibility of degradation between each test could be roughly evaluated by identifying the level of current leading to the initial quench. Figure 3.32 shows how this quench current in the case of the EPM-CFD sample did not decrease up until the 16th and 17th test where both were conducted at 220 V_{rms}/m for 50 ms. The quench current increases from test to test due to the increase of the voltage V_{source} and only drops in case of I_c degradation.

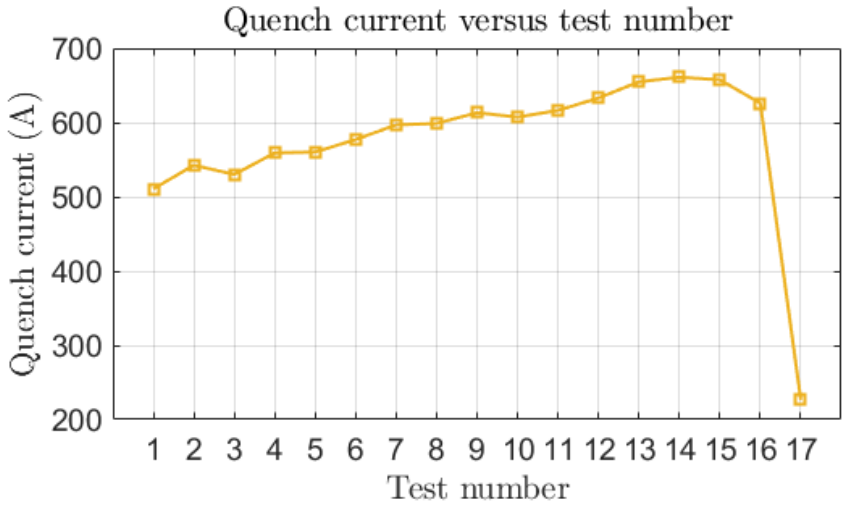

Figure 3.32: Analysis of the quench current at each AC limit test for a EPM-CFD tape sample.

In addition to the electrical measurements, the slow-motion footage of the sample quenching in liquid nitrogen was measured. The sample holder containing the tape could be placed horizontally inside the cryostat facing the transparent wall (Figure 3.33). Behind the sample, a small NdFeB magnet was positioned to initiate the quench in its middle. Outside of the cryostat, a slow-motion camera from *Phantom* records the quench behavior of the tape with a frame rate of 43000 fps and an exposure

time of 5 µs. In order to obtain a clean footage of the film boiling evolution, only two voltage taps were installed at each extremity of the sample to monitor the global electric field.

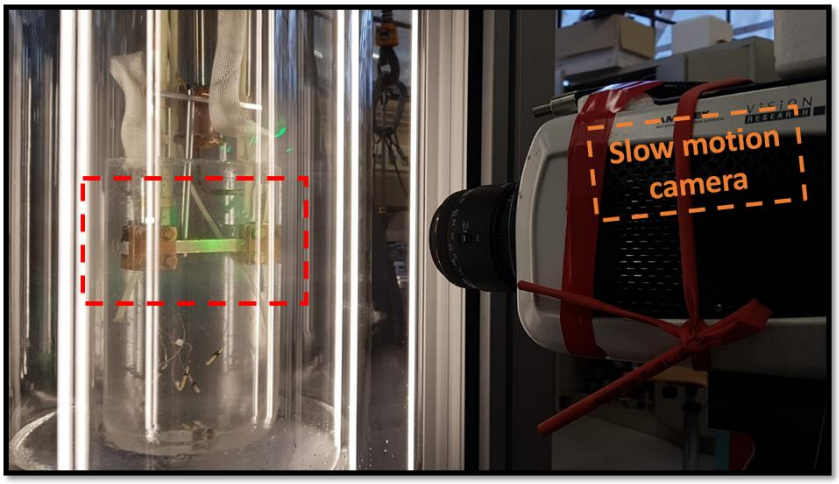

Figure 3.33: Picture of the slow-motion transport current set-up of Université Grenoble Alpes for filming the quench behavior of 2G HTS tapes in AC fault limitation tests. The transport current sample holder containing the sample is immersed vertically in a transparent cryostat to allow recording the footage.

Utilizing this technique, the signature behavior of the CFD architecture is spotted in the analysis of the film boiling frame by frame. The characteristic film boiling formation of the CFD appears in the beginning of each test (Figure 3.34). This visual result was useful for comparing performance with the CFD-graphite tape samples (section 4.4.4).

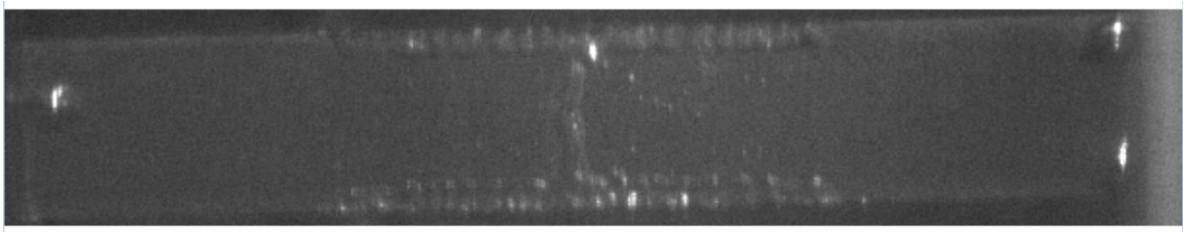

Figure 3.34: Picture of the H-shape film boiling formation of CFD-EPM 12 cm tape with copper coating in the beginning of the quench during the 15th AC limitation test.

3.5 CFD Simulations

In order to verify the possibility of incorporating different types of CFD, 3D finite element simulations were performed using the *COMSOL Multiphysics* 5.5 software with the Joule Heating module and a template provided by EPM. This template was originally conceived to demonstrate the concept of the CFD architecture boosting the NZPV of 2G HTS tapes [206] and it was used here as valuable tool for predicting certain behaviors during the NZP of other types of CFD structure. In this section, we provide a brief description of the geometry implemented, the materials considered and the basic equations used in the thermal-electric model.

3.5.1 The Geometry

The CC cross-section geometry considered for the simulations is shown in Figure 3.35 with the physical meshed layers: substrate (brown), buffer (yellow), REBCO superconductor (black) and the stabilizer surrounding all the structure (white grey). The green and blue regions do not represent an actual physical layer, but rather the high and low interfacial resistance regions between the stabilizer and REBCO along the width of the CC. The geometry in Figure 3.35 represents the structure of CFD tape, but it can be also used for a classic CC by considering a uniform low interfacial resistance along the whole width w.

One important remark is that in practice, the interfacial resistive layers are much thinner than the other layers (substrate-buffer-REBCO). These are approximated as 2D domains making the in-plane components of current density (J_x and J_y) neglectable. Moreover, due to the symmetry of this geometry, the computational time can be reduced by simulating only half of the CC's width using a symmetry plane along the length (x-axis).

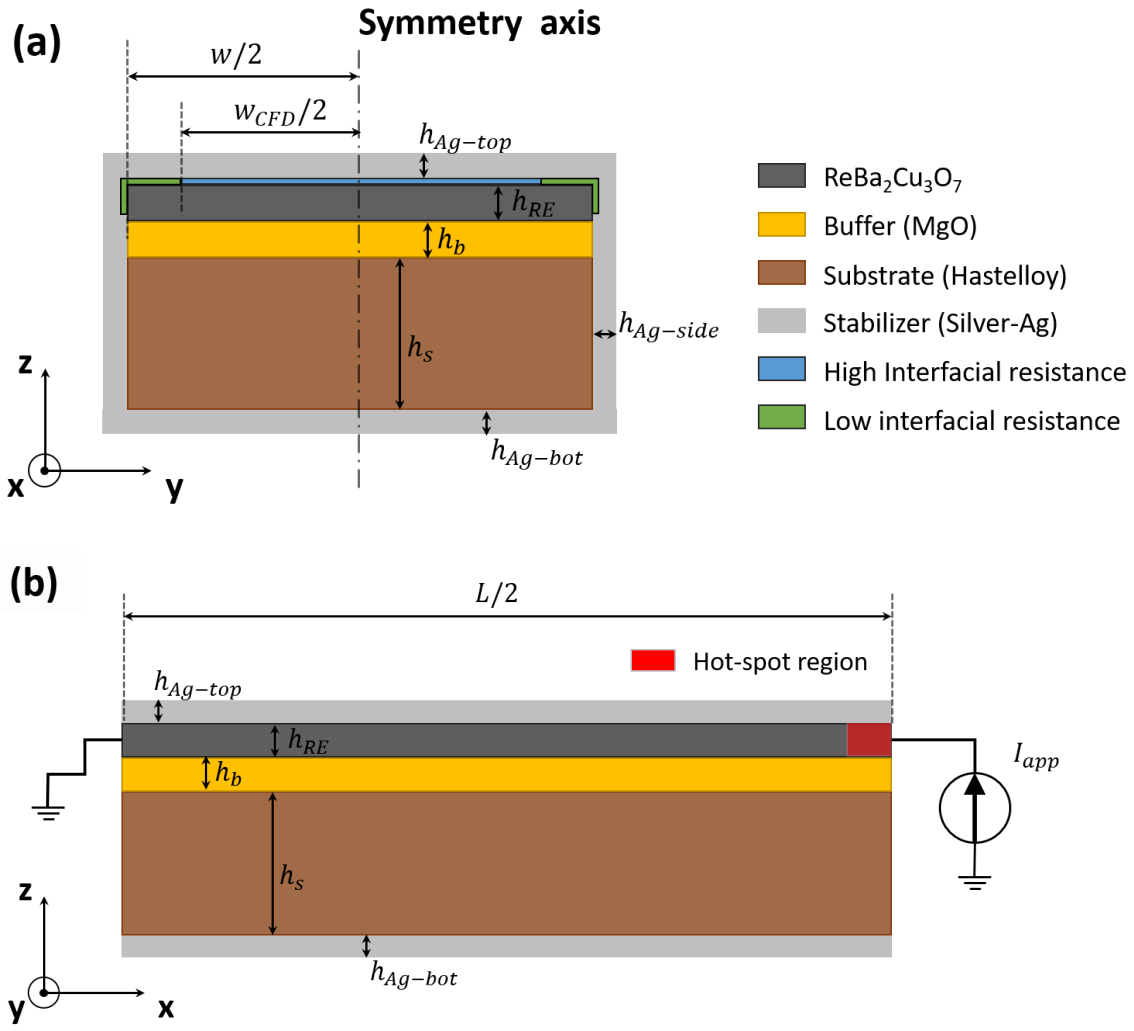

Figure 3.35: (a) Cross-section schematic drawing (not up to scale) of the dimensions considered for the 2G HTS CC geometry with CFD in the 3D finite element simulations performed using the COMSOL Multiphysics. This same geometry can be applied to a CC with uniform interfacial resistance by simply considering the High (blue) and Low (green) interfacial resistances with the same value in the parameters of the materials. (b) Longitudinal view of the 2G HTS CC considering a transport current

traveling across the REBCO layer and a hot-spot region. The different interfacial resistances and the side-stabilizer layer are not represented in this view for better visualization of the scheme.

3.5.2 The Simulated Materials

Since all the CC samples used in the experimental work of this thesis came from *THEVA GmbH*, the following materials were considered for each layer: Hastelloy for the substrate, MgO for the buffer, GdBCO for the REBCO and silver for the stabilizer. Apart from the GdBCO, all the electric and thermal properties such as density (kg/m^3), thermal conductivity (W/m-K), specific heat (J/kg-K) and resistivity (Ω-cm) can be easily found in the material science literature and added to the simulation as parameters to be interpolated from a table of values. *THEVA* traditionally uses GdBCO instead of YBCO, but given the similarities in the REBCO family a generic REBCO layer is consider by simply taking YBCO's thermal properties.

The only property that requires modeling is the non-linear behavior of the REBCO's conductivity as a function of temperature. This behavior is described here as the sum of two conductivities; one for the superconducting state $\sigma_{sup}(T)$ and one for the normal state $\sigma_n(T)$.

$$\sigma_{REBCO}(T) = \sigma_{sup}(T) + \sigma_n(T) \tag{3.15}$$

The term $\sigma_{sup}(T)$ can be described by the Power-Law in equation (3.16) and $\sigma_n(T)$ is described by the linear behavior of the resistance once $T > T_c$.

$$\sigma_{sup}(T) = \frac{J_c(T)}{E_0}\left(\frac{\|E\|}{E_0}\right)^{\frac{1-n(T)}{n(T)}} \tag{3.16}$$

The critical current density is defined as:

$$J_c(T) = \begin{cases} J_{c0}\left(\dfrac{T_c - T}{T_c - T_0}\right), & T < T_c \\ 0 \quad , & T \geq T_c \end{cases} \tag{3.17}$$

And the exponential n-value term is given by:

$$n(T) = \begin{cases} (n_0 - 1)\left(\dfrac{T_c - T}{T_c - T_0}\right)^{\frac{1}{4}} + 1, & T < T_c \\ 1 \quad , & T \geq T_c \end{cases} \tag{3.18}$$

Where T_c is the critical temperature, T_0 is the temperature of liquid nitrogen, J_{C0} is the initial critical current density at T_0 (in other words $J_c(T_0)$), E_0 is the critical electric field, $\|E\|$ is the norm of the electric field in time and n_0 is a fitting parameter.

The formation of the hot-spot to initiate the normal zone propagation (NZP) is accomplished by altering the initial current density distribution J_{c0} along the width and length (yx-axis) according to equation (3.19).

$$J_{c0} \rightarrow J_{c0}\left(1 - Ae^{-\left(\left(x-\frac{L}{2}\right)^2+\left(y-\frac{w}{2}\right)^2\right)/d^2}\right) \quad (3.19)$$

Where d corresponds to the width size of the defect in J_{c0} and A the amplitude of the defect. Implementing equation (3.19) into equation (3.17) lowers locally the I_c in one end of the tape (Figure 3.35(b)), thus creating the natural condition for the occurrence of a hot-spot. In addition, only in the first microseconds of the simulation, a small temporary heat source is applied in the same region of this lower I_c to push the hot-spot region to initiate a quench.

For properly solving the simulation, the Joule-heating model from *COMSOL Multiphysics* combines two set of equations from two separated standard embedded models; the "Electric Currents" model and the "Heat Transfer in solids" model. Therefore, the software solves simultaneously the equations for the voltage V and the temperature T as the simulation run. The detailed description of the theoretical physical equations used by *COMSOL* for solving V and T can be found in [206].

3.5.3 Simulation Example

As a practical example of the information that can be extracted from these NZPV simulations, w present here the results for a uniform THEVA tape and a CFD tape based on the same structure. Table 3-2 reveals all the major parameters considered for the geometry and the materials' properties.

Table 3-2: Parameters and numeric values for the NZPV simulations using the 2G HTS structure of THEVA tapes

Parameters	Value	Physical properties reference
Length (L)	6 cm	-
Width (w)	12 mm	-
Hastelloy substrate thickness (h_s)	95 µm	
MgO buffer thickness (h_b)	3 µm	
GdBCO thickness (h_{REBCO})	3 µm	
High interfacial resistance (CFD layer thickness)	100 nm	10 mΩ-cm^2
Low Interfacial resistance layer thickness	100 nm	100 nΩ-cm^2
Top, bottom and Sides - Ag stabilizer (h_{Ag-top}, h_{Ag-bot}, $h_{Ag-side}$)	1 µm	
Critical current density (J_{c0})	1.95 MA/ cm^2	
Critical temperature (T_c)	90 K	
Liquid nitrogen temperature (T_0)	77 K	
Critical electric field (E_0)	1 µV/cm	
n-value at T_0 (n_0)	15	
Defect amplitude (A)	0.9	
Defect size (d)	1 mm	
Applied current (I_{app})	200 A	

Using the parameters of Table 3-2 to simulate the NZPV, the evolution of temperature and voltage in time is obtained on all the meshed volume of the tape. As mentioned before, the uniform structure is accomplished by considering the interfacial resistance Ag/GdBCO uniform and with a fixed value of

100 nΩ-cm^2 and the CFD by part of the width (w_{CFD}) with 10 mΩ-cm^2. Figure 3.36 reveals the state of the temperature in the GdBCO layer at t = 3 ms for a uniform tape showing the virtual probes added to the same layer. These probes are equidistantly spaced along the length (y-axis) in the symmetry line of the geometry and the data is used to plot the local temperature and voltage evolution as shown in Figure 3.37.

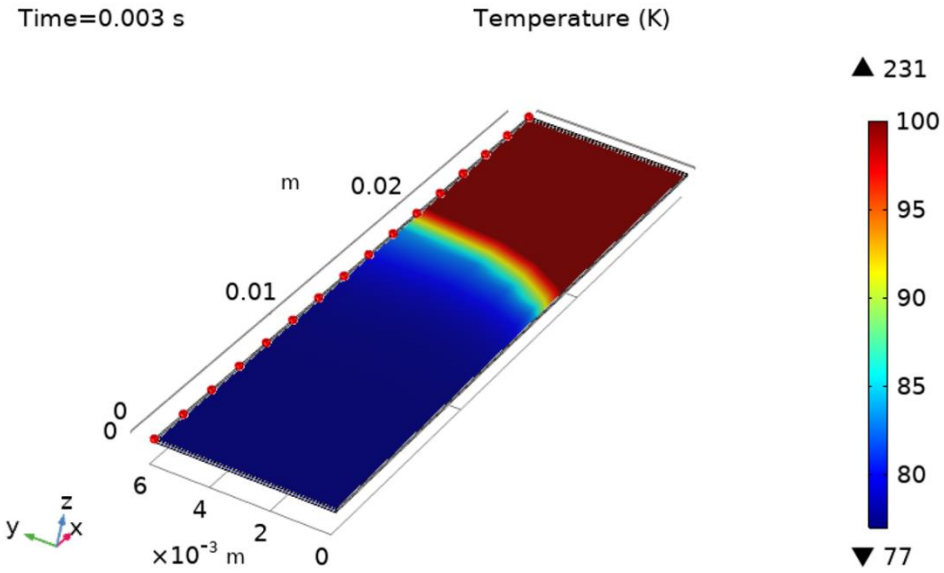

Figure 3.36: Isometric view of THEVA's CC showing, in color scale, the temperature evolution during the normal propagation zone for the parameters listed in Table 3-2. The interfacial resistance was considered uniform (100 nΩ-cm^2) for the whole Ag/GdBCO (no CFD).

The NZPV is extracted from the data in Figure 3.37 by considering a reference temperature line at 90 K intercepting the temperature curves. Each interception corresponds to the moment the REBCO layer reaches 90 K and is completely quenched. The NZPV is calculated by dividing the known distance between the probes by the time intervals correspondent to these intercepted points. This same analysis can also be done using the curves of voltage versus time to observe certain discrepancies in the NZPV and temperature distribution, but just the thermal analysis is sufficient to obtain an overall idea of the NZPV behavior here.

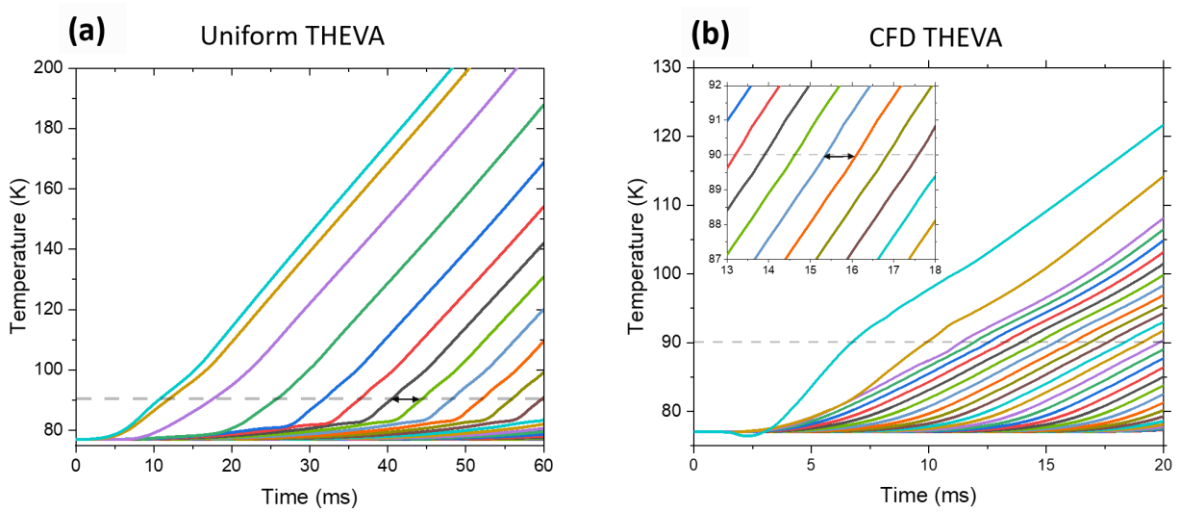

Figure 3.37: Graphs of the Temperature versus time for the array of virtual probes located along the tape's length (x-axis). (a) Uniform THEVA tape after 60 ms of simulations time. (b) CFC-THEVA tape after 20 ms of simulation time.

Furthermore, these simulations can perform a swipe over different values of applied current I_{app} to obtain the NZPV versus Current curve for the architecture under consideration. As an example, Figure 3.38 reveals two simulated NZPV curves for the two cases mentioned before: the uniform THEVA and the CFD-THEVA. The uniform THEVA curve (black solid line) seems to agree well with the experimental data collected using the technique described in section 3.4.3. In addition, the CFD-THEVA curve (blue solid line), shows a reasonable prediction of the NZPV boost when the interfacial resistance is increased from 100 nΩ-cm^2 to 10 mΩ-cm^2 over the width $w_{CFD} = 0.95\ w$.

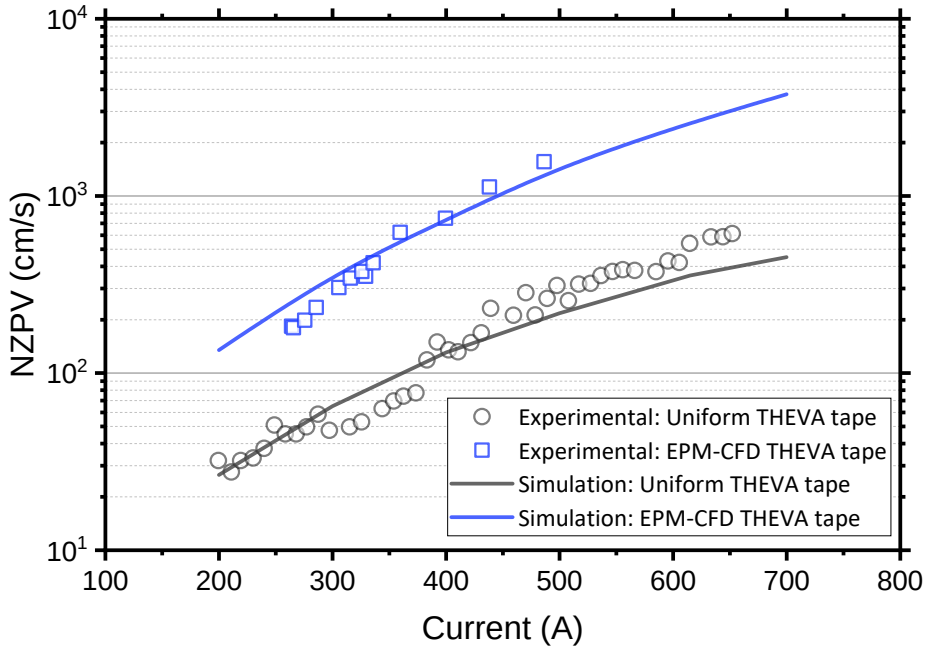

Figure 3.38: NZPV versus current for the experimental and simulated data of a classic THEVA tape with uniform low interfacial resistance and a THEVA tape with the standard CFD architecture created by EPM.

4 First Materials for the CFD Architecture

Finding the best approach to incorporate the CFD concept in the 2G HTS architecture of coated conductors revolves around tuning the right conditions for the creation of a practical high value of interfacial resistance in the CFD layer. However, as this chapter will illustrate, these conditions are not so obvious. Before tuning any of the known CFD parameters, one must first establish what are the critical conditions surrounding the integrity of a CC with the CFD behavior.

This chapter reports on how some of these "critical conditions" were found empirically during the first attempts of creating the CFD effect in THEVA tapes. These attempts followed the simplest approach of introducing known materials, e.g commercial epoxy and graphite composites in between the Ag/REBCO interface. The epoxy and graphite were chosen purely based on chemical stability with respect the REBCO film and compatibility with low cost deposition methods such as ink jet printing and spray-coating.

4.1 Characterizing the GdBCO Surface

Before considering the different deposition techniques and materials to play the role of the CFD layer on the REBCO film, an initial characterization of the available REBCO film was performed to assure chemical and physical compatibility of the superconductor with the envisioned CFD materials. For instance, the solution deposition of liquids with low-viscosity and low surface tension could penetrate into pre-existing pores [238] and cracks [239] of the REBCO film. This phenomenon could extend an expected acceptable thin surface degradation of the film, to an undesirable degradation across the thickness thus comprising the percolation of current. Moreover, in some cases, CC manufactures add extra special coatings like chlorine [240] for the protection of the film and such elements must be identified beforehand to predict possible harmful reactions with any new coatings.

4.1.1 SEM Analysis of the GdBCO Surface

The surface characterization on a 12x12 mm bare tape piece from *THEVA GmbH* composed of GdBCO/MgO/Hastelloy layers was performed by SEM. The top view of the GdBCO surface revealed the presence of unknown bodies/particles sparsely distributed across the surface (bright bodies in Figure 4.1(a)). The chemical characterization via EDX/SEM of one of these bodies exhibited the same elements Gd, Ba, Cu and O corresponding to the GdBCO surrounding material (Figure 4.1(c)). Therefore, speculating on the exact chemical composition of each particle solely on EDX wasn't possible. However, these bodies presented a neglectable gray scale shift in the backscattered image (Figure 4.1(b)), thus strongly suggesting a similar density to that of the superconducting GdBCO material.

It is well known in the literature of REBCO synthesis that virtually all vapor deposition methods, such as PLD, DC sputtering, and MOCVD can create precipitates on the surface of the films just the like

bodies/particles shown in Figure 4.1. The precipitate formation is very sensitive to the growth conditions and stoichiometry, and it can consist of the main $REBa_2Cu_3O_7$ phase and many different secondary phases. For instance, for $YBa_2Cu_3O_7$ synthesis some reported phases are: CuO, Y_2O_3, $YCuO_2$, $BaCu_2O_2$, YCu_2O_5 and Y_2BaCuO_{5-x}. Therefore, it is reasonable to affirm that these precipitates are not an exclusive aspect of THEVA's manufacturing procedures. One explanation provided by K. Fujiko is that the nucleation of these precipitates occurs at the initial stage of film growth due to the supersaturation of impurity phases [241].

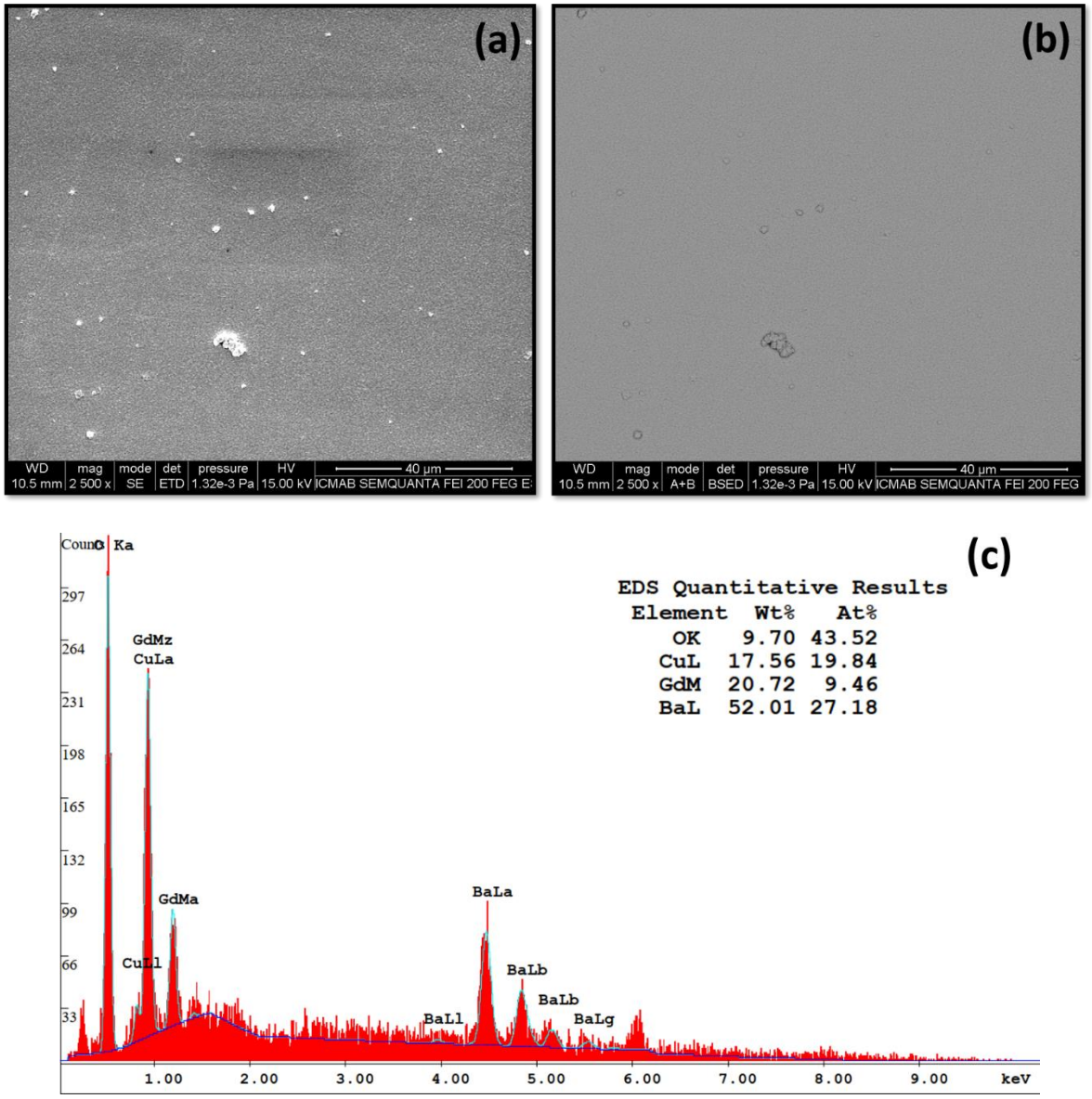

Figure 4.1: SEM images of a 12x12 mm bare piece of CC from THEVA GmbH *composed of GdBCO/MgO/Hastelloy layers. (a) Secondary Electrons (SE) image of the GdBCO surface. (b) Backscattered Electrons (BE) image of the GdBCO surface. (c) EDX analysis of a precipitate on the GdBCO film.*

From the planar perspective of Figure 4.1(a), some of these surface precipitates have dimensions surpassing 1 µm in diameter. For this reason, the 12x12 mm sample was tilted inside the SEM to acquire a second 3D view of the sample's surface. As shown in Figure 4.2(a), the precipitates have a considerable dimension perpendicular to the GdBCO surface sticking out to heights surpassing 1 µm.

This final analysis allowed to classify these precipitates as outgrowth peaks made of an unknown phase of the GdBCO material.

Like YBCO, most of the GdBCO oxide secondary phases are not conductive, e.g Gd_2O_3 and CuO, but some other phases are indeed as conductive as the main $GdBa_2Cu_3O_7$ phase at room temperature. In a c-AFM study performed by Martin Truchlý, it was shown that the surface degradation of YBCO in air is much slower in these precipitate phases, thus leading to a conductivity 20x higher than surrounding areas [242]. The possibility of having the majority of outgrowth peaks being from a phase with an electrical conductivity similar to that of the superconducting $GdBa_2Cu_3O_7$ phase presented a critical concern for the CFD interface. Depending on the density distribution of these peaks, the thickness of any CFD insulating material on top of such GdBCO/MgO/Hastelloy template would have to be very well-tuned in order to avoid short-circuits through the insulation happening between the final silver stabilizer and the "tall" peaks.

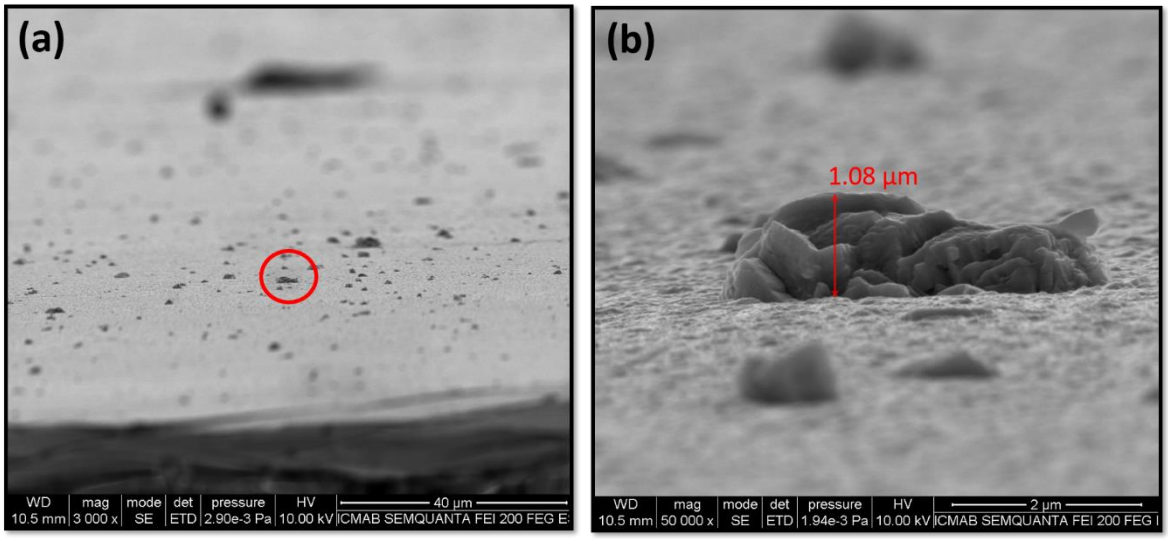

Figure 4.2: Tilted SEM images of the surface of a 12x12 mm bare piece of CC from THEVA GmbH composed of GdBCO/MgO/Hastelloy layers. (a) Secondary Electrons (SE) tilted view of the GdBCO surface revealing the presence of outgrowth peaks of GdBCO material. (b) Magnified SE image of one outgrowth peak.

4.1.2 AFM Analysis of the GdBCO

Foreseeing the possible conductive aspect of the outgrowth peaks of GdBCO on *THEVA*'s GdBCO/MgO/Hastelloy CC template, a topography AFM was performed for a 55x55 µm area of a 12x12 mm sample to verify their impact in the CFD interface. Figure 4.3(a) shows the topography scan of the sample revealing the randomly dispersed outgrowth peaks across the GdBCO surface with heights up to 700 nm. The natural curvature of the Hastelloy substrate was compensated with *Mountains* software to level the AFM data with a 3-point plane compensation.

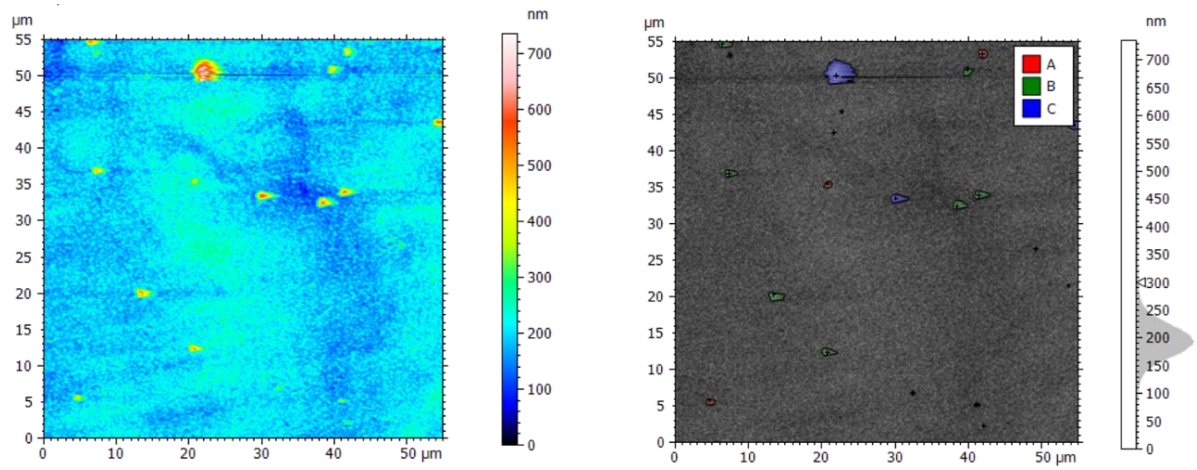

Figure 4.3: (a) 55x 55 µm AFM topography analysis on GdBCO surface of THEVA tape. AFM data was compensated with a 3-point plane method. (b) Particle classification study of the AFM topography. Particles presented a mean height around 200 nm, but only particles above 300 nm are shown.

Figure 4.3(b) shows a particle classification study performed with Mountains software considering these structures. Here, only structures above 200 nm are considered particles. Figure 4.4 shows the three height classifications, A, B and C for the 59 identified peaks. These appear to cover approximately 1% of the area with the majority ranging from 300 to 436 nm and only 10% above 436 nm in height.

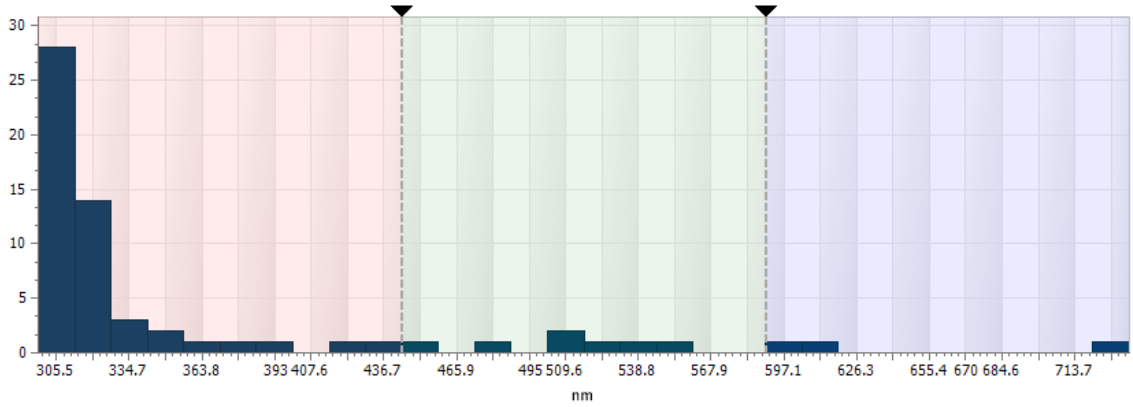

Figure 4.4: Particle height classification (A, B and C) chart of the structures found on THEVA's GdBCO material

Theoretically, if a high resistive CFD layer were to be implemented letting all the outgrowth peaks exposed and contacting the silver stabilizer/shunt, a 1% peak density would represent a substantial decrease of the CFD interfacial resistance. For example, considering the simulation model in subsection 2.4.3 where the CFD layer covers 90% of the HTS surface, $\rho_i^* \ll \rho_f$, and the low interfacial resistance of the edges is $\rho_i^* = 100$ nΩ-cm^2, if all the outgrowth peaks in contact with the silver had the same interfacial resistance of ρ_i^*, the CFD contact resistance would be:

$$R_{CFD} = \frac{100\ \text{nΩ-}cm^2}{1\%\ (55 \times 55)\ \mu\text{m}^2} = 0{,}33\ \Omega$$

This R_{CFD} represents the mean contact resistance over a 55x55 µm area on the CFD region. Dividing R_{CFD} by the same area, we see that the actual CFD specific contact resistance ρ_{CFD} would be

10^{-5} Ω-cm^2. This value is one order of magnitude below the "high" interfacial resistance threshold of 10^{-4} Ω-cm^2 to attain a significant 1-fold increase in the NZPV (Figure 2.16).

4.1.3 Estimating the Outgrowth Peaks Contact Resistance

In order to confirm the influence of the outgrowth peaks in the final CFD behavior, an experiment was conceived to estimate the interfacial resistance Ag/GdBCO-peaks. Three 12x25 mm samples of THEVA GdBCO tape were spin coated with an electric insulated layer of negative photoresist SU-8 2000 with thicknesses 200 nm, 400 nm and 800 nm. These thicknesses were chosen according to the particle classification A, B and C of Figure 4.4 to assess the influence of the height groups. With 800 nm of SU-8, almost all peaks should be covered, with 400 nm a bit more than half is covered and at 200 nm all peaks should be exposed. After the SU-8 deposition, all samples were sputtered with four silver contact pads (P1, P2, P3 and P4) of approximately 40 mm^2 as shown in Figure 4.5(a).

At room temperature, the average resistance between the pads was in the MΩ range and revealed a complete electric insulation between the silver and GdBCO. Therefore, all samples were annealed at 325 °C for one hour in 1 bar of oxygen atmosphere to lower the silver contact resistance at the GdBCO peaks without destroying the SU-8 layer. After annealing, all samples presented a significant decrease in the resistance between pads at room temperature, thus indicating the formation of an electrical path through the SU-8 layer. To assure the integrity of the SU-8 layer and rule out the presence of extra electrical paths other than the GdBCO peaks, the cross section of one sample was analyzed in SEM-FIB. As shown in Figure 4.5(b), the SU-8 creates a continuous interface Ag/GdBCO and so we could assume that any current flowing from the Ag to the GdBCO take the path of the peaks.

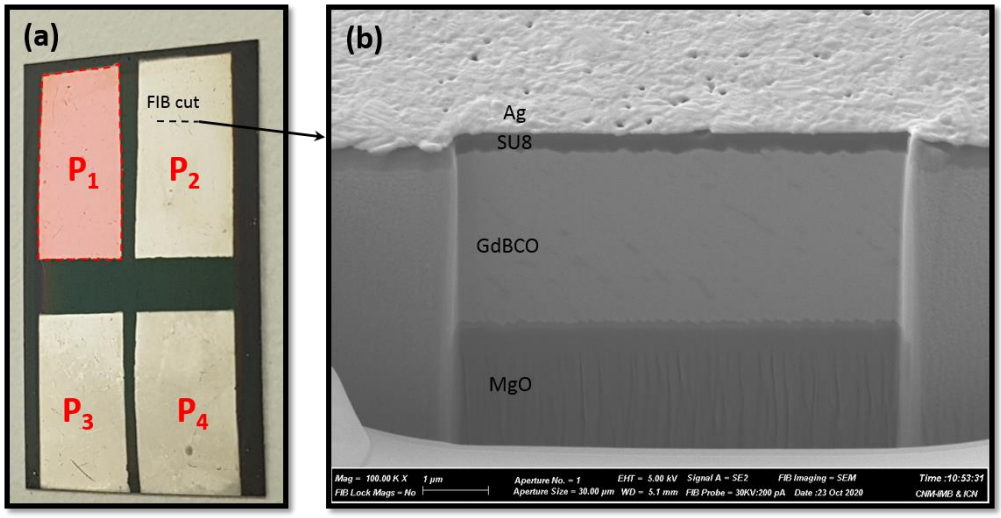

Figure 4.5: (a) 12x25 mm GdBCO tape sample fully covered with photoresist SU8 and four silver pads (P1, P2, P3 and P4). (b) Cross section FIB image of GdBCO tape sample after SU8 and Ag deposition.

For each sample, the global interfacial resistance was estimated by taking the I-V curves between each pair combination of silver pads at 77 K (in liquid nitrogen). From the linear I-V data, the resistances R_{xy} are taken, where xy represents permutation indexes of the pads ($x, y \rightarrow 1, \cdots 4$). The resistance R_{xy} is then multiplied by the area of their respective pad combinations to calculate the interfacial

resistances ρ_{xy}. As an example, the interfacial resistance ρ_{12} originated from pads P1 and P2 would be:

$$\rho_{12} = R_{12} \times A_{12} = R_{12} \times (A_1 + A_2)$$

The interfacial values are then averaged and the results were plotted with the standard deviation against the thickness of the SU-8 layer as shown in Figure 4.6. It is important to mention that this method of estimating the global interfacial resistance is a rough approximation that is only valid due to the order of magnitude found for the resistances R_{xy}. These values are considerably greater than the contact resistance of the current/voltage probes used to take the I-V curves. Consequently, all the resistance is assumed to be coming from the interface Ag/GdBCO-peaks. For an interfacial resistance below $10^{-4}\ \Omega\text{-}cm^2$, the measured resistance would be dominated by the contact resistance of the experimental probes and the bulk resistance of the silver pads, thus making this technique invalid.

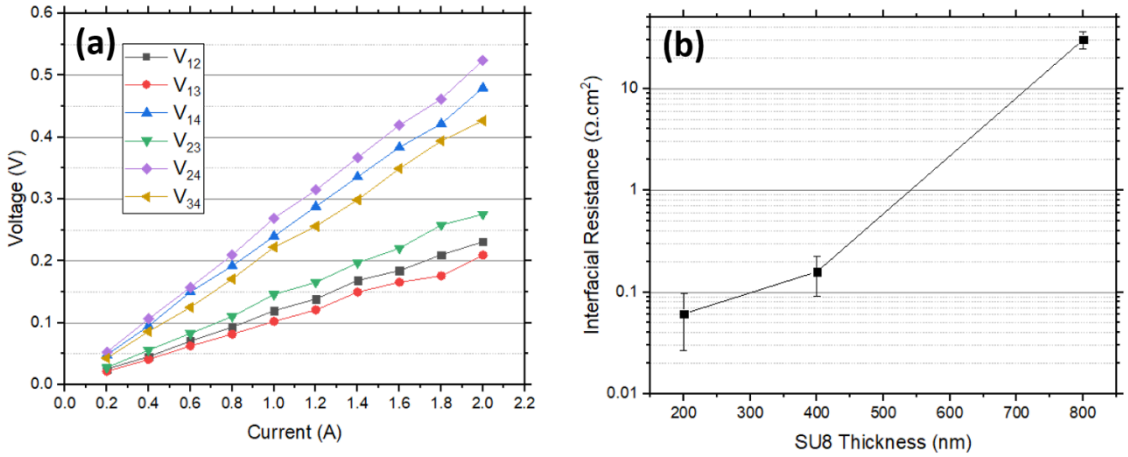

Figure 4.6: (a) I-V curves between silver pads for sample with 400 nm of SU-8 resin. (b) Global interfacial resistance versus SU-8 thickness.

The 800 nm of SU-8 created an interfacial resistance above $10\ \Omega\text{-}cm^2$, not enough to completely insulate the GdBCO from the silver layer, but enough to create the expected CFD effect as discussed in section 2.4.3. With 400 nm of SU-8, the resistance dropped two orders of magnitude, but interestingly no significant decrease was observed for 200 nm of SU-8. One simple explanation for this result is the partial covering of the GdBCO peaks by SU-8 residue. The peaks are not high enough to break the surface tension of the SU-8 solution during the spin coating deposition, they remain "wet", therefore, after the baking process, the epoxy does not sinter completely around the peaks. Since the GdBCO peaks are not in direct contact with the Ag layer, but rather partially covered by epoxy, annealing at 325 °C will not produce the expected sharp drop in contact resistance reaching $10^{-5}\ \Omega\text{-}cm^2$.

From the point of view of the CFD manufacturing, these results show that as long as the chosen CFD material provides a diffusion barrier for the silver at the GdBCO peaks, the high interfacial resistance will be preserved and an effective CFD effect will be present.

4.2 SU-8-CFD Tapes

The experimental confirmation of a high interfacial resistance on the surface of the GdBCO film covered with SU-8 photoresist led to a CFD manufacturing trial using the very same epoxy. Besides countering the presence of outgrowth peaks, this epoxy presents many relevant advantages:

- It is compatible with low-cost deposition techniques that could be easily implemented in a reel-to-reel CC production such as Ink Jet Printing (IJP) and slot-dye coating;
- The viscosity can be easily controlled for it to be spread over a thickness ranging from 200 nm up to 300 µm;
- The solution is a negative photoresist resin that becomes cross-linked under UV light, thus making the CFD patterning trivial during any fabrication process;
- And finally, this epoxy presents a very low mass loss up to 325 °C, thus allowing the annealing of the silver without compromising the structure of the CFD layer.

4.2.1 Depositing SU-8 on GdBCO for CFD Tests

In a CC reel-to-reel industrial process, the epoxy deposition should only come after the oxygenation of the REBCO layer, but before the silver coating and oxygen annealing as shown in Figure 4.7. However, to verify the feasibility of using the epoxy before any annealing optimization, CFD tape samples were manufactured utilizing commercial pre-oxygenated silver-coated tapes, with the layer structure Ag/GdBCO/MgO/Hastelloy provided by *THEVA*.

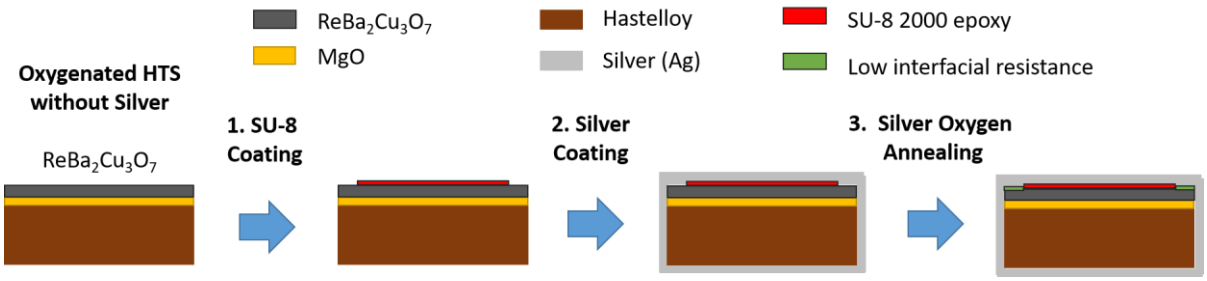

Figure 4.7: Workflow showing the cross-section stages of a tape sample for the incorporation of the CFD using the SU-8 epoxy in a reel-to-reel industrial process.

Figure 4.8 shows the proposed experimental steps for the SU-8-CFD incorporation. First, the silver layer is etched with a hydrogen peroxide solution just in the central part leaving the edges intact. The SU-8 resin is then spin coated at 3000 rpm for 1 min on top of the partially etched sample covering the whole surface. The sample is subsequently pre-baked at 90 ˚C for 5 min in ambient atmosphere and inserted in a UV light chamber for 15 min. In the chamber, the edges are protected from the UV light to avoid crosslinking and allow the final etching of the epoxy with acetone. After etching with acetone, the epoxy only covers the central part of the tape and defines the CFD pattern. Finally, the tape is sputtered with 1 µm of silver to finish the shunt coating.

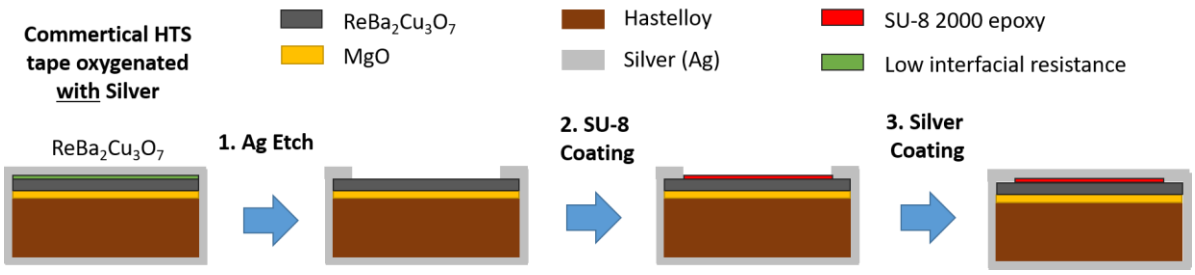

Figure 4.8: Workflow showing the cross-section stages of a tape sample for the incorporation of the CFD using the SU-8 epoxy.

Before attempting to fabricate a long length tape sample (> 10 cm) with the procedure of Figure 4.8, the effect of silver etching and depositing SU-8 on the critical current was evaluated via SHPM measurements. A piece of 30x12 mm of THEVA tape was silver etched along half of the length with a hydrogen peroxide solution leaving the other half unaltered as show Figure 4.9(a). Minutes after etching a SHPM measurement was performed at 77 K. By comparing the mean value of the field component B_z between the "virgin half" and the exposed half, we speculate substantial changes in I_c for the steps of the SU-8 deposition. Looking at the Hall-scan lateral view in Figure 4.9(b), we observe that the exposure of GdBCO to air for less than 2 hours yields an average 1 mT decrease in B_z. Considering the homogeneous magnetization of 3 µm of GdBCO film, this drop represents a thin layer degradation of less than 100 nm and a 2.5 % reduction from the original I_c. This same sample was subsequently spin coated with SU-8 and the B_z measured again. No further signs of degradation were noticed with the presence of the epoxy.

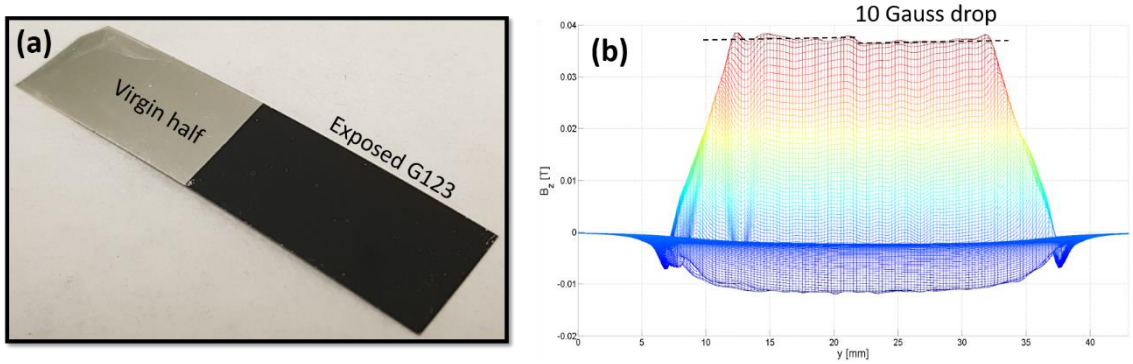

Figure 4.9: (a) 30x12 mm tape sample from THEVA with half of the silver etched. (b) Lateral view of the perpendicular trapped magnetic field B_z taken with SHPM at 77 K.

4.2.2 The NZPV of Epoxy-CFD Tapes

Accepting a 2.5% reduction in the critical current, two SU-8-CFD tape samples were fabricated at ICMAB following the procedure described in Figure 4.8 with 130x12 mm pieces from the commercial tape shown in Appendix Figure D-1. Both samples (Figure 4.10) were sent to *FASTGRID* partners in *École Polytechnique Montréal* (EPM) for NZPV and DC current limitation tests. In all the tests the voltage probes (ai3 to ai70) on the silver surface followed the disposition of the PCB shown in Appendix Figure C-1.

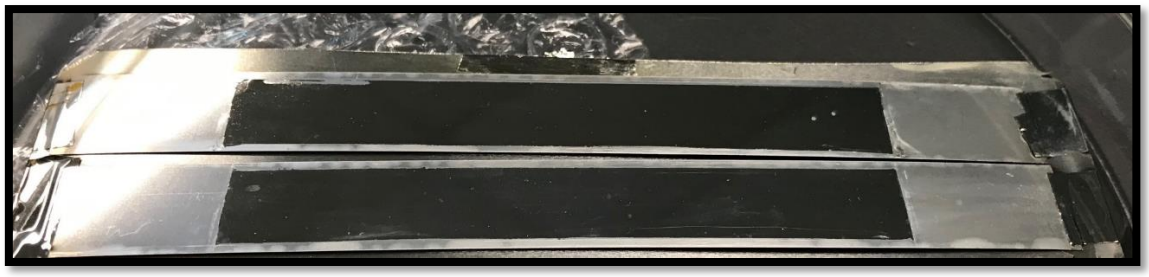

Figure 4.10: Two 130x12 mm SU-8-CFD tape samples created at ICMAB for NZPV and DC current limitation tests in EPM's laboratory. Sample #1 above and #2 below.

In the first NZPV test, sample #1 was pulsed with a current signal of 235 A/ms and a 6 ms dwell at 478 A (red dashed line in Figure 4.11(a)). A preliminary analysis of the global electric field (solid blue line in Figure 4.11) indicates that the sample only started quenching during the ramp down of current after the dwell. Since the current was not constant during the quench, it becomes difficult to make a precise estimation of the NZPV. Yet, considering 10 V/m as quench criteria, a constant current of 450 A and the electric field evolution on the left and right side of tape (Figure 4.11(b)), the NZPV was estimated safely in the range of **50-91 m/s**. This value is one order of magnitude above the experimental and theorical values found for the classic EPM-CFD shown in Figure 3.38. The epoxy certainly increased the interfacial resistance in the CFD region beyond 10^{-2} Ω-cm^2 and added an extra NZPV boost to the tape (Figure 2.16). In total, four NZPV tests were performed at the same current level of 450 A. The electrical behavior was consistent in all the tests and no direct measurement of the sample's I_c was performed since no signs of degradation could be noticed from the quench behavior.

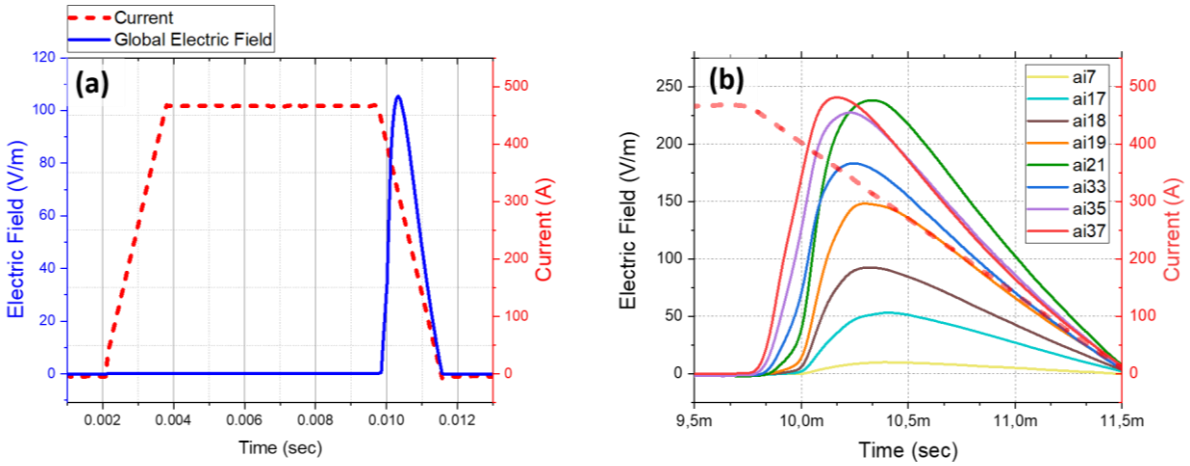

Figure 4.11: Electric Field x Current x Time curves for NZPV evaluation of sample #1. (a) Global Electric Field (solid blue line) across a 75 mm voltage taps during the 450 A current pulse (dashed red line). (b) Evolution of the Electric field in time during a 450 A current pulse for multiple voltage taps distributed across a 75 mm distance on the sample.

Following the NZPV tests with sample #2, in the 1st measurement, a pulse current of 500 A with 3 ms dwell was applied. A preliminary analysis of this 1st test reveals a similarly fast NZPV behavior between sample #1 and sample #2 (Figure 4.12). In the 2nd measurement, one of the current contacts quenched at 750 A while trying to determine I_c at 77 K indicating that the sample's critical current was over 750 A, which is consistent with the I_c expected for the reel FG-OXO-012 from THEVA shown in Appendix Figure D-1.

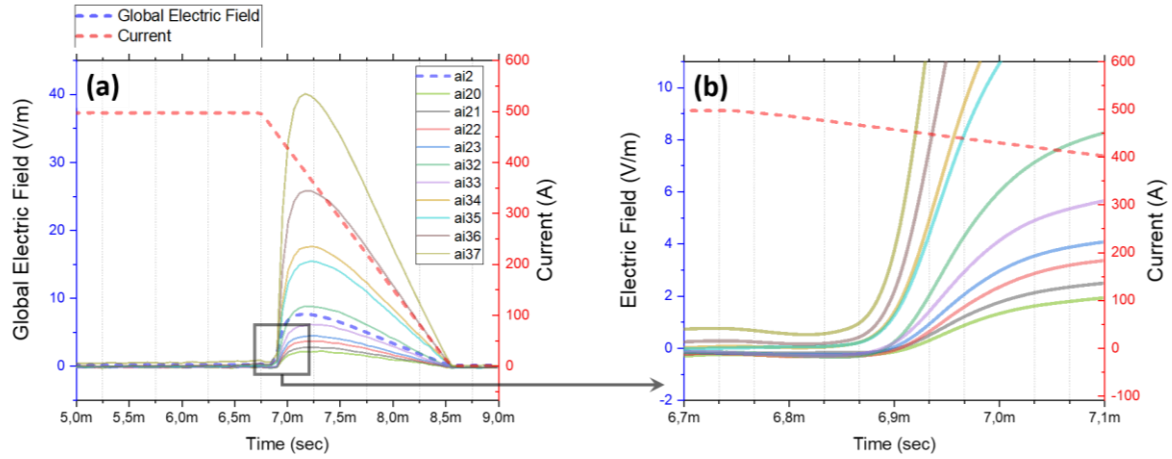

Figure 4.12: Electric Field x Current x Time curves for NZPV evaluation of sample #2. (a) Local and Global Electric Field across a 75 mm voltage taps during the 500 A current pulse of 3 ms. (b) Zoomed image of the region of interest for the evaluation of the NZPV.

In the 3rd measurement, the same current contact quenched at 700 A, indicating damage of HTS layer at the contact. In the 4th measurement, the same I_c test was performed and the sample quenched at 630 A. However, in the 4th test the tape did not quench at the current contact, but rather in the middle of the sample where the NdFeB magnet was positioned, thus indicating an I_c degradation following the 2nd and 3rd measurements. In order to avoid further degradation and allow a proper *post-mortem* investigation via Hall-scan measurements, no further transport current experiments were performed for sample #2.

4.2.3 DC Limitation Tests for SU-8-CFD Samples

The current limitation test was performed after the NZPV tests only on sample #1 and the results are shown in Figure 4.13. In the first limitation test, a voltage pulse of approximately 4 ms was applied and the fault current surpassed 900 A. At t = 2 ms, the sample's electric field increases beyond 85 V/m and the current is limited to 500 A indicating a first quench. At t = 2.2 ms the field dips below 65 V/m reaching a minimum at t = 2.4 ms and the current is limited below 300 A, thus indicating a second quench. After t = 2.4 ms the E-field spikes again reaching 90 V/m at 2.7 ms and in less than 0.2 ms it stabilizes around 70 V/m with no further current limitation. The stable value of the current during the second E-field spike suggests a behavior not related to a quench. Nevertheless, the presence of two quenches during limitation represents two stages for the resistive switch that are easily identifiable at t = 2.3 ms in Figure 4.13(b). After the first 1st limitation test, the I_c dropped from 820 A (prior to the limitation test) to 330 A. Moreover, a "crack-like" defect was spotted on the upper silver layer of the tape at the exact location where the critical current was reduced to 330 A. The origin of the crack will be discussed in the following section.

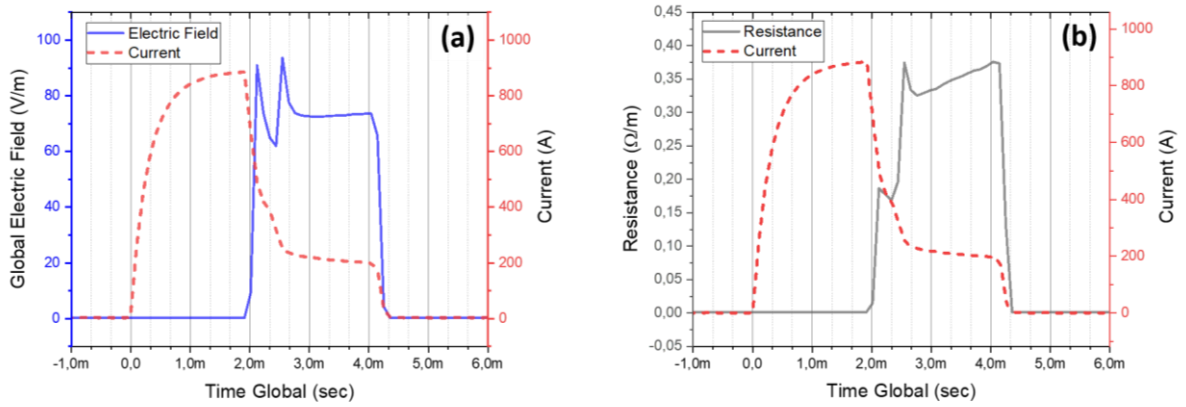

Figure 4.13: Current limitation test for sample FG-OXO-12(25) with SU-8 CFD. (a) Global Electric Field (solid blue line) across a 75 mm voltage taps during current fault (dashed red line). (b) Global Resistance (solid grey line) during current fault (dashed red line).

These NZPV tests have shown that samples with a CFD made of epoxy only remain intact if a quench happens for an applied current less than 500 A. If the quench happens for a current amplitude above 700 A, degradation in I_c is likely to occur. We highlight that sample #1 only showed degradation after the limitation test where the current was ~900 A.

4.2.4 *Post-Mortem* Investigation of SU-8-CFD Tapes

In order to understand the degradation mechanism on SU-8-CFD samples, the "crack" defect on the silver coating of sample #1 was investigated using FIB-SEM imaging. In Figure 4.14(a), a small section of the "crack" is shown with a yellow traced line defining the damaged region. Transversal to the damaged region, a FIB cross section cut was done 10 µm deep into the sample. Interestingly, no crack fracture is observable on the silver surface. In fact, the FIB cut reveals that the silver deformation came from a local buckling effect [243] that probably originated from the thermal stress during quench. Analyzing the sides of the FIB cut in Figure 4.14(b), we see that the SU-8 layer was delaminated following a fracture in the GdBCO material across the SU-8/GdBCO interface. However, the actual structural damage of the GdBCO layer is only seen in the center part of the cut (Figure 4.14(c)). In the backscatter analysis of Figure 4.14(d), another zone, delimited by the yellow traced line, presents a strong shift in the grey scale, thus indicating a phase change of the GdBCO crystal. This phase change suggests that a local temperature increase beyond 700 °C took place after the initial interfacial fracture in the SU-8/GdBCO boundary.

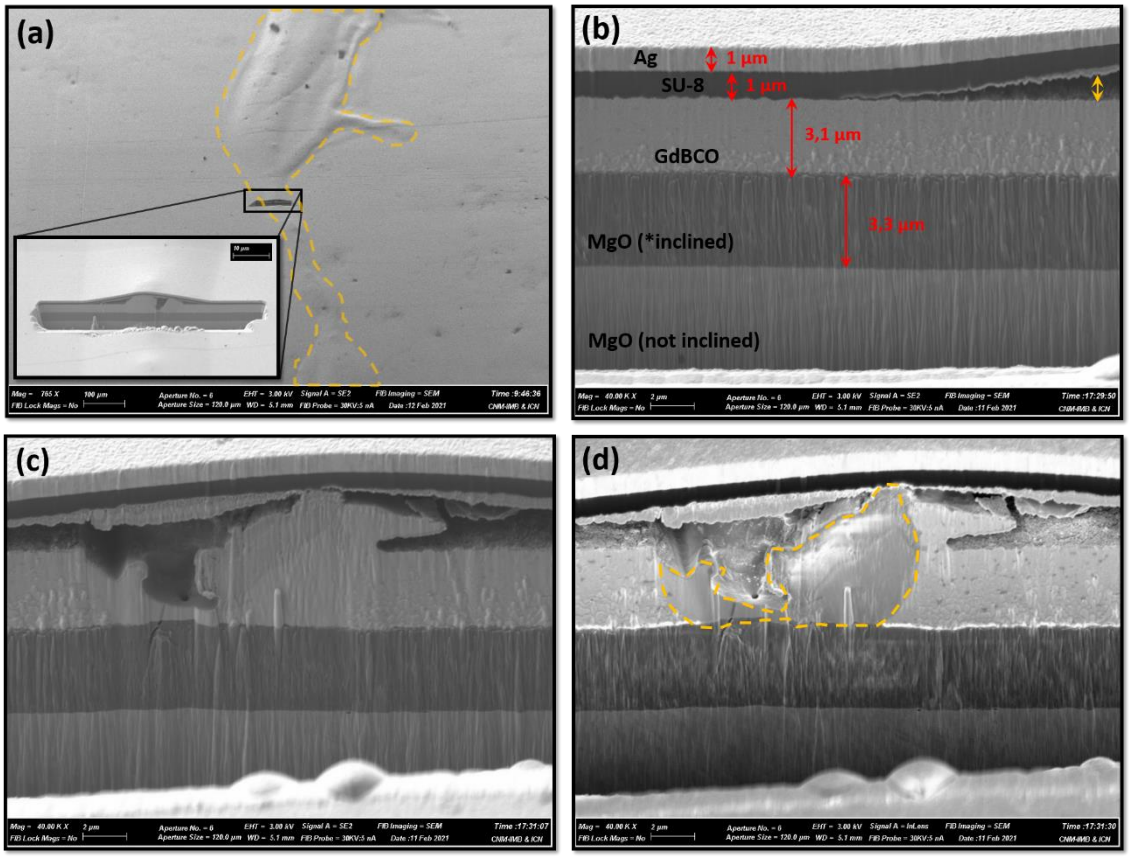

Figure 4.14: SEM-FIB analysis of the buckled silver region on SU-8-CFD sample #1 after current limitation tests. (a) Silver buckled region and transversal FIB cross section cut. (b) Left side of FIB cross section cut, (c) Secondary Electron (SE) image of the center of FIB cross section cut. (d) Backscatter Electrons (BSE) image of the center of FIB cross section cut.

In addition to the SEM-FIB imaging, Hall-scans of sample #1 and #2 were taken at 77 K to characterize the extension of the degraded region. Notably, the B_z field map of sample #1 in Figure 4.15(a) reveals more than one degraded region along the tape's length. Besides the expected defect in the buckled region around the 60 mm mark, three more damaged regions are spotted at the length marks of 40, 85 and 100 mm.

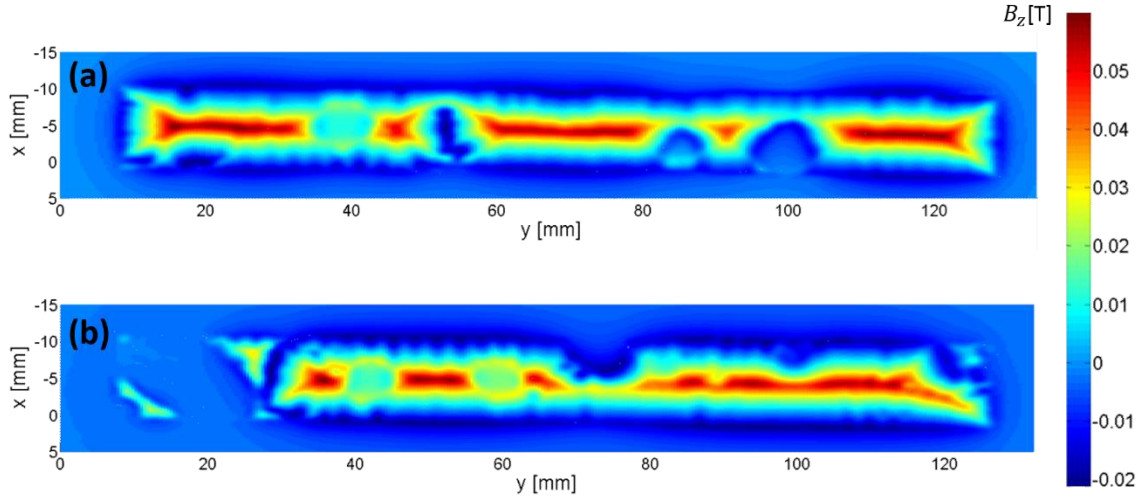

Figure 4.15: Perpendicular trapped field B_z measured by SHPM at 77 K of two 100 x 12 mm SU-8-CFD samples produced on top of THEVA ISD-MgO/GdBCO tape: (a) sample #1 and (b) sample #2.

The symmetrical distribution of the defects along the length reinforced the thermal stress character of the problem by suggesting a multi-node buckling effect. Furthermore, the same defect pattern is also seen in the B_z map of sample #2 in Figure 4.15(b). Apart from the expected left current contact damaged (y mark 10 to 30 mm), the pair of defects appears on the left side of the tape at the marks 40 and 60 mm.

4.3 Numerical Simulation of SU-8-CFD Tapes

To understand the delamination mechanism and degradation in SU-8-CFD tapes, numerical simulations were performed considering a classic EPM-CFD and the SU-8-CFD. In this section, the two cases were compared and used to formulate a simple explanation for the degradation phenomena.

4.3.1 Inter-Layer Temperature Gradients

Using the *COMSOL* template described in section 3.5, the simulation of the NZPV was performed for a CC with the SU-8-CFD structure. The CFD epoxy region is considered as boundary condition between the silver and the HTS. The *COMSOL* "Boundary" was set to a "Contact Impedance" of 10^{-3} S/m (same as the EPM-CFD case), but with an extra "Thin Thermally Resistive Layer" condition considering the SU-8 thermal conductivity of 0.2 W/m-K at room temperature. The quench current was set to 550 A and only two SU-8 thicknesses, 400 and 1000 nm, were tested due to extensive computational time needed.

For the two simulated cases, the evolution of temperature across the HTS length follows the same distribution shown in Figure 4.16. No potentially destructive temperature spikes were identified nor changes in the final NZPV value. From the point of view of the NZP thermal frontier, the presence of the epoxy appears to be irrelevant to the CFD behavior.

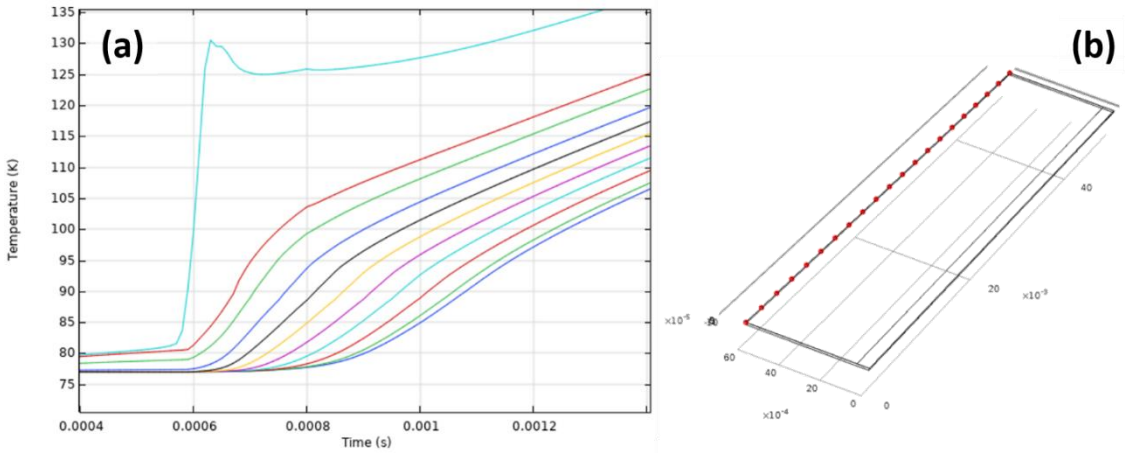

Figure 4.16: Simulation done in Comsol Multiphysics. (a) Simulated temperature evolution along 25 mm length of a SU-8-CFD tape during a quench at 550 A. (b) Sketch of simulated geometry for the CFD tape in Comsol Multiphysics. (Symmetry line at y=60 mm indicated by red dots). The red dots correspond to the positions where the temperature evolution is analyzed.

Still, when analyzing the temperature gradient across the thickness of the tape after the full propagation of the quench at t = 2.5 ms, a significant difference appears between the epoxy case and

the classic EPM-CFD case. Looking at Figure 4.17, we observe that the temperature gradient is rather high in the presence of the epoxy layer: 15000 K/mm for 400 nm of SU-8 and 20000 K/mm for 1 µm. In comparison, the temperature gradient in the EPM-CFD case is only 200 K/mm across 100 nm of degraded GBCO layer. Moreover, taking into account that the thermal conductivity can decrease 1 order of magnitude for epoxy compounds in cryogenic environment [244], these temperature gradients are considered very conservative values since the thermal conductivity of the epoxy was held constant at 0.2 W/m-K.

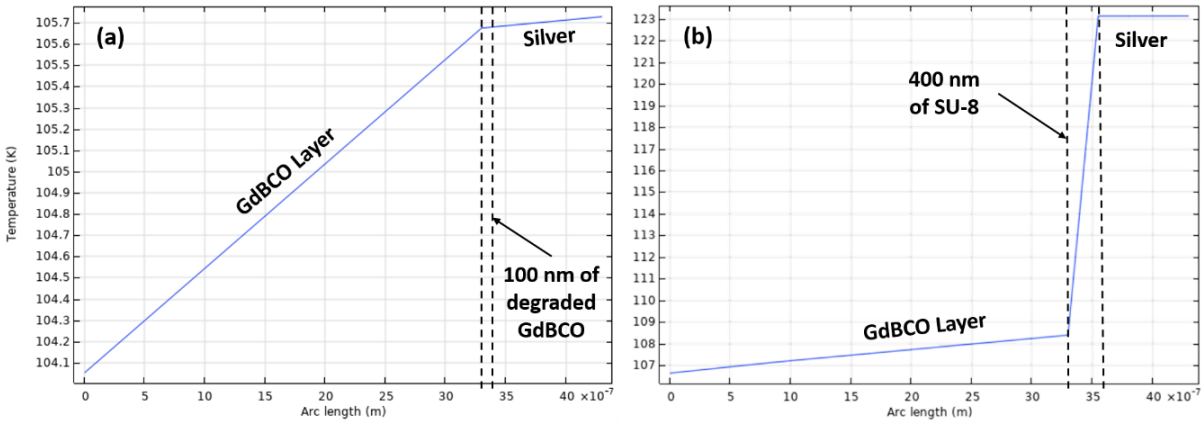

Figure 4.17: Simulated temperature distribution across the cross-section of two different CFD tapes during quench. (a) Classic EPM-CFD with 100 nm of degraded REBCO and (b) CFD with 400 nm of epoxy SU-8 2000.

In view of a significant temperature gradient, a second 2D simulation was performed using the "Thermal Expansion" module of *COMSOL Multiphysics* to estimate the order of magnitude of the correspondent thermal stress in the SU-8 layer. Considering a 20 µm section of 1 µm thick SU-8 with the properties found in the product datasheet [245], the resultant von Mises stress and deformation for a temperature gradient of 20000 K/mm across the thickness is shown in Figure 4.18. As expected, due to the high coefficient of thermal expansion, the segment buckles upwards experiencing a maximum stress of approximately 16 MPa. This value is coherent with other studies reporting transverse tensile stresses in the order of dozens of MPa causing severe I_c degradation and delamination in CC HTS tapes [246].

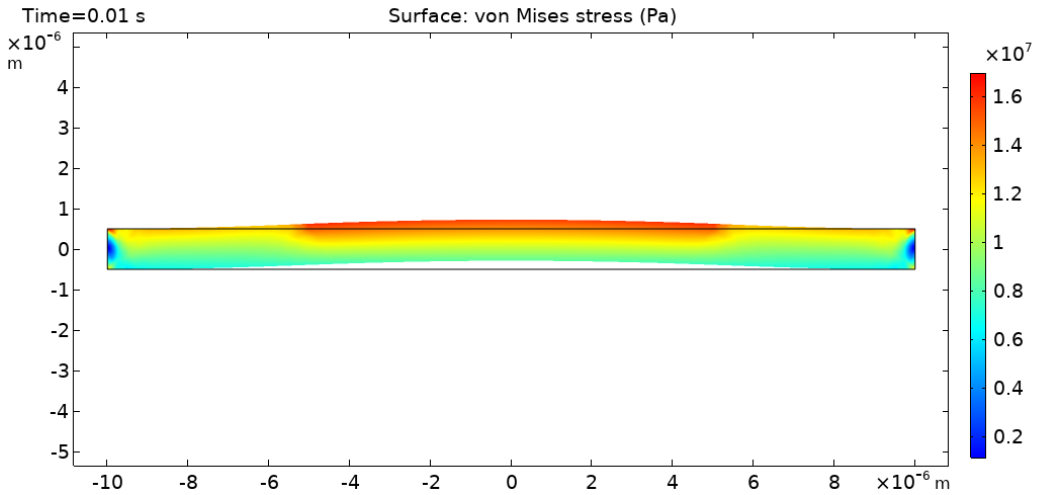

Figure 4.18: von Mises stress and deformation (5 scale factor) for a 20 µm length section of 1 µm thick epoxy exposed to a temperature gradient of 20000 K/mm. Simulation done with COMSOL Multiphysics Thermal expansion module.

In summary, the low thermal conductivity of the SU-8 epoxy in combination with the thermal distribution of the CFD effect induces an elevated temperature gradient across the layers during quench. Consequently, the gradient provokes a thermal stress in the order of MPa due to the epoxy high thermal expansion coefficient. Part of this stress is also experienced in the interface with the HTS layer, thus leading to an I_c degradation and possible delamination due to local buckling.

4.3.2 Secondary Delamination Effect

Overall speaking, the delamination of any chosen material on top of the REBCO film is a potentially harmful process for the superconducting properties. If the bonding strength of the material is higher than the yield stress of the REBCO film, the delamination will occur with partial removal of the superconducting material (Figure 4.14(c)). Furthermore, in the case of REBCO thin films, a surface fracture caused by the delamination can propagate cracks across the thickness, thus compromising the transport critical current of a conductor. Meanwhile, in the pursue of a compatible material for the CFD interface, a clean delamination (no fractures) between the HTS and the CFD remains a plausible scenario. Therefore, in this subsection, we briefly explore the possible effects of a clean delaminated region on the CFD interface.

Using the same numerical model of the previous subsection, the simulation of the NZPV was performed once again considering the CFD interface having a “Thin Thermally Resistive Layer” with an inhomogeneous thermal and electric conductivity. This inhomogeneity represents a delamination defect in the middle of tape whereas thermal and electric conductivity drops from 0.3 to 0.01 W/m-K (conductivity of air) and from 10^{-2} to 10^{-6} S/m respectively. Looking at the simulation result of Figure 4.19 we can see how the HTS temperature suddenly starts to increase faster in the defect (yellow line) once the thermal front of the quench reaches the region. After 8 ms the mean temperature of the tape is still below 430 K, but the delaminated zone already surpasses 500 K. In this situation, degradation of the delaminated zone is likely to occur due to oxygen loss.

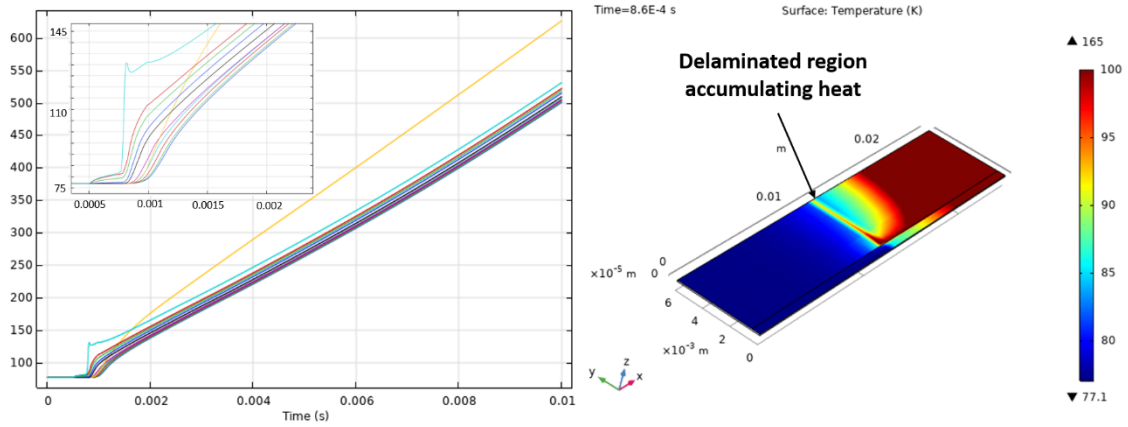

Figure 4.19: Comsol Multiphysics simulation showing the temperature evolution along 25 mm length of a SU-8-CFD tape during a quench at 550 A with inhomogeneous thermal and electric conductivity.

In summary, this simulation highlights the importance of the metallic shunt adherence onto the HTS layer regardless of the type of delamination suffered by the epoxy. Once the epoxy losses physical contact with the HTS, the zone becomes a new synthetic hot-spot. The temperature increase in the

hot-spot might not be enough to completely burn directly the tape, but it can de-oxygenate the zone and compromise the average critical current.

4.4 Graphite CFD

In general, epoxy polymers like SU-8 can be used in many different applications due to lightweight, durability, low production cost and easy to scale deposition. However, it's common knowledge that polymers are thermal/electrical insulators, which hinders their implementation in other applications where heat dissipation becomes a critical factor like electronic packaging. For this very reason, for two decades now, researchers have focused on the development of polymers doped with special fillers capable of boosting the thermal conductivity from the 0.2-0.5 W/m-K range beyond 10 W/m-K. Among many of the different fillers, e.g copper, silver, diamond powder, boron nitride, aluminum nitride, etc., graphite nano-composites raise a special interest because of their abundance, relatively low cost production and lightweight when compared to other carbon allotropes [247].

In this section, we report on the experimental attempt to avoid degradation issues related to the low thermal conductivity of polymer composites by substituting the previous SU-8 epoxy for a commercial graphite-based lacquer compound.

4.4.1 Manufacturing Route for Graphite-CFD

Among all the commercial techniques used to deposit graphite for the functionalization of surfaces, the use of dispersions of colloidal graphite stands out as a simple inexpensive way for making non-metallic bodies electrically conductive [248]. Therefore, a commercial graphite spray lacquer GRAPHIT 33 was chosen to attempt the graphite deposition on the HTS material. This spray solution consists of fine flakes of graphite suspended in an alcohol isopropyl and hydrocarbons, C3-4-rich, petroleum distillate. Besides the commercial convenience, the water-free solution of the spray helps minimize the surface degradation attributed to a chemical reaction with water vapor (subsection 1.5.3)[71].

Ideally, like the SU-8 CFD, the graphite CFD layer should be deposited after oxygenating the HTS material, but before the silver deposition and annealing. However, according to the GRAPHIT 33 datasheet the maximum temperature of the graphite film before decomposition ranges from 250 to 300 °C. The reason for this range limit is found in the TGA-thermogram [249] shown in Figure 4.20. In the range of 250 to 400 °C, the C=H, C-H and C-O bonds of the polymeric binder suffers a thermal decomposition leading to a loss 18% by weight with a peak degradation rate at 330 °C.

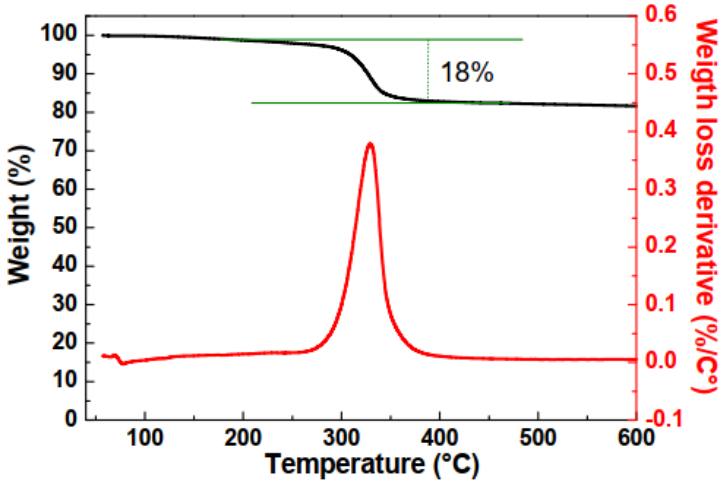

Figure 4.20: TGA–thermogram and derivative thermogravimetric plot profile of a typical dried Graphit 33 sample. This figure was taken from [249] *with permission.*

This temperature limitation would not allow the annealing of a silver coating layer without risk compromising the graphite film. Furthermore, possible reactivity in the interface HTS/graphite would also have to be considered for temperatures above 300 °C. Fortunately, the moderate electrical conductivity of the graphite film allows electroplating copper or nickel to the layer, thus simplifying the shunt coating after CFD incorporation.

The suggested manufacturing workflow for the graphite CFD is shown in Figure 4.21. The manufacturing steps start with a commercial silver coated HTS tape as template. First, the tape is silver etched in the middle section to expose the HTS layer and leave silver strips along the edges. Afterwards, with the help of a mask, the colloidal graphite is sprayed on top of the exposed HTS at room temperature. Subsequently the fresh graphite ink layer is cured in a furnace at 100 ˚C for 1 hour in ambient atmosphere to decompose the organic binder of the lacquer. At last, a 1 µm thick layer of copper (or nickel) is deposited, preferably via electroplating, to give the tape its final metallic shunt coating. Apart from allowing electroplating, the graphite layer protects the HTS material from harmful copper diffusion [72].

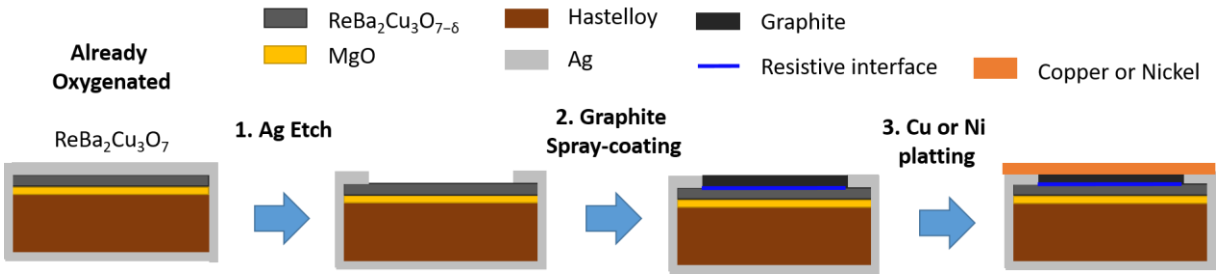

Figure 4.21: Experimental workflow for implementing the graphite-CFD architecture in the 2G HTS CC architecture.

4.4.2 Testing Graphite Compatibility with GdBCO

In the literature of REBCO synthesis, the presence of carbon is referred to as a contaminant residue that accumulates in the grain boundaries of the REBCO films and creates current percolation issues

[250]. In addition, there is also the possibility of carbon interstitial incorporation in adjacent cites of the CuO2 planes, leading to a reduction of critical temperature and current density. However, recent studies have reported significant enhancements in mechanical properties [251] and maximum J_c values [252] for YBCO samples doped with Carbon Nano Tubes (CNTs) in a solid-state reaction route. With such a wide range of outcomes, the effect of the graphite on the superconducting properties of the HTS layer was evaluated utilizing the same Hall scan technique discussed in subsection 4.2.1.

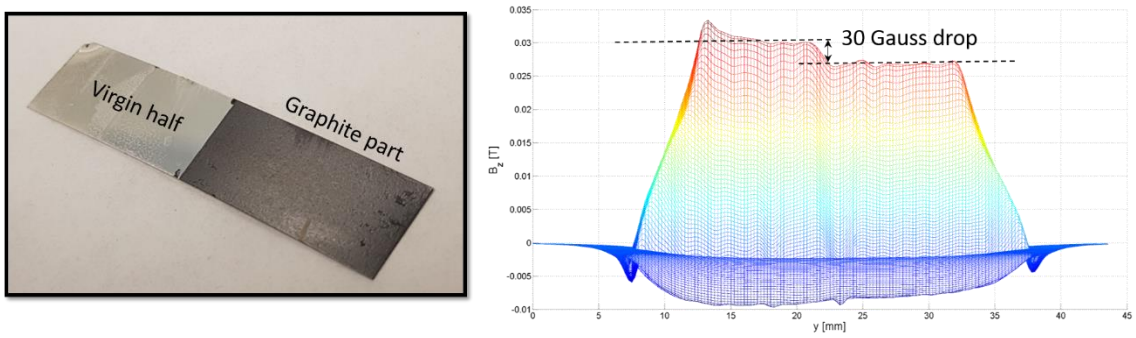

Figure 4.22: On the left, 30x12 mm GdBCO THEVA tape sample half spray-coated with graphite. On the right, lateral view of the trapped magnetic field $B_z(x,y)$ taken with SHPM at 77 K.

Looking at the longitudinal view of B_z in Figure 4.22, we observe that spray-coating the GdBCO with colloidal graphite after silver etching yielded an average of 3 mT decrease in B_z. This amplitude drop represents a GdBCO layer degradation of almost 300 nm and consequently a 10% reduction of the original I_c. According to the SEM images, the morphology of the final graphite film covering the HTS material consists of overlapped graphite platelets connected together in a coplanar manner. Moreover, TEM measurements of the Graphit 33 ink performed by the Institute for Polymers Composites and Biomaterials (IPCB-CNR) show that the platelets are hundreds of nanometers large [249]. Consequently, since the platelets are considerably bigger than any pore or grain boundary in the GdBCO, it is very unlikely that the 3 mT drop in magnetization observed in the Hall-scan was caused by current percolation issues related to carbon contamination. It is more reasonable to assume a similar effect of that of using silver paint for HTS bonding [72]; the organic carrier used in compounding of the ink wicks in along pores and grain boundaries, thus degrading the bulk properties.

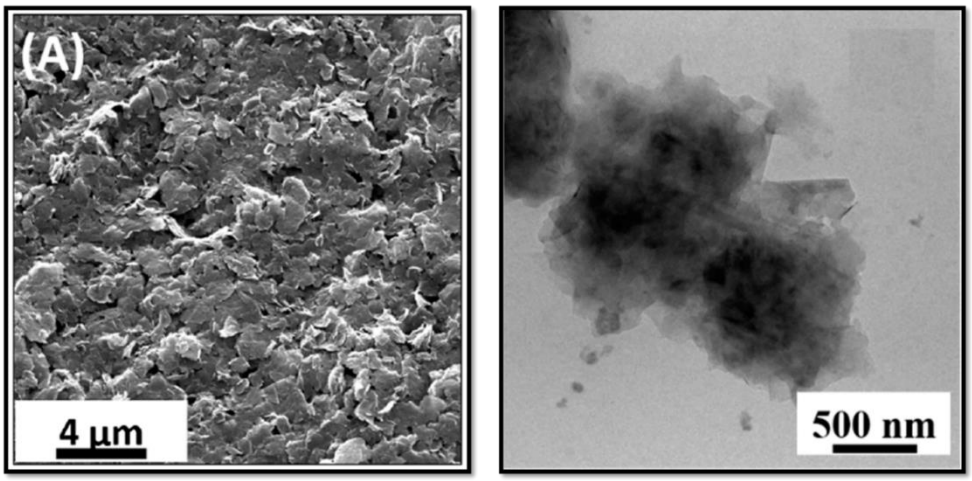

Figure 4.23: Electron microscopy images of a deposited film of Graphit 33. (a) SEM image of the surface of the graphite film after curing it for 1 hour at 100 ˚C. (b) TEM image of one single platelet of graphite dissolved in the Graphit 33 ink. Figure (b) was taken from [249] *with permission.*

4.4.3 DC Limitation Tests with Graphite-CFD

One long graphite-CFD sample of 12 cm was prepared at ICMAB using commercial HTS tape from reel FG-ICMAB-001 (Appendix Figure D-2) and sent to *FASTGRID* partners in EPM for the evaluation of the NZPV and the DC limitation. The precise NZPV value could not be obtained using the technique described in subsection 3.4.3 due to an issue with the array of voltage probes on the surface of the sample after the DC limitation tests. The copper shunt making the electric contact with the probes pealed underneath the probes after quench. Relevant details of this issue will be discussed in the next subsection. Consequently, the NZPV had to be inferred qualitatively using the DC limitation setup and analyzing the global and local electric field evolution across the sample in hot-spot regime with the voltage probes array shown in Appendix Figure C-2.

The results for the limitation test of the graphite-CFD sample ($I_c \sim 500\ A$ in Appendix Figure D-2) with a uniform THEVA tape sample ($I_c \sim 1000\ A$) are compared in Figure 4.24. For both samples the amplitude of voltage pulse was chosen in order to reproduce the hot-spot time with fault current close to the sample's I_c. In both graphs of Figure 4.24, the current (red dashed line) decreased and the electric field (solid blue line) rose after t = 4 ms indicating the formation of a normal zone. For the uniform tape in Figure 4.24(a), the gradual linear increase of the electric field corresponds to the slow propagation of the normal zone increasing the resistance and limiting the current. The fact that the electric field value did not stabilize by the end of the fault confirms that the 12 cm sample was not fully quenched after the pulse. Oppositely, for the graphite-CFD tape in Figure 4.24(b), the current sharply decreased when the normal zone was created, the electric field rose and stayed rather constant for the rest of the fault thus indicating a fast NZPV.

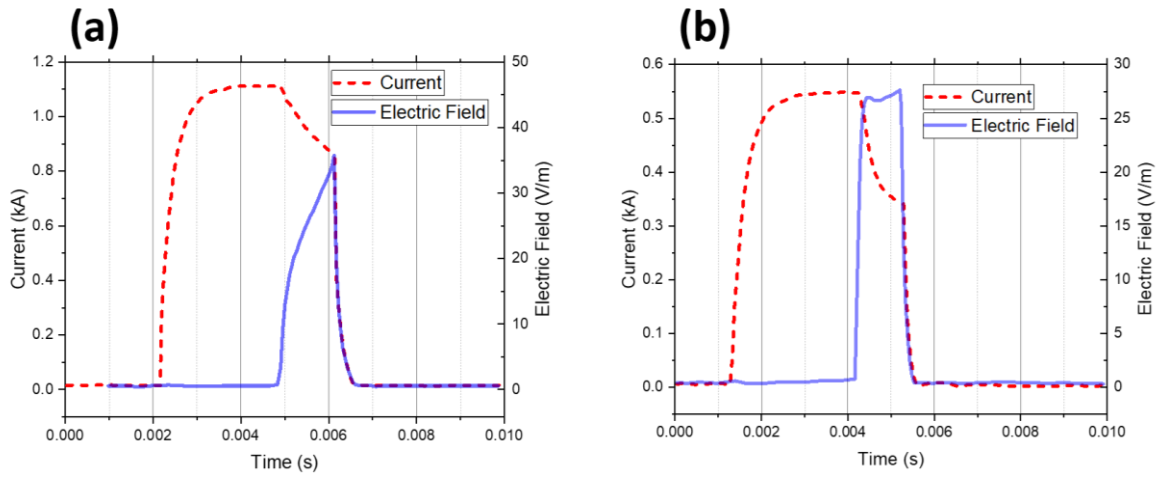

Figure 4.24: Current and Electric Field time evolution for a uniform tape (a) and a graphite-CFD tape (b) during current limitation in hot-spot regime. Results in partnership with EPM.

Figure 4.25 reveals that the initial quench started at the current contacts instead of the NdFeB region (ai37-ai38) on both sides of the tape, most likely due to joule heating, and spread out through the whole length. Considering 10 V/m as the quench criteria and the electrical field evolution from both sides, one could safely affirm that the NZPV is above 500 cm/s for a current of 425 A which with matches the experimental and theoretical predictions shown in Figure 3.38.

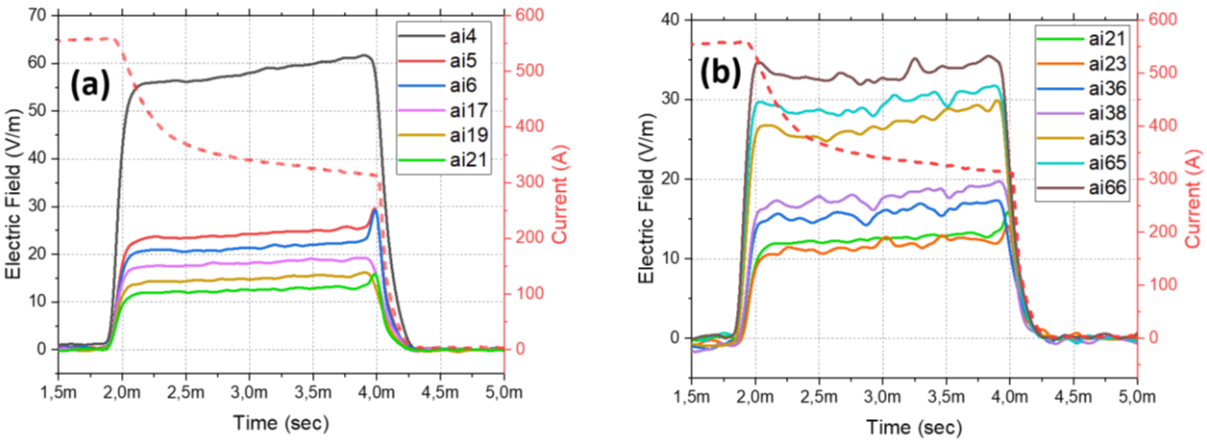

Figure 4.25: Local Electric Field (solid lines) and Current (dashed red line) evolution across the length of a graphite-CFD tape for a DC limitation test of 4 ms in hot-spot regime. (a) Voltage probes on the left side of the tape; (b) Voltage probes on the right side of the tape.

No degradation of the initial I_c was observed after the limitation tests in hot-spot regime and the NZPV boost could be confirmed for the graphite-CFD architecture. Yet, no further tests were performed, neither in the clear-fault regime nor in NZPV conditions (constant current) due to the pealing process of the copper/graphite shunt.

4.4.4 AC Limitation Tests with Graphite-CFD

In addition to the DC limitation tests, AC limitation tests at 77 K were also performed in collaboration with *FASTGRID* partners in Université Grenoble Alpes for one graphite-CFD sample. A total of 21 AC tests with 50 ms duration were performed: 20 tests with a low prospective current fault using 30 V_{rms}/m for evaluating the robustness in hot-spot regime, and one test at 60 V_{rms}/m for assessing the clear fault condition. In Figure 4.26, the result for the 20th limitation test illustrates the non-destructive limitation behavior in the hot-spot regime. The prospective fault current at 30 V_{rms}/m is close to the critical current (I_c~500 A) of the tape, resulting in a quench half cycle after the fault. No reduction of the quench current was observed between the 20 consecutive tests, thus suggesting no substantial critical current degradation.

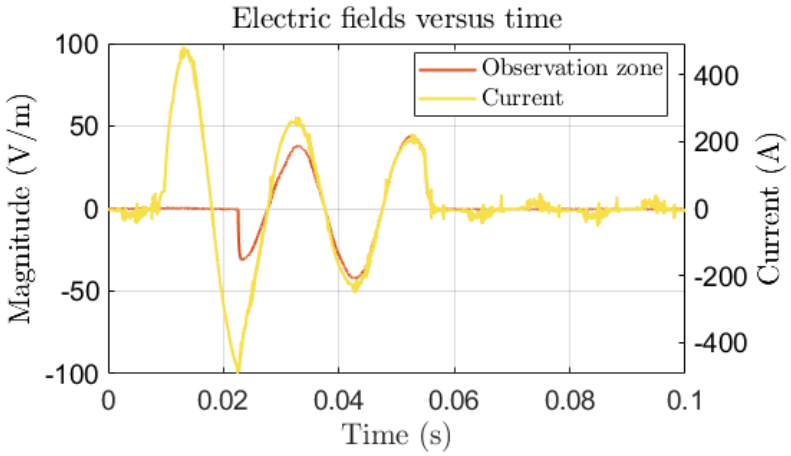

Figure 4.26: Graphite-CFD test in AC Limitation at 30 V_{rms}/m for 50 ms fault duration in the hot-spot regime.

The slow-motion video recordings of the tape during the AC limitation at 30 V_{rms}/m confirmed the full quench propagation across the sample in less than 100 µs, giving enough margin to assume a NZPV above 500 m/s at 500 A rms. Figure 4.27 shows two different moments of the film boiling formation during the quench propagation. At frame t = 21.32 ms, the center and the edges of the tape quench simultaneously creating an "H" shape boiling that matches the expected current distribution of the CFD (subsection 3.4.6). In less than 60 µs, at t = 21.38 ms, the film boiling covers the 56 mm space between the voltage taps. In the final clear fault test at 60 V_{rms}/m, no electrical signs of degradation were observed during the fault. However, the tape suffered localized peeling of the copper/graphite shunt and the test sequence was interrupted. The reasons and consequences for the pealing are discussed in the following section.

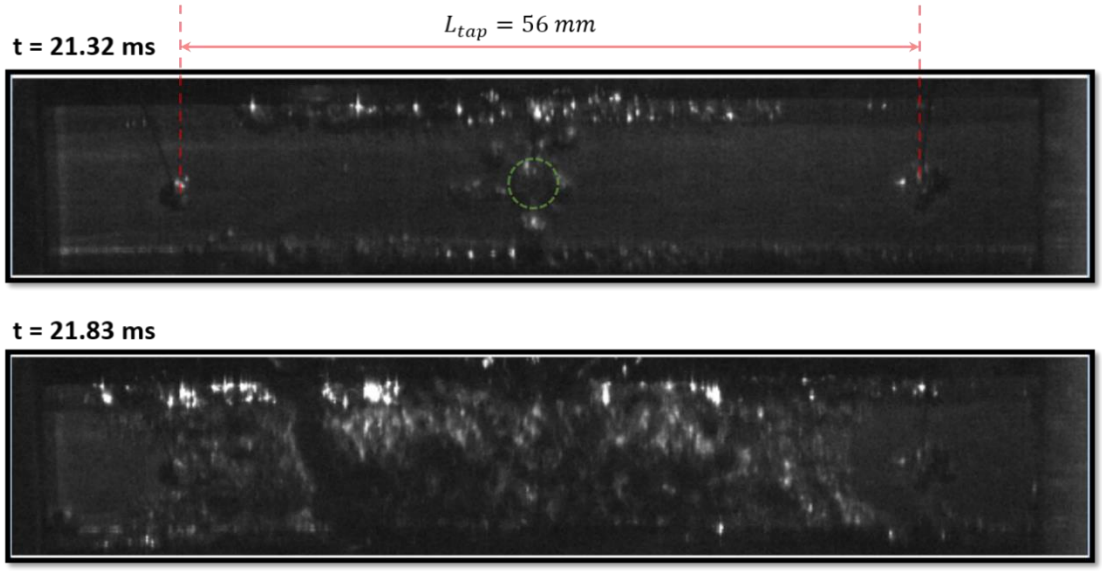

Figure 4.27: Picture of the film boiling formation at the beginning of the quench of the 15th AC limitation test on a 12-cm-long graphite-CFD sample with a copper shunt. The "H" shape of the film boiling indicates the presence of the CFD effect.

4.4.5 Post Current Limitation Evaluation

By visually analyzing the tape's surface during the slow-motion quench footage of each AC limitation test, we could identify a gradual delamination of the graphite/copper layers happening between tests. The actual shunt loss/pealing exposing the GdBCO only became visual after the clear fault test (Figure 4.28(b)). The delamination took place mainly in the regions where the heat amassing was expected: in the middle of the tape where the NdFeB magnet (Figure 4.28(c)) was positioned, at both ends close to the current contacts, and at both voltage taps Figure 4.28(d).

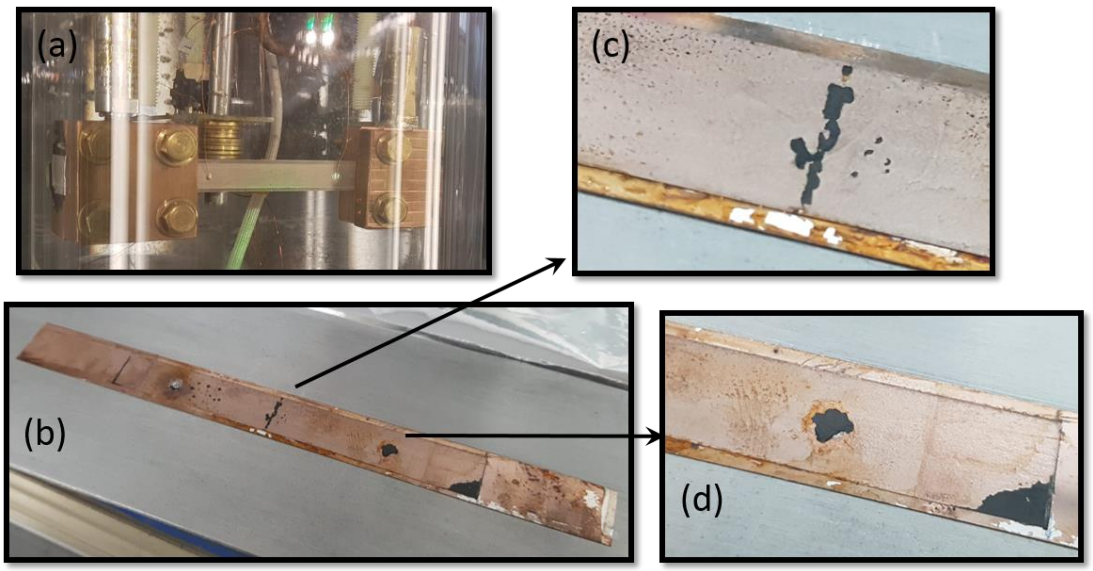

Figure 4.28: (a) CFD-graphite tape on the AC limitation test setup. The sample is inside a transparent cryostat with liquid nitrogen. (b) CFD-graphite tape on the SHPM Al holder after the AC limitation tests. (c) copper pealing in the tape central part where the Neodymium magnet was positioned. (d) copper pealing in the voltage tap and in a region under the current contact.

Possible degradation due to the pealing of the copper shunt was evaluated by analyzing the B_z distribution at 77 K using ICMAB's Hall scan set-up. Figure 4.29 indicates that even after major pealing of the copper, the graphite-CFD tape presented no critical current degradation. This result reinforces the previous assumption that the CFD concept by itself increases substantially the robustness of the tape during any quench condition.

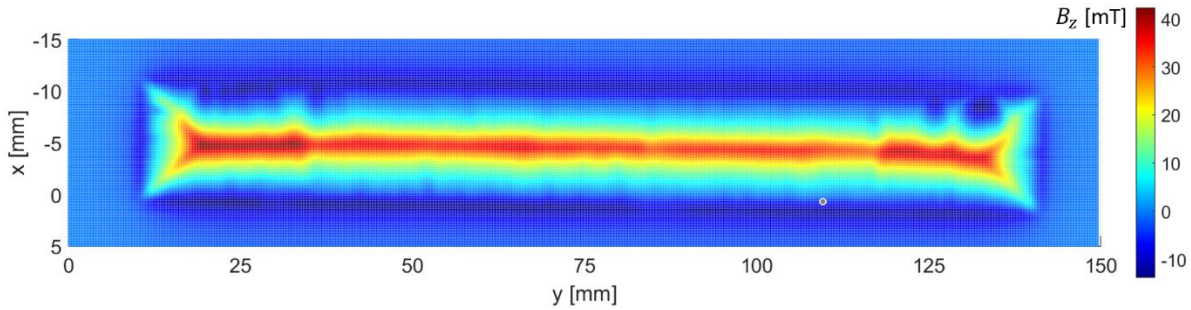

Figure 4.29: Top view of the $B_z(x,y)$ the trapped field component of 120x12 mm CFD-graphite tape after 21 consecutive AC limitation tests.

A SEM-FIB cross-section cut of a none-delaminated region on the graphite-CFD is shown in Figure 4.30. Looking at Figure 4.30(a), we notice that the spray of colloidal graphite left a highly porous layer of

10 µm of graphite on top of the GdBCO. Since no I_c degradation was observed after the limitation tests, it was assumed that the porosity had no critical effect on the desired thermal conductivity of the layer. However, Figure 4.30(b) reveals that the porosity is also present in the interface with the GdBCO, thus leading to a poor contact interface. This poor adherence interface was likely the cause of delamination happening during the quench.

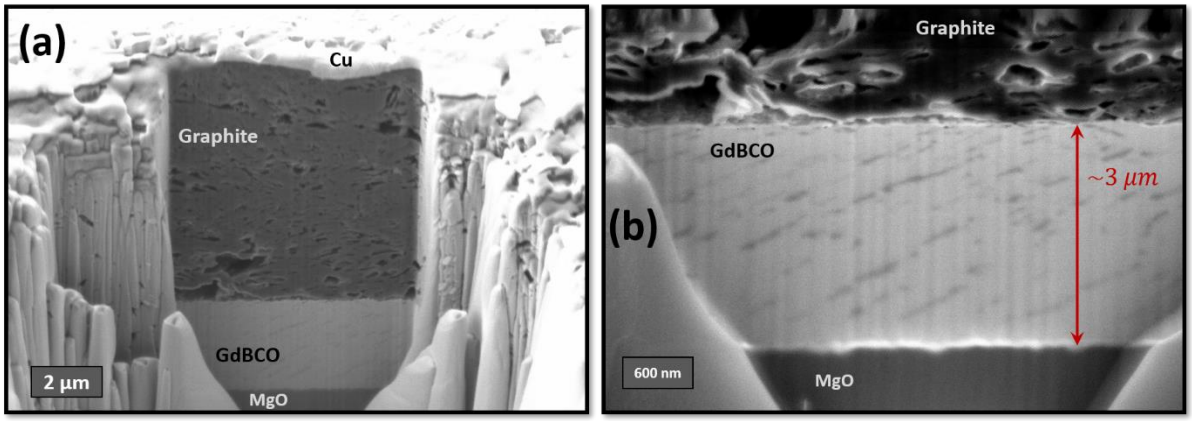

Figure 4.30: (a) Secondary Electron (SE) SEM-FIB cross-section image of the Ag/Graphite/GdBCO/MgO layers. (b) Backscatter Electrons (BSE) SEM-FIB of the interfaces Graphite/GdBCO/MgO.

5 The Yttria-CFD Route

In the standard 2G HTS CC fabrication processes, the oxygenation of the REBCO layer and the silver annealing after the stabilizer/shunt evaporation, are performed in a single oxygen annealing treatment reaching temperatures above 500 °C as shown in subsection 3.1.4. Due to this fabrication aspect, from a conservative manufacturer point of view, it becomes highly attractive to create the high resistive interface of the CFD prior to the annealing /oxygenation of the REBCO layer. However, due to the silver diffusion into the REBCO material for temperatures above 400 °C (subsection 1.5.3), any attempt to form a high resistive interface leaving pure silver in direct contact with the REBCO would fail. With these restrictions in mind, the best scenario would be adding an extra layer in between the silver and the REBCO capable of blocking silver diffusion during the annealing and at the same time having minimum effect on the oxygen incorporation process of the REBCO film.

This chapter reports on the experimental attempts of reaching a scalable CFD architecture using a chemical solution deposition (CSD) approach that has been previously used to prepare high quality functional thin films [173,216,253]. These experiments were conducted in parallel with the experiments of chapter 4 in order to maximize the chances of success during the *FASTGRID* project. The CSD of yttria (Y_2O_3) nanolayers were experimentally tested in collaboration with *FASTGRID* partners at *Oxolutia* for two different stages (two routes) in the classic CC manufacturing sequence of, namely before and after the oxygenation process of the REBCO layer.

5.1 1st Manufacturing Route for Yttria-CFD

In order to confirm the possibility of using yttria to create the CFD pattern, bare THEVA tapes consisting of GdBCO/MgO/Hastelloy were used as template. These tape samples in this first fabrication route were neither oxygenated nor silver coated prior to the yttria's deposition. The sequence of experimental steps needed for the yttria-CFD incorporation are illustrated in Figure 5.1.

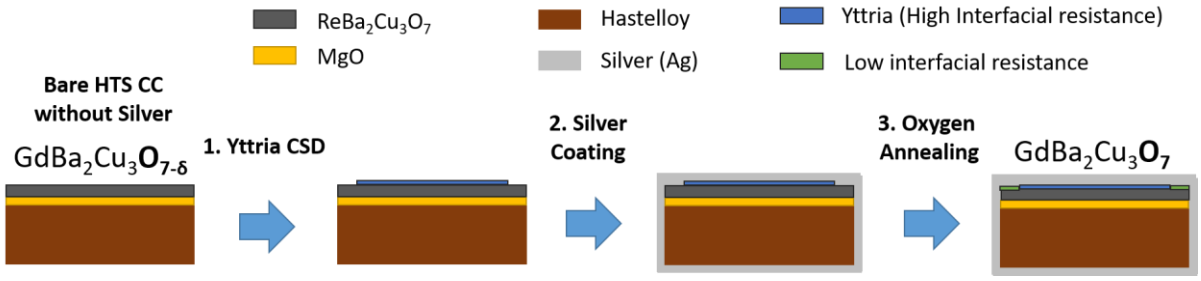

Figure 5.1: Sequence of experimental steps for the first Yttria-CFD route: The yttria is deposited directly on to the GdBCO layer via CSD prior to any oxygen annealing process, i.e post-oxygenation.

In the 1st step, 85-90% of the tape's width (12 mm) is coated with a Y ink and pyrolyzed to create an amorphous yttria layer [216]. This process was either accomplished by the company *Oxolutia* via ink jet printing in the case of long length sample (>1 m) or at ICMAB's laboratory via spin-coating for small samples (<15 cm). In the 2nd step, the tape is silver coated with (500-1000 nm). Finally, in the 3rd step, the tape is annealed in oxygen atmosphere to load the necessary oxygen content into the GbBCO layer

and create the orthorhombic superconducting structure. Figure 5.2 illustrates the whole process showing a 50x12 mm tape sample after the sequence of experiments described in Figure 5.1.

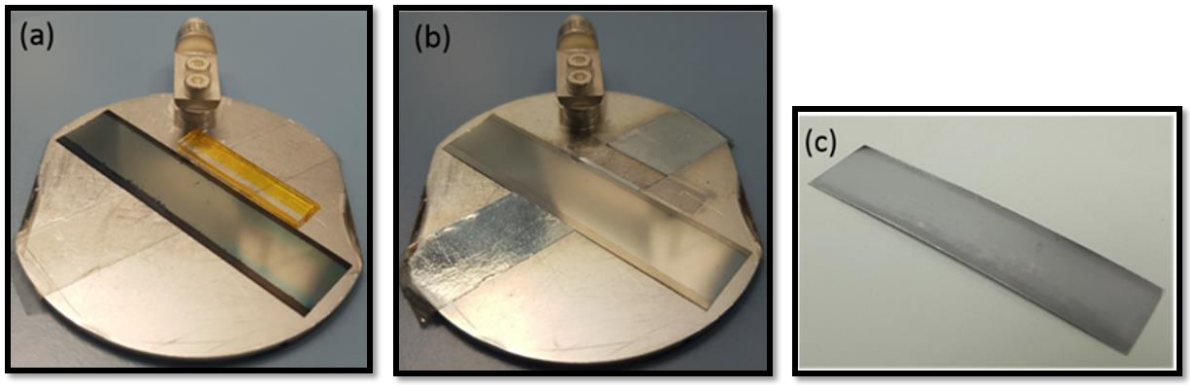

Figure 5.2: (a) Bare GdBCO tape (GdBCO/MgO/Hastelloy) after being ink jet printed with yttria; (b) Yttria-CFD GdBCO tape (Ag/Y_2O_3/GdBCO/MgO/Hastelloy) after being silver coated by magnetron sputtering; (c) Yttria-CFD GdBCO tape after silver annealing in oxygen atmosphere.

Undoped yttrium oxide/yttria (Y_2O_3) is a well-known p-type conductor in high oxygen partial pressure environment like air [254,255]. The self-diffusion of the oxygen ion is orders of magnitude bigger than the yttrium cation diffusion and it increases with increasing oxygen partial pressure with the exponent of approximately 1/6 [254]. Still, according to the initial studies of M.F. Berard [255], in contrast to the yttrium cation diffusion, the oxygen self-diffusion in the single crystal is not enhanced by grain boundaries with large grains (> 10 µm); the presence of a few grain boundaries only enhanced the diffusion of slower species, but not the diffusion of the faster species. However, more recent studies for the case of solid electrolytes for solid oxide fuel cells (SOFC) [256] have shown that nanocrystalline microstructures (< 150 nm) exhibit higher ionic conductivity than a microcrystalline one [257]. The higher amorphous phase content in the nanocrystalline material due to the amorphous structure intergranular boundaries leads to easier diffusion of O^{2-} ions [258,259]. Therefore, it was expected that the amorphous yttria layer, partially-crystalline by the post oxygenation process (subsection 3.1.4), would retain similar or better oxygen diffusion properties to that of the known polycrystalline structure.

Initial assumptions about the oxygenation time were made with the experimental data from Y. Ikuma et al. [260] for polycrystalline yttria in 0.066 bar of PO_2 for the temperature range of 300-600 °C (Figure 5.3). The yttria oxygen lattice diffusion $D_{l,O}$ (orange dashed line) is consistently 2 orders of magnitude slower than the YBCO's diffusion in the c-axis D_c (black dashed line) thus, even with a thin 100 nm thick yttria layer covering the film GdBCO, according to equation (1.15) the saturation time for the oxygen to cross the yttria barrier would take 39 hours at a constant temperature of 450 °C. However, this assumption neglects two factors: the $D_{l,O}$ increase due to the PO_2 increase (1 bar) in the oxygenation process of the GdBCO; and the near-surface oxygen diffusion $D_{s,O}$ of 1-4 orders of magnitude faster than the lattice $D_{l,O}$ in the same 300-600 °C range [261]. Assuming, these additional effects could lead to an effective yttria diffusion $D_{Y_2O_3} \approx D_c$ (cm^2/s), if the yttria-CFD layer were to be maintained at ~100 nm, oxygen could surpass the yttria barrier in a viable time (< 12 h) to allow the oxygenation of the GdBCO film.

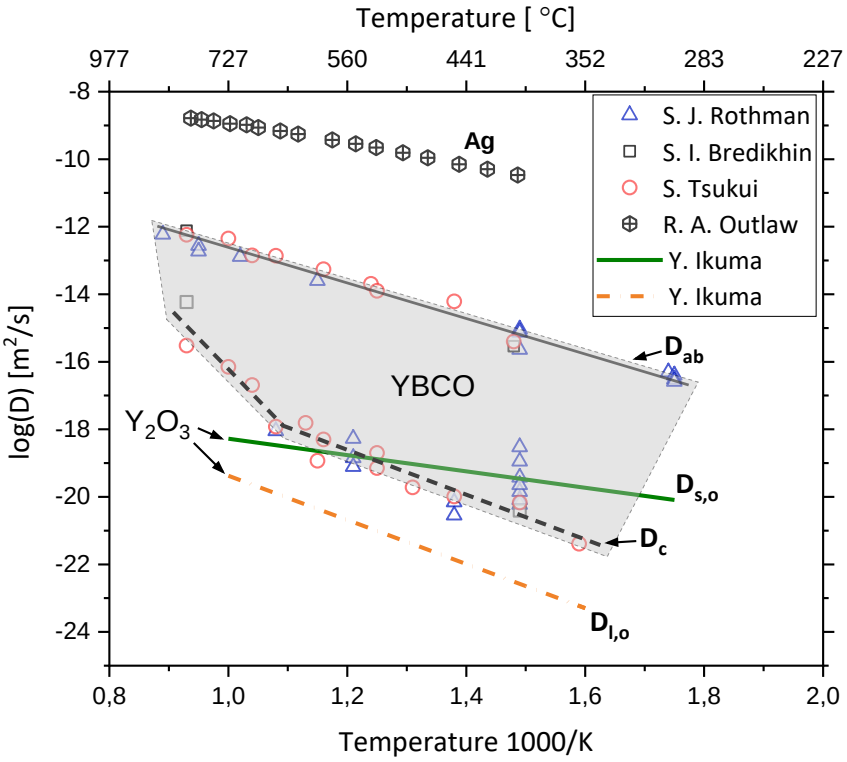

Figure 5.3: Arrhenius plot of chemical diffusion coefficients of oxygen in YBCO and polycrystalline Y_2O_3 from different authors: oxygen tracer study from S. J. Rothman (blue triangles); oxygen tracer study from S. I. Bredikhin (black squares); oxygen tracer study from S. Tsukui (red circles); oxygen tracer study from Y. Ikuma (solid green line and dashed orange line); The oxygen diffusion in silver (crossed black hexagons) is also plotted from R. A. Outlaw data for comparison. The light grey area delimits the bulk oxygen diffusion of a generic oriented YBCO film.

5.1.1 The Yttria Thickness

A batch of 1-meter of Yttria-CFD tape, was prepared at a printing speed of 13 m/h, and heat-treated at 300 °C for 10 min in air in Oxolutia's facility. Figure 5.4(a) show the SEM-FIB cross-section image of a GdBCO tape deposited with amorphous yttria confirming the absence of porosity in the final 400 nm thick layer. Figure 5.4(b) shows a microscopic top view section of the edge of the yttria layer on top of the GdBCO. The microscopic analysis revealed that the variation of the width of the yttria layer were approximately 1% (100 µm).

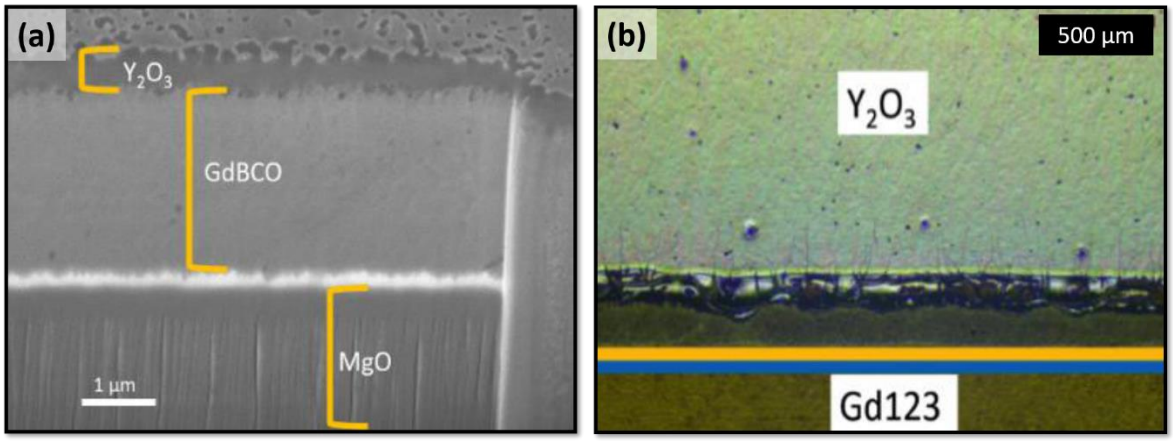

Figure 5.4: (a) FIB-SEM image of THEVA deposited with yttria via ink jet printing; (b) Optical image of top-section of a bare THEVA tape deposited with yttria using ink jet printing.

Multiple 5x12 mm sample pieces were cut from the 1-meter batch Y_2O_3/GdBCO/MgO/Hastelloy tape in order to test THEVA's standard temperature profile for the oxygen annealing in the presence of 400 nm of IJP-yttria. The 5x12 mm samples were sputtered with ~400 nm of silver and subsequently annealed in 1 bar of 0.6 L/min oxygen flow with THEVA's temperature profile (section 3.1.4). The evaluation of the oxygenation process was conducted by performing a Scanning Hall Probe Microscopy (SHPM) measurement at 77 K.

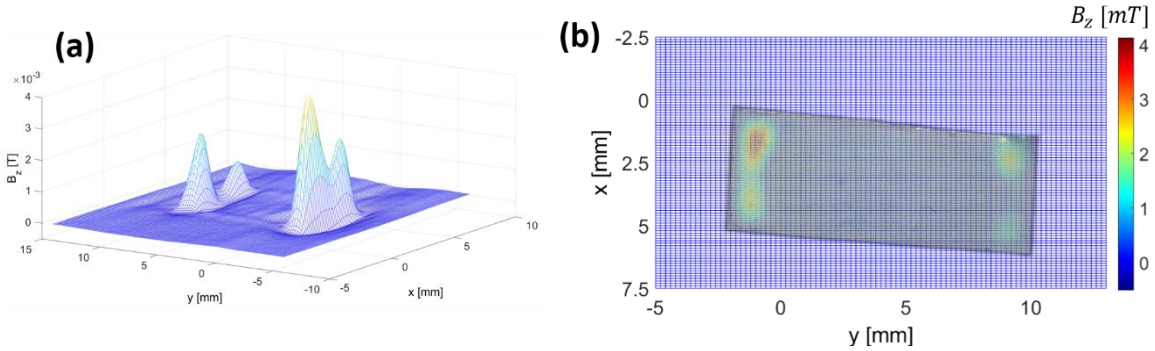

Figure 5.5: Scanning Hall Probe Microscopy (SHPM or Hall-scan) for a 5x12 mm tape sample from THEVA deposited with 400 nm of yttria-CFD via IJP. The sample was deposited with 500 nm of silver via sputtering and oxygen annealed with THEVA's temperature profile.

As exemplified in Figure 5.5, all 5x12 mm samples deposited with a 400 nm thick amorphous yttria-CFD presented an absence of the expected trapped field B_z along the middle section of the width (y-axis) after oxygen annealing with THEVA's temperature profile. This B_z pattern indicated a complete absence of the superconducting properties along the region coated with the yttria. In order to assure that the loss of properties was not strictly related to the degradation of the GdBCO due to reactivity during the pyrolysis of the Y-ink, another 1-meter batch of IJP yttria-CFD with ~220 nm thick yttria was produced following the same procedure previously described.

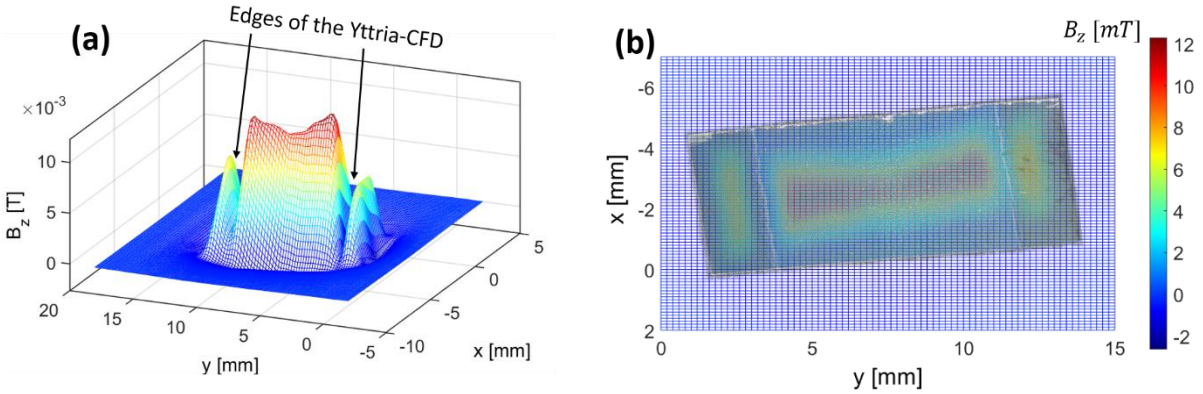

Figure 5.6: Scanning Hall Probe Microscopy (SHPM or Hall-scan) for a 5x12 mm tape sample from THEVA deposited with ~220 nm of yttria-CFD via IJP and 500 nm silver via sputtering after oxygen annealing with THEVA's temperature profile.

All 5x12 mm samples deposited with a ~220 nm thick yttria-CFD layer presented considerably higher values of B_z and better homogeneity across the film after the oxygen annealing (Figure 5.6(a)) when compared to the previous ~400 nm thick yttria samples (Figure 5.5(a)). This observation indicated that the yttria thickness was indeed the major barrier for oxygen incorporation during the annealing process. However, as illustrated in Figure 5.6(b), an absence of field B_z along the edges of the deposited IJP-yttria layer still indicated a strong loss of the superconducting properties along the yttria

edges. SEM images, taken along the cross-section of a 5x5 mm sample piece of the batch with ~220 nm IJP-yttria without silver, revealed a significant increase of the yttria thickness near the edges (Figure 5.7(b)) of layer when compared to the central part of the tape (Figure 5.7(a)).

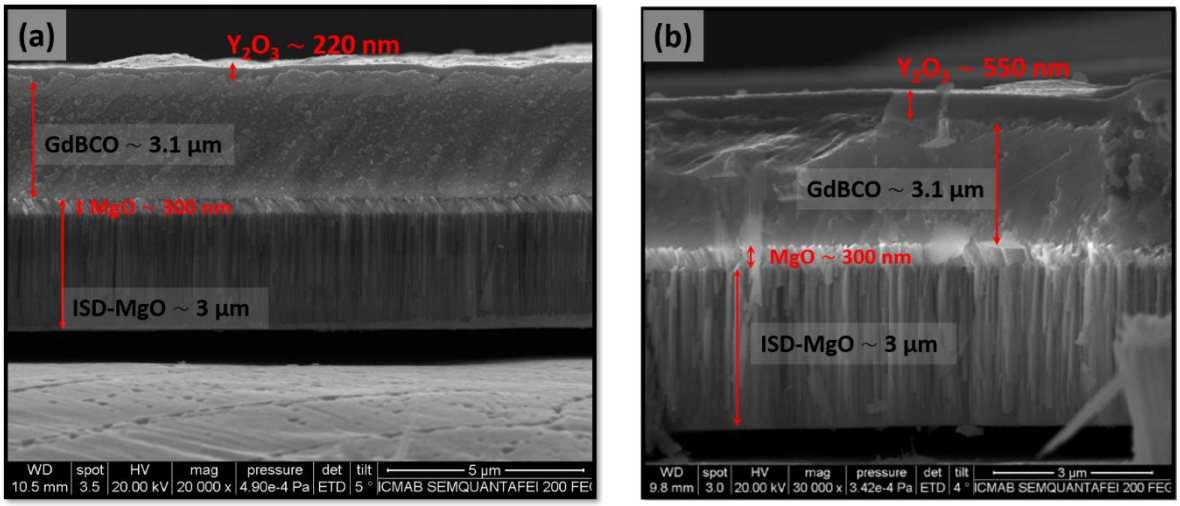

Figure 5.7: SEM cross-section images of the width of a tape sample (GdBCO/MgO/Hastelloy) ink jet printed with yttria. (a) Center of the yttria layer shows a thickness of ~220 nm. (b) Edge of the yttria layer shows thickness of ~550 nm.

This preliminary attempt to incorporate the CFD architecture with amorphous nanolayers of yttria revealed that a thin amorphous yttria thickness bellow 220 nm was crucial when trying to oxygenate the bilayer Y_2O_3/GdBCO layer with THEVA's temperature profile. Maintaining a homogenous IJP-yttria thickness across the tape's width was not a trivial task and became an indispensable technical challenge that required some dedicated investigation in partnership with the company *Oxolutia* S.L.

5.1.2 The Halo Effect

The excessive thickness along the edges of the final Ink Jet Printed yttria layer (Figure 5.8(a)) is an issue also known as the "Halo" effect in the flexographic printing industry [262]. The halo effect is commonly recognized when the ink extends beyond the edges of printed areas on the substrate, creating a halo-like outline (Figure 5.8(b)).

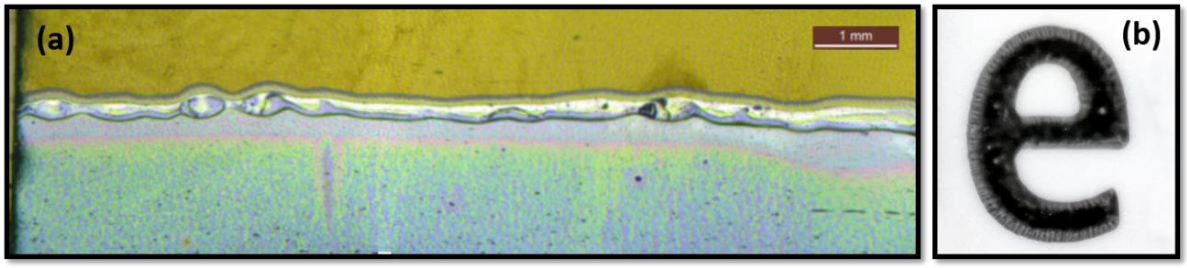

Figure 5.8: (a) Halo effect of ink jet printing the Y ink along the edges of the CFD layer. (b) The halo effect of flexographic printing the letter "e" with an excess of ink.

The two main causes for the formation of Halos in flexo printing are irregular ink pressure during printing and/or excess of transferred ink. Flexographic is a pressure-sensitive process, too much pressure from the printing cylinder onto your substrate will push the ink into places it doesn't belong.

On the other hand, too little pressure could lead to other issues, such as “skip out” [263]. However, in IJP the ink is simply deposited on to the substrate via droplets coming from a moving nozzle. The ink should not experience any significant change in pressure during deposition, thus narrowing down the issue to an ink excess.

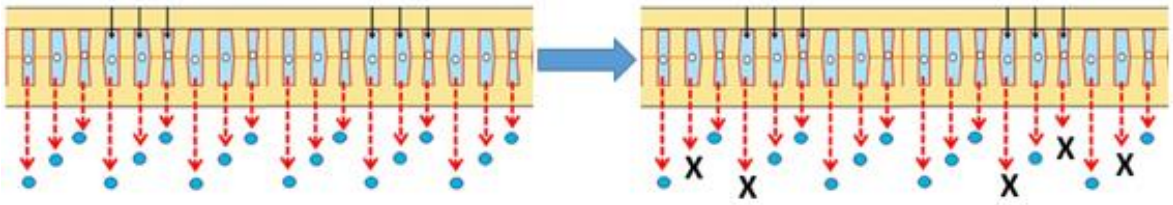

Figure 5.9: New printing configuration (right side) which permits decreasing the lip's thickness and this way, improve the superconducting properties of the CFD system.

To achieve a continuous yttria layer, enough ink must be used to wet completely the GdBCO substrate, but still it can be too much to create a homogenous deposition. This issue usually requires an optimization of the substrate's surface energy or the ink's viscosity/surface tension. Nonetheless, for practical purposes, *Oxolutia* decreased the film thickness on the edges by alternating the working nozzles of the print head hovering the edges of layer during IJP (Figure 5.9). By deactivating every second nozzle in the printing head during deposition, the excessive thickness along the edges could be diminished without compromising the layer continuity.

The effectiveness of the technique was confirmed by applying the up-graded deposition to a new 1-meter of bare GdBCO tape. Figure 5.10 shows the microscopic characterization of a 5x12 mm sample cut from the 1-meter batch and the improvement in the homogeneity of the yttria outline is evident when comparing Figure 5.4(a) and Figure 5.10(b). In Figure 5.10(b), the slight shift in color from the blueish center to a reddish outline still indicates a small variation in thickness of 100 nm approximately. This assumption was later confirmed by analyzing the sample in cross-sectional SEM (Figure 5.11).

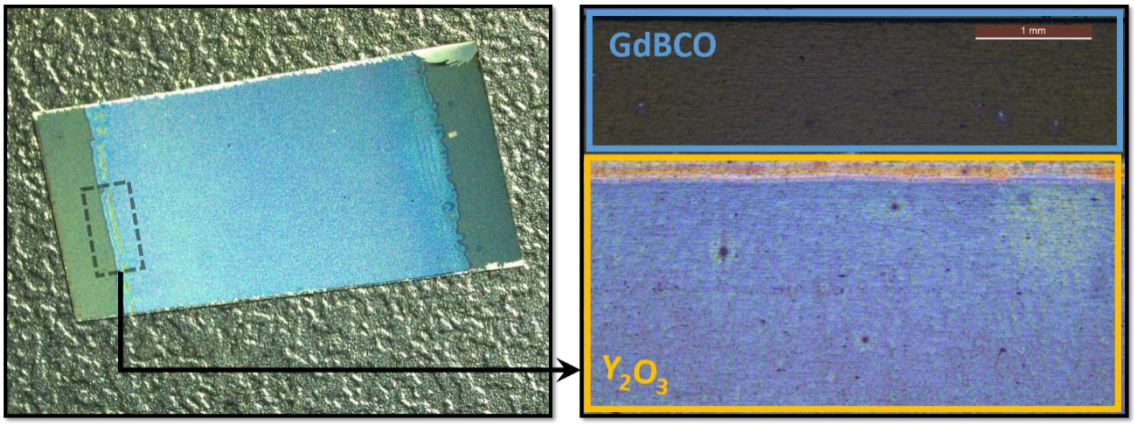

Figure 5.10: (a) Magnified image of top-section of a THEVA tape deposited with yttria using ink jet printing; (b) Microscopic image of the yttria layer outline after upgrading the ink jet printing on THEVA tape.

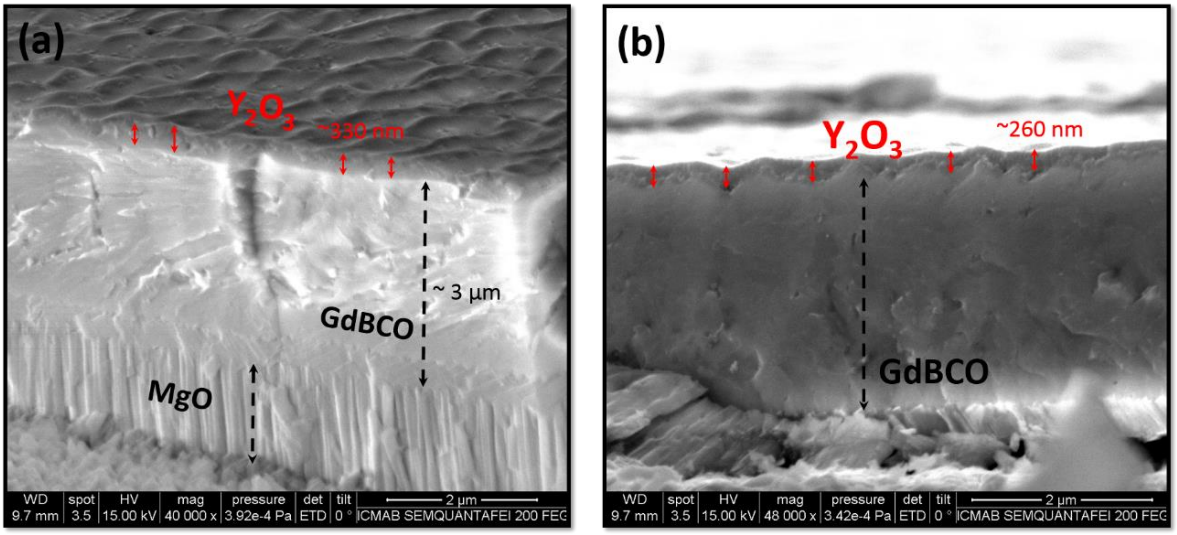

Figure 5.11: (a) SEM cross-sectional view of sample from Figure 5.10: (a) on the edge of the yttria layer; (b) on the center of the yttria layer.

After achieving an yttria layer with a thickness variation of less than 100 nm across the width, THEVA's annealing temperature profile was re-tested for samples of 30x12 mm and 50x12 mm cut from the 1-meter batch. Once again, samples were sputtered with 500 nm of silver and annealed in an oxygen flow of 0.6 L/min with THEVA's temperature profile. Figure 5.12 shows the SHPM field B_z at 77 K for a 50x12 mm sample with no degradation in the field distribution. Moreover, the sample presents a maximum field of 40 mT approximately with a variation of less than 5% indicating a high homogeneity of the superconducting properties.

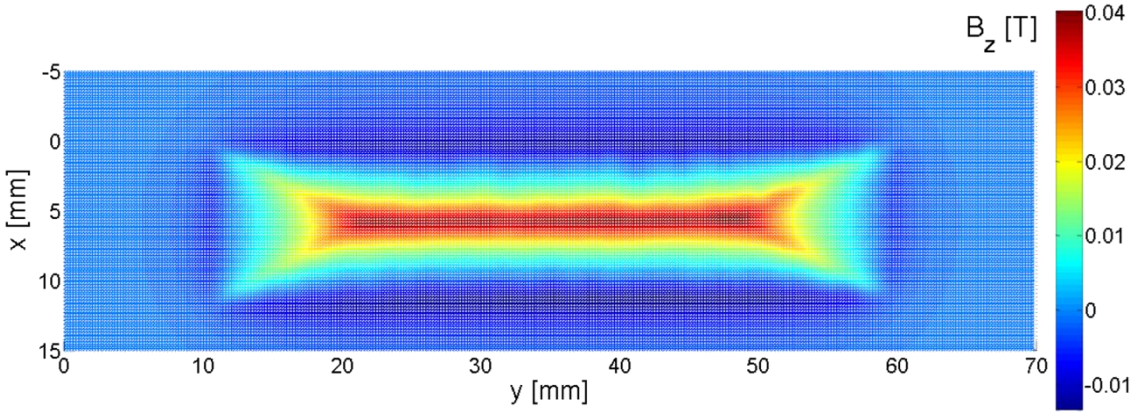

Figure 5.12: Perpendicular trapped field B_z measured by SHPM of one Yttria-CFD sample with yttria thickness varying between 100-200 nm. Sample was oxygenated with two THEVA temperature cycles in a flow of oxygen of 0.3 L/min.

By solving the inverse Biot-Savart problem described in section 3.3.1 for Figure 5.12 we obtained a map of the current density distribution inside the sample (Figure 5.13). It is interesting to point out how the current density on both ends of the tape reduces to half of the values found in the middle section. This phenomenon comes from the GdBCO inclined deposition method utilized by THEVA. In Figure 5.13 the c-axis of the GdbCO crystal has a 30 ° inclination with respect the Hastelloy substrate [55,56], thus creating an anisotropic distribution of current density between the x and the y-axis in [264].

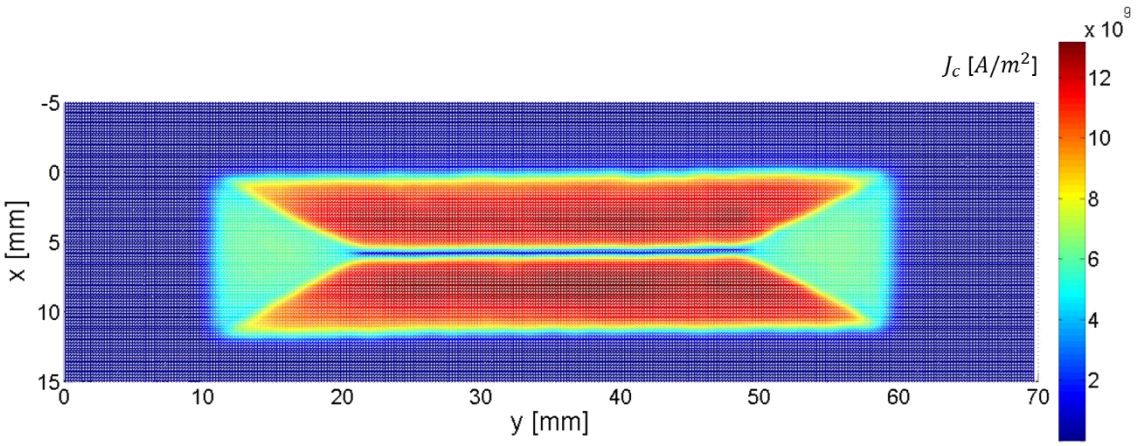

Figure 5.13: Current density distribution J_c calculated from the B_z map shown in Figure 5.12.

Integrating the current densities along the y-axis in Figure 5.13 we could estimate the overall current flowing inside the tape to be 532 A. Correcting this value for a 20% decay in B_z field due to magnetic relaxation after the field cooling, the critical current should be close to 638 A. Table 5-1 shows the critical current estimated from Hall mapping for Yttria-CFD tapes from two batches of Yttria-CFD samples, namely SDP-FG-87 and SDP-FG-92.

Table 5-1: Critical current of Yttria-CFD samples after THEVA's oxygenation profile.

Batch number	Sample	Size [mm]	$\sim I_c$ [A]
87	#3	30x12	632
87	#4	50x12	636
87	#5	50x12	628
87	#6	50x12	590
93	#1	30x12	601
93	#2	30x12	604
93	#3	30x12	640

5.1.3 Temperature Gradients & Long Samples

In the previous section, we have shown the experimental IJP conditions for a successful incorporation of the yttria layer in small samples (< 5 cm) of THEVA tape. Nevertheless, in order to test CFD samples in electrical transport measurements (subsection 3.4), a minimum length of 10 cm was required to avoid problems in the current contacts. The major challenge while scaling up the production of Yttria-CFD samples from 5 cm to 10 cm is well illustrated by the field distribution B_z along the length of the tape in Figure 5.14. For all samples with length above 7 cm and an yttria thickness below 300 nm, a consistent inhomogeneous B_z field pattern similar to Figure 5.14 was observed after oxygen annealing with THEVA's temperature profile (Figure 3.3). This was an indication that the GdBCO was loading oxygen at different rates on certain regions during the heat treatment inside the furnace.

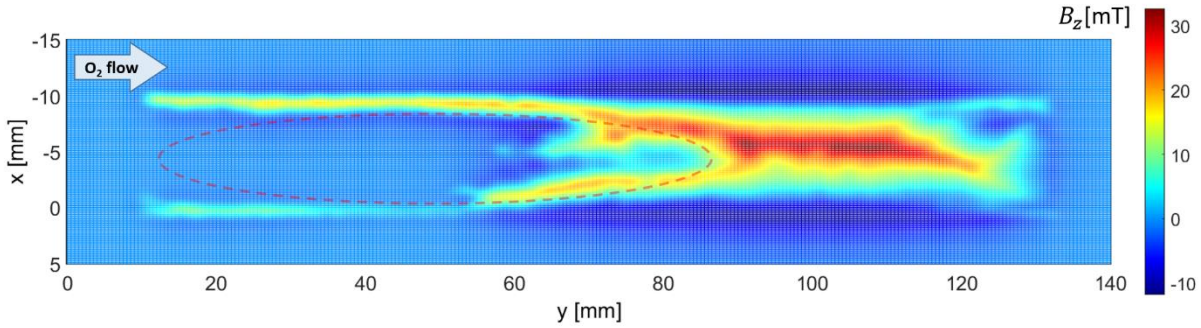

Figure 5.14: Perpendicular trapped field B_z measured by SHPM of a 100 x 12 mm THEVA tape sample with the Yttria-CFD structure. Sample was oxygenated with two THEVA temperature cycles in a constant oxygen flow of 0.3 L/min. The dashed red ellipse indicates a whole half of the tape that is not magnetized due to oxygen deficiency.

Given the recurrent parabolic aspect of the distribution of B_z consistently appearing on the sample's side closer to the oxygen inlet inside the tube (arrow in Figure 5.14) and knowing that the rate of oxygen diffusion is a well-known thermal activated process (subsection 1.6.3), the B_z inhomogeneity was related to the presence of temperature gradients linked to a fast oxygen flow inside the small 10 cm isothermal region of the static furnace. This assumption was strengthened by performing simulations in *COMSOL* using the Conjugated Heat Transfer module in a steady state analysis. The 10 cm tape sample was simulated inside a 1 m long quartz tube of 22 mm diameter, with oxygen flux ranging from 0.01 to 0.9 L/min and the tube's outside wall middle region at a constant 575 ˚C. Figure 5.15 highlights the simulation main results by showing how the temperature distribution inside the quartz tube is distorted as the gas flow increases. At 0.3 L/min the 10 cm sample inside the tube can end up experiencing gradients bigger than 30 °C along its length.

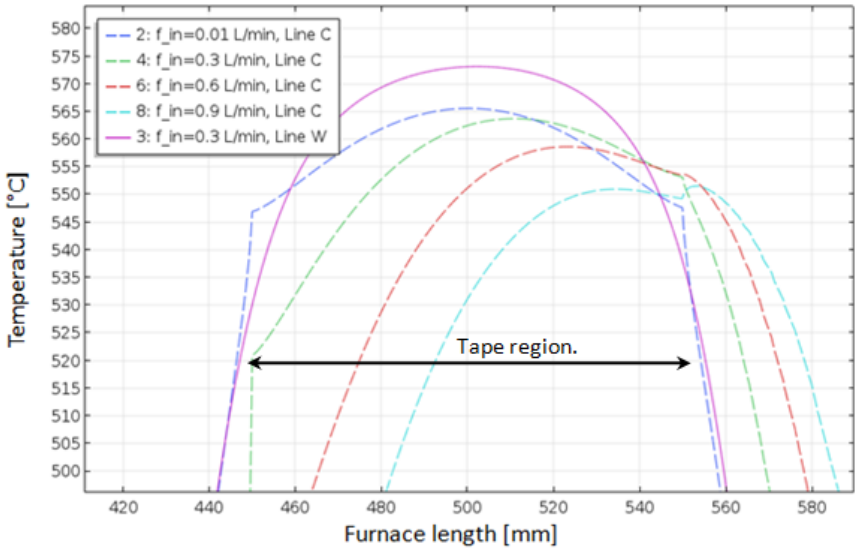

Figure 5.15: COMSOL simulation of the temperature distribution inside ICMAB's tubular furnace for different values of oxygen flow. Line W indicates the position along the outside wall of the quartz tube inside the furnace. Line C indicates the position along the axial line of the quartz tube.

The effect of the simulated temperature gradients was confirmed by an experiment to verify the direct influence of the oxygen flux on the final superconducting properties. A diagram of the experiment setup for the oxygen flow control is illustrated in Figure 5.16. The HTS tape sample is positioned inside a 1 m quartz tube and the tube is inserted in a 30 cm long tubular furnace with a 15 cm isotherm

region. Both Inlet and Outlet of the quartz tube are connected together by a second PTFE tube with small *Sunon* fans inside and a valve added to the Outlet of the quartz tube. By initially purging the air inside the system with pure oxygen in the Inlet and closing the outlet valve afterwards, the gas flow is controlled by the propeller fans to achieve values ranging from 0.03 to 0.9 L/min. This set up was implemented to avoid oxygen wasted for high gas flow values during long annealing times.

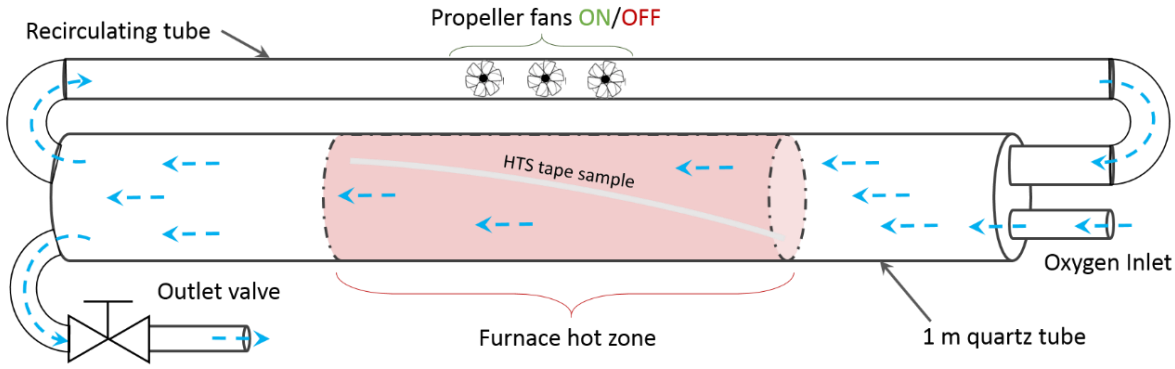

Figure 5.16: Experimental diagram for a high oxygen flux control during oxygen annealing of Yttria-CFD tapes.

Figure 5.17 shows the SHPM measurements of the trapped field B_z for an yttria-CFD sample annealed four times with the same temperature profile, but under different values of oxygen flow. This 15 cm tape piece, was cut from a IJP batch deposited with ~200 nm of yttria and coated with 1 µm of silver previous to the annealing experiments. The temperature profile used for the results shown in Figure 5.17 (a), (b) and (c) was: 10 °C/min to 500 °C, 5 hours dwell at 500 °C and 10 °C/min to room temperature. Comparing the B_z(x,y) maps of (a), (b) and (c), it becomes clear that as the flux diminishes from 0.9 to 0.1 L/min the intensity and homogeneity of the trapped field B_z improved considerably across width and length of the sample. However, this correlation was only seen across the CFD region coated with yttria. The yttria-free edges of the sample did not present any significant change in B_z with the change in the flux.

In the final result shown in Figure 5.17(d) the minimum flux of 0.1 L/min was maintained and the temperature dwell was increased from 500 to 600 °C. Once again, we observe an improvement of B_z across the length (y-axis). Moreover, we also notice an expected maximum field drop from 15 mT to 10 mT due to a lower oxygen equilibrium stoichiometry at higher temperatures.

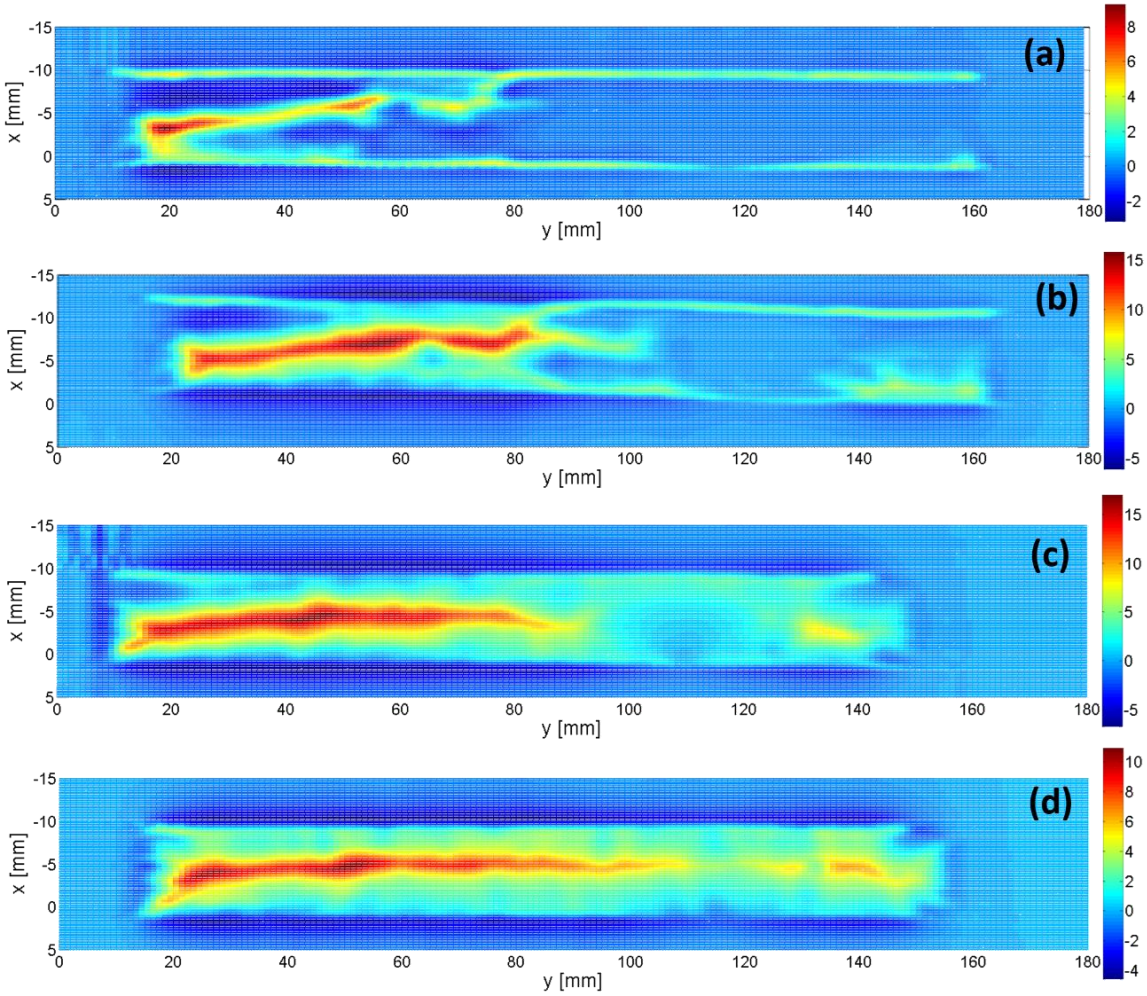

Figure 5.17: Perpendicular trapped field B_z maps done by SHPM at 77 K for a 150 x 12 mm Yttria-CFD sample with 200 nm of ytrria. (a) B_z map after 1st oxygen annealing at 500 °C in a unidirectional oxygen flow of 0.9 L/min. (b) B_z map after a 2nd oxygen annealing at 500 °C in a unidirectional oxygen flow of 0.6 L/min. (c) B_z map after a 3rd oxygen annealing at 500 °C in a unidirectional oxygen flow of 0.1 L/min. (d) B_z (x,y) map after a 4th oxygen annealing at 600 °C in a unidirectional oxygen flow of 0.1 L/min.

The effect of a minimum flow of oxygen was investigated with a second Yttria-CFD sample of 150 x 12 mm. This sample was annealed with THEVA's temperature profile and the minimum available flux of 0.03 L/min. Performing a SHPM afterwards for the B_z map at 77 K (Figure 5.18 (a)) confirmed the critical influence of even small temperature gradients on the final homogeneity of the superconducting properties along the tape's length (y-axis).

The inevitable temperature gradient coming from the conditions of the experimental setup had to be countered to create practical long samples for transport tests. This was accomplished by implementing a second annealing process maintaining the same 0.03 L/min flux, but reverting the flow direction. The homogeneity improvement of the B_z distribution after the 2nd annealing is shown in Figure 5.18(b).

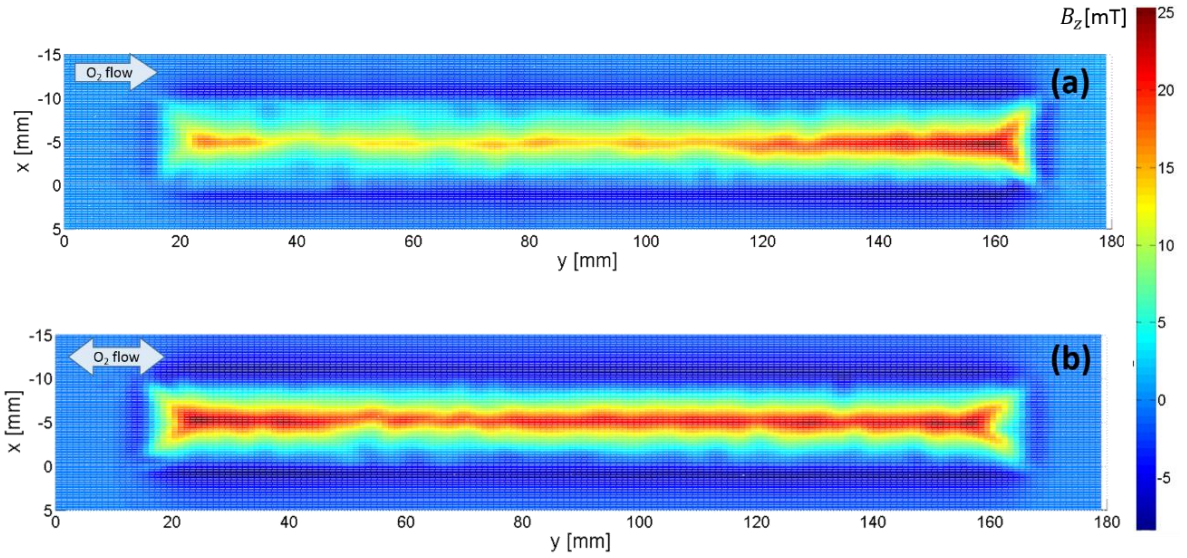

Figure 5.18: Perpendicular trapped field B_z measured by SHPM at 77 K for a 150 x 12 mm Yttria-CFD sample. (a) B_z map after 1st oxygen annealing using THEVA's temperature profile in a unidirectional oxygen flow of 0.03 L/min. (b) B_z map after a 2nd oxygen annealing using THEVA's profile and reversing the oxygen flow (0.03 L/min) direction.

The effectiveness of the bidirectional flux of oxygen during the annealing in the final amplitude and homogeneity of B_z was reassured by re-annealing the sample shown in Figure 5.14 with the same 0.3 L/min flux, but reversing the flow direction. The B_z distribution after the second annealing process is shown in Figure 5.19. This sample was sent to KIT for Fluoresce Thermal imaging measurements and the results are discussed in following subsection 5.2.1.

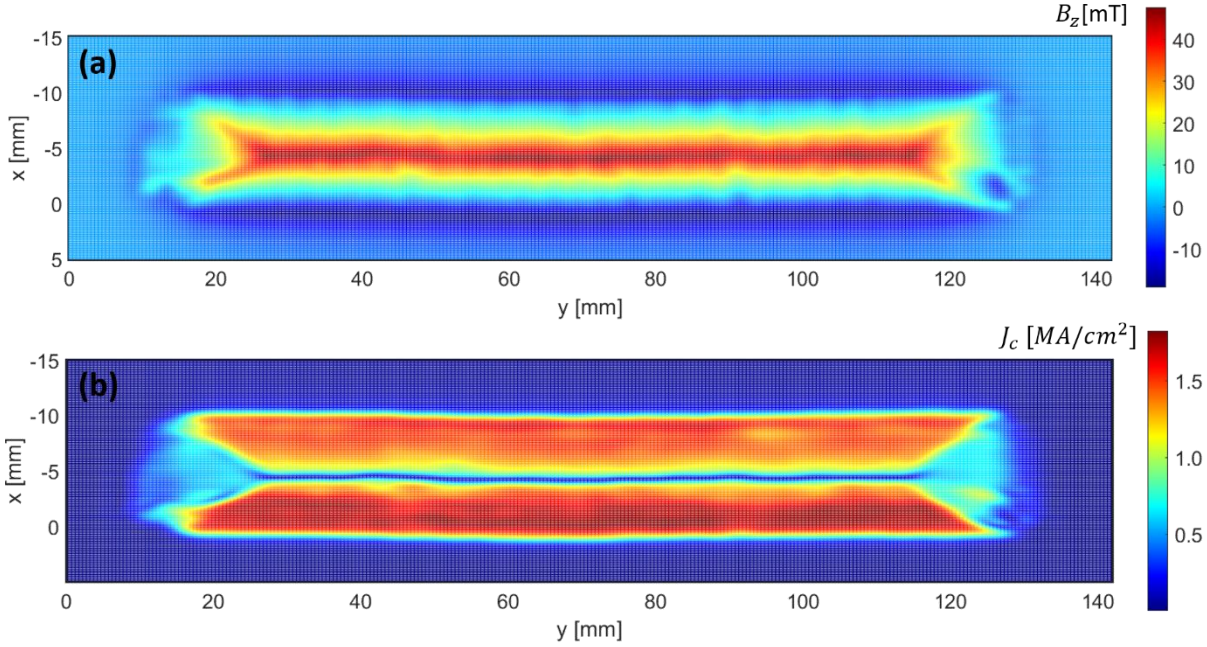

Figure 5.19: Scanning Hall Probe Microscopy (SHPM) measurements for 110 x 12 mm Yttria-CFD sample. Sample was oxygenated with two THEVA temperature cycles in a flow of oxygen of 0.3 L/min. (a) Perpendicular trapped field B_z distribution in mT. (b) Critical current density distribution J_c in MA/cm^2 calculated from the B_z distribution.

5.1.4 Improving the Oxygen Annealing Profile for Yttria-CFD Tapes

Even performing the oxygen annealing twice with bidirectional oxygen flux to prevent temperature gradients, in Oxolutia's facility the reproducibility of the SHPM results seen in the previous section was less than 10%. The majority of the Yttria-CFD samples presented a clear deficiency of oxygen content in the region covered by the IJP-yttria as shown in by the SHPM of Figure 5.20 (yellow dashed rectangle). For the majority of samples, the magnetization signal of B_z was only seen along the edge of the tape not covered with the yttria ink. These results strongly suggest that the main path for the oxygen happens in the z-axis direction perpendicular to the CC's surface through the exposed grain boundaries of the oriented GdBCO film. This assumption is completely coherent with the fact that even though $D_{ab} \gg D_c$, if one would consider a pure oxygen bulk diffusion starting from both yttria-free edges of the tape, the saturation time for the oxygen to travel 5 mm across the width with D_{ab}= 10^{-14} m^2/s at 500 °C would still be in the order of 10^4 hours. The oxygen gas must have access to the grain boundaries in the surface of the GdBCO to complete the oxygen loading throughout the ~3 µm thickness in a reasonable time period.

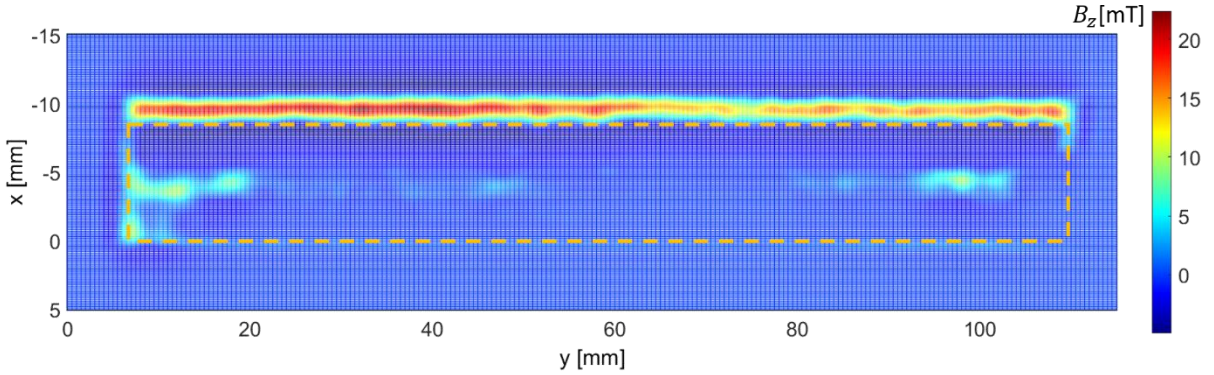

Figure 5.20: Perpendicular trapped field B_z measured by SHPM for Yttria-CFD sample of 100 x 12 mm and 1 µm of silver. Sample was oxygenated with two THEVA temperature cycles and a 0.03 L/min oxygen flow. The yellow dashed rectangle indicates the region of the tape covered with the yttria layer.

In order to overcome the presence of yttria blocking the O^{2-} ions from accessing the grain boundaries on the GdBCO surface, a new temperature profile was empirically conceived. In this new profile, the asymmetry of saturation times for in- and out-diffusion in the GdBCO film - as discussed in section 3.3.2 - was considered as way to try to pump oxygen in a thermal cycle. The incorporation was assumed to be purely thermal driven by bulk diffusion and excorporation to be a surface limited reaction with $\tau^{out} \gg \tau^{in}$. The main idea behind this profile was to speed up the oxygen bulk diffusion by going to a high temperature (> 600 °C) and assume that once the oxygen index reaches a value above $\delta \sim 0.5$, higher indexes should be possible to achieve by stabilizing the temperature for longer periods at a lower temperature value (< 500 °C). These processes are then repeated reversing the direction of the oxygen flow and expecting that the low out-diffusion would maintain a positive net value for oxygen loading. With this behavior in mind, a new temperature treatment called High-Low profile was formulated as shown in Figure 5.21.

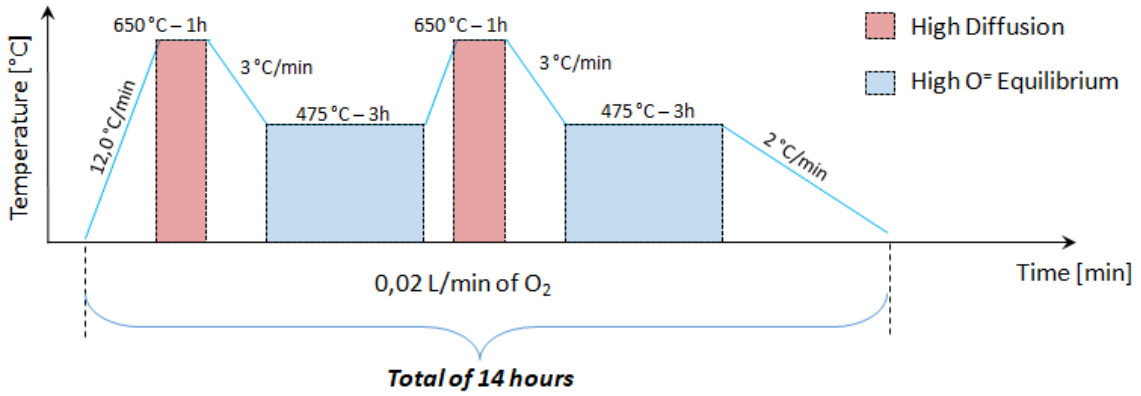

Figure 5.21: High-Low temperature profile. This High-Low sequence consists of two cycles of two temperature dwells, one at 650 °C other at 475 °C.

The effects of oxygenating with the High-Low sequence are seen by comparing the B_z distribution before (Figure 5.20) and after (Figure 5.22) the treatment. The improvement in field homogeneity and amplitude along the tape's length and width is evident. After several successful re-oxygenation attempts on long (> 10 cm) CFD samples, this temperature profile was applied for fabricating 15 cm CFD samples. All samples oxygenated with this High-Low sequence presented a homogenous B_z distribution with I_c variations less than 10%.

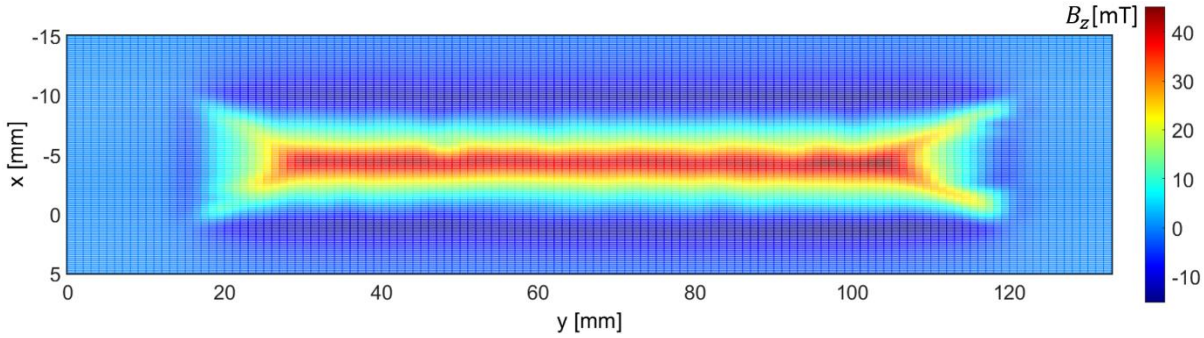

Figure 5.22: Perpendicular trapped field B_z measured at 77 K by SHPM for the sample shown in Figure 5.20 after the sample was re-oxygenated with the 650 °C/475 °C High-Low sequence using 0.03 L/min of bidirectional oxygen flow.

5.2 NZPV Measurements for Yttria-CFD

This section presents and discusses the NPZV experiments performed on long (> 10 cm) yttria-CFD samples treated with THEVA's and the High-Low temperature profile. Samples were measured via Fluorescence Thermal Imaging at Karlsruhe Institute of Technology (KIT) and by *FASTGRID* partners at Ecole Polytechnique Montréal (EPM) using the NZPV system described in subsection 3.4.3.

5.2.1 Fluorescence Thermal Imaging

The Yttria-CFD sample shown in Figure 5.19 was sent to partners in KIT for the evaluation of the NZPV via Fluorescent Thermal Imaging described in section 3.4.4. The sample was coated with EuTFC, heat

treated at 175 °C for 30 minutes in air and mounted onto the sample holder shown in Figure 5.23. One pair of voltage taps was positioned onto the tape's surface with 56 mm spacing in between and another pair of voltage taps (probes) was attached to the current contacts to monitor possible issues with the contact resistance at the current contacts. A summary of all the 12 tests performed is shown in Table 5-2.

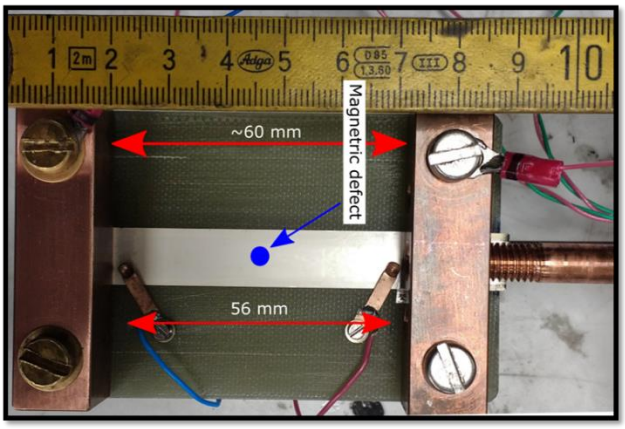

Figure 5.23: Yttria-CFD tape sample mounted onto the sample holder of the Fluorescent Thermal Imaging system of KIT.

The 1st measurable quench happened in test 4 with a current pulse of 650 A. This level of quench current infers a critical current I_c in the same range of the calculated I_c using the J_c(x,y) distribution map calculated with the Hall map of Figure 5.19(b).

Table 5-2: Summary of all electric measurements performed in the Fluoresce Thermal Imaging system for a Yttria-CFD sample. All the current pulses were applied for a 10 ms duration and a rise and fall time of less than 0.5 ms.

#	Pulse [A]	Evaluation	Saved frames	Observation
1 - 3	50 - 500	No quench	2500	No high voltage detected at the current contacts.
4	650	Quench	7500	Huge voltage spike saturating the 1 V range of the AD converter.
5 - 8	550 - 640	No quench	2500	No reduction of I_c (no damage of sample).
9	650	Quench	2500	Quench over a small area, not as big as #1.
10	650	Quench	2500	Quench over a small area. Current is increased and AD converter's set to range 5 V.
11	680	Quench	8000	Voltage exceeded the maximum 5 V limit.
12	640	No quench	2500	No damage of sample

Looking at the electric measurements of test 4 in Figure 5.24(a), we observe a sharp voltage increase at t = 35.5 ms saturating the 1 V range of the A/D converter (flat-peak signal of blue curve). At the same time, the current (red dashed line) dropped sharply down to 300 A until the end of the pulse, thus indicating that the current source was driven into voltage-limitation. Usually, voltage-limitation in this system is caused by the presence of a high resistance in the path of the current that can come from the HTS CC normal state or an open-circuit. The case of an open circuit would imply the rupture of the sample, but the absence of a voltage signal in the subsequent tests 5 to 8 ruled out the occurrence of degradation.

The second and 3rd quenches in tests 9 and 10 occurred at the same current level of 650 A, thus confirming the integrity of the average I_c. However, these quenches only propagated in a small area around the magnetic defect (< 1 cm); therefore, no data was acquired for a reliable analysis of the NZPV. Only at test 11, with an applied pulse of 680 A, a significant quench propagation could be recorded in slow-motion and analyzed to estimate the NZPV.

Looking at electrical behavior of test 11 in Figure 5.24(b), once again the current source operated under current-limitation at 10 V. In this situation, comparing Figure 5.24(b) with the limitation behavior of the classic EPM-CFD in Figure 4.24(b) initially suggests the presence of the CFD. Nonetheless, the CFD behavior could not be confirmed due to the saturation of the A/D converter at 5 V. Afterwards, test 12 was conducted with a pulse of 640 A and no quench was detected as expected from a non-degraded sample.

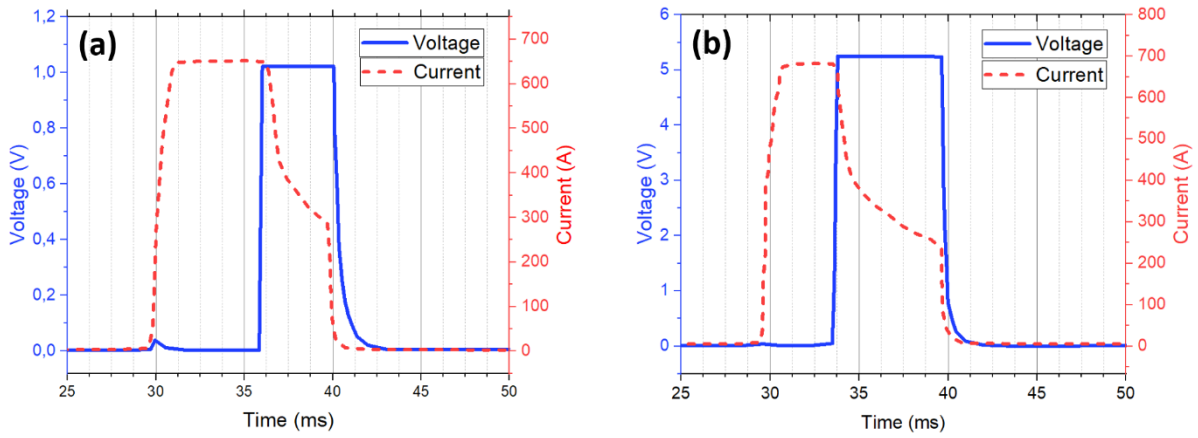

Figure 5.24: (a) Electrical signal for the quench event during test 4 at 650 A pulse. (b) Electrical signal for the quench event during test 11 at 680 A pulse.

In Figure 5.25 we analyze the raw footage and thermal image side by side for three moments during test 11. At 16.40 ms the tape start presenting signs of film boiling, but no quench takes place. At t = 17.00 ms a round normal zone is formed in the region of the magnetic defect and, immediately after, both sides of the tape also start quenching in the same region. As the quench propagates across the length, the distinction between normal zone in the center and edges becomes less noticeable. At t = 21.00 ms the normal zone front takes the whole middle cross-section of the tape and the quench propagation stops due to the 10 V limitation of the current source. Since the applied current of 680 A was not held constant during the normal zone propagation, the NZPV could not be precisely evaluated. Table 5-3 shows how the drop in the current during the test slowed down the NZPV. In addition, from the temperature distribution at t = 17.00 ms, we can notice how the thermal front along the yttria-free edges propagates as far as the front in the center of the sample. This behavior points out to a uniform current diversion to the silver across the cross-section of the tape.

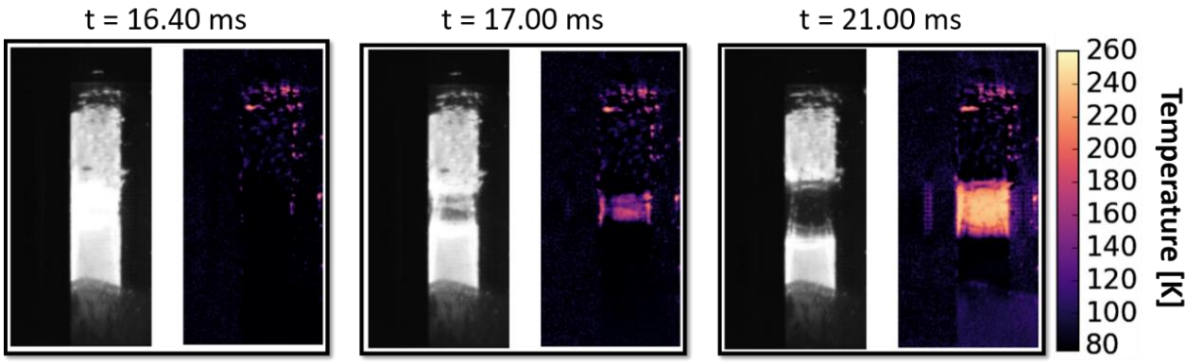

Figure 5.25: Thermal and raw frames for three different moments during the quench propagation during test 11.

Table 5-3: NZPV data from test 11, 680 A. The relative time for the quench start is ~16.4-16.6 ms.

Absolute Time [ms]	Relative Time [ms]	Distance [mm]	NZPV [m/s]	Current [A]
34.7	0.4	3	7.5	650
35.7	1.4	5	3.57	370
38.1	3.8	7	1.84	260

In conclusion, from the electrical behavior analysis (Figure 5.24) and the images from the slow-motion video (Figure 5.25) of the thermal front, no significant NZPV boost could be confirmed for the yttria-CFD sample. The uniform temperature distribution suggested the absence of the expected current crowding, thus indicating a partial failure in the insulation of the CFD yttria.

5.2.2 NZPV Measurements

Following the inconclusive results given by the fluorescence thermal imaging measurements taken for an yttria-CFD sample annealed with THEVA's and ICMAB's High-Low temperature profile, another yttria-CFD sample was produced at ICMAB and tested by *FASTGRID* partners at EPM. The NZPV experiments were conducted with the transport system described in section 3.4.3 where higher pulsed currents could be sustained for longer dwell times.

The NZPV at 77 K versus the applied current data are shown in Figure 5.26. Comparing the NZPV obtained for the yttria-CFD with the uniform architecture from *THEVA*, the same NZPV is obtained. These NZPV measurements at EPM confirmed the absence of the CFD effect for the yttria-CFD tapes following the 1st manufacturing route (Figure 5.1).

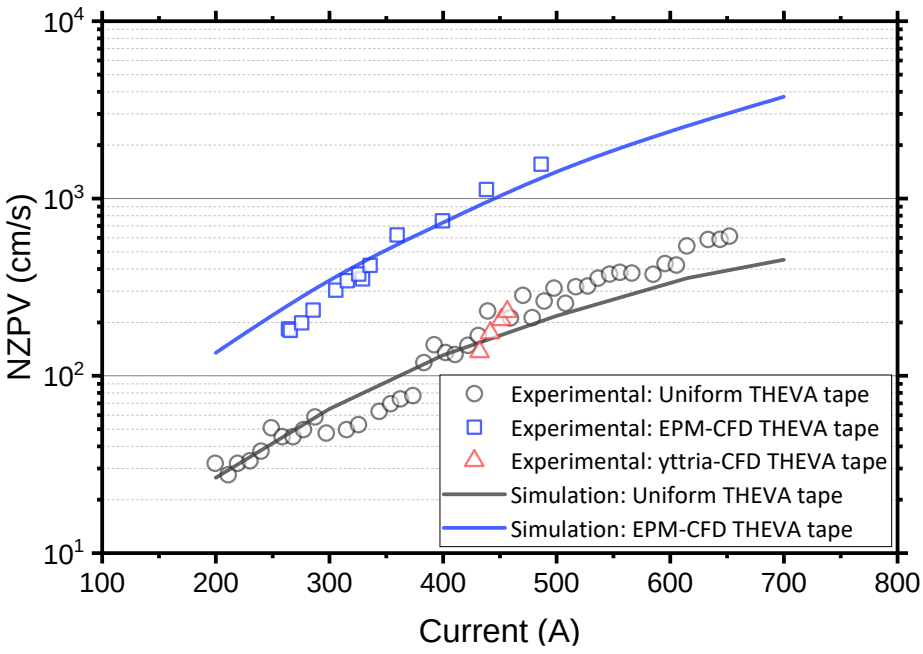

Figure 5.26: Comparison of NZPV versus Current for 1st route of Yttria-CFD in comparison with other architectures: Uniform tape and classic CFD from EPM.

5.3 Instability of the Yttria Layer

The absence of the CFD behavior on the first Yttria-CFD samples indicated that the IJP yttria layer was not efficiently creating a high interfacial resistance between the silver and the GdBCO. In an effort to find the origins of the undesired low interfacial resistance, yttria-CFD samples were analyzed with TEM-EDS, *in-situ* ECR measurements, X-ray diffraction, AFM and SEM/EDX.

5.3.1 Amorphous Yttria Before & After Oxygenation

In this subsection, we discuss the cross-section analysis of two yttria-CFD samples via TEM/EDS. These two samples should represent the tape in the last two stages of the yttria incorporation: before and after oxygen annealing with the High-Low temperature profile (Figure 5.21). First sample (#1), was ink jet printed with yttria, pyrolyzed at 450 °C and silver coated, but not oxygenated (Figure 5.27). The second sample (sample #2 in Figure 5.29), was ink jet printed with yttria, also pyrolyzed at 450 °C, silver coated and annealed in 1 bar of oxygen atmosphere with the High-Low temperature profile (Figure 5.21).

Figure 5.27 shows the TEM cross-section of sample #1 where nine points across the layers GdBCO/Y_2O_3/Ag were analyzed by EDS (Figure 5.28). Inside the GdBCO layer, points eds1, eds2 and eds3, presented an expected rich distribution of Gd, Ba, Cu and O and were here used as base line for comparison with the other points. In the vicinity of the GdBCO/Y_2O_3 interface, point eds4 and eds5 revealed a 100-200 nm region in the GBCO layer still rich in Gd and Cu, but generally depleted in Ba.

This same barium deficient phase was seen in eds5 A with a small diffusion of Y into the GdBCO layer that is confirmed in the eds6 analysis for the yttria layer where we clearly see the Y peak at 2 keV.

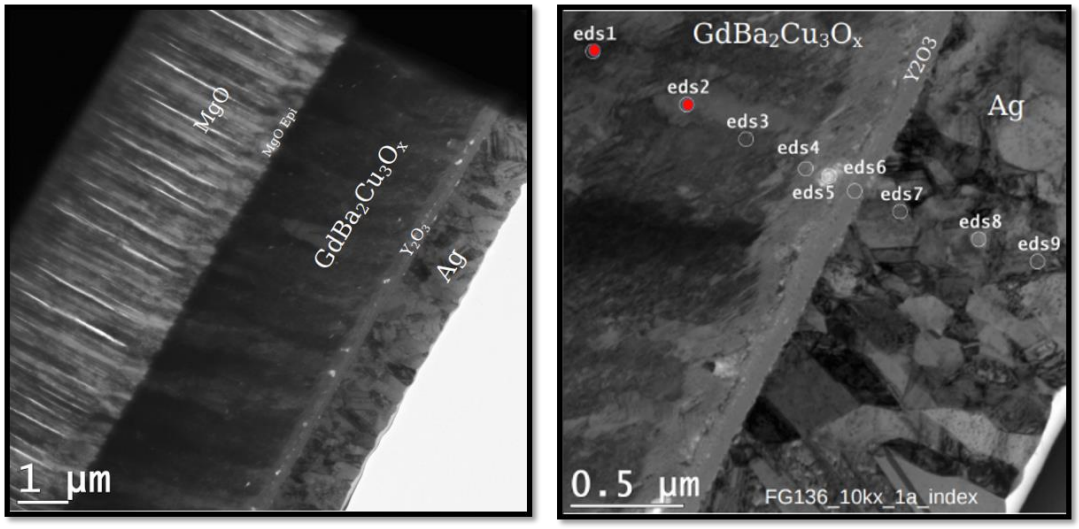

*Figure 5.27: TEM cross-section analysis of an Yttria-CFD sample **before** the oxygenation process. (a) Overall cross-section view of the layers Ag/Y_2O_3/GdBCO/MgO. (b) EDS points in the Ag/Y_2O_3/GdBCO layers responsible for the CFD.*

Furthermore, point eds6 revealed the same counts of Gd, Ba and Cu in the amorphous yttria. An explanation for this element distribution is the diffusion of Gd, Ba and Cu towards the Y_2O_3 layer during the pyrolysis step of the yttria ink. Yet, no silver was found in the eds6 for the Y_2O_3 layer, neither in the GbBCO layer. Silver is only present in the spectra of points eds7, eds8 and eds9 as expected. This first analysis of an Yttria-CFD sample before oxygen annealing confirms the presence of an yttria barrier layer, acting as an interfacial impedance between the silver coating and the GdBCO film.

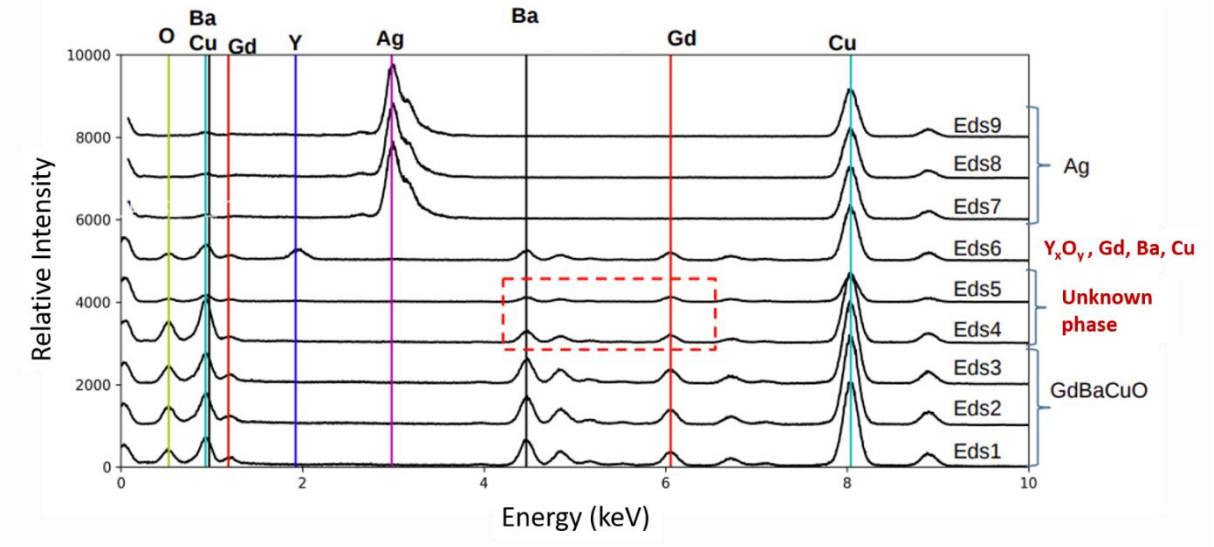

*Figure 5.28: EDS spectra for 9 points across the Ag/Y_2O_3/GdBCO layers **before** the oxygen annealing (sample #1).*

Figure 5.29 shows the TEM cross-section of sample #2 revealing that the yttria layer is no longer dense and well-defined between the silver and the GdBCO. The EDS spectra for the eight points across the Ag/Y_2O_3/GdBCO layers is shown in Figure 5.30. As observed in the GdBCO film of sample #1, points eds1, eds2 and eds3 presented an expected rich distribution of Gd, Ba, Cu and O, meanwhile, in the region close to the yttria interface, points eds4 and eds5 reveals the same distribution with a barium

deficiency. The differences between sample #1 and #2 starts at point eds4 where a small trace of Y was spotted close to the Y_2O_3/GdBCO interface together with some Ag. In the "yttria layer region", point eds5 also shows traces of Ag, but interestingly almost neither Y nor Gd was found.

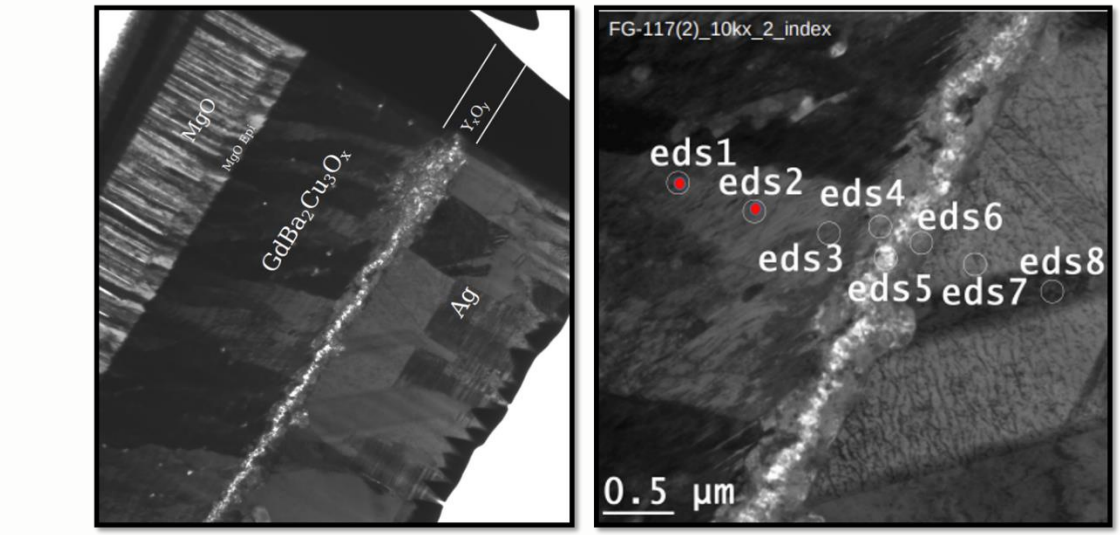

*Figure 5.29: TEM cross-section analysis of a Yttria-CFD sample **after** the oxygenation process. (a) Overall cross-section view of the layers Ag/Y_2O_3/GdBCO/MgO. (b) EDS points in the Ag/Y_2O_3/GdBCO layers responsible for the CFD.*

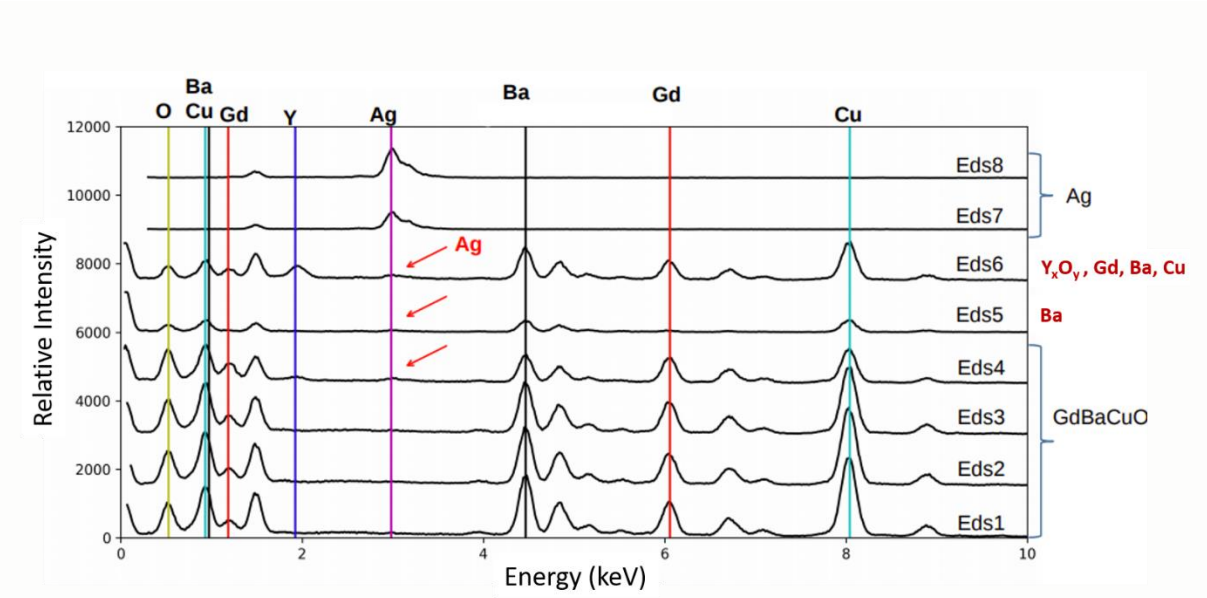

*Figure 5.30: EDX spectra for 8 points across the Ag/Y_2O_3/GdBCO layers **after** the oxygen annealing (sample #2).*

This TEM result revealed a silver diffusion mechanism from the tape's metallic shunt through the Y_2O_3 all the way to the GdBCO during the oxygenation/annealing process. A preliminary conclusion would be that the yttria layer is not stable during the oxygen annealing, allowing a substantial amount of silver to diffuse and thus creating a low interfacial resistance with the GdBCO layer, which destroys the CFD effect.

5.3.2 Evaluating the Yttria-CFD Insulation via ECR Measurements

The previous TEM images revealed a clear structural instability of the yttria layer during the thermal treatment required for the oxygen loading of the GdBCO film. The change in morphology allowed silver to cross the yttria barrier and compromised the high interfacial resistance HTS/silver needed for the CFD effect. However, the exact temperature for this phenomenon to occur was unknown. Samples oxygenated with the High-Low temperature profile were exposed to a maximum of 650 °C. If the amorphous IJP yttria were stable for temperatures below 650 °C, oxygenation after silver sputtering could still be accomplished in a practical timeframe by simply creating a new temperature profile at low temperatures. In order to identify the temperature range where silver breaches through the yttria insulation, a simple ECR experiment was assembled.

As a reference sample, a 12x12 mm piece of bare GdBCO tape was assembled in the ERC measurements setup and exposed to a sequence of 5 temperature dwells as shown by the solid red line of Figure 5.31. The objective of this experiment was to track the resistance of the sample going up and down in temperature dwells (from 400 - 600 °C and down to 400 °C) to assure the reversibility of the GdBCO resistive state for a constant 1 bar of oxygen pressure. Looking at the black curve of Figure 5.31, we confirm that the final resistance values at 400 and 500 °C, before and after the 600 °C dwell are the same.

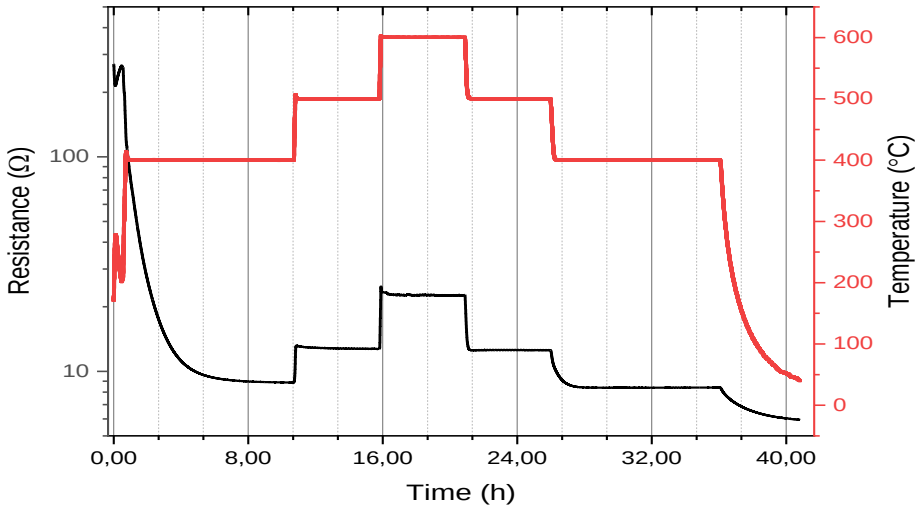

Figure 5.31: ECR In-situ resistance measurements for GdBCO reference samples (no Ag and no Yttria) during oxygen annealing at different temperature dwells.

For the actual insulation test, a 12x12 mm sample piece was cut from 1-meter batch of pyrolyzed IJP-yttria tape without silver coating. The sample was then mounted onto the *in-situ* resistance measurements setup with four silver wires bonded to the sample's surface in a specific pattern as shown in Figure 5.32: One voltage contact (V-) and one current contact (I-) were positioned on top of the GdBCO; the other two contacts, V+ and I+ were positioned on top of the yttria layer. Due to the yttria's high resistance path in the way of the current, this configuration should measure high resistance values (> 100 kΩ), unless the silver pad made with Ag-ink at the end of the silver wires diffuses through the yttria insulation in a thermal driven effect during the annealing. After mounting the wires, the sample was annealed in an atmosphere of 1 bar of oxygen with the temperature profile depicted by the red line in Figure 5.33.

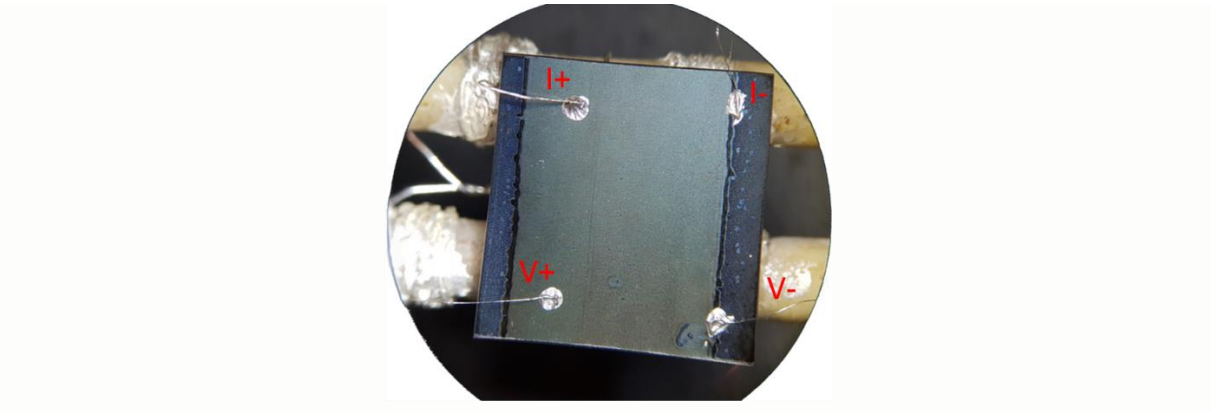

Figure 5.32: Yttria-CFD sample of 12x12 mm bonded with four silver wires for ECR measurements.

At room temperature, the yttria insulates with a resistance above 100 kΩ. However, the resistance drops sharply two orders of magnitude as temperature increases to the first 400 °C dwell. Nonetheless, the actual critical drop in resistance only happens after the 500 °C dwell. The resistance drops below 100 Ω and continuously decays until the 600 °C dwell. Once the temperature stabilizes at 600 °C the resistance also stabilizes, indicating a connection with the GdBCO layer. This conclusion is reinforced by comparing the resistance during the 600 °C dwells, before and after the 650 °C dwell. The resistance, in both 600 °C dwells, stabilizes at the same values indicating oxygen loading saturation of the GdBCO. After the 650 °C dwell, the remaining temperature dwells represent the resistance readings coming purely from the GdBCO. The silver is completely "short-circuited" through the yttria layer with the GdBCO.

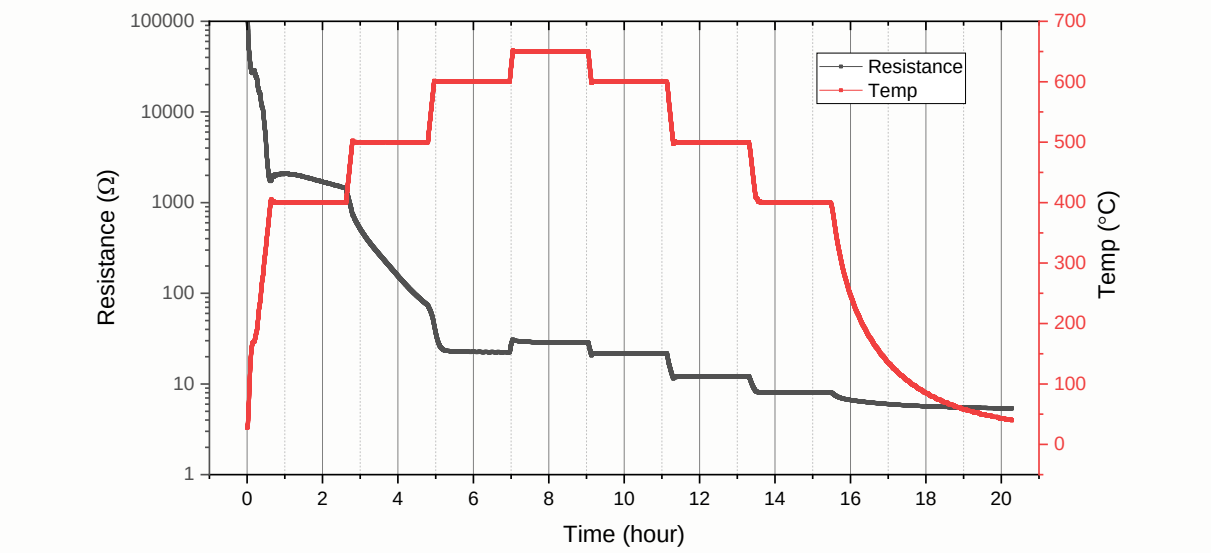

Figure 5.33: ECR In-situ resistance measurements of the amorphous yttria layer on top of a 12x12 mm GdBCO/MgO/Hastelloy tape sample during oxygen annealing at different temperature dwells.

SEM images of the yttria surface before (Figure 5.34(a)) and after (Figure 5.34(b)) being exposed to the temperature profile shown Figure 5.33 confirms the yttria's morphology change from a dense amorphous phase to a discontinuous sparse crystalline structure.

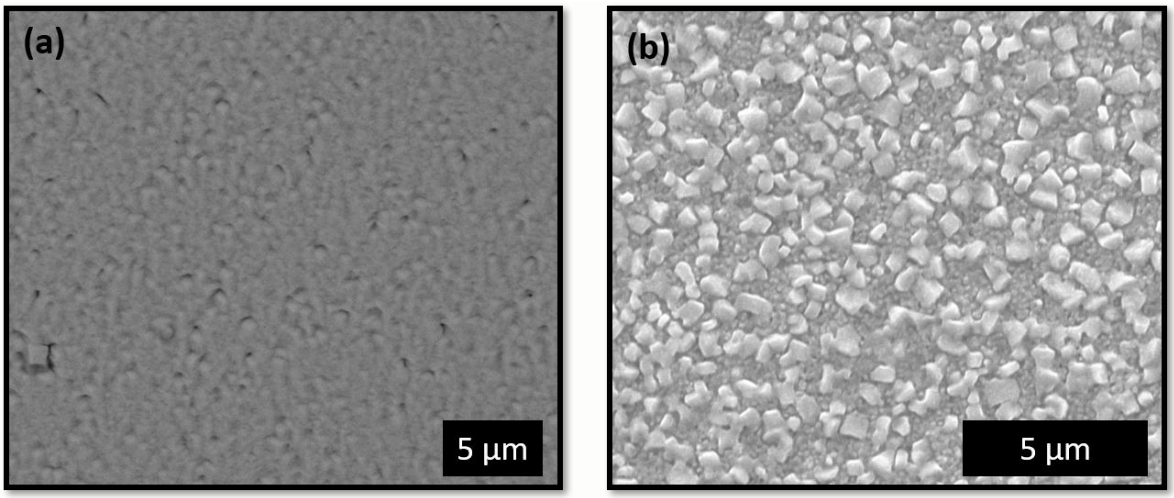

Figure 5.34: (a) Dense amorphous yttria layer on top of the GdBCO after pyrolysis at 450 °C. (b) Spare crystalline formation on top of the GdBCO substrate after ECR in-situ resistance measurements reaching 600 °C.

An X-ray diffraction analysis of the sample after the heat treatment shown in Figure 5.33 (red curve) confirms the formation of crystalline body-centered cubic yttrium oxide on top of the GdBCO layer. In Figure 5.35, we find the crystalline epitaxial phases (003), (004), (005), (006) and (007) for the GdBCO structure plus an inclined MgO (200) epitaxial phase [265]. The characteristic peaks (111) and (200) of the γ-phase nickel alloy (Hastelloy) with face-centered cubic (fcc) crystal structure from the substrate were clearly detected [266]. As mentioned before, the presence of polycrystalline yttria was confirmed by the (400) and (222) peaks at 2θ= 29.15° and 33.8° respectively (JCPDS card number 41-1105). This result is in accordance with a previous SUMAN study [267] where the onset crystallization of yttrium acetate was observed to take place between 520 - 550 °C being nearly completed at 580 °C.

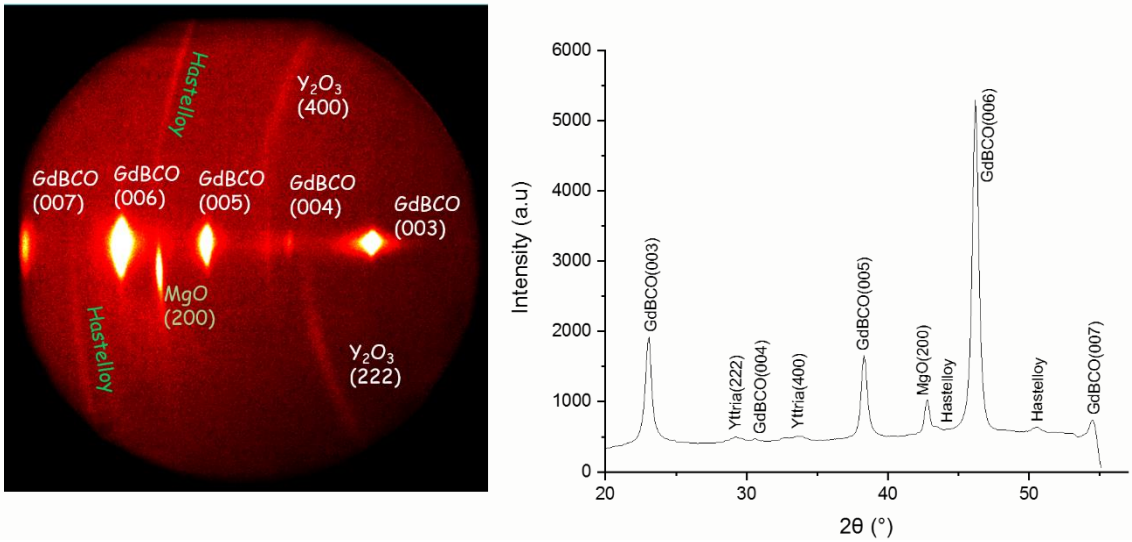

Figure 5.35: X-ray diffraction pattern taken with GADDS using Cu-αK radiation for a Yttria-CFD sample without silver coating after being annealed in oxygen atmosphere. (a) GADDS XRD pattern; (b) integrated θ - 2θ XRD pattern of the film.

Based on the ERC *in-situ* resistance measurements and the XRD spectra, it was concluded that the IJP yttria layer is unable to electrically insulate the silver after its phase transition from amorphous to crystalline. In order to maintain the continuity of the yttria in the amorphous phase during oxygenation, a practical upper limit temperature of 500 °C was stipulated.

5.3.3 Saturation Times for GdBCO Covered with Yttria

The compromise of the Yttria-CFD layer during oxygenation at temperatures above 500 °C created the need for a new temperature profile capable of oxygenating the GdBCO layer and annealing the silver without jeopardizing the high interfacial resistance Ag/Y_2O_3/GdBCO. Still, previous preliminary oxygenation attempts on yttria-CFD tapes (subsection 5.1.1) had shown that the yttria's presence could significantly change the final oxygen content by slowing down the diffusion process if the thickness was kept thick ($\geq$ 400 nm). In an effort to verify the possibility of oxygenating the GdBCO with IJP-yttria under 500 °C, the oxygen saturation times at different temperatures were taken via ECR in *in-situ* resistance measurements following the same procedures described in section 3.3.2 for a 12x12 mm sample with IJP yttria-CFD. The result was then compared to the bare GdBCO sample (without silver and without CFD). Figure 5.36 shows the disposition of the silver wires on the surface of the sample ink jet printed with 115 nm of yttria and pyrolyzed at 450 °C (no silver coating added).

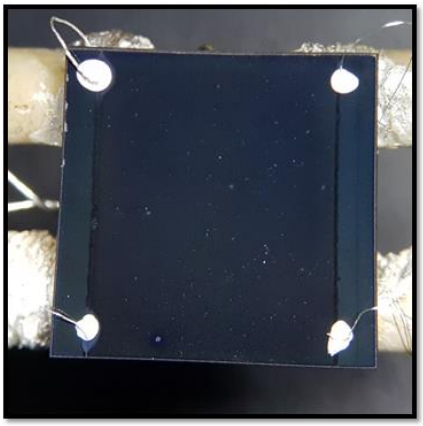

Figure 5.36: (a) 12x12 mm yttria-CFD sample mounted onto the ECR set-up without silver coating.

In Figure 5.37, we see the time constant τ dependence with the temperature for the in- and out-diffusion process for two samples: the bare GdBCO control sample and a GdBCO sample with 115 nm of yttria. In both samples, the time to equilibrate the sample's resistance increases exponentially with decreasing temperature, as expected for a thermally activated process. For the bare GdBCO sample the effective time constant τ_{eff}^{in} goes from 0.01 to 2 hours in the temperature range of 350 °C to 500 °C and in the case of the GdBCO with 115 nm of yttria, it increases from 0.2 to 8 hours in the same temperature range. Therefore, we observe an increase of one order of magnitude in τ_{eff}^{in} due to the addition of 115 nm of an amorphous yttria layer.

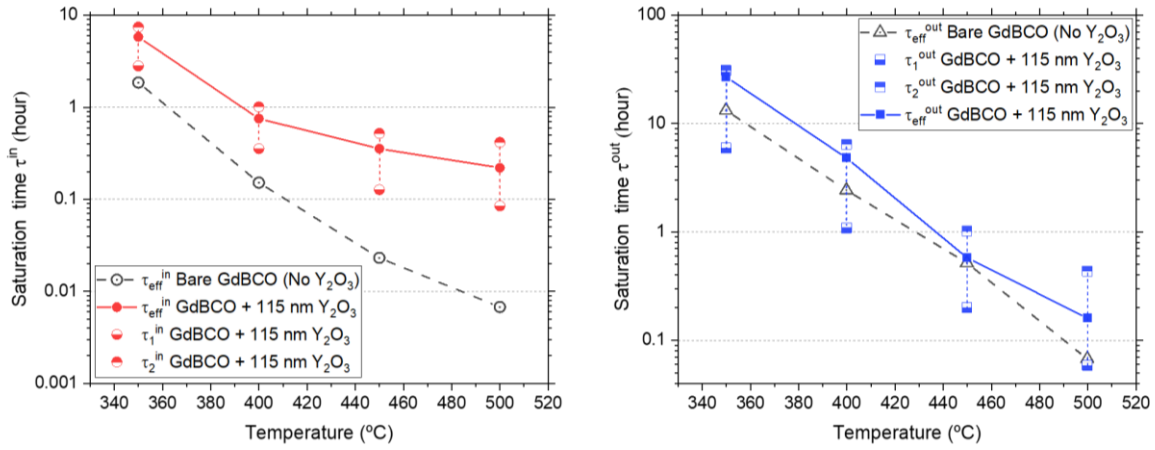

Figure 5.37: (a) Comparative analysis of saturation times for 115 nm yttria-CFD sample and a bare sample in oxidising enviroment; (b) Temperature dependence of τ for reducing (out) atmosphere.

Considering the overall loading time to reach the equilibrium concentration of oxygen in the film $t_{eq} = 4 \times \tau$, it would be expected a minimum time of 36 hours for an optimum GdBCO doping at 350 °C in the presence of 115 nm of yttria. This requirement, although initially unattractive from an industrial point of view, seems to indicate a feasible time for in-diffusion of oxygen in the yttria-CFD structure. However, when we evaluate these oxygenation times in long samples (> 10 cm), small variations (< 100 nm) in the yttria thickness seem to have a great impact in the homogeneity of the oxygen loading. The effect of these variations on the final oxygen content of the GdBCO after the oxygen annealing is better visualized with the SHPM map of Figure 5.38. A 110x12 mm tape sample was cut from the same IJP-yttria-CFD batch used in the ECR study, sputtered with 1 µm of silver and subsequent annealed in 1 bar of oxygen atmosphere at 450 °C for 10 hours with a ramp up of 10 °C/min and a cool down ramp of 1.5 °C/min. According to the saturation time curves of Figure 5.37, 10 hours at 450 °C should be more than enough for the GdBCO to reach oxygen equilibrium throughout the full length of the sample with a yttria coating of 115 nm. However, the final B_z distribution reveals a clear inhomogeneity of the superconducting properties across the width of the tape (x-axis). In addition, the effect of using a unidirectional oxygen flux of 0.03 L/min was once more seen in the B_z distribution across the length (y-axis) in Figure 5.38.

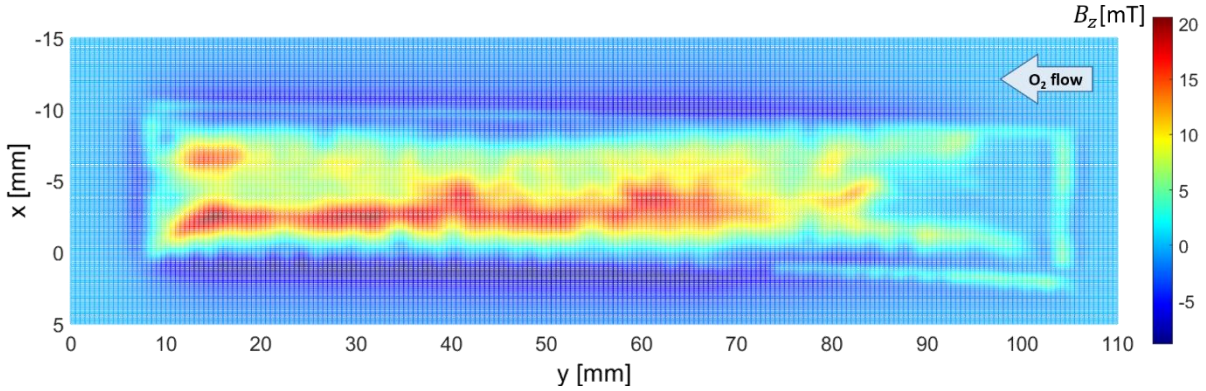

Figure 5.38: Perpendicular trapped field B_z measured by SHPM at 77 K for a 110 x 12 mm GdBCO tape sample coated with 115 nm thick Yttria-CFD and 1 µm thick silver shunt/stabilizer. Sample was oxygenated in a tubular furnace at 450 °C for 10 hours with a low unidirectional oxygen flow of 0.03 L/min.

The interference of the amorphous yttria layer in the oxygen loading was reassured by re-annealing the sample shown in Figure 5.38 with the High-Low temperature profile from subsection 5.1.4 in a bidirectional oxygen flow (subsection 5.1.3). Figure 5.39 shows the B_z distribution after the second annealing treatment revealing a substantial improvement of the B_z amplitude and homogeneity. After this test, it became clear that the positive effect of annealing at high temperatures (> 500 °C) was linked to the yttria layer coarsening during the crystallization thus creating a path for silver diffusion and oxygen in-diffusion.

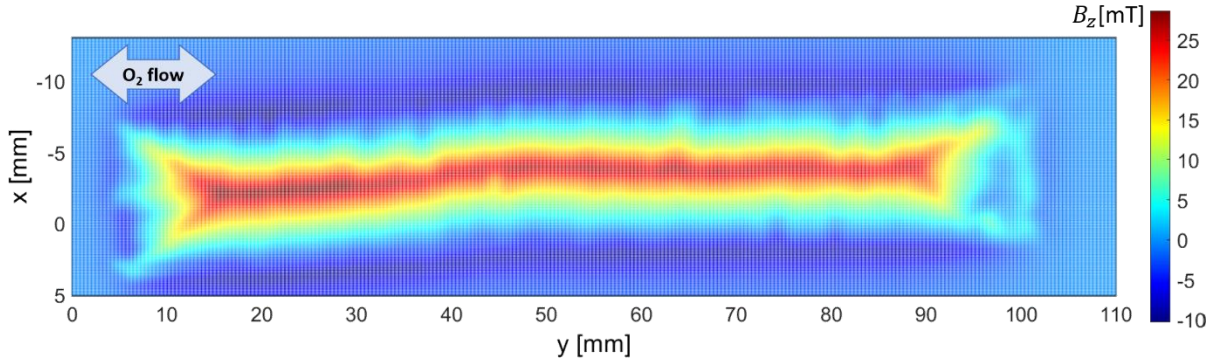

Figure 5.39: Perpendicular trapped field B_z measured by Scanning Hall Probe Microscopy (SHPM or Hall-scan) at 77 K for a 110 x 12 mm GdBCO tape sample coated with 115 nm thick Yttria-CFD and 1 µm thick silver shunt/stabilizer. Sample from Figure 5.38 was re-oxygenated in with the High-Low temperature profile with a low bidirectional oxygen flow of 0.03 L/min. One can notice a misalignment of the sample's width (x-axis) in the range 10 to 40 mm along the y-axis. This distortion in the position of the sample was caused by a small change in the position of the sample during the Hall-scan.

In another oxygenation attempt, a 110x12 mm sample deposited with 91 nm of yttria, was annealed for 48 h at 450 °C in 1 bar of oxygen atmosphere. By considerably extending the annealing time and decreasing the yttria thickness we achieved a better continuous distribution of B_z along the length (y-axis) as shown in the SHPM map of Figure 5.40. Still, the homogeneity of this specific sample along the width (x-axis) was unsatisfactory for performing transport current tests.

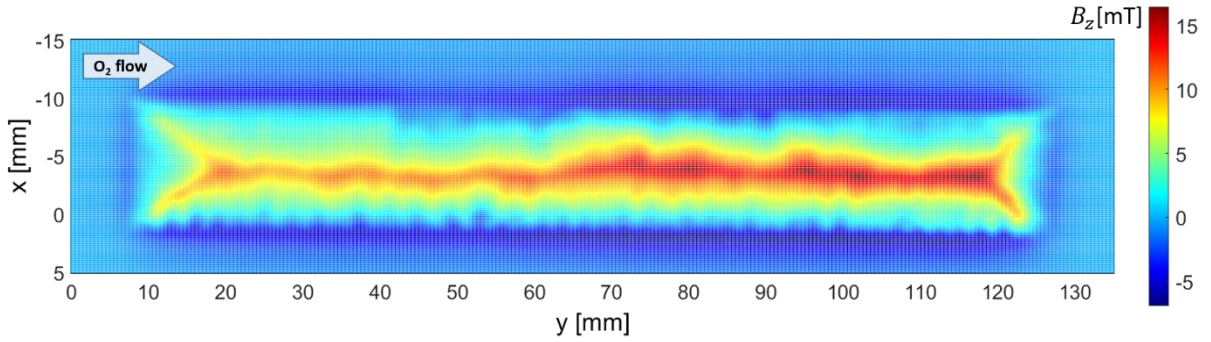

Figure 5.40: Perpendicular trapped field B_z measured by SHPM for a 110 x 12 mm tape sample coated with 91 nm Yttria-CFD and 1 µm silver. Sample was oxygenated in a tubular furnace at 450 °C for 48 hours with a low oxygen flow of 0.03 L/min.

Among many temperature profiles attempts to homogeneously load oxygen across long (> 10 cm) length Yttria-CFD samples while maintaining the yttria in the dense amorphous phase, only one temperature profile gave satisfactory results. The result is shown in Figure 5.41. The sample was cut from a GdBCO tape batch deposited with an average 136 nm of yttria and sputtered with 1 µm of silver. Afterwards, the sample was annealed for 48 hours at 500 °C in 1 bar of oxygen atmosphere with a 10 °C/min ramp up and a cool down ramp to room temperature of 3 days. The oxygen flux was set

to 0.03 L/min flux with a change in flux direction after every 24 h. Due to an excessive amount of time needed in this process, only one specimen was produced.

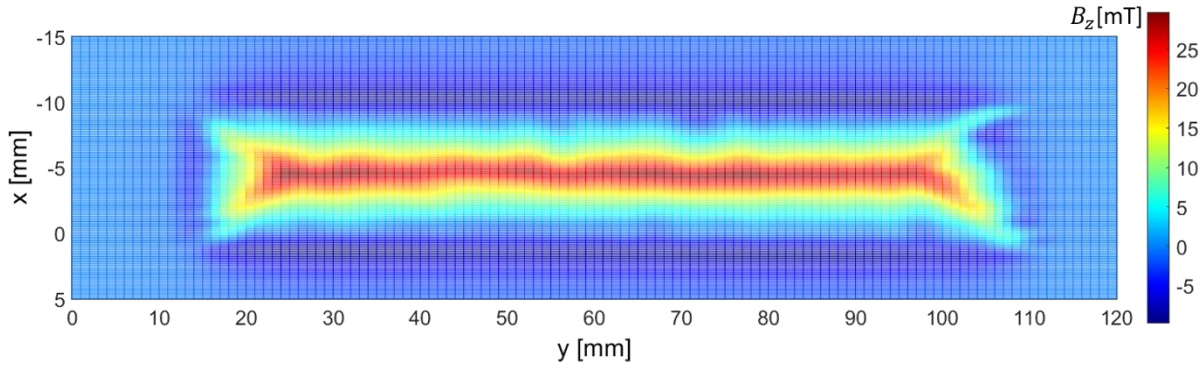

Figure 5.41: Perpendicular trapped field B_z measured by Scanning Hall Probe Microscopy (SHPM or Hall-scan) for a 95 x 12 mm GdBCO tape sample coated with 136 nm of Yttria-CFD and 1 µm silver. The sample was oxygenated in a tubular furnace at 500 °C for 48 hours and cooled down to room temperature in 5 days in 1 bar of low oxygen flow of 0.01 L/min.

5.4 CFD with Stable Amorphous Yttria

In the previous section, a new annealing temperature profile was developed to avoid the crystallization of the yttria layer during the oxygenation of the GdBCO film. Utilizing this new process, a 10 cm Yttria-CFD tape was conceived with an acceptable level of current density distribution for transport current tests (Figure 5.41). In this section, we show the NZPV measurements performed at ICMAB for this sample and the evaluation of the GdBCO film after the tests.

5.4.1 NZPV Measurements of Stable Yttria-CFD

Figure 5.42 shows the sample from Figure 5.41 mounted onto the sample holder described in subsection 3.4.1, without the current contacts. To collect the electrical and thermal information during the tests, the sample was mounted with 7 thermocouples and one pair of voltage taps spaced 4.7 cm in between. Before cooling the system with liquid nitrogen, the I-V curve of the sample at room temperature was taken to verify the tape's resistance at room temperature.

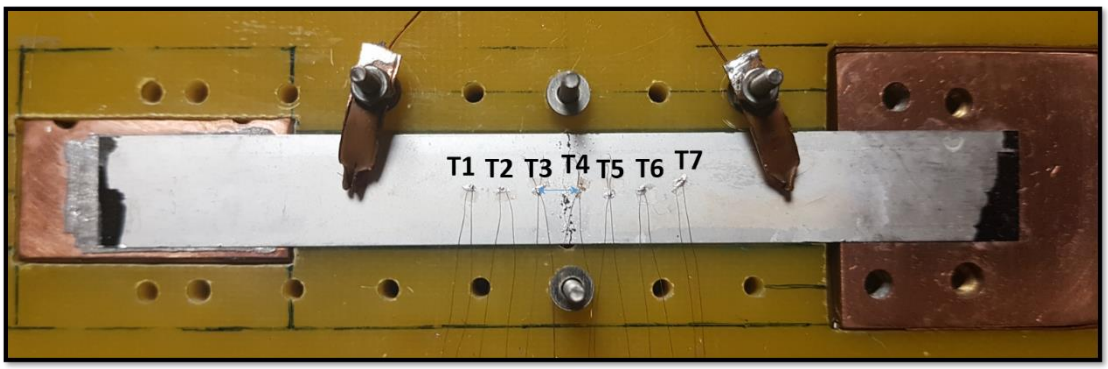

Figure 5.42: Yttria-CFD sample onto ICMAB's sample holder for transport current tests. Sample was mounted with 1 pair of voltage taps and 7 thermocouples for quench monitoring.

After verifying the room temperature resistance at 5.2 mΩ/cm, the system was cooled with liquid nitrogen and the I-V curve for the sample was measured in transport current to determine the I_c in self-field (Figure 5.43). The curve was taken by applying current pulses of 30 ms duration. Utilizing the Power Law and considering the critical electric field 1 µm/cm, the natural I_c was estimated at 389 A with a n-value of 24.3.

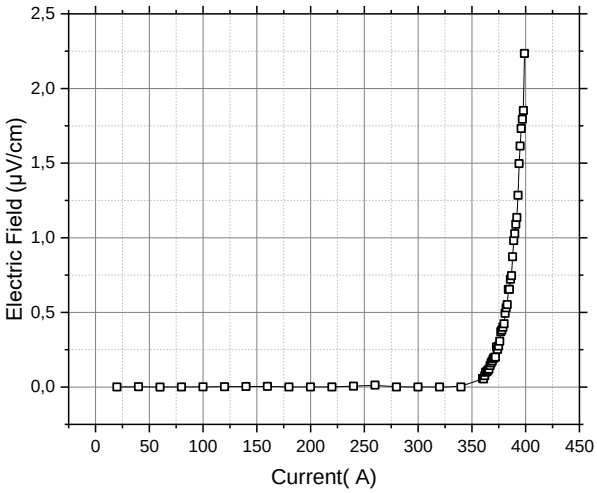

Figure 5.43: Sample I-V curve for the extraction of the critical current.

Once the tape's initial I_c was determined as reference, a NdFeB magnet was positioned on the center of the of tape to lower the I_c locally and create the condition for the hot-spot regime. The artificial I_c value in the presence of the magnet was not directly measured, but inferred with current pulses of 30 ms with lower amplitudes. Since no quench was detected up until 360 A an artificial I_c drop between 360 and 389 A was assumed. The sample quenched during the last current pulse with a 370 A amplitude. The global voltage and the temperature values during the quench are shown in Figure 5.44(a) and Figure 5.44(b) respectively.

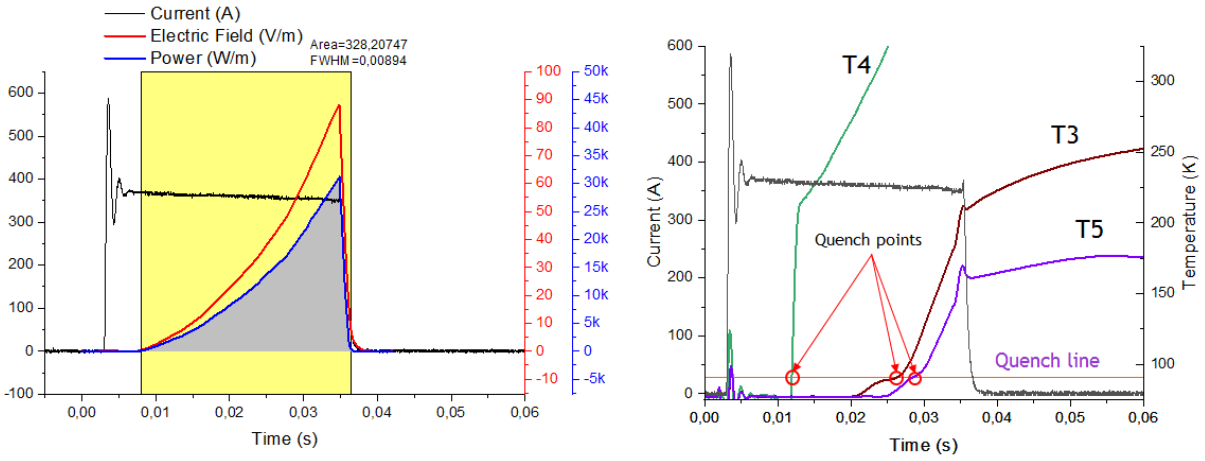

Figure 5.44: Analysis of a quench in hot-spot regime with constant current of 370 A and 30 ms dwell for a Yttria-CFD tape sample of 95 x 12 mm.(a) Global Electric field (V/m), Current (A) and Power density (W/m) signals for sample during the current pulse. (b) Thermocouple readings for the sample current pulse.

In Figure 5.44(a), an analysis of the evolution of the electric field (blue curve) across the 4.7 cm voltage taps indicates an absence of the CFD effect. The current pulse (black curve) starts at t=3 ms, stabilizes

in 370 A at t=7 ms and drops down to zero at t=35 ms. The beginning of the quench is considered to take place when the sample's electric field reaches 10 V/m at t=15 ms. The field "slowly" increases in a ramp reaching a maximum of 89 V/m in the end of the current pulse at t=35 ms. This profile of electric field is the same observed in THEVA tapes with uniform low interfacial resistance as mentioned in subsection 4.4.3; it indicates a slow propagation of the normal zone once the hot-spot region is created.

Figure 5.44(b) reinforces the initial conclusion taken from Figure 5.44(a) by showing the temperature evolution of the thermocouples across the tape's length. Only thermocouples T3, T4 and T5 showed significant temperature increase for the NZPV analysis. T4 was positioned in the middle of the sample together with the magnet. Naturally, T4 probe had the sharpest temperature rise surpassing 300 K at t=25 ms and reached the critical temperature of 92 K at t=12 ms. After 300 K, the T4 probe physically detached from the sample and readings were lost. The two adjacent probes T3 and T5, reached 92 K at t=26.5 ms and 29 ms respectively, never surpassing 250 K. Taking the average NZPV from T4 to T3 and T4 to T5 we find an overall NZPV of 25 cm/s at 370 A. Looking back at Figure 3.38, this NZPV value is in the same range of a tape with uniform low interfacial resistance.

5.4.2 Analysis of *Post-Mortem* Yttria-CFD Sample

After the first NZPV test, the I_c of the sample studied in the previous subsection dropped to zero indicating a full local degradation of the superconducting properties. The degraded zone in center of the tape was easily spotted by performing a Hall-scan at 77 K to analyze the B_z map of the sample as shown in Figure 5.45.

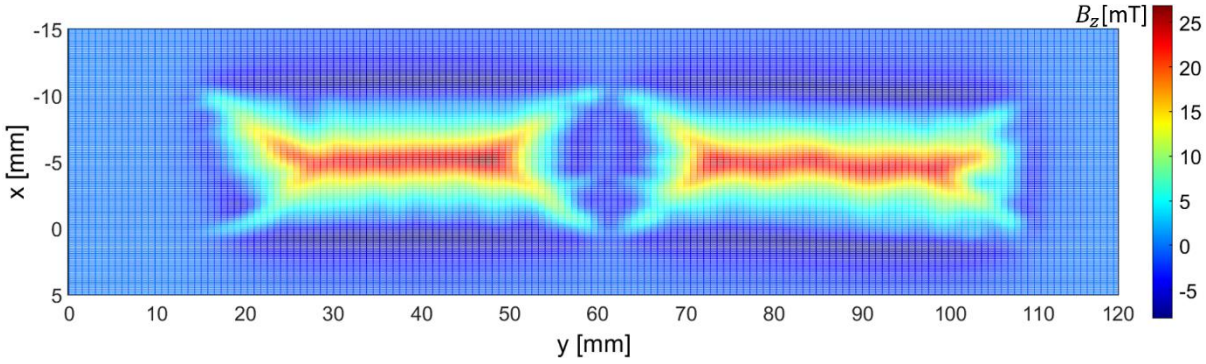

Figure 5.45: Perpendicular trapped field B_z measured at by Scanning Hall Probe Microscopy (SHPM or Hall-scan) at 77 K for the Yttria-CFD sample shown in Figure 5.42 after one DC current pulse of 360 A for 30 ms.

This local degradation can be better explained if we correct the electric field for a voltage distribution just in the quenched region of 10 mm between T3 and T5. Integrating the power density curve (blue curve) in Figure 5.44(a) and multiplying by the length 4.7 cm, indicates a total heat dissipation of 15.42 Joules. Considering the thermal capacity c_p (J/cm^3-K) of the THEVA tape in Appendix A and 10 mm of the quenched region in an adiabatic process, this would imply a ΔT of more than 1000 °C. This ΔT calculation although not precise, is easily translated to the damage visually observed onto the silver layer and the degradation seen with the Hall-scan located in the middle of the tape. Given the

slow NZPV value found for this sample and the total energy dissipated during the quench, this was an expected damage.

In order to identify the source of the low interfacial resistance slowing the NZPV, the CFD interface was analyzed with SEM-FIB imaging for a cross-sectional cut of 5x1 µm onto the sample. Figure 5.46(a) shows the secondary electron image of the Ag/Y_2O_3/GdBCO layers indicating the presence of a compact yttria layer separating the silver and the GdBCO. In the backscattered image of Figure 5.46 (b), we can notice small variations on the yttria's thickness along the 5 µm cut, but no significant diffusion of silver to the GdBCO could be confirmed from these images. In this scenario, the only plausible path for the silver to short-circuit through the yttria would be the conductive GdBCO outgrowth peaks discussed in chapter 4. Still, theoretically, if this were the case, a minor increase in the NZPV should have been observed.

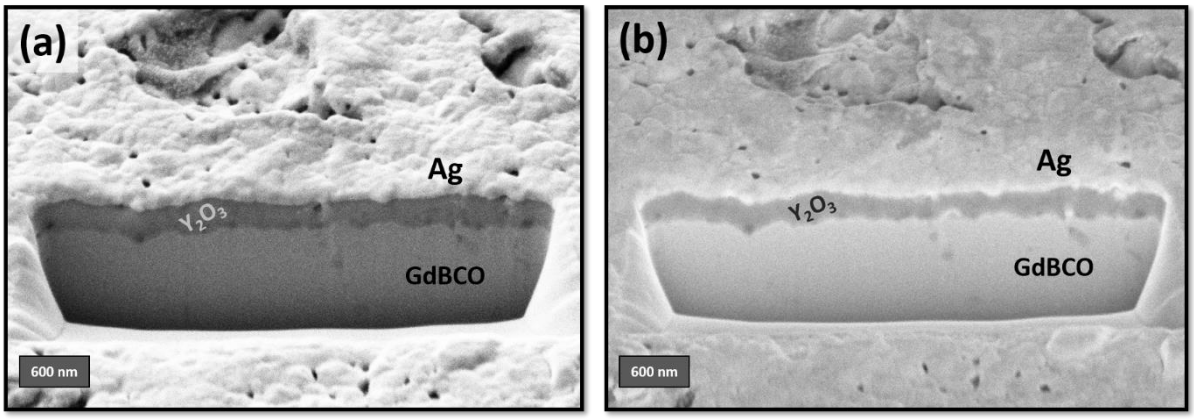

Figure 5.46: SEM-FIB cross section image of Yttria-CFD region on sample from Figure 5.45. (a) Secondary Electrons (SE) image; (b) Backscattered Electrons (BSE) image.

5.4.3 AFM of the Stable Yttria Layer

Following the results of the previous subsection surrounding the unknown origins of the silver short-circuit, we recall here the ERC measurements shown in Figure 5.33. As discussed previously, the sharp drop in resistance after 500 °C indicates how the yttria ceases to insulate due to coursing during crystallization. Nevertheless, in the same 2-hour dwell at 500 °C it is also noticeable that the resistance dropped from 1000 Ω to 70 Ω indicating the formation of an electrical path through the amorphous phase. Considering such decay rate of resistance, the 48 hours annealing at 500 °C for the sample shown in Figure 5.41 probably led to a direct contact of silver with the GdBCO. However, if this electrical path existed solely due to the presence of outgrowth peaks, the interfacial resistance should have stayed in the 10^{-5} Ω-cm^2 range and the sample would have shown a small detectable increase in the NZPV (subsection 5.4.1). The presence of the peaks does not fully explain the absence of a high interfacial resistance leading to a slow NZPV in the presence of a solid amorphous yttria layer.

In order to confirm the presence of a second electrical path for the silver, a 6x12 mm sample piece of Y_2O_3/GdBCO/MgO/Hastelloy tape was especially prepared for c-AFM measurements. The sample was taken from a IJP yttria-CFD batch deposited with ~200 nm of yttria. One 50 nm thick silver pad was sputtered on to the yttria region covering approximately 50% of the yttria's surface (Figure 5.47). After

sputtering, two droplets of Ag-ink were added to the yttria-free edges of the GdBCO layer. The sample was then annealed for 5 hours at 500 °C in 1 bar of oxygen atmosphere allowing the silver to diffuse and wet the surface of the yttria. Finally, the sample was mounted onto a conductive metallic disc for c-AFM measurements as shown in Figure 5.47. To complete the c-AFM circuit for the conductive AFM tip, the two silver droplets on the exposed GdBCO edges were used to ground the sample to the metallic disc using silver wires.

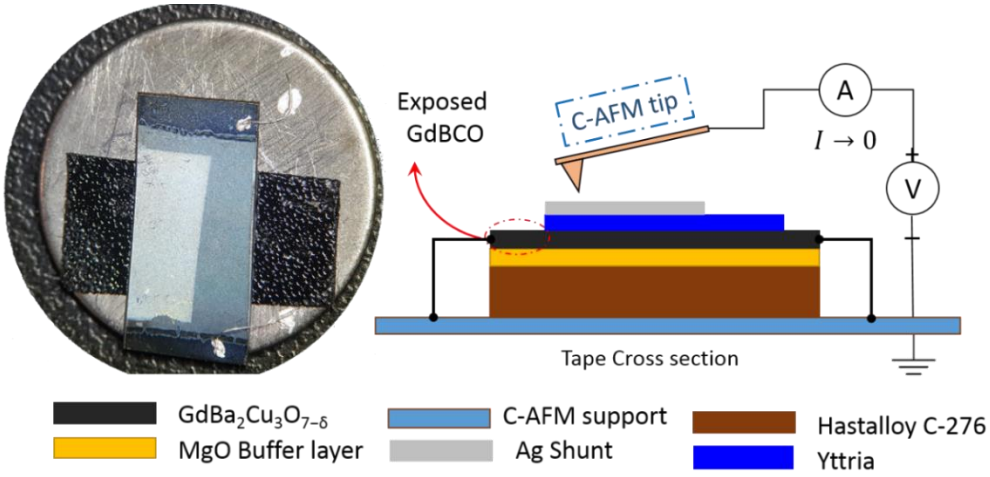

Figure 5.47: Schematic drawing of the conductive Atomic Force Microscopy (c-AFM) preparation of a small 5x12 mm Yttria-CFD tape sample partially coated with 50 nm of Ag. The yttria-free edges of the GdBCO film were ground to the metallic disc to transport the current.

Figure 5.48(a) shows the topography for a 5x5 µm scan on top of the sputtered silver pad and Figure 5.48(b) shows the conductivity readings for the same scan for a bias voltage of 1.2 V. The bright zones in Figure 5.48(b) correspond to areas with high conductivity and the dark zones with low conductivity. It is noticeable how the analyzed area is dominated with high conductivity zones that reach values up to 400 µA, almost 5 orders of magnitude higher than the dark zones. Moreover, when overlapping the conductivity and topography maps, we find a correspondence between elevated zones and low conductivity zones. These seem to be same regions where silver is less visible after the annealing. In addition, given that the conductivity distribution of Figure 5.48(b) does not match the expected topography for the GdBCO peaks, this result strongly suggests that the peaks are not the only electrical path contributing to the low interfacial resistance in the yttria-CFD. One assumption would be the presence of a subtle inter-layer diffusion of silver happening through the amorphous yttria. This diffusion, although significant to the CFD interface, was undetectable to the FIB cross-section analysis shown in the previous section.

Understanding all the nuances of the silver diffusion mechanism on top of the yttria layer was a study out of the scope of this thesis. From a practical point of view, the slow NZPV value and the c-AFM results directly lead to another crucial temperature constraint in the fabrication process of the CFD: In the presence of a silver layer, the amorphous yttria is unable to maintain a high interfacial resistance after being oxygen annealed at 500 °C due to silver diffusion.

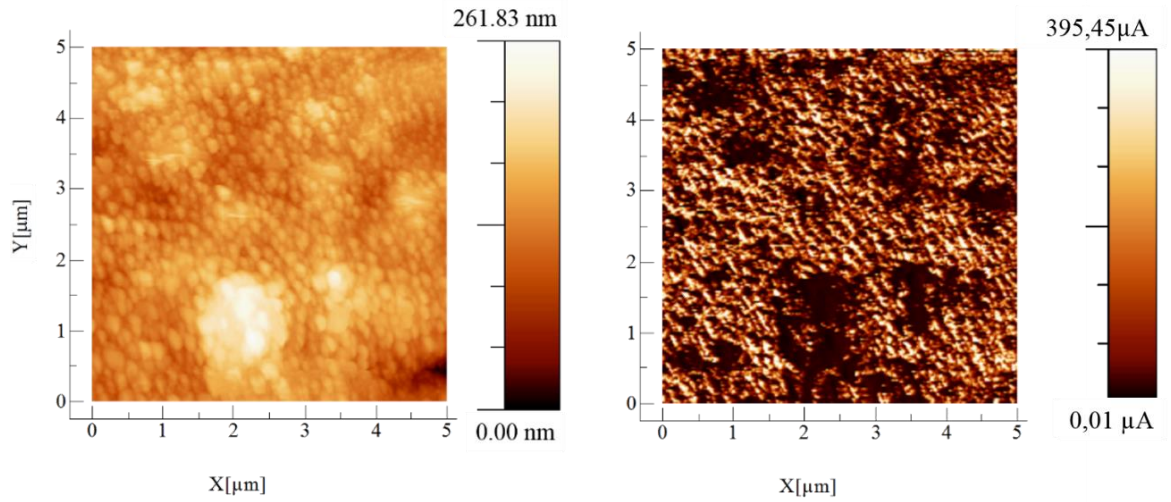

Figure 5.48: Conductive Atomic force microscopy (c-AFM) measurements for a small 5x12 mm Yttria-CFD sample partially coated with 50 nm of Ag. (a) Topography image of the 5x5 µm scan; (b) conductivity reading for the 5x5 µm scan.

5.5 Second Yttria-CFD Manufacturing Route

The aforementioned 500 °C restriction in the temperature profile of the oxygen annealing completely hinders the possibility of loading oxygen in the HTS layer in the presence of a thin yttria layer. As seen in subsection 5.3.3, annealing below 500 °C would imply impractical saturation times for the in-diffusion of oxygen. Therefore, the deposition of yttria was relocated in the steps of the standard 2G HTS CC manufacturing process to complete the CFD architecture.

This section reports on the experiments revolving a 2nd Yttria-CFD route where the HTS layer is oxygenated previously to the IJP yttria deposition. The suggested manufacturing process for this second *pre-oxygenation* route is shown in Figure 5.49.

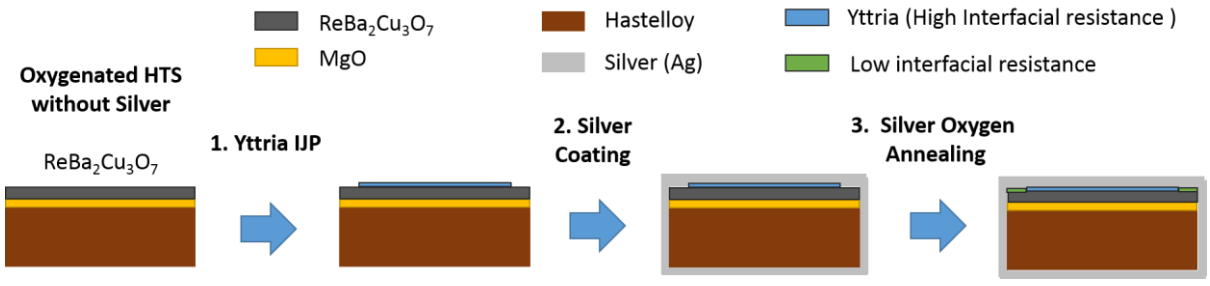

Figure 5.49: Second manufacturing workflow route for Yttria-CFD incorporation into 2G HTS CC. Step 1: Yttria Ink Jet Printing or spin coating onto the ReBCO layer. Step 2: Silver coating (sputtering or evaporation) to form the shunt layer. Step 3: Silver annealing in oxygen atmosphere to create the low contact resistance along the edges of the tape.

5.5.1 2nd Yttria-CFD Route Impact on the Final I_c

The second Yttria route, although simpler, creates new technical considerations for the thermal treatments used in the manufacturing steps. For instance, since the tape is oxygenated previously to the yttria IJP deposition, the pyrolysis temperature of the Y-ink has to be reconsidered to avoid the risk of significantly reducing the oxygen content in the REBCO film. This risk was evaluated by using the Hall-scan to compare the B_z distribution, before and after yttria deposition, for three 12x50 mm samples pyrolyzed and silver annealed at different temperatures: 350 °C, 400 °C and 450 °C. All samples were THEVA bare tapes consisting of GdBCO/MgO/Hastelloy oxygenated without silver at ICMAB. In Figure 5.50, we show an example of the comparative B_z analysis before (a) and after (b) for the sample with yttria pyrolyzed at 400 °C for 3 hours. After pyrolysis, the average field (and I_c) dropped more than 50%, and amplitude variations (inhomogeneity) increased to 15%. The pyrolysis results for all samples are shown in Table 5-4. As the pyrolysis temperature increases ,we observe not only a considerable drop in magnetization, but also an increase in the inhomogeneity along the length.

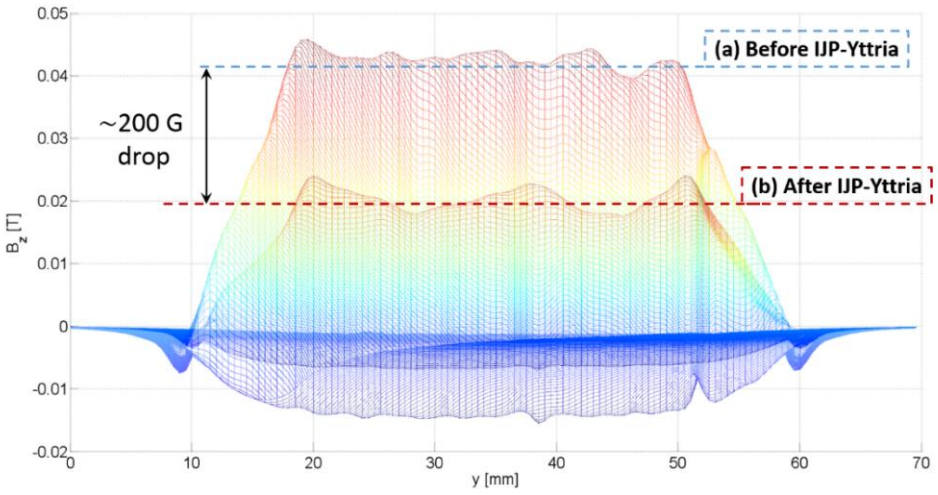

Figure 5.50: Longitudinal B_z distribution comparison of a 12x50 mm GdBCO THEVA tape, before (a) and after (b) spin-coating deposition of yttria with pyrolysis at 400 °C. Sample Before yttria was oxygenated without silver coating.

Looking at Figure 5.50 and the result columns “after pyrolysis” in Table 5-4, we can reach the premature conclusion that incorporating the yttria layer would create a tape with half of the initial critical current. In these conditions it becomes hard to advocate for the benefits of having a boosted NZPV given that half the original critical current would double the cost of an HTS CC used in an SFCL. However, in all samples, the subsequent silver deposition and oxygen annealing after pyrolysis significantly increased the magnetization values and reduced their inhomogeneity. This result can be seen in the last two columns (“after annealing”) of Table 5-4. The gains in the average magnetization after silver annealing seem to be more substantial for the temperatures 350 °C and 400 °C. In Figure 5.51, we show the highest magnetization recovery happening for the sample pyrolyzed and annealed at 400 °C for 3 hours.

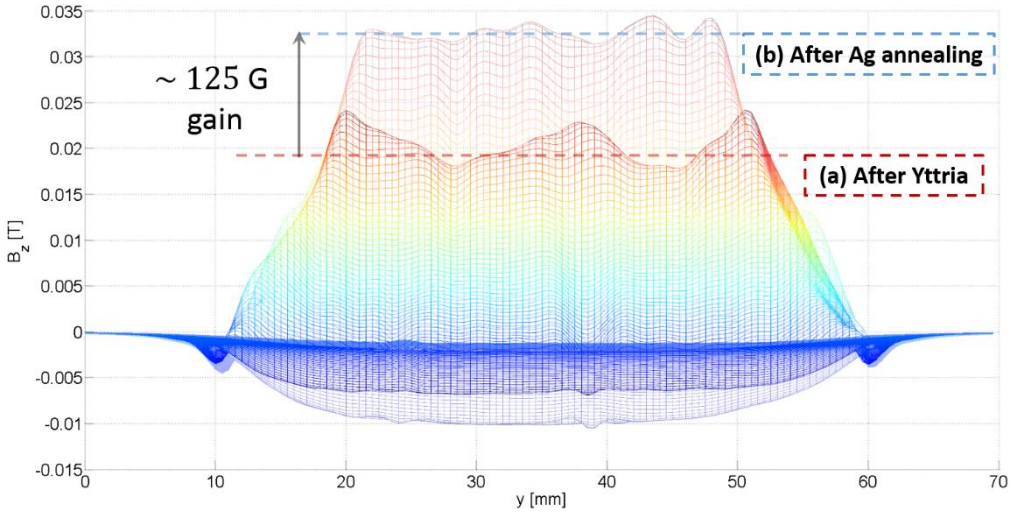

Figure 5.51: Longitudinal B_z distribution comparison of a 12x50 mm GdBCO THEVA tape, before (a) and after (b) silver sputtering and oxygen annealing at 400 °C. The sample was coated with 300 nm of silver before the oxygen annealing.

Obviously, annealing at higher temperatures reduces the oxygen content of the GdBCO crystal. Nevertheless, since pyrolysis and annealing were both executed with the same temperature profile, seeing the increase in magnetization after silver annealing illustrates how the silver plays a vital role in the oxygen in-diffusion of the HTS layer. We here speculate that the portion of diffused silver during annealing accelerates the in-diffusion of oxygen by creating conductive channels through the amorphous yttria.

Table 5-4: B_z distribution comparison of a three 12x50 mm GdBCO THEVA tape samples before and after yttria ink pyrolysis and silver annealing at three different temperatures: 350 °C, 400 °C and 450 °C. All samples were coated with 300 nm of silver before the oxygen annealing.

Virgin sample without Ag (before pyrolysis)		**Pyrolysis & Annealing**	**After Yttria-CFD pyrolysis**		**After Yttria-CFD, Ag sputtering and oxygen annealing**	
Avg. Field [mT]	I_c [A]	**[°C]**	Avg. Field [mT]	I_c [A]	Avg. Field [mT]	I_c [A]
41.2 ± 19	505 ± 29	**350**	19 ± 33	242 ± 49	30 ± 23	371 ± 23
42.1 ± 25	517 ± 35	**400**	20 ± 38	249 ± 53	32 ± 21	392 ± 29
41.8 ± 27	513 ± 37	**450**	21 ± 58	245 ± 79	29 ± 35	360 ± 49

Certainly, further reducing the pyrolysis/annealing temperature could help achieve a better I_c performance by securing the initial oxygen content of the GdBCO. However, processing the yttria below 350 °C could lead to an incomplete decomposition of the organic compound in the ink during pyrolysis. Furthermore, in the case of the silver annealing, it could lead to insufficient low values of interfacial resistance on the yttria-free edges of the tape. Therefore, we safely set the pyrolysis/annealing temperature at 400 °C expecting a 20% reduction in the original critical current.

5.5.2 CTL Measurements for 2nd Route of Yttria-CFD

To confirm the CFD effectiveness of the amorphous yttria thermally treated at 400 °C, the CTL of the sample shown in Figure 5.51 was measured by *FASTGRID* partners at EPM following the procedures described in section 3.4.2. The experimental data and the 2D potential distribution fit are shown in Figure 5.52(a). A straightforward look at the potential distribution across the width (y-axis) for different planes along the length in Figure 5.52(b) reveals the parabolic voltage distribution characteristic of the CFD architecture. Utilizing the fitting process described in [234], the best fitting for surface potential is found for the parameters shown in Table 5-5.

Table 5-5: Parameters used to fit the CTL experimental data with the semi-analytical model described in section 3.4.2. The experimental data was taken for a THEVA CC altered with the yttria-CFD architecture.

Parameters	Value
w	12 m
w_f	11 mm
d	1 µm
l_0	1 mm
R_f	0.1 Ω-cm^2
R_0	10 µΩ-cm^2
ΔV	200 µV

The parameters of Table 5-5 lead to a CTL of $\lambda = 3.14$ mm, which agrees with the CTL values found for CFD samples created by EPM [235]. Moreover, this fitting suggests that the interfacial resistance along the yttria CFD edges is far from the usual value of 10^{-7} Ω-cm^2 considered for CFD simulations, but seems to be coherent with the experimental measurements of J. Ekin for Ag/YBCO interfaces [73] annealed at 400 °C. Applying the formula $R_i \approx R_0/(1-f)$ from [206], the overall interfacial resistance R_i is estimated to be 10^{-4} Ω-cm^2. This value, as discussed in [72], is in the limit for maintaining a practical current contact size for tapes operating in continuous current transport above 500 A. This suggestes the need to anneal the final silver layer at temperatures above 400 °C to further reduce the interfacial resistance Ag/GdBCO.

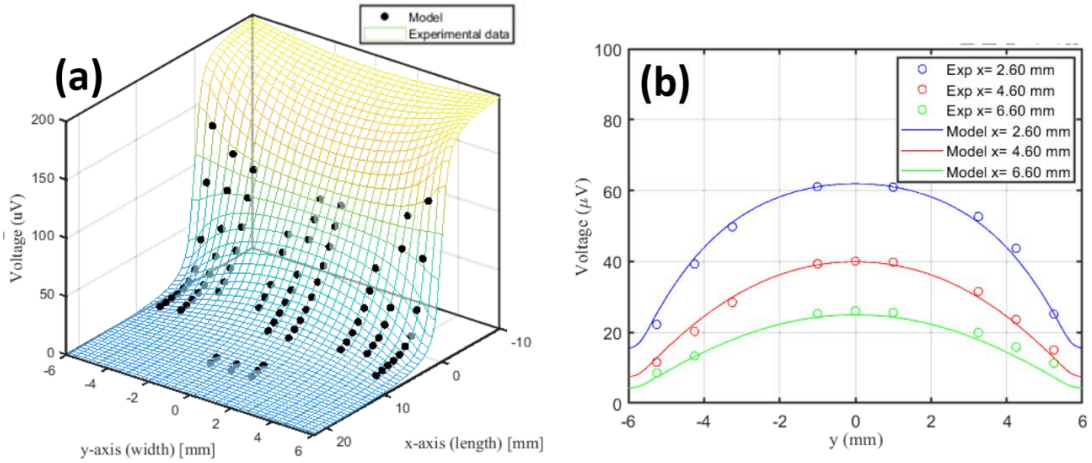

Figure 5.52: CTL measurements for a small 12x50 mm yttria-CFD sample at 77 K. (a) Experimental data and fitted semi analytical (SA) model for potential distribution on the surface of the sample. (b) Parabolic potential distribution along the width (y-axis) of the sample.

These CTL measurements confirmed the presence of the CFD signature behavior in a small (12x50 mm) pre-oxygenated Yttria-CFD sample with silver annealed at 400 °C. Since silver diffusion is less intense at lower temperatures, it is also reasonable to assume that the same CFD behavior would be found for other samples annealed at 350 °C.

5.5.3 NZPV Measurements for 2nd Route of Yttria-CFD

After confirming the presence of the CFD architecture via CTL measurements in the 2nd Yttria-CFD route, two long Yttria-CFD samples of 12x140 mm were manufactured at ICMAB using the procedure shown in Figure 5.49 and measured for the NZPV in the experimental setup described in section 3.4.3. Both samples had the pyrolysis of the Y ink and the oxygen annealing of the silver done at the same temperature of 400 °C for 1 hour. All NZPV results related to these two samples (#1 and #2) are portrayed in the graph of Figure 5.53.

The initial NZPV measurements with sample #1 revealed that the standard configuration with the current contacts covering 1.5 cm of the CC were not enough to avoid quenching the tape underneath the current leads when applying currents pulses beyond 350 A. Using the same conservative assumptions of section 2.4.2 for calculating the current contact area, the interfacial resistance for the 350 A scenario is roughly estimated to be slight above 10^{-5} Ω-cm^2 which is in agreement with the value found in the fitting of the CTL measurements of the previous section 5.5.2. The sample holder was adapted to increase the size of the current contacts to 2.5 cm and avoid excessive joule heating. With the assistance of larger current contacts, the first sample #1 presented an $I_c \sim$ 390 A, and a consistent 4 - 5x increase in the NZPV in the 230-390 A range (blue squares + solid line) when compared to the uniform architecture of THEVA.

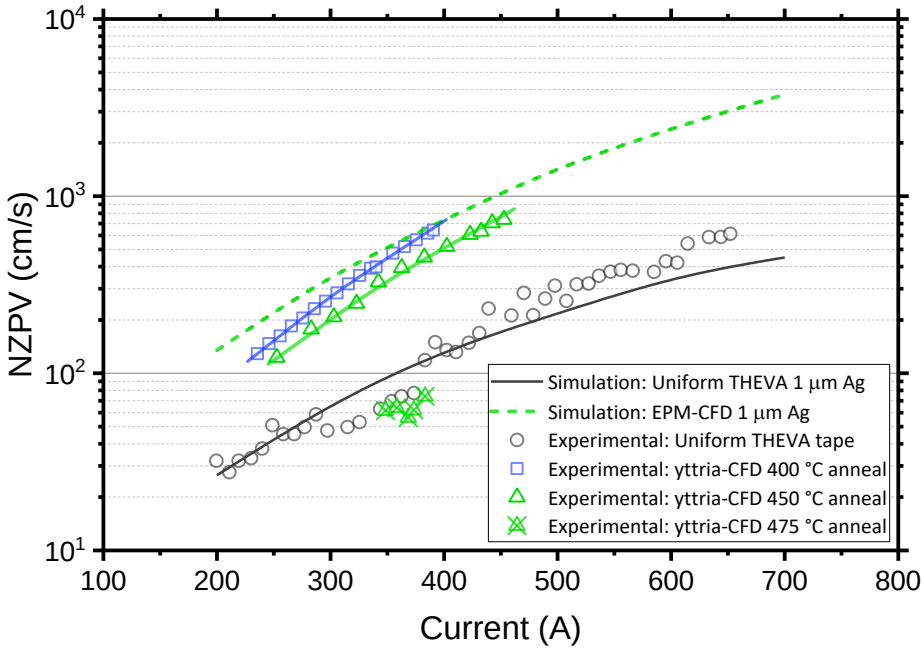

Figure 5.53: Comparison of NZPV versus Current for 2nd route of Yttria-CFD in comparison with other architectures: Uniform tape, classic CFD from EPM and 1st Yttria-CFD route.

In order to avoid the risk of quenching and damaging sample #2 due to the same high interfacial resistance found in sample #1, sample #2 was re-annealed in EPM's laboratory at 475 °C in 1 bar of oxygen atmosphere for 1 hour. This specific temperature was chosen based on the *in-situ* yttria insulation measurements shown in subsection 5.3.2 with two objectives in mind: Reduce the interfacial resistance Ag/GdBCO in the yttria-free edges of the tape, and avoid an excessive silver diffusion in the yttria-CFD interface. After re-annealing at 475 °C, sample #2 presented no quench issues with the current contacts and the I_c was found to be similar to sample #1 ($\sim$ 390 A), but no increase of the NZPV was observed (crossed green triangles in Figure 5.53). The silver diffusion after re-annealing at 475 °C was enough to completely bypass the yttria insulation responsible for the CFD effect.

The effect of silver diffusion in the CFD structure was confirmed by re-annealing sample #1 at 450 °C for 1 hour in 1bar of oxygen atmosphere and re-measuring the NZPV. In Figure 5.53, the final NZPV curve after annealing at 450 °C (green triangles) shifted $\sim$20% below the original NZPV curve (blue squares) indicating some loss of the initial CFD effect. Nevertheless, the final NZPV still remained 3x higher than the uniform THEVA tape (dark circles) and demonstrated the effectiveness of the second Yttria-CFD route to significantly boost the NZPV.

Furthermore, re-annealing sample #1 at 450 °C provoked an unexpected increase in the final I_c from 390 A to a value beyond 450 A (green triangles). This minor I_c enhancement in sample #1 reinforces once again the role of the silver stabilizer layer acting as a catalytic element for the surface reactions revolving the oxygen incorporation process of the GdBCO film. The precise I_c value could not be determined because of a premature quench happening once again at the 2.5 cm current contacts for currents above 450 A. Using again equation (2.2), the new interfacial resistance was estimated to be close to 10^{-6} Ω-cm^2. This resistance although not ideal would be enough to guarantee the practical use of the yttria-CFD CC. Nevertheless, as future work a dedicated experiment to verify these estimated values of interfacial resistance should be conducted.

6 Sulfide-CFD Route

As mentioned throughout the previous chapters, the most attractive manufacturing route for the CFD revolves around finding the right technique to add the high interfacial resistance on the HTS material without affecting other technical aspects of the standard CC manufacturing procedures. From this point of view, it becomes evident that the best approach is to create the CFD interface on the available layers of the final 2G HTS commercial tape. However, the task of accessing the Ag/REBCO interface without having to refabricate the expensive silver stabilizer is, in theory, a very complex procedure. The known metallic impurities in silver such as Cu, Ni, Sn, In, Cd, Sb and Pb that could react with the oxygen of the GdBCO in the Ag/GdBCO interface and form a high resistance oxide have a diffusion coefficient of about $10^{-12} - 10^{-25}$ cm^2/s in the 100 - 500 °C range. Using equation (1.15) from subsection 1.6.2, one could verify that diffusing these metals through a 1 µm thick silver layer would require months of annealing for temperatures below 300 °C [268]. With this challenge in mind, this chapter discusses and presents the results for the 4th (and last) CFD manufacturing route, aiming for the chemical alteration of the silver shunt with a faster impurity diffusion process.

6.1 Classic CFD with Silver Sulfide

In normal pressure and temperature conditions, pure silver does not form any significant amount of oxide layer on its surface, therefore making it chemically inert to oxidation also under cryogenic temperatures [269]. However, silver is susceptible to corrosion in the presence of sulfur-containing gases like hydrogen sulfide, sulfur vapor, sulfur dioxide and others. In this corrosive reaction, silver sulfide (Ag_2S), a black inorganic compound also known as patina or tarnish, is formed.

6.1.1 The Sulfide-CFD Route

Commonly, for silver used in electronics and jewelry, the formation of tarnish is highly undesirable and usually removed with commercial silver polishes [270]. However, this method removes the sulfide crystals through abrasion, thus resulting in loss of silver material each time the tarnish layer is polished. Nevertheless, tarnish can also be removed chemically through a reduction reaction targeting the sulfur atoms in the Ag_2S compound. In this technique, the right temperature and pressure conditions are chosen, together with a reducing agent (hydrogen gas for instance), to remove the tarnish by forcing the formation of a third disposable compound containing the sulfur. Theoretically, in this reduction process no actual silver is lost as residue. Indeed, this technique has been proven to be extremely effective in recovering ancient historical pieces made of silver due to minimum changes in the silver morphology [271].

Given the simplicity of the reported techniques used for studying tarnish formation and recovering silver alloys, a new chemical sulfidation route was investigated for creating the CFD architecture. Using the available silver coating on the commercial 2G HTS tapes as template, the sequence of experimental steps needed for this Sulfide-CFD route was planned as illustrated in Figure 6.1.

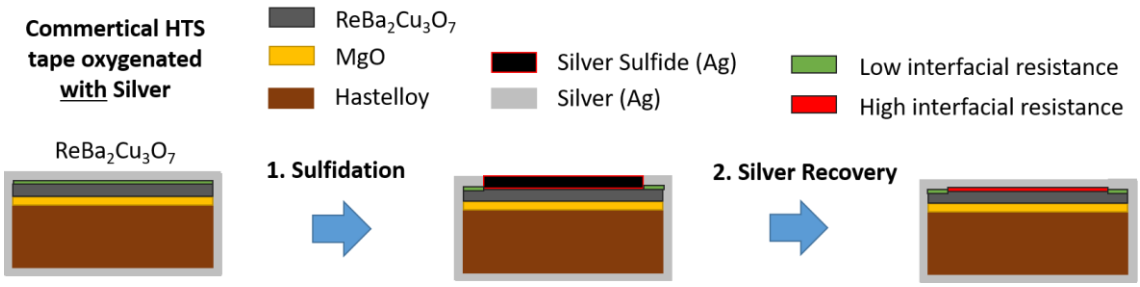

Figure 6.1: Suggested experimental workflow for the incorporation of Sulfur-CFD tapes in commercial silver coated tapes.

In the 1st step called "Sulfidation", the silver edges of the tape are masked leaving 85-90% of the tape's width (12 mm) exposed for the tarnishing process. The different technical approaches used for creating the Ag_2S are discussed in the following subsections. In the sulfidation process the full thickness of the exposed silver is converted to Ag_2S leading to an Ag_2S/REBCO interface. Knowing that the resistivity of silver sulfide is 7–10 orders of magnitude higher than that of silver [272], the S diffusion to form Ag_2S should increase the interfacial resistance and create the CFD pattern. Once the high interfacial resistance is present, the sulfide is reduced back to metallic silver in the 2nd step, the "Silver Recovery". By reducing the silver sulfide, we should be able to reconstruct the original conductive silver shunt layer of the tape without having to re-sputter the coating. Evidently, to avoid losing the high resistance interface, no oxygen annealing process is performed afterwards.

6.1.2 Sulfur/Silver Liquid Reaction

As mentioned before, silver is susceptible to corrosion in the presence of sulfur-containing gases, however the silver can also be tarnished when entering contact with bodies or solutions containing sulfur. For instance, liver of sulfur is a yellow brittle solid mixture containing potassium and sulfur (potassium sulfide, potassium bisulfide, potassium polysulfide, and/or potassium thiosulfate) mainly used for metalworking to create different colors of patina on silver and copper alloys. By rubbing the yellow solid lump of liver of sulfur on to the surface of a silver alloy one can produce a significant thick layer of tarnish in matter of minutes. However, it has been practically observed that the reaction rate is better controlled using the liver solid lump in a diluted water solution [273]. For this very reason liver of sulfur is also commonly sold in the form of a pre-mixture of liquid or gel paste. This modern gel is added with stabilizers that extend the shelf life of the product and allow the reactivity to last much longer. In addition, this inexpensive gel/liquid could be easily adapted to the IJP expertise of the SUMAN group at ICMAB [64].

With all these advantages in mind, the first sulfidation experimental attempt was performed with a commercial sulfur gel traded by the name "Liver of Sulfur Extended Life Gel (XL Gel)", and 12x12 mm pieces of GdBCO 2G HTS tape from THEVA, coated with approximately 1.2 µm of pure silver. According to [273], for properly tarnishing silver, the sulfur solution must be warmed usually between 30 °C and 50 °C, but never above 50 °C, otherwise the liver of sulfur will rapidly decompose to potassium sulphate (K_2SO_4) and potassium carbonate (K_2CO_3), neither of which has any oxidizing action. The purest liver of sulfur, has a dark yellow color that fades to light yellow and finally white as the compound ages and decomposes. Therefore, using this color criteria, different sulfur solutions were tested by diluting the XL gel with 200 ml of distilled water in a 300 ml PYREX beaker on a hot-plate as

shown in Figure 6.2(a). Table 6-1 shows the practical decomposition times needed for different solutions' concentrations at different temperatures.

Table 6-1: Liver of sulfur decomposition times needed for different solutions' concentrations held at different temperatures.

XL-gel in 200 ml of water	*21 °C (RT)*	*30 °C*	*35 °C*	*40 °C*	*45 °C*	*50 °C*
0.5 ml	3 h 28min	3 h 19min	3 h 01min	2 h 27min	1 h 11min	29 min
1,0 ml	3 h 17min	3 h 07min	2 h 46min	2 h 16min	1 h 01min	25 min
1,5 ml	3 h 12min	3 h 03min	2 h 48min	2 h 00min	48 min	18 min
2,0 ml	2h 02 min	1 h 41 min	57 min	25 min	12 min	11 min

Figure 6.2(b) shows an example of one 12x12 mm sample stuck to a glass slide with polyimide tape masking the edges leaving only the middle section of silver coating exposed to the solution reaction. For each solution of Table 6-1, a glass slide containing the sample was dipped in the sulfur solution and removed every 5 or 10 minutes for visual inspection and evaluation of the silver.

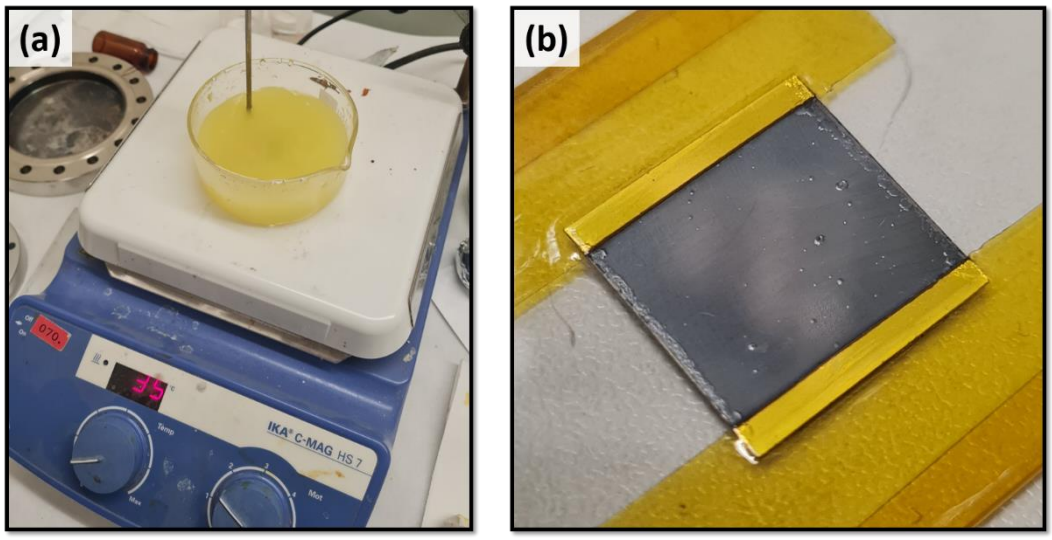

Figure 6.2: (a)Solution XL gel + water in a 300 ml PYREX beaker resting on a hot-plate with temperature control via thermocouple. (b) Example of one 12x12 mm HTS sample with silver coating stuck to a glass slide with polyimide tape masking the edges. This picture was taken after the sulfidation.

The formation of a polycrystalline layer of cubic α-Ag_2S (acanthite) on the surface of silver was confirmed via X-ray diffraction (Figure 6.3). In Figure 6.3(b), we find all the expected peaks for θ-2θ from 20 - 55 ° [274] plus two intense peaks for metallic silver (*JCPDS* file *No*. 04-0783) indicating the presence of a considerable amount of the metal underneath the sulfide.

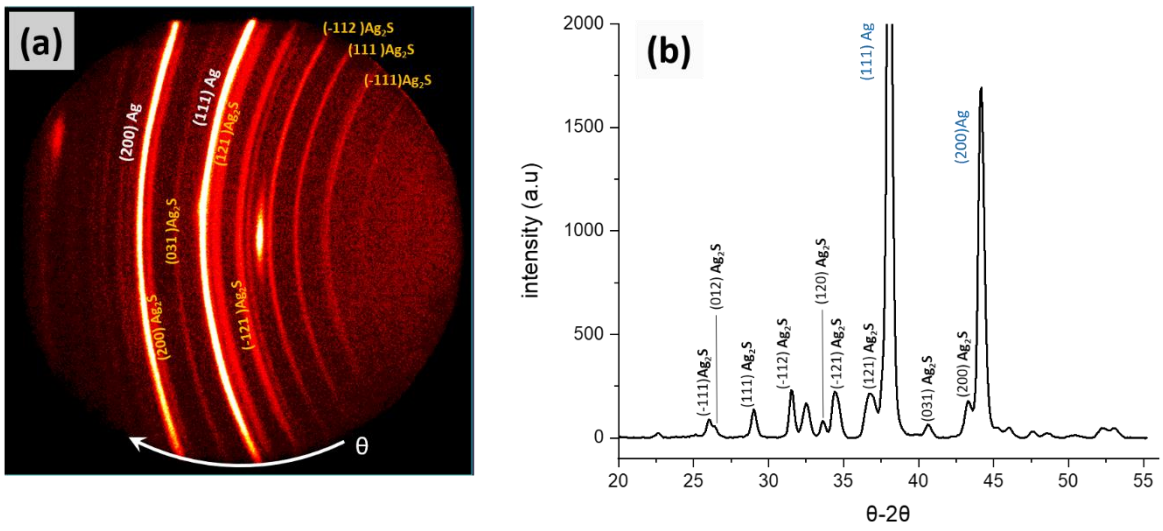

Figure 6.3: X-ray diffraction spectra of α-Ag_2S on top of the silver layer shunt of GdBCO 2G HTS tape.

The visual evaluation of the sulfide thickness formation was accomplished by taking into account the "thin film interference" phenomena. When light hits the thin film of tarnish on the silver, part of the light gets reflected by the top of the sulfide layer and another part gets refracted (passes through) only to be reflected by the silver underneath the sulfide. When the top reflected light part recombines with the light coming from the bottom tarnish, colors are created in an interference process. The final color depends solely on the thickness of the tarnish layer. In the initial phase, the color shifts from yellow through red-brown towards blue, as the thickness increases from 10 to 100 nm. After 100 nm, only the natural black opaque color of silver sulfide is observable [275]. In Figure 6.4 a tarnished silver-plated cup is shown with the interference colors.

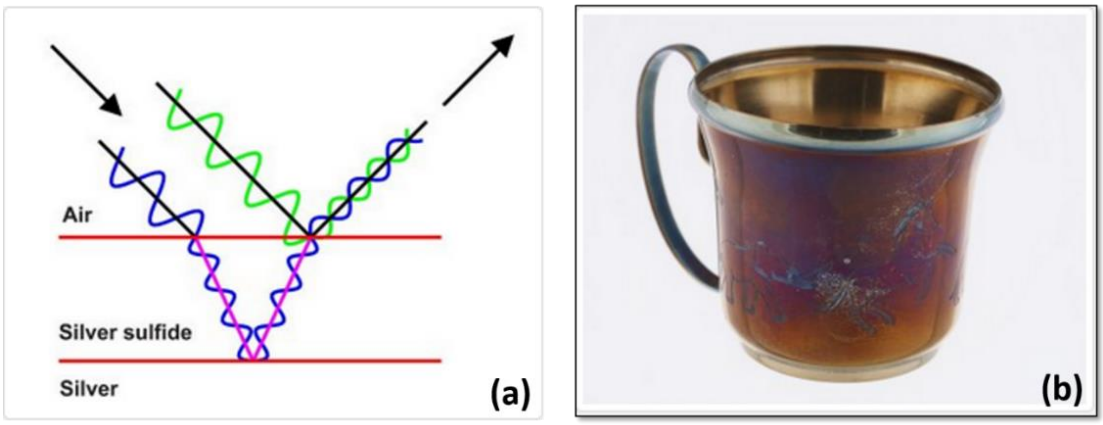

Figure 6.4 (a) Schematic drawing of the double path for light being reflected from the silver sulfide on top of tarnished silver. (b) Tarnished silver-plated cup with different interference colors. Figures taken from the Canadian Conservation Institute (ICC).

For all the different solutions below 30 °C, the sulfide formation was too slow. Even for the highest 2.0 ml concentration at 30 °C, after 30 min exposure, only shades of yellow appeared on the silver. Dark red and brown colors only start to appear after 2 hours, but the reaction was halted by the gradual decomposition of the solution. The formation of a dense black silver sulfide layer was only achieved for solutions at 40 °C or above with the best result found for 1 ml of XL gel at 40 °C.

6.1.3 Silver Sulfide Layer on the REBCO via Liquid Reaction

For all solutions where the black sulfide layer was formed, a blistering formation was noticed on the surface of the patina as pictured in Figure 6.5. As the sulfidation reaction continued, some of the blisters suffered major pealing leaving the HTS layer exposed. It is known that in case of high concentrations of liver of sulfur, the oxidation process will develop too quickly leading to a flaky patina layer [273]. This effect was evident in one attempt of directly applying the XL gel onto the silver and slowly heating it up to 40 °C. The reaction rate became inhomogeneous and uncontrollably fast leading to a complete pealing and loss of the silver layer.

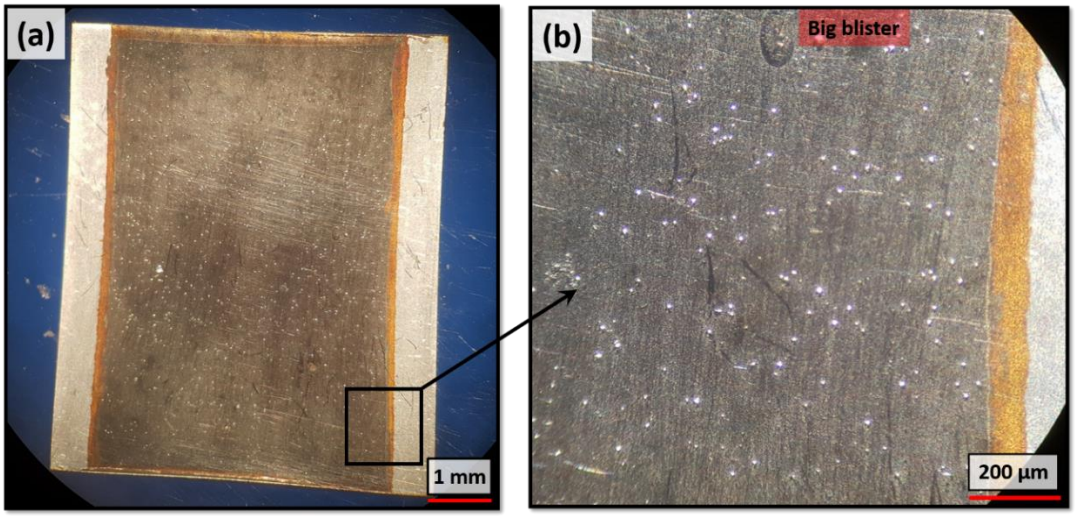

Figure 6.5: (a) Commercial 12x12 mm 2G GdBCO tape piece from THEVA with silver, after 10 minutes reaction with liver of sulfur 1 ml solution at 40 °C. (b) Magnified view of the blistering formation on the surface of the patina. The majority of blisters presented a diameter in the 20 µm range with some occasional ones reaching 100 µm.

Nevertheless, in the case of the diluted solution, the blistering of the patina happened even for low concentrations where the reaction took hours to reach the dark patina surface, thus ruling out fast localized reaction rates. In order to identify the origin of the blistering process, the cross section of one sample treated with liquid sulfur was investigated in SEM-FIB imaging as shown in Figure 6.6. The full FIB cut in Figure 6.6(a) provides an overall view of the state of the Ag_2S/Ag/GdBCO/MgO layers transitioning from the compact Ag_2S region into the middle of one of the blisters. The magnified view in the middle of the cut (Figure 6.6(b)) characterizes this transition revealing the formation of an unknown composite (GdBCO + S) in the interface Ag/GdBCO, followed by a structural fracture across all the GdBCO layer (dashed yellow line). Moreover, a second magnified view on the center of the blister (Figure 6.6(c)) exposes the presence of intense GdBCO degradation in both interfaces: Ag/GdBCO and GdBCO/MgO. This pattern indicates the existence of an infiltration path for the sulfur solution connecting both interfaces.

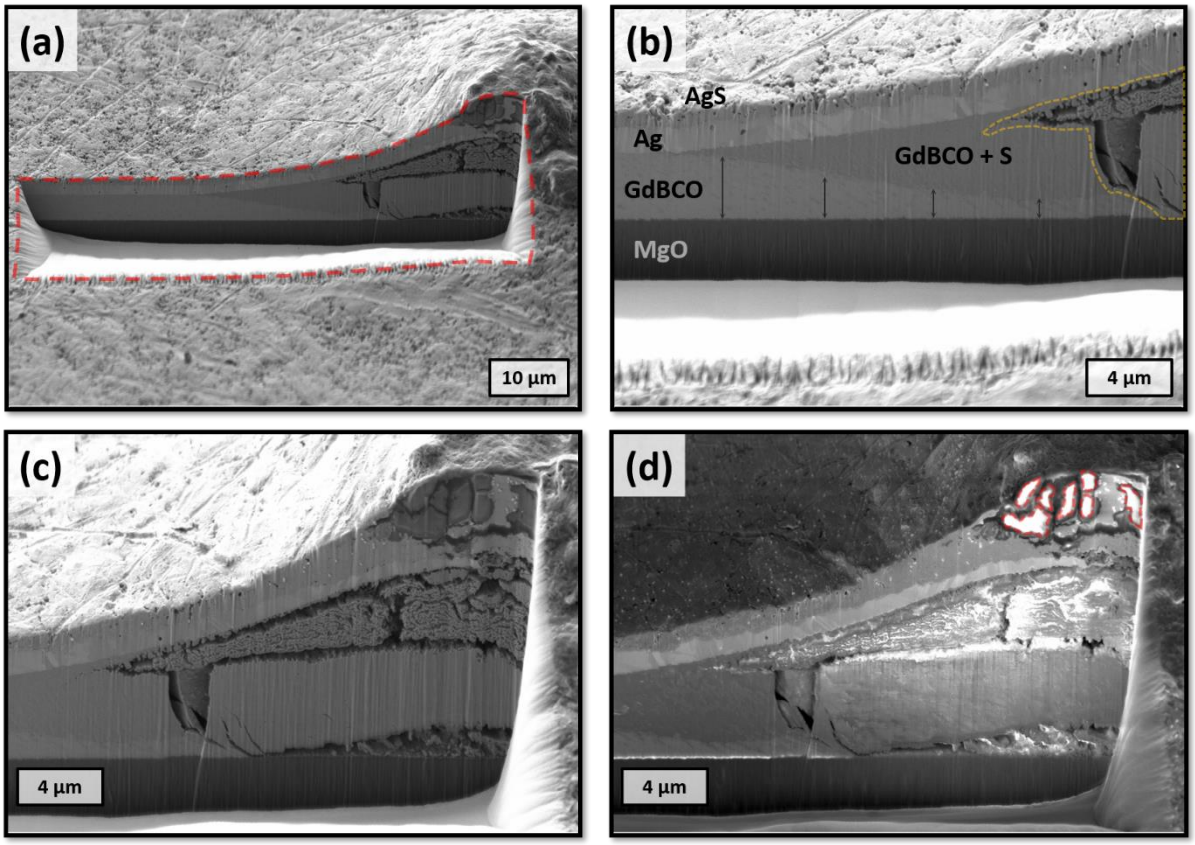

Figure 6.6: SEM-FIB images of the Ag_2S /Ag/GdBCO/MgO layers after the liquid sulfur reaction. (a) SE image of the cross section cut on the side of a blister. (b) SE image showing the transition from the damaged cross section region (GdBCO + S) to the non-damage region. (c) SE image of the center of the blister region showing damage in the Ag/GdBCO and GdBCO/MgO interfaces. (d) BE image of (c).

In this scenario, the known presence of the GdBCO outgrowth peaks originated at the MgO substrate (subsection 4.1.1), conveniently explains the infiltration path for the liquid sulfur. The peaks cover 1% of the GdBCO's surface and can reach heights comparable to the silver thickness (up to 1 µm). During the liquid sulfur reaction, the peaks would be the first GdBCO regions exposed to the corrosion environment of the liquid sulfur, thus creating channels for infiltration all the way down to the substrate. This explanation is reinforced by the Backscatter image of Figure 6.6(d), where residue pieces of degraded GdBCO are spotted in the Ag_2S layer suggesting the presence of a GdBCO material in the silver region before the sulfidation reaction.

The impossibility of tarnishing the silver stabilizer with liquid sulfur due to infiltration and localized corrosion of the GdBCO outgrowth peaks lead to an investigation of alternative reactions for the sulfidation.

6.1.4 Sulfur/Silver Gas Reaction

In the dense literature of conservation of silver and silver alloys [276], tarnishing is usually studied with ordinary atmosphere gases containing sulfur. Although the type of corrosive gas may change from study to study, the two most commonly used gases are: sulfur vapor (S_n) and hydrogen sulfide gas (H_2S). For H_2S, the reaction is known to be endothermic (ΔH = + 10 kJ/mol) and is described by the equation below:

$$2Ag(s) + H_2S\ (g) \leftrightarrow Ag_2S(s) + H_2(g)$$

Therefore, the reaction cannot happen without heating or having an oxidizing agent like atmospheric oxygen. Oppositely, the reaction with sulfur vapor is exothermic (ΔH = -32 kJ/mol) and is described by the simple following equation:

$$2Ag(s) + S\ (g) \leftrightarrow Ag_2S(s)$$

Consequently, the sulfur vapor is able to react with silver without the need of extra heat or other oxidizing gases. From a practical approach, utilizing sulfur vapor becomes easier since only one specimen concentration needs to be controlled experimentally. Moreover, considering the toxicity levels of H_2S [277], a special setup would have to be built to safely work with this gas. Nonetheless, the thermodynamic advantage of the S_n reaction makes the corrosion more severe than in the H_2S case. With all these considerations, sulfur vapor was chosen to act as the corrosive gas for tarnishing the silver on top of the HTS CC.

The sulfidation tests were performed in a glass reaction chamber (a Mason Jar) of 500 mL with a tight rubber sealed lid as shown in Figure 6.7. The seal ensured minimum changes in the sulfur vapor concentration due to gas leaks during the experiments. A sublimed sulfur powder -100 mesh 99.5% from *Alfa Aesar* was used as source for the vapor. With the melting temperature of 115.21 °C for sulfur at 1 atm, a fix temperature of 130 °C was chosen to melt the powder and generate the sulfur vapor in vapor pressure condition. According to [278], at this temperature, the total sulfur pressure would be dominated by the partial pressure of S_8 allotropes molecules and so, we utilize the ideal gas equation to calculate the amount of sulfur powder needed to reach the saturation point:

$$n = \frac{PV}{RT} = \frac{5 \times 10^{-5}\ [atm]\ \times 500\ [ml]}{8.314\ [J/(K\text{-}mol)] \times 130\ [°C]} = 0.00000755711\ [mol] \rightarrow 1{,}94\ mg\ of\ S$$

Considering that part of the sulfur vapor will react with silver and form the sulfide, in order to maintain the concentration constant during the reactions, all experiments were overdosed with 10 mg of sulfur powder.

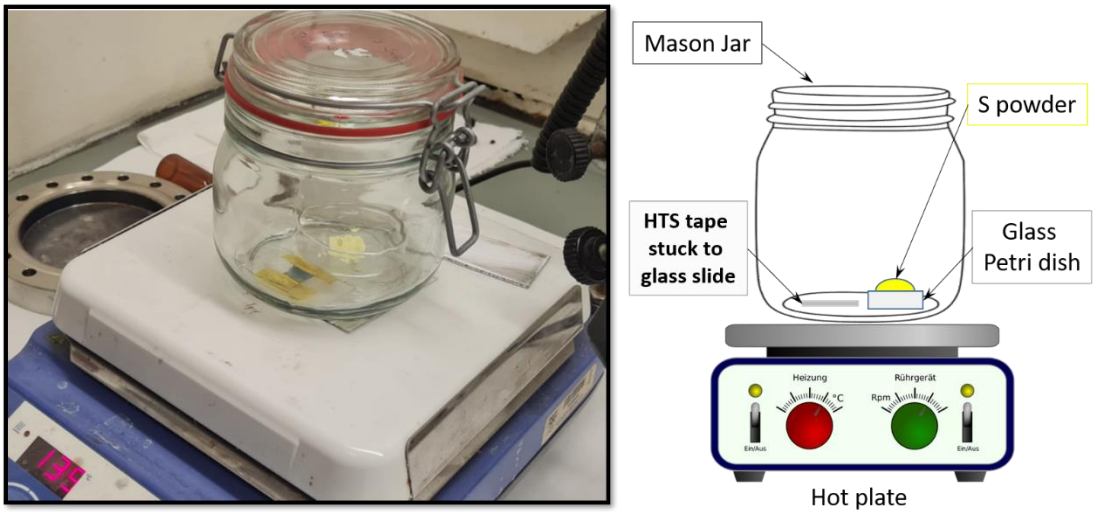

Figure 6.7: Picture and schematic drawing of the experimental set-up used for sulfiding the silver stabilizer of 2G HTS CCs with sulfur vapor. The Manson Jar is hermetically sealed to avoid vapor leaks.

The sequence of images in Figure 6.8 show the practical experimental steps used for evaluating the rate of the chemical reaction between the sulfur and the silver on the HTS samples quantitatively. Like in the previous section, 12x12 mm THEVA samples were stuck to a glass slide with polyimide tape masking the edges and exposed to the sulfur gas for different time periods. Dark patina layers only start appearing after 40 min of reaction as shown in Figure 6.8(a). Differently from the liver of sulfur solution, no blistering was observed for any of the dark patina layers produced. However, for reactions above 1 hour, part of the silver sulfide layer became loose and could be easily brushed off with a cotton swab. The effect on the patina aspect after brushing the sulfide is portrayed in Figure 6.8(b). After brushing, the remaining sulfide layer was chemically removed with a commercial polisher "Tarni-Shield®" solution to verify the presence of a metallic silver core underneath (Figure 6.8(c)).

In reality, for the majority of samples, the remaining silver thickness after polishing was inferred via electrical measurements as illustrate in Figure 6.8(d). Four gold-plated pogo pins were utilized for measuring the resistance between the two virgin silver strips on the sides of the sample. Assuming a homogenous sulfide reaction across the silver surface, the silver thickness could be estimated considering the silver's resistivity and the dimensions of the sulfided silver region on the sample. By subtracting the calculated metallic silver thickness after sulfidation from the known initial thickness, we were able to estimate the corrosion rate in our experimental condition. In Figure 6.10(a) we show the corroded silver layer thickness as a function of the exposure time to the sulfur vapor at 130 °C.

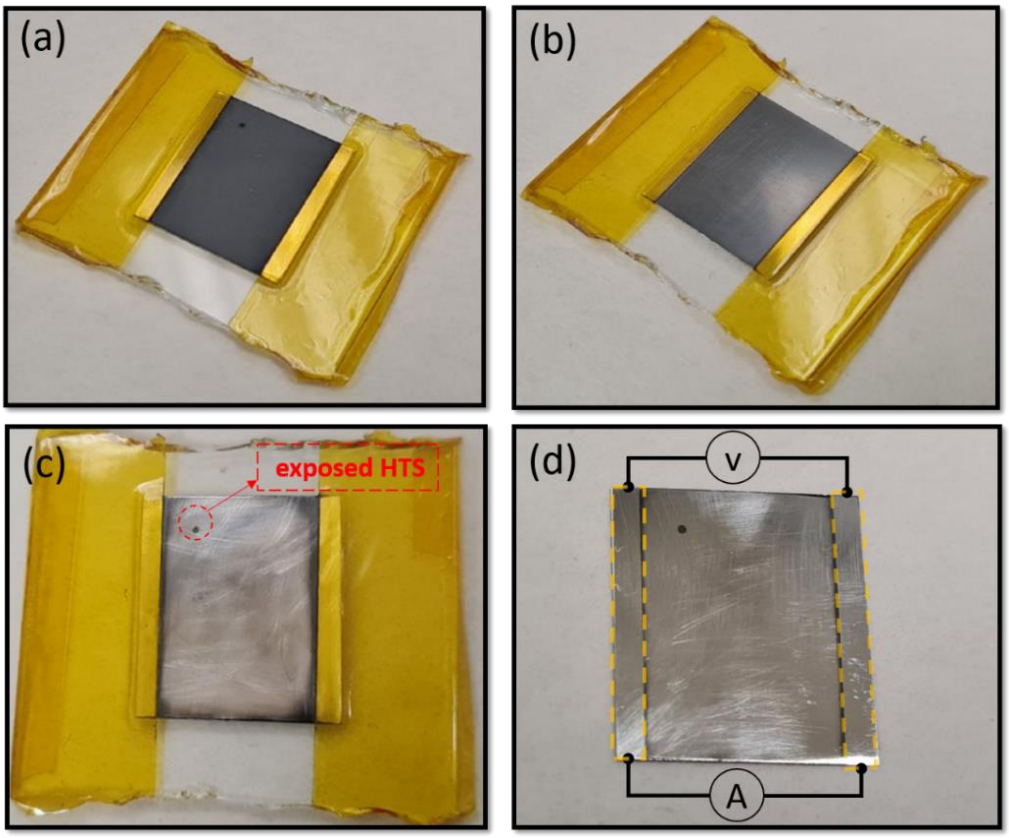

Figure 6.8: Experimental steps for corrosion analysis of the silver layer of a 12x12 mm sample after sulfidation reaction. (a) Sample after being exposed to sulfur vapor for a certain amount of time. (b) Sample after being brushed to remove the loose excess of silver sulfide. (c) Sample after being polished with commercial polisher to remove the silver sulfide. (d) Sample out off the glass slide ready for resistance measurements for Ag thickness estimation.

The morphology of the dark patina is shown in the SEM image of Figure 6.9(a). The agglomeration of randomly oriented silver sulfide grains ranging from 500 nm to 2 µm creates a rough and dense layer of patina. Aside from the polisher technique shown in Figure 6.8(c), the presence of a silver core underneath the patina was also evaluated with SEM-FIB imaging as shown in Figure 6.9(b). Although rough, the sulfide layer forms a continuous interface with the silver without any apparent porosity.

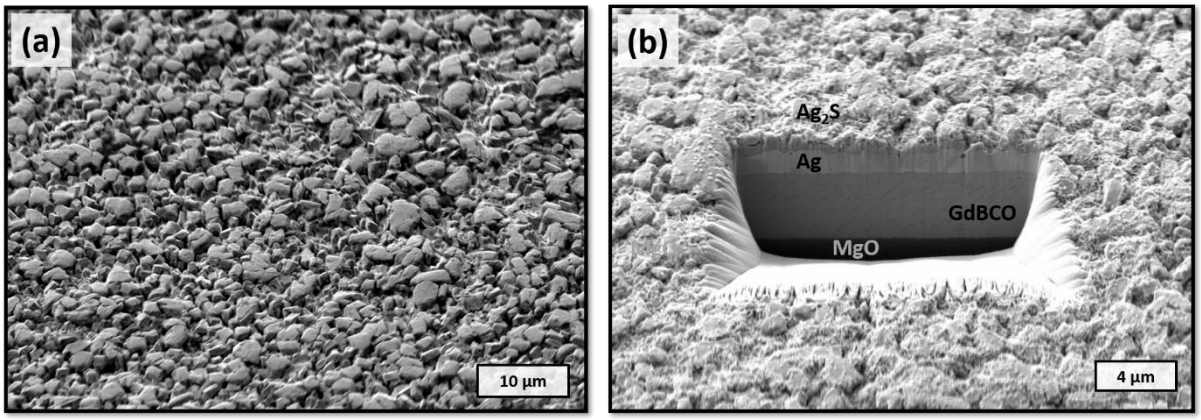

Figure 6.9: SEM and FIB images of the dark patina layer formed after sulfidation with S_8 vapor. (a) SEM images of the sulfide morphology. (b) FIB cross section analysis of the Ag_2S/Ag/GdBCO interfaces after 2h of sulfidation.

The graph in Figure 6.10 shows that the corrosion rate at 130 °C follows a linear trend in the first 120 minutes, but seems to accelerate afterwards. As vapor exposure time increases, variations in the reminiscent silver thickness also increases. This phenomenon can be noticed by the increase of the error bars of the data as exposure time increases. However, more importantly, the continuity of the interface is also affected by the sulfidation time. Allowing the reaction to continue even after full consumption of the silver layer around 240 min, creates pores in the Ag_2S/GdBCO interface as shown in the SEM-FIB image of Figure 6.10. From the studied Graphite-CFD route of section 4.4, it is known that pores in the interface could lead to a shunt pealing during the quench thermal shock. Accordingly, to avoid significant porosity in the interface Ag_2S/GdBCO and to tarnish the full silver layer, the proper sulfur vapor exposure time was set for 3h45 min in the chamber.

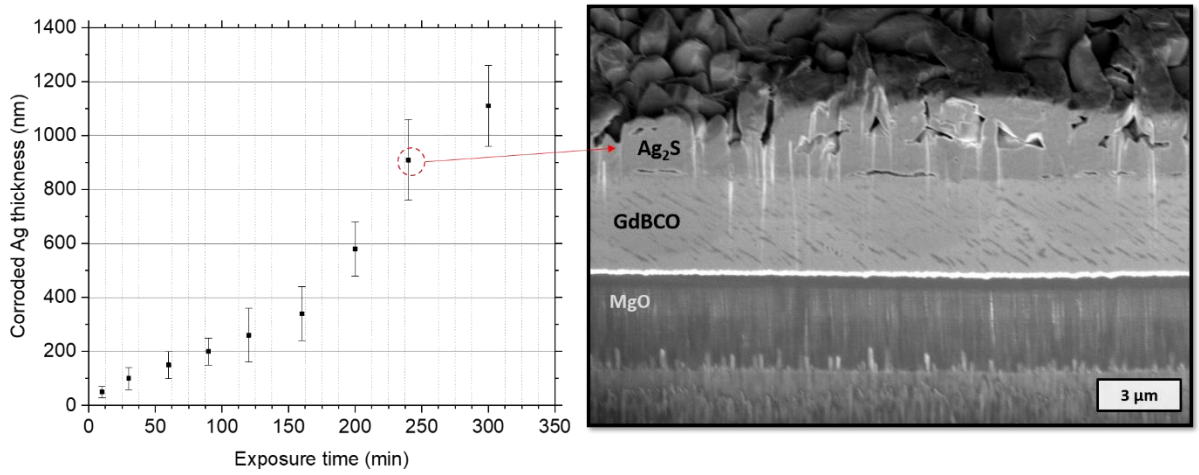

Figure 6.10: (a) Rate of conversion of silver into silver sulfide as a function of exposure time to sulfur vapor at 130 °C. The error bars indicate small variations in the final silver thickness underneath the silver sulfide. (b) Cross-section SEM-FIB image of the layers Ag_2S/GdBCO/MgO showing a continuous and porous interface Ag_2S/GdBCO after 250 minutes of sulfur vapor exposure.

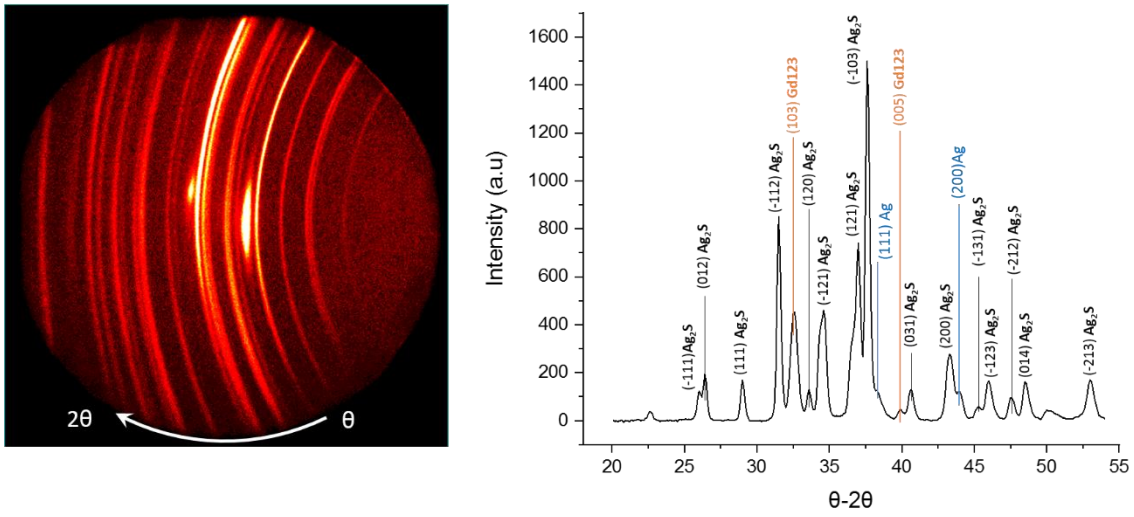

Figure 6.11: Diffraction pattern taken with GADDS for sulfided silver on top of the GdBCO tape substrate. (a) GADDS XRD pattern. (b) integrated θ-2θ XRD pattern of the film.

The formation of a polycrystalline layer of cubic β-Ag_2S on the surface of silver was again confirmed via X-ray diffraction. In Figure 6.11, we find all the expected peaks for θ-2θ from 20 to 55 ° [274] plus two peaks for metallic silver [279].

6.1.5 CTL Measurements of Sulfide-CFD Tapes

In order to confirm the presence of a high interfacial resistance in the Ag_2S/GdBCO interface, one tape sample of 5 cm length was sulfided with the CFD pattern and evaluated via CTL measurements by *FASTGRID* partners at EPM (section 3.4.2). The experimental data of the potential distribution and the fitting of the semi-analytical (SA) model are shown in Figure 6.12(a).

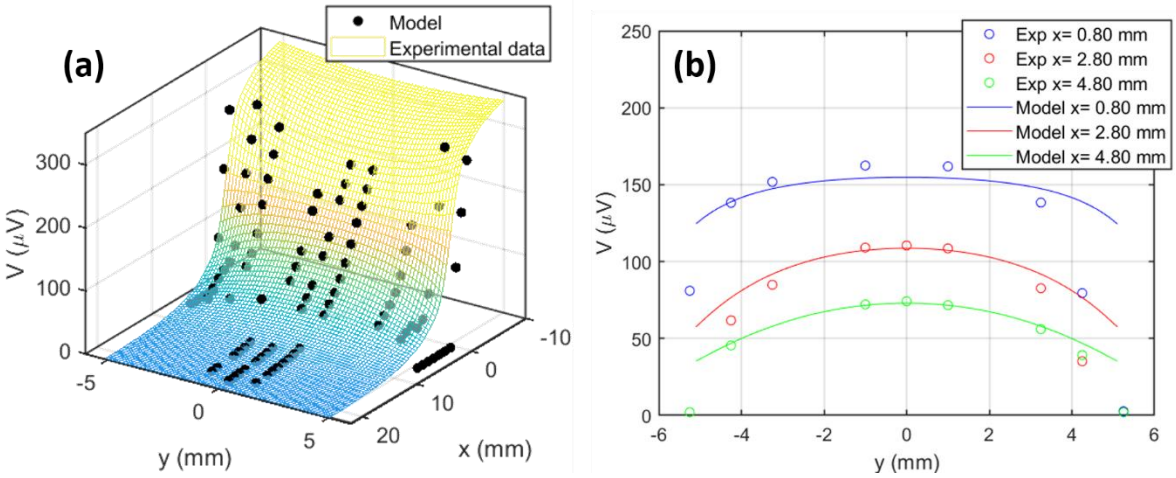

Figure 6.12: CTL measurements for a small 12x30 mm sulfide-CFD sample at 77 K. (a) Experimental data and fitted semi-analytical (SA) model for potential distribution on the surface of sample. (b) Parabolic potential distribution along the width (y-axis) of sample. The fit was performed only for the CFD region.

Differently from the standard CFD samples created with EPM's etching method, the SA model could not fit well the data around $y = 0$ and $y = \pm w/2$ simultaneously. Since this sample was made with a different technique leaving silver sulfide in between the GdBCO and the silver, it is possible that the sample doesn't respect all the exact assumptions of the SA model like the steep transition between high resistive interface (R_f) and low resistive interface (R_0). Nevertheless, a reasonable fit for the surface potential was found considering only the sulfide-CFD region around $y = \mp 10.2$ mm with the parameters shown in Table 6-2.

The value of R_f was indeed high (1 Ω-cm^2), but due to the incomplete fitting of the width, the ratio R_f/R_0 could not be properly estimated to quantify the CFD effect. However, the experimental data of the potential distribution across the width (y-axis) for different planes along the length (Figure 6.12(b)) confirms the parabolic voltage distribution characteristic of the CFD architecture. Moreover, using the pair of equations (3.16) and (3.17) the CTL was found to be $\lambda = 4.27$ mm. This value is 30% greater than the yttria-CFD architecture, thus implying a slightly faster NZPV.

Table 6-2: Parameters used to fit the CTL experimental data with the semi-analytical model described in section 3.4.2 . The experimental data was taken for a THEVA CC altered with the sulfide-CFD architecture

Parameters	Value
w	10.2 m
w_f	10.2 mm
d	1 µm
l_0	1.5 mm
R_f	1 Ω-cm^2
ΔV	300 µV

6.1.6 NZPV Measurements for the Sulfide-CFD Tape

After confirming the presence of the CFD architecture qualitatively via the CTL measurements in the Sulfide-CFD route, two long sulfide-CFD samples of 12x140 mm were manufactured at ICMAB for measuring the NZPV in EPM's experimental setup (section 3.4.3). The objective of these samples was to assure the presence of a NZPV boost before transferring experimental effort to the "Silver Recovery" step (Figure 6.1). Therefore, both samples were sulfided in two separate processes following the procedure described in subsection 6.1.4 and re-sputtered with 1 µm of silver. The NZPV results related to these two samples (#1 and #2) are portrayed in Figure 6.13.

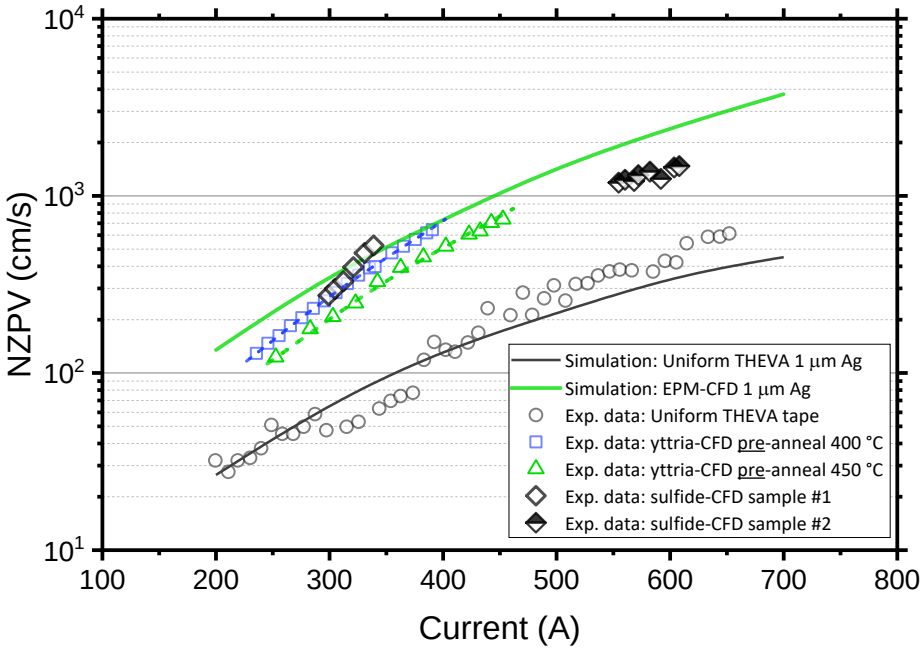

Figure 6.13: NZPV versus applied current for two Sulfide-CFD samples made at ICMAB with the sulfidation of the silver shunt. The experimental data is plotted against the 1st and 2nd route of Yttria-CFD and the uniform tape for comparison.

The measurements for sample #1 revealed a substantial NZPV increase of 5-7x in comparison to the uniform tape in the current range of 295-360 A. This increase is equivalent to the yttria-CFD route annealed at 400 °C and proves the efficiency of the silver sulfide in creating the high interfacial resistance required for the CFD effect. In addition, sample #2 also presented a NZPV boost in the range of 550-610 A, but the increase was below the simulated EPM-CFD's reference line (green solid line). This NZPV shift between samples indicated that the sulfidation process of the silver did not create the same final interfacial resistance Ag_2S/GdBCO for both samples. The cause of this discrepancy in the NZPV boost will be addressed in the next section.

6.2 Restoring the Silver Shunt

As illustrated in Figure 6.1, the sulfidation of the silver stabilizer/shunt is only the first step for the suggested sulfide CFD route. In order to attach current leads on the CC and make a practical use out of the REBCO film, the surface of the CC in contact with the current lead must be conductive to properly inject the transport current and avoid destructive joule heating. In this manner, recreating a metallic highly conductive layer on top of the sulfide becomes critical for making the sulfide CFD design a useful approach. For this very reason, the sulfide-CFD concept was conveniently thought out as a way to recycle the silver stored in the sulfide layer and use it to reconstruct (at least partially) the initial metallic silver stabilizer. This section presents and discusses the results for two different approaches capable of recovering the sulfide back to metallic silver on top of the REBCO film on an industrial scale.

6.2.1 Silver Recovery with Atmospheric Plasma Gun

Hydrogen is known to act as a strong reducing agent for metal oxides and sulfides [280]. However, for the reaction to effectively occur, a required input energy of 435 kJ/mol is needed to dissociate the molecular hydrogen (H_2) into the reactive atomic hydrogen (H) form. Heating the H_2 gas directly is proven to be an effective route for reducing sulfide minerals [281], but is far from being considered a practical technique due to requiring a constant high temperature (> 800 °C). Another common way is to create hydrogen plasma by exciting the H_2 gas with a high frequency AC voltage in a low-pressure controlled chamber [282]. Plasma reduction processes have a lot of potential in the field of restoration of fine metals surfaces, due to the absence of ablation to the target layer [271]. Nevertheless, the requirements for industrial manufacturing can be quite extensive and the use of chambers may create new technical difficulties due to size limitations and the full immersion in hydrogen plasma. To overcome these situations, plasma can also be created in atmospheric conditions by processing the gas in an electric arc [219]. An example of this technique is the Pulsed Atmospheric Arc Technology (PAA Technology®), whereas by controlling the vortex flow of a gas the arc between two electrodes is stabilized to form the plasma flame [220].

The PAA Technology® is already commercially available and has been proven to be quite effective for highly oxidized Cu alloys [283,284] and historical silver coins [271]. Therefore, GdBCO tape samples processed with sulfur vapor were sent to *Relyon Plasma GmbH* laboratories for silver recovery tests with atmospheric pressure plasma. All tests were performed in the plasmabrush® PB3 system described in subsection 3.1.5 and in [220] with a compressed forming gas 95/5 (N_2/H_2) flow of 50 L/min and 54 kHz of excitation frequency. The variables used for optimizing the results from sample to sample are shown in Table 6-3 for 6 samples. After the plasma treatment, all samples were evaluated via Hall-Scan magnetization measurements and selected for SEM-FIB inspection according to the amount of visible silver reduced from the sulfide layer.

Table 6-3: Optimized parameters for the silver sulfide treatment with the plasmabrush® PB3 system of Relyon Plasma GmbH Laboratories. This table shows only 6 samples out of the 16 samples tested. The underlined values in each column point out the change in parameters from sample to sample for optimization of the silver recovery.

Sample N°	#14	#13	#12	#18(1)	#34	#35
***Working distance** [mm]*	15	<u>25</u>	<u>15</u>	15	15	15
***Speed PG31** [mm/s]*	100	100	100	100	<u>200</u>	200
Number of cycles	10	10	2	<u>6</u>	6	<u>12</u>
***Offset between cycles** [mm]*	0	0	0	0	4	variable
***Power Limit** [%]*	100	100	100	100	100	100
Nozzle type	A250	<u>A450</u>	A450	A450	A450	A450
Pause Between cycles	None	None	None	None	<u>10 s break after 2 cycles</u>	10 s break after 2 cycles
Silver formation	None	Little	Some	Full Recovery!	Some	Significant
Hall- scan Evaluation	None	No damage	No damage	Severe Damage	No damage	Half degradation

In the columns of Table 6-3, the underlined values represent important parameters of the PB3 system that had to be changed to substantially increase silver formation and avoid degradation issues in the HTS layer. The first positive result is seen for sample #12 using the nozzle A450 with 15 mm working distance and a 100 mm/s traveling speed. After two cycles of plasma exposure, shades of white start to appear onto the dark patina layer as shown in in Figure 6.14(a). A microscopic inspection of the sulfide layer (Figure 6.14(b)) confirms the inhomogeneous formation of silver islands all over the surface. Dense and disperse regions of silver agglomerations take place side by side creating the greyish pattern observed in Figure 6.14(a).

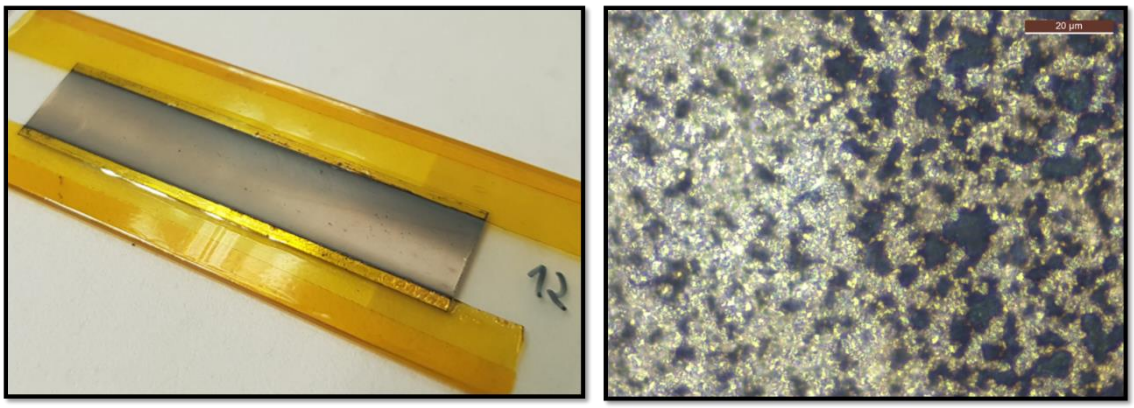

Figure 6.14: (a) 50x12 mm Sulfide-CFD tape same after two cycles of atmospheric pressure plasma treatment with nozzle A450 and 15 mm of working distance. (b) Microscopic view of the silver formation of top of the sulfide layer.

Comparing the SEM image of the pure sulfide layer on Figure 6.9(a) and the partial recovered silver sulfide layer of Figure 6.15(a), a clear change in the morphology is noticed. Besides changing the topographical aspect, the sulfide layer also became porous after plasma treatment. This porosity is better seen in the backscatter SEM-FIB cross-section analysis of the Ag_2S/Ag/GdBCO layers in Figure 6.15(b) where pores appear across the thickness and in the GdBCO interface. In addition, the backscatter SEM-FIB image reveals the formation of silver bodies not only on the surface of the sulfide, but also across the thickness in the form of small crystals randomly distributed. Because silver is 30% denser than silver sulfide, the formation of crystals inside the sulfide layer might explain the increase in porosity of the layer due to volume loss during the reduction process from sulfide to silver. No electrical tests could be performed for sample #12 due to the lack of electric continuity on the recovered silver layer.

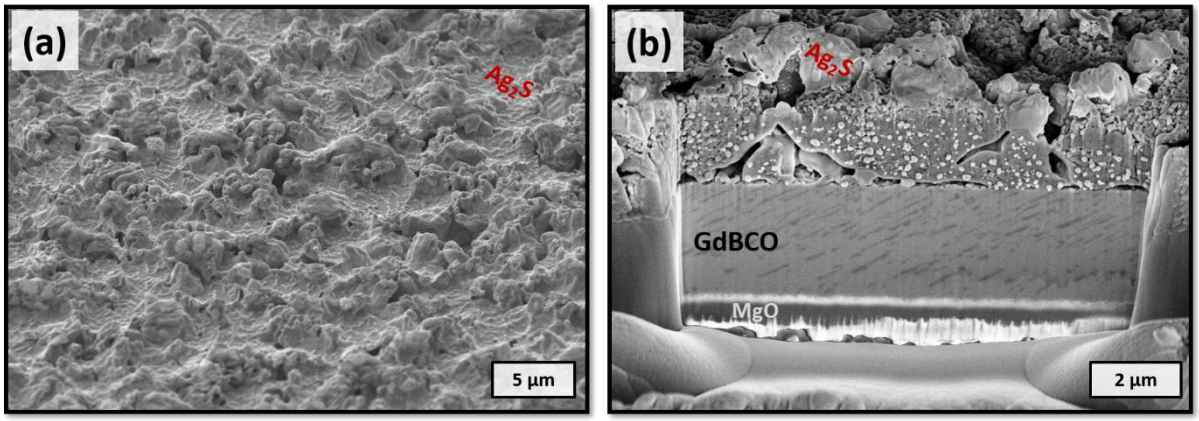

Figure 6.15: SEM and FIB images for sample #12 (a) SEM image for morphological characterization of the silver sulfide layer on a HTS tape after atmospheric pressure plasma brushing treatment. (b) SEM-FIB backscattered image of the cross section (Ag + Ag_2S)/GdBCO after atmospheric pressure plasma brushing treatment.

In order to try recovering the full layer of silver, sample #18(1) was treated with 4 additional cycles, completing a total of 6 cycles. After the treatment, the silver appeared to be fully recovered with a resistance less than 1 Ω/mm, but no further tests were performed due to a severe degradation of the superconducting properties on the HTS layer. The degradation is seen in the B_z field distribution of Figure 6.16 measured at 77 K. The absence of magnetization across the length in the middle of the sample corresponds to the region in the path of the moving plasma flame. Moreover, the presence of silver blisters on the back of sample #18 strongly suggests a degradation coming from the overheating of the sample. According to the datasheet of the A450 nozzle [221], the static temperature of the plasma flame at a 15 mm working distance should be around 450 °C, enough to de-oxygenate the HTS material if the sample and the plasma flame reach thermal equilibrium.

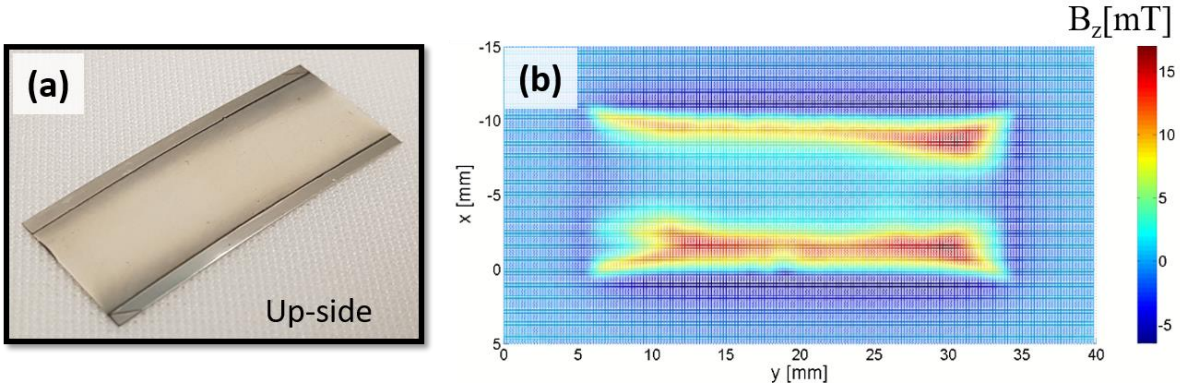

Figure 6.16: (a) Sample #18(1) after atmospheric pressure plasma treatment. (b) Perpendicular trapped field B_z measured at 77 K by SHPM for sample #18(1) after atmospheric plasma treatment.

Sample #34 represents an attempt to diminish heat amassing by increasing the traveling speed of the plasma nozzle over the sample with 10 second breaks between every 2 consecutive cycles. The amount of silver recovered was the same found in sample #12 with no signs of degradation coming from the Hall-Scan measurements. Therefore, sample #35 was processed in the same conditions as sample #34, but adding 6 more cycles to complete the sulfide reduction. After 12 cycles a significant amount of sulfide was reduced to silver, but not enough to confirm the full reaction since the silver sheet resistance was found in the 1 Ω/cm range. Silver blisters were found on the back of the sample indicating the re-occurrence of overheating. Furthermore, as shown in Figure 6.17(b), the Hall-scan

magnetization measurements of sample #35 confirmed the partial degradation of the superconducting properties along the region where the plasma brushing took place.

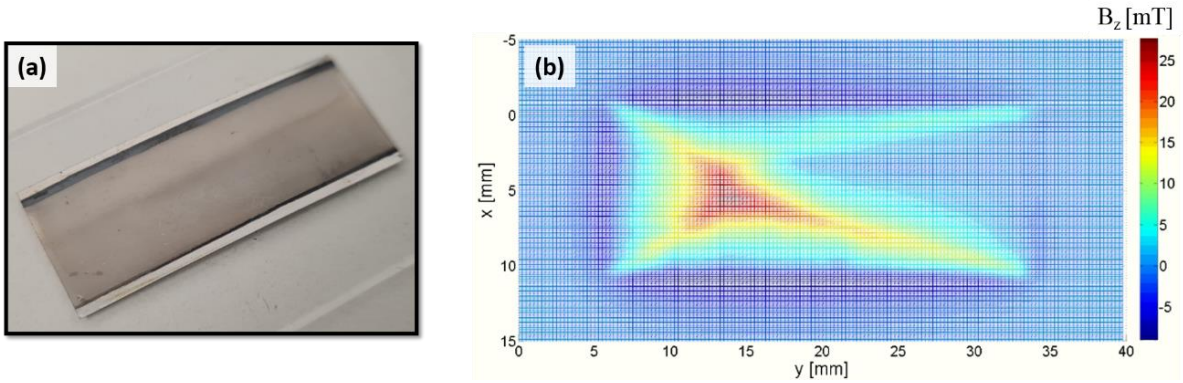

Figure 6.17: (a) Sample #35 after atmospheric pressure plasma treatment. (b) Perpendicular trapped field B_z measured at 77 K by SHPM for sample #35 after atmospheric plasma treatment.

In summary, the silver recovery from the sulfide on the GdBCO CC via atmospheric plasma treatment has shown to be possible. Utilizing the plasma brushing PB3 system in certain conditions creates a continuous, but irregular silver layer on top of the sulfide after some brushing cycles. However, this technique still requires major optimization for achieving a full silver shunt recovery without thermally degrading the HTS layer. Furthermore, the increase presence of pores in the interface Ag/GdBCO after the plasma brushing must be taken into consideration for the NZPV tests to avoid the shunt pealing during the quench.

6.2.2 Silver Recovery with Low-Pressure Hydrogen Plasma

Due to the temperature limitation in the atmospheric plasma PB3 system, a second attempt to reduce the silver sulfide into metallic silver was perform in a low-pressure plasma chamber. Silver coated *THEVA* tape samples with fully sulfided CFD patterns (example in Figure 6.18(a)) were processed in a commercial system Femto Plasma-Surface-Technology 40 kHz 100 W at the Universitat Politècnica de Catalunya (UPC). All samples were treated with the available hydrogen gas mixture Ar/H_2 (95/5) using a 10 sccm flow at a pressure of 0.4 mbar and 33% of the maximum power for different time periods ranging from 15 min to 1 h.

In a visual inspection, the results for all samples were independent of the plasma processing time. As shown in Figure 6.18(b), all samples presented an evident color shift in the region of the sulfide strip, from opaque black to opaque white, thus suggesting the formation of a rough metallic silver layer. However, minutes after removing the samples from the chamber, the silver stripe aspect shifted from pure white to a yellowish pattern. Subsequently, a couple of hours after, the grey stripe began to peal exposing the GdBCO layer underneath as shown in Figure 6.18(c). Perhaps some sulfur residues in the GdBCO interface continue the corrosion reaction once the “fresh” recovered silver was exposed to the ambient atmosphere.

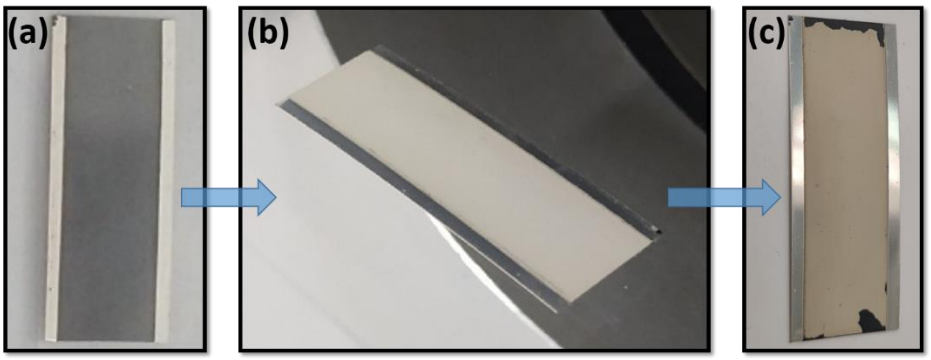

Figure 6.18: Three stages of silver sulfide reduction with low-pressure hydrogen plasma on THEVA tape. (a) Fully sulfided CFD pattern after sulfur gas exposure. (b) CFD sample minutes after low-pressure hydrogen plasma treatment of 15 min. (c) CFD sample 2 hours after low-pressure hydrogen plasma.

For the majority of sulfide-CFD samples, SEM-FIB cross-sectional images of the Ag/GdBCO /MgO layers (Figure 6.19) after the low-pressure plasma treatment confirmed the formation of an extremely rough and porous layer of silver. Similar to the case of atmospheric plasma treatment (section 6.2.1), the porosity extended throughout the whole Ag/GdBCO interface, thus leading to a poor adherence of the final recovered silver layer and subsequent flaking of the coating (Figure 6.18(c)).

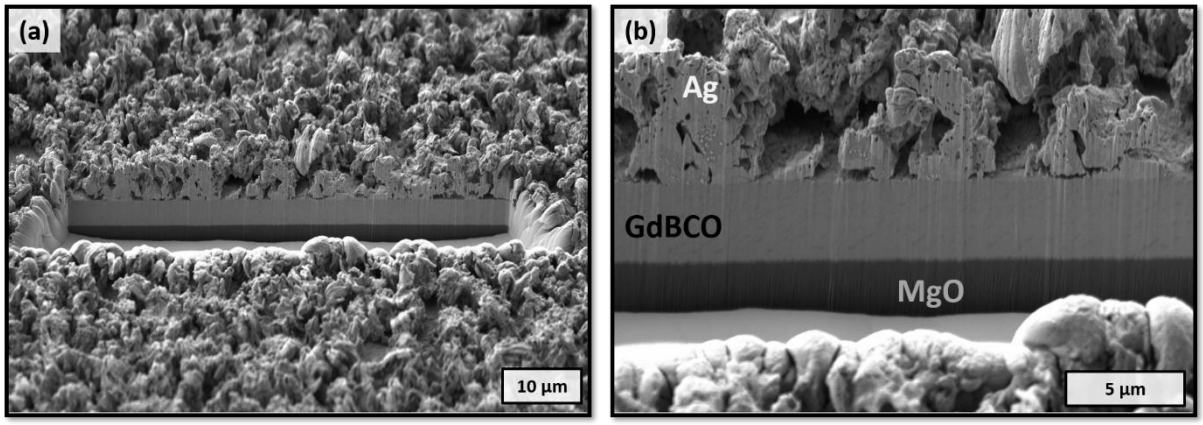

Figure 6.19: SEM-FIB images of the cross-section Ag/GdBCO/MgO after the low-pressure plasma treatment. (a) Full FIB cut view. (b) Magnified view of the Ag/GdBCO interface revealing high porosity of the silver layer.

However, some samples with an incomplete sulfidation process revealed a different silver morphology after the low-pressure plasma treatment. These "incomplete" samples initially did not present the full conversion of silver to sulfide throughout the whole thickness across the delimited CFD region thus leaving a metallic thin silver core underneath the sulfide in certain areas (Ag_2S + core Ag in Figure 6.20(a)). After the plasma treatment, these Ag_2S + Ag regions also presented a rough and porous layer of recovered silver, but with a continuous sturdy Ag/GdBCO interface capable of maintaining the adherence of the Ag coating even after mechanical scratches (blue dashed line Figure 6.20(b)).

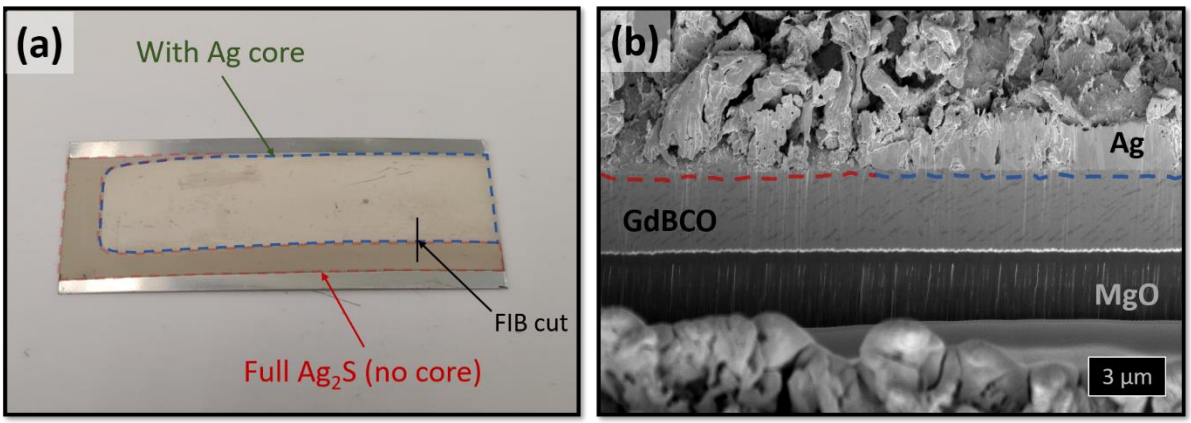

*Figure 6.20: (a) 30x12mm Ag/GdBCO /MgO/Hastelloy tape sample partially sulfided with the CFD pattern **after** the low-pressure atmospheric plasma treatment. (b) SEM-FIB image of the cross-section Ag/GdBCO/MgO after the low-pressure plasma treatment: Porous Ag/GdBCO interface in the Full Ag_2S region (red dashed line) and continuous Ag/GdBCO interface in the region with previous Ag core (blue dashed line).*

According to the SHPM analysis of the B_z field, samples treated with low-pressure plasma presented no detectable reduction in their initial critical current. Nevertheless, the inevitable flaking of the recovered silver stabilizer hindered the continuity of this CFD approach.

6.3 b-CFD Architecture with Sulfide

As briefly commented in section 2.4, increasing the interfacial resistance Ag/HTS is not the only path to create the CFD effect and boost the NZPV on 2G HTS CC tapes. The current crowding during the quench can also be achieved using the already existing buffer layer (MgO for THEVA tapes) as an insulation for splitting the current path [210]. In order to divert the current around the buffer, one must fine-tune the thickness ratio between the tape's top and bottom metallic shunt layer [210]. This buffer-CFD (b-CFD) concept does not require any change in the interfacial resistance to create the CFD effect. Although simpler in theory, it presents a major technical challenge due to the extremely thin thickness of silver (20 – 100 nm) required for the upper shunt layer. In this thickness range, silver is known to agglomerate (dewetting) if annealed in oxygen beyond 400 °C [213], thus making it impossible to have a continuous silver layer and properly oxygenate the REBCO film in a manufactural timeframe. Another approach could be to physically or chemically etch the silver of the final top layer on the commercial tape, which, besides the loss of precious silver material, would also require a very practical, precise and cheap etching technique; something that still needs to be developed for the industrial application.

In this latter scenario, the sulfidation process of silver (section 6.1.4) would emerge as a potential method for implementing the b-CFD architecture. Instead of allowing the sulfidation to take place across the full silver thickness and possibly compromising the Ag/HTS interface, the process could be halted to leave some metallic silver in the HTS interface. By tuning the exposure time to sulfur vapor, the remaining silver thickness could be tuned to create the correct top-bottom shunt ratio needed for the b-CFD effect. Figure 6.21 illustrates the concept of partial sulfidation for creating the b-CFD.

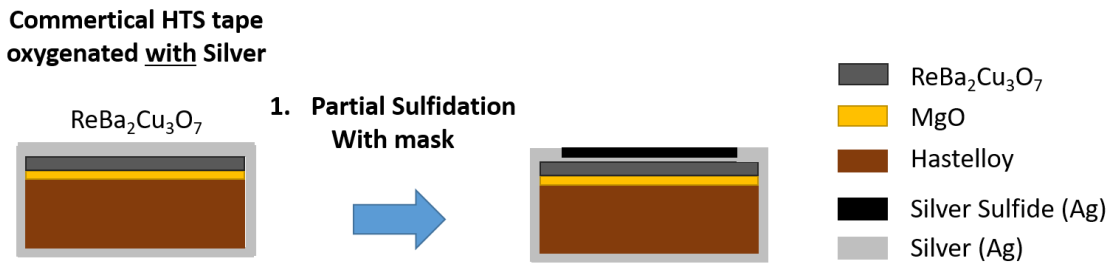

Figure 6.21: Suggested experimental workflow for the incorporation of Sulfur b-CDF tapes in commercial silver coated tapes.

This approach is also attractive because the formation of silver sulfide, in theory, does not "etch" the silver material from the shunt layer. As long as the silver sulfide remains attached to a core layer of metallic silver, a significant amount of the actual silver shunt material should remain stored in the sulfide composition. Moreover, the presence of a thin electrically conductive layer acting as a metallic core underneath the sulfide, allows for new possibilities of reducing the sulfide via electrochemical techniques [285–287] such as:

- Galvanic (cathodic) reduction - when the source of energy for the reaction comes from the formation of a galvanic cell where the tarnished object acts as a cathode (the sulfide on the silver) and a less noble metal, usually zinc or aluminum, acts as an anode [288].

- Electrolytic reduction - when the source of energy for the reduction reaction is external like a small generator or a battery. The two most common methods described for this in the conservation literature are [285]: normal reduction and consolidative reduction. Normal electrolytic reduction uses a DC power supply and the consolidative reduction [289] employs a half-wave AC power supply. As mentioned before, both techniques require a metal core to be present in the object.

These electrochemical techniques could be used for a selective restoration of the sulfide region. Therefore, creating silver only in zones expected to be used as current contact. These zones would present a bigger effective contact area for current leads and consequently reduce the current contact size.

6.3.1 b-CFD Simulations

Tuning the top and bottom thicknesses of the metallic shunt in the CC to achieve a b-CFD effect instead of altering the interfacial resistance Ag/GdBCO in the classic CFD way can be a simpler approach, but it might also come with a different NZPV performance. In order to analyze the influence of the new proposed "sulfide b-CFD" in the final NZPV of the CC, the simulation template of section 3.5 was used to evaluate THEVA's CC architecture with different combinations for the top and bottom shunt thicknesses.

In these simulations the interfacial resistance was considered uniform across the width with a fixed value of 100 nΩ-cm^2 and only the variable h_{Ag-top} was altered to test different thicknesses. The simulated NZPV curves for the b-CFD structure in comparison with the other architectures are shown in Figure 6.22.

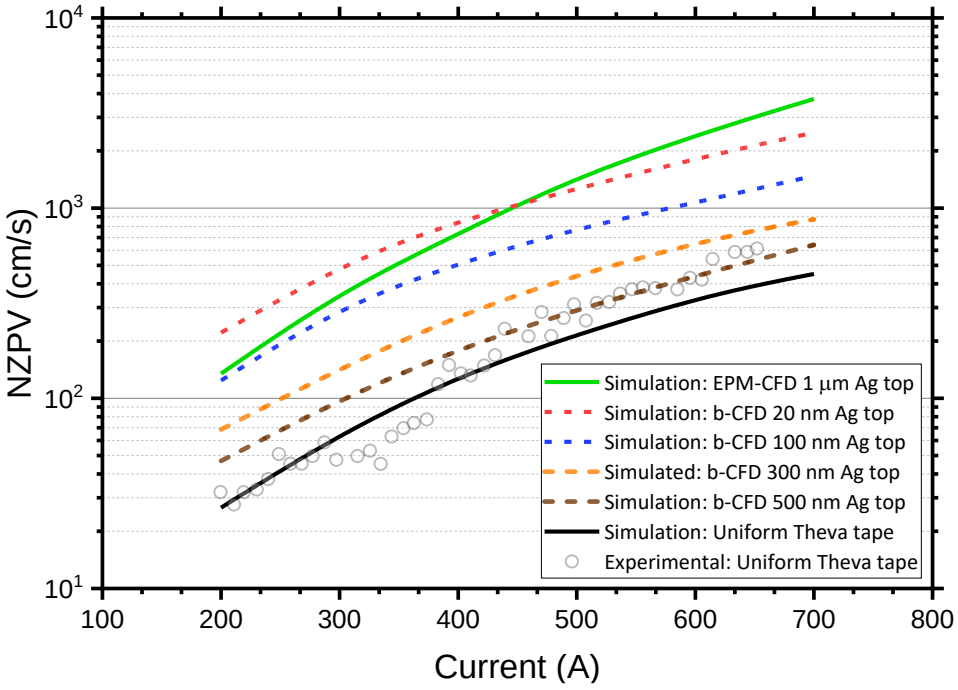

Figure 6.22: NZPV versus Current of the simulated b-CFD architecture in comparison with other architectures; Uniform low interfacial resistance tape and classic CFD from EPM.

Comparing the different simulated b-CFD curves (dashed lines) in Figure 6.22, it becomes clear that the highest NZPV is achieved with the thinnest top silver stabilizer of 20 nm thickness. Bellow 450 A, the NZPV performance for the b-CFD with 20 nm of silver even surpasses that of the simulated classic CFD. However, as the top silver thickness increases from 20 nm to hundreds of nanometers, the NZPV increase is less significant, becoming neglectable at 500 nm. Nonetheless, even with 100 nm of silver, the expected simulated NZPV for the b-CFD would be significant and comparable with the classic EPM-CFD in the 200-450 A range.

6.3.2 NZPV Evaluation of b-CFD Samples with Ag_2S

Two Sulfide-b-CFD samples of approximately 12x130 mm were manufactured at ICMAB utilizing the sulfur vapor method described in subsection 6.1.4. Both samples were cut from a commercial reel of THEVA tape with an average critical current of 517 ± 36 A (Appendix Figure D-2), masked with polyimide along the edges of the top silver shunt, and sulfided for 230 minutes in two separate processes. After the sulfur processing, both tapes were mechanically polished by hand with a lint free cloth for removing the sulfide excess and subsequently sent to *FASTGRID* patterns in EPM for NZPV evaluation and current limitation tests.

Before starting the actual NZPV tests, both samples were tested for their critical currents at 77 K: Sample #1 presented an I_c ≈ 340 A and sample #2 an I_c ≈ 413 A. These values reveal an I_c reduction of approximately 35% and 19% respectively, thus indicating that the sulfide formation reached the GdBCO interface and possible degradation took place. After determining I_c, the NZPV for both samples was measured for different applied current levels at 77 K as shown in Figure 6.23.

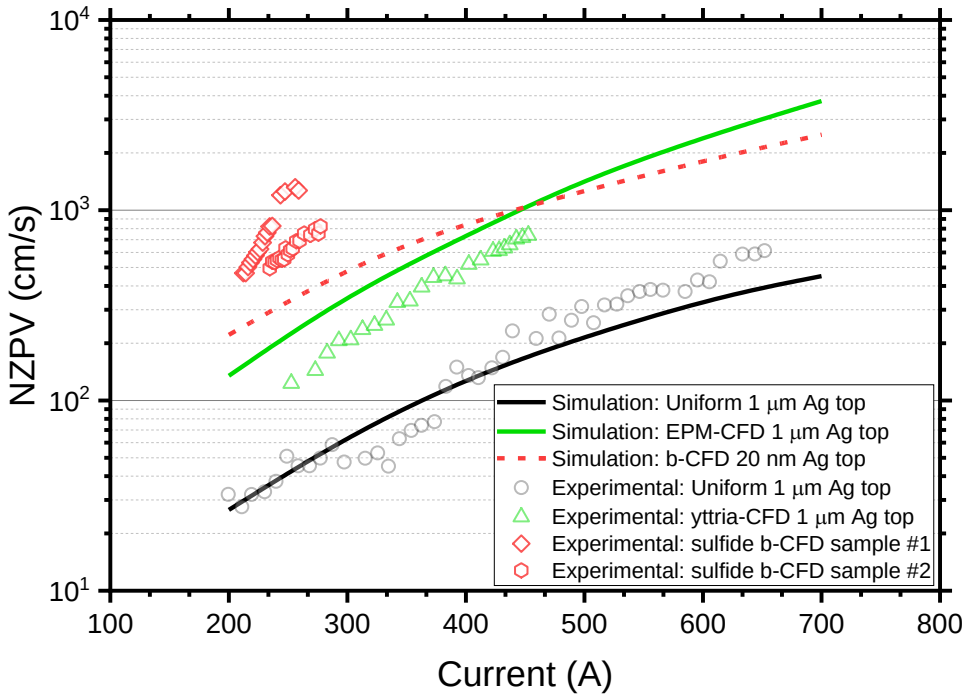

Figure 6.23: NZPV versus applied current for two Sulfide b-CFD samples, experimentally made at ICMAB with sulfidation of the silver shunt. The b-CFD experimental data is plotted against the 1st and 2nd route of Yttria-CFD, uniform tape and classic CFD from EPM.

Both b-CFD samples presented a significant 10x increase in NZPV in the range 200-300 A when compared to the uniform tape, and a 5x NZPV when compared to the 2nd Yttria-CFD route. Such NZPV increase was beyond the maximum expected simulated curve (red dashed line in Figure 6.23) of 20 nm of silver and reinforces the assumption that all the top silver stabilizer was converted into sulfide. One could affirm that part of the NZPV boost could be related to an increase in the conductor's resistance due to the conversion of almost 1 µm of silver into sulfide. However, the room temperature resistance of the b-CFD tapes was only ~15-20 % higher than the average 4.4 mΩ/cm linear resistance of THEVA's uniform tape with full silver shunt. Meaning that only a minor part of the NZPV enhancement came from the "missing" shunt layer. No degradation of I_c in the b-CFD samples was observed after the NZPV measurements.

Evidently, creating the b-CFD effect on a CC leaving 20 nm (or less) of silver stabilizer after vapor sulfidation would be ideal to achieve the best NZPV performance. However, seeing a possible 35% reduction in I_c due to sulfur degradation in the Ag_2S/GdBCO interface and looking back at the sulfidation rate of Figure 6.10, sulfiding a 1 µm thick silver film down to an homogenous 20 nm layer without risking some I_c reduction would be very difficult due to the unprecise reaction rate of the current sulfur vapor technique. In this case, working with an expected 100 nm range for the top silver stabilizer would be a more realistic perspective.

Furthermore, an important remark was that the NZPV data measured along the left and right side of the magnetic defect was not symmetric for these samples. The plotted NZPV values shown in Figure 6.23 are an average between the right and left sides of the tape. This could explain the NZPV slight deviation between samples. However, this result could also indicate an inhomogeneous sulfidation leaving an asymmetric thickness of silver along the tape.

6.3.3 DC Limitation Tests for b-CFD Samples with Ag_2S

After the NZPV measurements, sample #1 was tested in DC limitation utilizing the set-up described in subsection 3.4.5 with the voltage array illustrated in the Appendix Figure C-2 and a NdFeB magnet positioned in the middle of the length.

Initially, the sample was tested in a sequence of voltage pulses of 4 ms increasing the amplitude from 5 to 12 V. Between 5 and 6 V, the fault current level around the sample's critical current ($I_c \approx 340$ A) led to a limitation in hot-spot regime. The hot-spot regime is exemplified in Figure 6.24(a) where the current stabilizes around 350 A at t = 2 ms and only later at t = 2.3 ms, the global E-field increases sharply to 15 V/m in less than 300 µs indicating the quench of the sample at t = 2.5 ms.

Figure 6.24(b) shows the evolution of the local electric field across the length on the left side of the sample according to the disposition of the voltage taps illustrated in Appendix Figure C-2. With probe ai38 being the hot-spot point of origin and taking 2 V/m as the quench criteria, is evident that the quench did not spread over the full length of the tape. Still, the quench did spread considerably over 3.3 cm instead of just a few millimeters as it would be the case for a uniform tape with low interfacial resistance. This feature allowed the tape to limit 30% of the fault without suffering damages from the original hot-spot. In addition, probe ai38 reveals how the electric field remained stable at 40 V/m in the original hot-spot location thus hindering excessive heat accumulation.

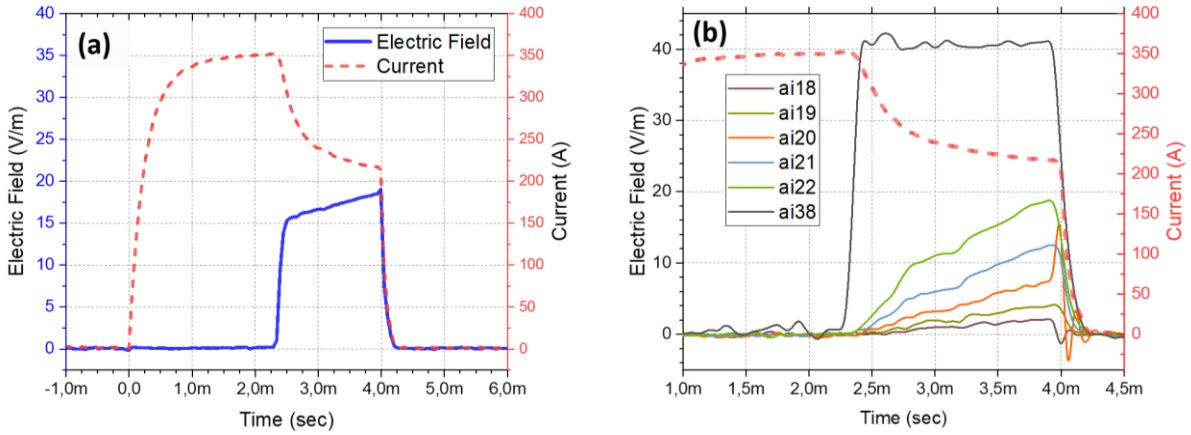

Figure 6.24: Electric field and current evolution during DC limitation tests for b-CFD tape done with silver sulfide. DC limitation in hot-spot regime for 4 ms fault with 5 V in the capacitors. (a) Global electric field evolution of the sample during fault limitation. (b) Local electric field evolution across the length of the sample during fault limitation.

For voltages beyond 6 V, the fault current level surpassed 400 A and the clear-fault regime was reached. This condition is exemplified in Figure 6.25(a) where a 12 V voltage pulse was applied. The current (red dashed line) peaked at 500 A surpassing the sample's critical current ($I_c \sim 340$ A), thus making the sample rapidly switch to the normal state limiting the current to 300 A. Looking at Figure 6.25(b) and considering 10 V/m as the quench criteria, one can confirm that the clear-fault condition induced a quench across the full length in less than 100 µs.

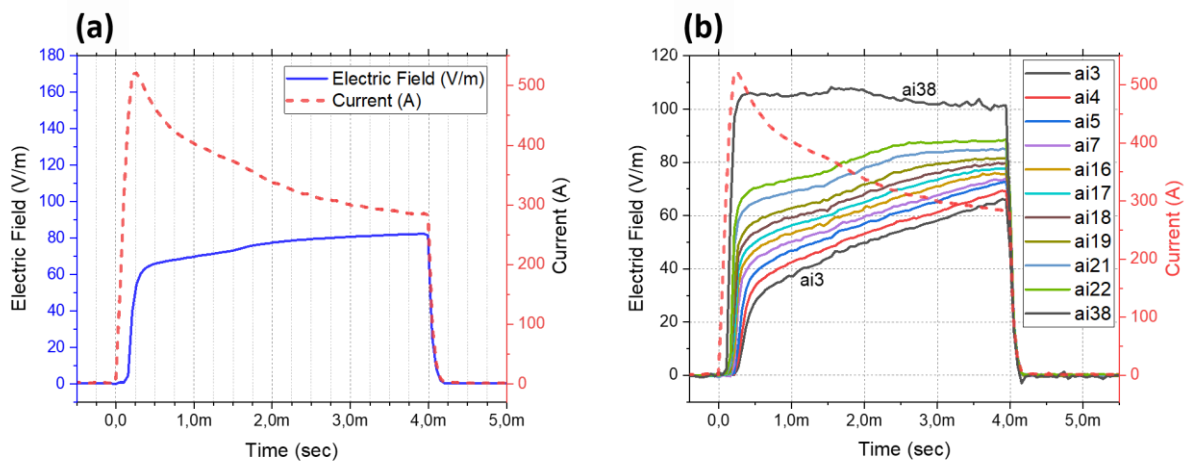

Figure 6.25: Current and electric field evolution during DC limitation tests for b-CFD tape done with silver sulfide. DC limitation in clear-fault for 4 ms fault with 12 V in the capacitors. (a) Global electric field evolution of the sample during fault limitation. (b) Local electric field evolution across the length of the sample during fault limitation.

The sample's critical current remained unaltered after all limitation tests using 4 ms voltage pulses from 5 to 12 V. Therefore, a second sequence of tests was performed holding the applied voltage at 12 V and increasing the fault time from 4 ms up to 40 ms. The limitation behavior of the sample for the 40 ms fault test is shown in Figure 6.26(a). The current peaked at 500 A and was immediately limited down to 200 A after 40 ms. The E-field increased sharply in the beginning and stabilized around 95 V/m. From the E-Field and Current curves in Figure 6.26(a), the power density (W/m) over time is calculated, and by integrating the area under the power density curve, the total energy density (J/m) dissipated during limitation is found to be 756 J/m. Considering an adiabatic process across the tape's cross-section (width x thickness), and the known range of energy density $\int_{T_{op}}^{T_t} c_p(T)dT$, the maximum average temperature was estimated to be 300 K and agrees with the fact that the sample suffered no reduction of its initial I_c after the test.

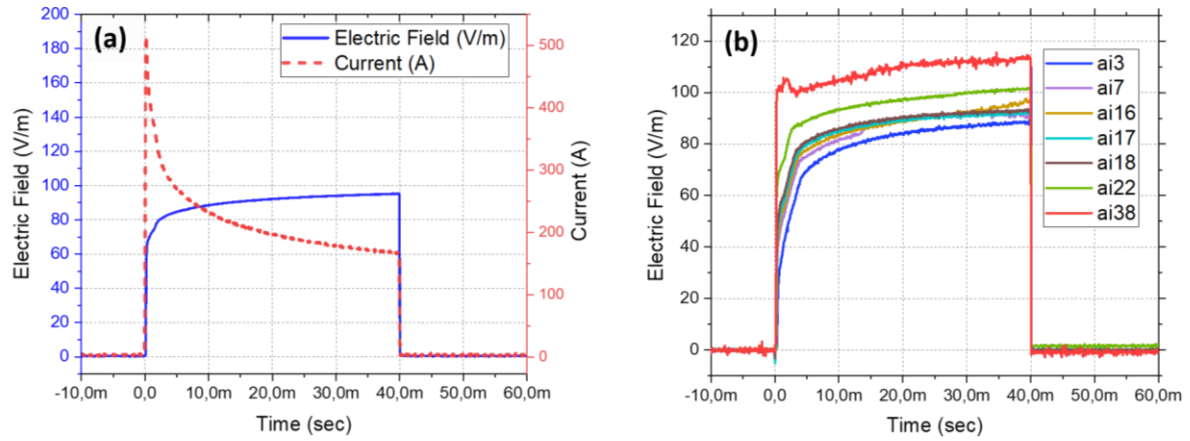

Figure 6.26: DC limitation test for 40 ms fault with 12 V discharge for b-CFD tape with silver sulfide. (a) Global electric field evolution of the sample during fault limitation. (b) Local electric field evolution across the length of the sample during fault limitation.

Figure 6.26(b) shows that the electric field gradient across the length reached a maximum of 15 V/m between probes ai3 and ai38 located at one end of the tape and at the magnet position respectively. This is an indication of a fairly homogenous quench behavior, as expected from a clear-fault scenario.

The sample did not present any degradation of I_c after the DC limitation tests at 12 V ranging from 4 to 40 ms and subsequently, the tests were ceased.

7 Conclusion and Outlook

The hot-spot formation in the state-of-the-art 2G HTS coated conductors is basically a combination of two factors: A local quench happening along the tape's length, and a slow propagation of the normal zone (NZPV). Indeed, the chances of a local quench can be minimized by suppressing external sources of temperature disturbance with better cryogenic designs, but due to the reel-to-reel manufacturing process of the REBCO film, natural I_c fluctuations along the tape's length makes the hot-spot scenario an intrinsic issue for HTS tapes. If the current being transported across the tape reaches a value close to the tape's average I_c, regions with lower-I_c can spontaneously quench and - due to a low thermal conductivity k (W/m-K) and high heat capacity c_p (J/m^3-K) of the compound materials in the wire - the slow NZPV helps develop a hot-spot. This issue is expected in all superconducting device designs with long lengths (>10 m) of HTS tape, such as magnets, motors and generators, but it becomes crucial for resistive Superconducting Fault Current Limiters (SFCL).

As discussed in section 2.3, the price of a resistive SFCL is directly linked to the cost of the amount of conductor needed to safely limit the current fault in the clear-fault scenario ($I_p > I_c$). Since the commercial price of 200-250 €/kA/m is not expected to decrease substantially in the near future, the length constrain is directly linked to the electric field under limitation E_{lim}. Considering only the traditional metals and alloys used in the 2G HTS architecture (Copper, Silver, Nickel and Hastelloy), the value of E_{lim} can either be increased by reducing the amount of stabilizer (Silver, Copper or Nickel) to strengthen the wire's final resistance ρ (Ω-m) or by increasing the amount of Hastelloy to bump up the heat capacity c_p. However, reducing the stabilizer material makes the tape vulnerable to the hot-spot regime ($I_p \approx I_c$) since the critical current limit I_{c-lim} is also reduced and its value can go below the actual I_c of the tape. Therefore, adding Hastelloy material becomes the preferable way to increase E_{lim} and I_{c-lim} simultaneously.

Still, in order to have a bendable wire for making coils, a practical tape thickness of about 600 µm is required and E_{lim} reaches a practical limit around 150 V/m. This value represents a substantial cost reduction in comparison with the 50 V/m of the standard tapes manufactured today, but simply increasing the substrate thickness to 600 µm is not a viable solution for the problem since all 2G HTS CC manufactures have opted to increase the engineering critical current density J_e by reducing the Hastelloy substrate thickness below 100 µm. The current reel-to-reel systems in the industry are not prepared to work with such thick Hastelloy substrate. In the current state of the 2G architecture, the best solution for the hot-spot scenario must be found with the available standard substrate thicknesses ranging from 30 to 100 µm or with another new easy-to-adapt substrate material.

The solution for this E_{lim} and I_{c-lim} conundrum was investigated in the *FASTGRID* project for a resistive SFCL operating in HVDC with three different attempts of directly enhancing the thermal properties of the wire:

- High-$c_p$shunt: Coating the stabilizer with a low-cost insulator with high thermal capacity c_p
- Hastelloy shunt: Solder a 500 µm thick Hastelloy shunt on top of the silver stabilizer with a 10 µm thick layer of tin solder
- Sapphire substrate tape: Grown the REBCO film on top of long sapphire ribbons (1 m) with high thermal diffusivity (cm^2/s).

Although promising, all of these attempts do not tackle the main issue of the hot-spot formation revolving the inherit slow normal zone propagation velocity (NZPV) of the 2G HTS architecture. In fact,

adding Hastelloy or a high-c_p material to the shunt layer only further reduces the NZPV, making the wire thicker and extremely dependent on the thermal properties of the extra shunt material. Increasing c_p might be useful, but it does not seem to be the ultimate solution for creating a robust HTS tape against the hot-spot.

The current flow diverter (CFD) is a concept that has proven to be able to substantially increase the NZPV of tapes by more than one order of magnitude while being able to maintain a low interfacial resistance for practical current contacts. However, the experimental method developed by the original creators at EPM of etching and re-sputtering silver is not viable for the production of long lengths of HTS tape. Therefore, still in the framework of the *FASTGRID project,* this thesis investigated new manufacturing routes capable of re-creating the CFD effect in commercial 2G HTS CC using THEVA tape as template.

7.1 Epoxy-CFD

In the initial characterization of THEVA's REBCO film, we found that the outgrowth peaks made of an unknown GdBCO phase are conductive and can reach dimensions of up to 1 µm in height on the surface of the superconducting GdBCO film. When covering 1% of the relative area, these peaks can indeed affect considerably the final interfacial resistance between the silver stabilizer and the REBCO. However, when testing the short-circuit effect with the epoxy SU-8 2000, even with thin 200 nm layers, the interracial resistance was kept high enough (~100 mΩ-cm^2) for creating the expected CFD effect.

Based on the interfacial resistance measurements performed with the epoxy SU-8, the same epoxy was considered as a possible material for creating tapes with the CFD structure. As a preliminary test, pre-oxygenated 5 cm tapes were altered to include a ~500 nm thick SU-8 layer in between the silver stabilizer and the HTS material. The SHPM measurements indicated no significant degradation of the tape's superconducting properties coming from the epoxy after the CFD alteration. However, the NZPV and DC limitation transport tests provoked a recurrent degradation of the I_c for samples above 10 cm. After the transport tests, the SHPM measurements of the B_z distribution revealed a consistent defective pattern across the length of the samples, thus indicating a degradation due to the quench thermal stress. Complementary to the SHPM, SEM-FIB cross-sectional images confirmed the link between the degradation of the GdBCO and the occurrence of a buckling process happening in the SU-8/GdBCO interface. Furthermore, *COMSOL* simulations for the SU-8-CFD structure showed that due to the epoxy low thermal conductivity (0.3 W/m-K at RT), a large temperature gradient across the epoxy layer is created during quench (20000 K/mm). Such gradient, in combination with a high coefficient of thermal expansion can theoretically produce a Von Mises stress up to 16 MPa in the SU-8/GdBCO interface capable of delaminating the shunt layer (subsection 4.3.1).

The SU-8-CFD route led to the conclusion that in order for any epoxy composite to be compatible with the CFD architecture, both thermal conductivity and thermal expansion, should be improved to minimize temperature gradients and thermal stress. Improving the low thermal conductivity (0.2 - 0.5 W/m-K) of polymers with fillers is a well-known, proven method that has been under intense research for two decades now [290,291]. However, to fabricate polymer-based nanocomposites in an industrial commercial scale with high thermal conductivity is still a challenge because of difficulties such as filler aggregation and large inter-filler thermal contact resistance [292]. Moreover, the thermal conductivity of the polymer depends upon filler size, mixing conditions, filler dispersion and chemical interaction

between polymer matrix and the filler [293]. Whereas the mechanical properties such as tensile strength and young modulus, depends on the filler geometry and size. Pursuing the tuning of all these parameters would defeat the main purpose of the study to find a simple effective low-cost solution for the CFD application. Therefore, alternative commercial coating processes for easy scalability were investigated.

7.2 Graphite-CFD

In the 2nd CFD route, a commercial colloidal solution of graphite platelets traded by the name Graphite 33 was considered for creating the CFD tape. This water-free low-cost solution was spray-coated on top of the GdBCO surface of pre-silver-etched tape samples and a preliminary evaluation via SHPM measurements revealed only a minor decrease of 10% in the original I_c. Moreover, due to the reasonable electrical conductivity of the coating composed of superposed graphite platelets (100-600 nm size), the shunt layer of the CC could be reconstructed inexpensively via copper electroplating afterwards. Accordingly, spray coated graphite-CFD samples with I_c~500 A were electroplated with copper and tested in DC and AC fault limitation. The relative NZPV boost due to the CFD in comparison with the uniform tape was confirmed as well as the robustness of the tape against the hot-spot regime. However, in both experimental set-ups (AC and DC), due to the porosity of the graphite in the GdBCO interface, the coating did not have the best adhesion for withstanding the thermal shock cycles of each quench and all samples showed a major pealing of the Cu/Graphite layers. Nevertheless, the use of conductive graphite nanoparticles retains its potential as a low-cost simple method for creating the CFD effect if a reduction of the graphite porosity in the interface can be achieved, as this will improve adhesion with the ceramic GdBCO. Reducing the particle's size of the filler or changing the matrix and/or matrix-filler ratio could be two methods to accomplish this. Albeit, decreasing the particle size below 100 nm might lead to a substantial increase in the graphite nanocomposite price, therefore the polymeric matrix and matrix-filler ratio might be a better approach to fill the graphite pores and improve the adhesion with the GdBCO. The initial SU-8 2000 appears to be a good substitute since similar advantages have been accomplished with carbon nano tubes (CNT) [294]. But still, filler aggregation is a major technical issue that will most likely require effort in future works for advancing this technique [295].

7.3 Yttria-CFD

The 3rd CFD route consisted of using chemical solution deposition (CSD) methods such as spin coating and ink jet printing to coat the REBCO layer with nanolayers of insulating amorphous yttria (Y_2O_3). In the first attempt of this route, the bilayer Y_2O_3/GdBCO was oxygen-annealed in a single process after the silver coating, i.e. "*post-oxygenation*". However, this approach has shown to be impractical due to temperature restrictions regarding the compatibility of the GdBCO and yttria. In order to load oxygen in the GdBCO and achieve an orthorhombic structure with high I_c, the yttria thickness should not overstep the 250 nm range. Yet, in this thickness range, above 500 °C, the thin yttria tends to crystalize and lose density thus allowing silver diffusion. As a consequence, interfacial resistance drops below 10^{-5} Ω-cm^2 and the CFD effect is extinguished. On the other hand, when trying to maintain the amorphous phase oxygenating below 500 °C, for short periods (less than a day), the final average I_c

presented unacceptable fluctuations of 60% across the length due to inhomogeneous oxygen in-diffusion in the GdBCO film. It was only with long oxygenation periods of several days that an acceptable I_c value with 10% deviation was achieved and yet, no CFD effect was observed. No concrete evidence was found to explain precisely the absence of the CFD in the later samples, but a reasonable speculation is the presence outgrowth peaks short circuit effect coming from the GdBCO substrate, in combination with a subtle silver diffusion hard to detect via SEM-FIB imaging.

Satisfactory results were only found in the second attempt of the yttria-CFD route where the GdBCO film was annealed in oxygen prior to depositing the yttria and the silver layers, i.e. "*pre-oxygenation*". According to the SHPM analysis, the yttria deposition by CSD reduced I_c by ~50% after pyrolysis at 400 °C. However, after the silver deposition and subsequent oxygen annealing, additional oxygen incorporation recovered I_c to ~75 % of its original value, thus essentially validating the potential of this CFD processing approach. The presence of the current crowding effect, characteristic of CFD effect, was confirmed via special CTL measurements and the expected associated NZPV boost was tested with the fabrication of long length CFD samples (> 10 cm). For the sample having the silver annealed at 400 °C, the NZPV increased 4-5x in comparison with the uniform tape. Unfortunately, the contact resistance on the current leads was estimated in the 10^{-4} Ω-cm^2; too high for operating above 500 A. This issue was countered by re-annealing the sample at 450 °C, leading to a 20% drop in the previous 4-5x NZPV and an increase > 15% in I_c. This result illustrated once more the problem of silver diffusion through the yttria-CFD, but also reinforced the importance of the silver acting as a catalytic element for the surface reactions to initiate the oxygen incorporation in the GdBCO.

In summary, with CSD methods for depositing yttria nanolayers in a *pre-oxygenation route,* it was possible to implement the CFD architecture for the first time with a low-cost commercial technique. The next step would be to use the same technique to reproduce the yttria-CFD in long lengths (> 1 m) and reassure the industrial feasibility to manufacturers.

Furthermore, it was concluded that for the *post-oxygenation* of the REBCO film with the CFD architecture to be successful, the future CFD material under consideration should:

- Be a poor electronic conductor, chemically stable and capable of maintaining its crystalline and/or amorphous structure in 300 - 500 °C;
- Be a decent oxygen ionic conductor with a bulk diffusion coefficient D not too far below YBCO's ab-plane diffusion $D_{ab} = 10^{-11} - 10^{-9}$ cm^2/s (considering the same temperature range of 300 - 500 °C, with a coating thickness < 10 µm);
- Have a poor silver diffusion D_{Ag} of at least one order of magnitude below D_{ab} so that oxygen diffusion may act faster to finish oxygenation before compromising the CFD interface in case of an unavoidable silver diffusion.

In fact, ceramic insulators with high oxygen ionic diffusion are the main research topic of electrolyte materials for applications in solid oxide fuel cells (SOFC)[256] and oxygen filters. Zirconia and Ceria doped with rare earth oxides (Sm_2O_3, Y_2O_3, Gd_2O_3, etc.) are the most promising materials for the solid electrolyte [296], being Yttria-stabilized zirconia (YSZ) the most commonly used due to its resistance against the reducing atmosphere present in both the anode and cathode side of the SOFC [297]. In the case of the CFD architecture, manufacturing Ceria-based & YSZ coatings, by sintering them at temperatures above 1000 °C [298], is not suitable because of the inevitable melting of REBCO and

consequential loss of the biaxial texture [299]. However, the most recent methods for depositing gadolinia-doped ceria (GDC) layers by MOCVD at low temperatures, could be a solution for depositing a CFD coating with the temperature restrictions of the REBCO [300,301]. In addition, ionic conductivity of GDC at temperatures of 500–600 °C is similar to the ionic conductivity of sintered YSZ electrolytes at temperatures > 1000 °C (Figure 7.1)[302,303].

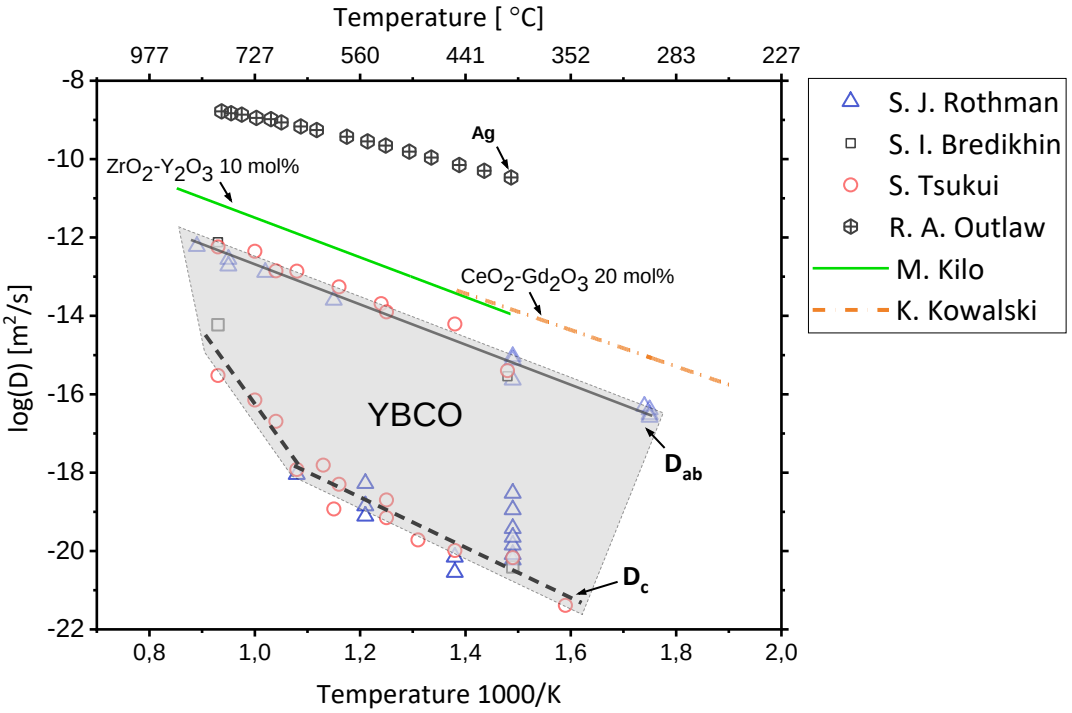

Figure 7.1: Arrhenius plot of chemical diffusion coefficient of oxygen in YBCO, Yttria Stabilized Zirconia (YSZ) and Gadolinia Doped Ceria (GDC) from different authors: S. J. Rothman (blue triangles); S. I. Bredikhin (black squares); S. Tsukui (red circles); YSZ from M. Kilo (green solid line); GDC from K. Kowalski (orange dashed line); The oxygen diffusion in silver is also plotted from R. A. Outlaw data for comparison (crossed black hexagons). The light grey area delimits the bulk oxygen diffusion of a generic oriented YBCO film based on the data collection.

Nevertheless, to the current knowledge, a material with all the previously listed requirements that can also be consistently deposited in a compatible low-cost technique, like spray-coating or IJP at low temperatures, remains unknown. As of now, the only practical solution for achieving a more attractive CFD tape with the *post-oxygenation* approach seems the functionalization of the CFD coating with pores to promote the diffusion path of oxygen (subsection 5.3.3). Albeit, this method will require a thorough investigation of the aspect ratio of the pores to halt silver diffusion during the oxygen annealing.

7.4 Sulfide-CFD

In the 4th CFD route, the initial Sulfide-CFD concept was devised with the intention of simplifying the CFD manufacturing by bypassing the need to anneal the final REBCO film and silver stabilizer in oxygen atmosphere. Therefore, starting with commercial GdBCO silver coated tapes, the idea was to alter the silver composition on the stabilizer in a controllable chemical process capable of reaching the Ag/REBCO interface and increasing the interfacial resistance. Differently from the majority of metal

oxides, the sulfide formation has an almost linear reaction rate on the surface of silver [304] allowing a fast diffusion process to reach the Ag/REBCO interface. In addition, the sulfide could be converted back to metallic silver using a reduction reaction with active hydrogen to restore the stabilizer/shunt electric conductivity. For this manner, sulfur (S) was chosen as the primary element to form silver sulfide (Ag_2S) across the ~1 µm thick silver stabilizer, only to be reduced back to silver (Ag) afterwards to complete the CFD.

The liquid reaction containing sulfur compounds has shown to be incompatible with the GdBCO tapes from THEVA due to liquid infiltration and corrosion through the outgrowth peaks (i.e. precipitates) which jeopardize the GdBCO film. Alternatively, the gas reaction with the allotrope S_8 was quite successful in providing a controllable reaction for the sulfide formation. The S-gas technique was applied to 5 cm tape samples and the CTL measurements confirmed the presence of the CFD current crowding effect due to the presence of sulfide. Furthermore, a considerable NZPV boost of 4-5x was also measured experimentally for 10 cm samples sulfided with the CFD pattern and re-sputtered with silver. However, the final step of reducing the sulfide back to silver was and still is the major challenge for this Sulfide-CFD approach. Recovering the silver with atmospheric plasma and forming H_2/Ar gas is possible, but it is difficult to avoid overheating the tape with the moving plasma flame. And even though avoiding the heat from the atmospheric plasma with a low-pressure hydrogen plasma chamber was very effective, the porosity in the final silver layer led to subsequent pealing of the final stabilizer. However, the porosity in the Ag/GdBCO interface was not detected in the sulfide layers containing an underlining metallic silver core after the low-pressure plasma treatment. This important feature of the sulfide reduction led to one final attempt to create the CFD effect with the buffer-CFD architecture.

With the assistance of the gas sulfidation technique to reduce the thickness of the top stabilizer from 1 µm to ~100 nm on a commercial silver coated GdBCO CC, the top/bottom thickness ratio of the shunt was tuned to create the b-CFD effect. Samples of 14 cm length were created with this Sulfide-b-CFD technique and tested for the NZPV revealing a remarkable increase above 10x in comparison to the uniform tape for the range 200-300 A. In addition, one 14 cm sample with I_c~340 A was tested in DC limitation for hot-spot and clear-fault conditions. In hot-spot regime, the tape presented fast limitation response completing the current limitation in less than 4 ms and, in clear-fault regime, the E_{lim} was pushed up to an average of 95 V/m for 40 ms without any signs of I_c degradation. Nevertheless, the NZPV improvement between the left and right side of b-CFD samples presented a noticeable disparity indicating irregularity in the silver core thickness underneath the sulfide.

At the moment, the sulfide-b-CFD retains an enormous potential as an extremely simple method to boost the NZPV in any commercial 2G HTS CC with a silver coating finish. Still, before implementing this technique in large scale, a consistent thickness of the silver core under the sulfide must be achieved. This technical aspect deserves a standalone study controlling the S_8 partial pressure to identify all the variables controlling the homogeneity of the sulfidation reaction.

References

[1] J.S. Galsin, Physical Effects of Impurities in Metals, in: Impurity Scatt. Met. Alloy., Springer US, Boston, MA, 2002: pp. 93–123. https://doi.org/10.1007/978-1-4615-1241-7_5.

[2] H.K. Onnes, Further experiments with Liquid Helium. G. On the Electrical Resistance of Pure Metals, etc. VI. On the Sudden Change in the Rate at which the Resistance of Mercury Disappears., K. Ned. Akad. van Wet. Proc. 14 (1991) 818–821. https://doi.org/10.1007/978-94-009-2079-8_17.

[3] A.C. Rose-Innes, E.H. Rhoderick, A.M. Goldman, Introduction to Superconductivity, Am. J. Phys. 38 (1970) 1048–1049. https://doi.org/10.1119/1.1976539.

[4] W. Meissner, R. Ochsenfeld, Ein neuer Effekt bei Eintritt der Supraleitfähigkeit, Naturwissenschaften. 21 (1933) 787–788. https://doi.org/10.1007/BF01504252.

[5] H. London, F. ; London, The electromagnetic equations of the supraconductor, Proc. R. Soc. London. Ser. A - Math. Phys. Sci. 149 (1935) 71–88. https://doi.org/10.1098/rspa.1935.0048.

[6] Jeffrey W. Lynn, High Temperature Superconductivity, Springer New York, New York, NY, 1990. https://doi.org/10.1007/978-1-4612-3222-3.

[7] V.L. Ginzburg, On Superconductivity and Superfluidity (What I Have and Have Not Managed to Do), as well as on the'Physical Minimum' at the Beginning of the 21st Century, ChemPhysChem. 5 (2004) 930–945. https://doi.org/10.1002/cphc.200400182.

[8] A.A. Abrikosov, Nobel Lecture: Type-II superconductors and the vortex lattice, Rev. Mod. Phys. 76 (2004) 975–979. https://doi.org/10.1103/RevModPhys.76.975.

[9] U. Essmann, H. Träuble, The direct observation of individual flux lines in type II superconductors, Phys. Lett. A. 24 (1967) 526–527. https://doi.org/10.1016/0375-9601(67)90819-5.

[10] O. V. Dobrovolskiy, D.Y. Vodolazov, F. Porrati, R. Sachser, V.M. Bevz, M.Y. Mikhailov, A. V. Chumak, M. Huth, Ultra-fast vortex motion in a direct-write Nb-C superconductor, Nat. Commun. 11 (2020) 3291. https://doi.org/10.1038/s41467-020-16987-y.

[11] J.N. RJABININ, L.W. SHUBNIKOW, Magnetic Properties and Critical Currents of Supra-conducting Alloys, Nature. 135 (1935) 581–582. https://doi.org/10.1038/135581a0.

[12] J. Bardeen, M.J. Stephen, Theory of the Motion of Vortices in Superconductors, Phys. Rev. 140 (1965) A1197–A1207. https://doi.org/10.1103/PhysRev.140.A1197.

[13] M.P.A. Fisher, Vortex-glass superconductivity: A possible new phase in bulk high-Tc oxides, Phys. Rev. Lett. 62 (1989) 1415–1418. https://doi.org/10.1103/PhysRevLett.62.1415.

[14] R.H. Koch, V. Foglietti, W.J. Gallagher, G. Koren, A. Gupta, M.P.A. Fisher, Experimental evidence for vortex-glass superconductivity in Y-Ba-Cu-O, Phys. Rev. Lett. 63 (1989) 1511–1514. https://doi.org/10.1103/PhysRevLett.63.1511.

[15] G. Fuchs, B. Holzapfel, K.H. Müller, L. Schultz, Superconductors: Basic Properties and Materials Development of MgB2, in: Encycl. Mater. Sci. Technol., Elsevier, 2006: pp. 1–6. https://doi.org/10.1016/B0-08-043152-6/02023-4.

[16] P.W. Anderson, Theory of Flux Creep in Hard Superconductors, Phys. Rev. Lett. 9 (1962) 309–311. https://doi.org/10.1103/PhysRevLett.9.309.

[17] P.W. ANDERSON, Y.B. KIM, Hard Superconductivity: Theory of the Motion of Abrikosov Flux Lines, Rev. Mod. Phys. 36 (1964) 39–43. https://doi.org/10.1103/RevModPhys.36.39.

[18] W.H. Warnes, D.C. Larbalestier, Analytical technique for deriving the distribution of critical currents in a superconducting wire, Appl. Phys. Lett. 48 (1986) 1403–1405. https://doi.org/10.1063/1.96923.

[19] C. Plummer, J. Evetts, Dependence of the shape of the resistive transition on composite inhomogeneity in multifilamentary wires, IEEE Trans. Magn. 23 (1987) 1179–1182. https://doi.org/10.1109/TMAG.1987.1064997.

[20] E.H. Brandt, Universality of Flux Creep in Superconductors with Arbitrary Shape and Current-Voltage Law, Phys. Rev. Lett. 76 (1996) 4030–4033. https://doi.org/10.1103/PhysRevLett.76.4030.

[21] E. Zeldov, ’ ", N.M. Amer, G. Koren, A. Gupta, R.J. Gambino, M.W. Mcelfresh, Optical and Electrical Enhancement of Flux Creep in YBa2Cu307-b Epitaxial Films, 62 (1989) 26.

[22] A. Motaman, S. Barua, D. Patel, M. Maeda, K. Cheong, J.H. Kim, S.X. Dou, M.S. Al Hossain, Power-Law Relationship Between Critical Current Density, Microstructure, and the n-Value in MgB2 Superconductor Wires, J. Supercond. Nov. Magn. 27 (2014) 1643–1645. https://doi.org/10.1007/s10948-014-2504-5.

[23] T. Onogi, T. Ichiguchi, T. Aida, Power-law dissipative behavior in high-Tc superconductor, Solid State Commun. 69 (1989) 991–993. https://doi.org/10.1016/0038-1098(89)90010-0.

[24] C.P. Bean, Magnetization of Hard Superconductors, Phys. Rev. Lett. 8 (1962) 250–253. https://doi.org/10.1103/PhysRevLett.8.250.

[25] J.G. Bednorz, K.A. Müller, Possible high-Tc superconductivity in the Ba-La-Cu-O system, Zeitschrift Für Phys. B Condens. Matter. 64 (1986) 189–193. https://doi.org/10.1007/BF01303701.

[26] M.K. Wu, J.R. Ashburn, C.J. Torng, P.H. Hor, R.L. Meng, L. Gao, Z.J. Huang, Y.Q. Wang, C.W. Chu, Superconductivity at 93 K in a new mixed-phase Y-Ba-Cu-O compound system at ambient pressure, Phys. Rev. Lett. 58 (1987) 908–910. https://doi.org/10.1103/PhysRevLett.58.908.

[27] M. Magnuson, T. Schmitt, V.N. Strocov, J. Schlappa, A.S. Kalabukhov, L.-C. Duda, Self-doping processes between planes and chains in the metal-to-superconductor transition of YBa2Cu3O6.9, Sci. Rep. 4 (2015) 7017. https://doi.org/10.1038/srep07017.

[28] H.A. Blackstead, D.B. Chrisey, J.D. Dow, J.S. Horwitz, A.E. Klunzinger, D.B. Pulling, Superconductivity in PrBa2Cu3O7, Phys. Lett. A. 207 (1995) 109–112. https://doi.org/10.1016/0375-9601(95)00653-K.

[29] J.D. Jorgensen, B.W. Veal, A.P. Paulikas, L.J. Nowicki, G.W. Crabtree, H. Claus, W.K. Kwok, Structural properties of oxygen-deficient YBa2Cu3O7- delta, Phys. Rev. B. 41 (1990) 1863–1877. https://doi.org/10.1103/PhysRevB.41.1863.

[30] N.. Andersen, M. von Zimmermann, T. Frello, M. Käll, D. Mønster, P.-A. Lindgård, J. Madsen, T. Niemöller, H.. Poulsen, O. Schmidt, J.. Schneider, T. Wolf, P. Dosanjh, R. Liang, W.. Hardy, Superstructure formation and the structural phase diagram of YBa2Cu3O6+x, Phys. C Supercond. 317–318 (1999) 259–269. https://doi.org/10.1016/S0921-4534(99)00066-0.

[31] S. Graser, P.J. Hirschfeld, T. Kopp, R. Gutser, B.M. Andersen, J. Mannhart, How grain boundaries limit supercurrents in high-temperature superconductors, Nat. Phys. 6 (2010)

609–614. https://doi.org/10.1038/nphys1687.

[32] D. TER HAAR, Collected Papers of L.D. Landau, Elsevier, 1965. https://doi.org/10.1016/C2013-0-01806-3.

[33] H. Maeda, Y. Tanaka, M. Fukutomi, T. Asano, A New High- T c Oxide Superconductor without a Rare Earth Element, Jpn. J. Appl. Phys. 27 (1988) L209–L210. https://doi.org/10.1143/JJAP.27.L209.

[34] M.A. SUBRAMANIAN, C.C. TORARDI, J.C. CALABRESE, J. GOPALAKRISHNAN, K.J. MORRISSEY, T.R. ASKEW, R.B. FLIPPEN, U. CHOWDHRY, A.W. SLEIGHT, A New High-Temperature Superconductor: Bi2Sr3-x Cax Cu2O8+y, Science (80-.). 239 (1988) 1015–1017. https://doi.org/10.1126/science.239.4843.1015.

[35] C.L. Briant, E.L. Hall, K.W. Lay, I.E. Tkaczyk, Microstructural evolution of the BSCCO-2223 during powder-in-tube processing, J. Mater. Res. 9 (1994) 2789–2808. https://doi.org/10.1557/JMR.1994.2789.

[36] L.K. Antonova, A. V. Troitskii, G.N. Mikhailova, T.E. Demikhov, S. V. Samoilenkov, A.A. Molodyk, J. Noudem, P. Bernstein, Current-carrying capability of GdBa2Cu3O7−x HTSC tapes in magnetic fields in the temperatute range of 2–100 K, Bull. Lebedev Phys. Inst. 44 (2017) 61–65. https://doi.org/10.3103/S1068335617030034.

[37] Charles Poole ; Horacio Farach ; Richard Creswick ; Ruslan Prozorov, Superconductivity, 2nd ed., Elsevier, 2007. https://doi.org/10.1016/B978-0-12-088761-3.X5021-2.

[38] S. Maekawa, M. Sato, eds., Physics of High-Temperature Superconductors, Springer Berlin Heidelberg, Berlin, Heidelberg, 1992. https://doi.org/10.1007/978-3-642-84718-9.

[39] A. Di Trolio, G. Grimaldi, G. Mattei, A.M. Testa, Structural and superconducting properties of EuBa 2 Cu 3 O 7 x thin films grown by off-axis pulsed laser deposition, Supercond. Sci. Technol. 17 (2004) 1009–1013. https://doi.org/10.1088/0953-2048/17/8/010.

[40] R. Suryanarayanan, R. Nagarajan, H. Selig, L. Ben-Dor, Preparation by sol–gel, structure and superconductivity of pure and fluorinated LaBa2Cu3O7−d, Phys. C Supercond. 361 (2001) 40–44. https://doi.org/10.1016/S0921-4534(01)00290-8.

[41] C. Andreouli, A. Tsetsekou, Synthesis of HTSC Re(Y)Ba2Cu3Ox powders: the role of ionic radius, Phys. C Supercond. 291 (1997) 274–286. https://doi.org/10.1016/S0921-4534(97)01636-5.

[42] J.L. Macmanus-Driscoll, Materials chemistry and thermodynamics of REBa2Cu3O7?x, Adv. Mater. 9 (1997) 457–473. https://doi.org/10.1002/adma.19970090602.

[43] R. Liang, D.A. Bonn, W.N. Hardy, Evaluation of CuO2 plane hole doping in YBa2Cu3O6+x single crystals, Phys. Rev. B. 73 (2006) 180505. https://doi.org/10.1103/PhysRevB.73.180505.

[44] J. Jung, H. Darhmaoui, H. Yan, Universal behaviour of and in YBCO thin films, Supercond. Sci. Technol. 11 (1998) 973–977. https://doi.org/10.1088/0953-2048/11/10/015.

[45] H. Krauth, Development and Large Scale Production of NbTi and Nb3Sn Conductors for Beam Line and Detector Magnets, in: Supercollider 2, Springer US, Boston, MA, 1990: pp. 631–644. https://doi.org/10.1007/978-1-4615-3728-1_58.

[46] Y. Kazuhisa, O. Kazuya, I. Tetsuya, G. Tomoji, Y. Syuji, J. Tetsuji, Fabrication of Superconducting Oxide Wires by Powder-in-tube Method, US-4906609-A, 1990.

[47] O. V. Kharissova, E.M. Kopnin, V. V. Maltsev, N.I. Leonyuk, L.M. León-Rossano, I.Y. Pinus, B.I.

Kharisov, Recent Advances on Bismuth-based 2223 and 2212 Superconductors: Synthesis, Chemical Properties, and Principal Applications, Crit. Rev. Solid State Mater. Sci. 39 (2014) 253–276. https://doi.org/10.1080/10408436.2013.836073.

[48] T.P. Beales, J. Jutson, L. Le Lay, M. Mölgg, Comparison of the powder-in-tube processing properties of two (Bi2−xPbx)Sr2Ca2Cu 3O10+δpowders, J. Mater. Chem. 7 (1997) 653–659. https://doi.org/10.1039/a606896k.

[49] Y. Iijima, N. Tanabe, Y. Ikeno, O. Kohno, Biaxially aligned YBa2Cu3O7−x thin film tapes, Phys. C Supercond. 185–189 (1991) 1959–1960. https://doi.org/10.1016/0921-4534(91)91104-C.

[50] X. Obradors, T. Puig, Coated conductors for power applications: materials challenges, Supercond. Sci. Technol. 27 (2014) 044003. https://doi.org/10.1088/0953-2048/27/4/044003.

[51] M.P. Paranthaman, T. Izumi, High-Performance YBCO-Coated Superconductor Wires, MRS Bull. 29 (2004) 533–541. https://doi.org/10.1557/mrs2004.159.

[52] A. Goyal, M.P. Paranthaman, U. Schoop, The RABiTS Approach: Using Rolling-Assisted Biaxially Textured Substrates for High-Performance YBCO Superconductors, MRS Bull. 29 (2004) 552–561. https://doi.org/10.1557/mrs2004.161.

[53] W. Prusseit, R. Nemetschek, C. Hoffmann, G. Sigl, A. Lümkemann, H. Kinder, ISD process development for coated conductors, Phys. C Supercond. Its Appl. 426–431 (2005) 866–871. https://doi.org/10.1016/j.physc.2005.01.054.

[54] M. Bauer, R. Metzger, R. Semerad, P. Berberich, H. Kinder, Inclined Substrate Deposition by Evaporation of Magnesium Oxide for Coated Conductors, MRS Proc. 585 (1999) 35. https://doi.org/10.1557/PROC-585-35.

[55] Z. Aabdin, M. Dürrschnabel, M. Bauer, R. Semerad, V. Große, W. Prusseit, O. Eibl, Growth Behavior of DyBa2Cu3O7-δ Thin Films Deposited by Inclined Substrate Deposition for Coated Conductors, Phys. Procedia. 36 (2012) 1445–1449. https://doi.org/10.1016/J.PHPRO.2012.06.240.

[56] T. Zilbauer, P. Berberich, A. Lümkemann, K. Numssen, T. Wassner, G. Sigl, High quality ISD MgO buffers on large scale, flexible metal substrates for RF applications of HTS thin films, Supercond. Sci. Technol. 19 (2006) 1118–1123. https://doi.org/10.1088/0953-2048/19/11/005.

[57] W. Prusseit, C. Hoffmann, R. Nemetschek, G. Sigl, J. Handke, A. Lumkemann, H. Kinder, Reel to Reel Coated Conductor Fabrication by Evaporation, IEEE Trans. Appl. Supercond. 16 (2006) 996–998. https://doi.org/10.1109/TASC.2006.873263.

[58] A. Usoskin, Long-Length YBCO Coated Stainless Steel Tapes with High Critical Currents, in: AIP Conf. Proc., AIP, 2006: pp. 713–719. https://doi.org/10.1063/1.2192414.

[59] G.-M. Shin, R.-K. Ko, K.-J. Song, J.-M. Yoo, C. Park, S.-H. Moon, S.-I. Yoo, Sm-doped YBCO Coated Conductor on the IBAD MgO Template Fabricated by MOD Process, MRS Proc. 1001 (2007) 1001-M05-06. https://doi.org/10.1557/PROC-1001-M05-06.

[60] T.T. Thuy, A.S. Hoste, A.G.G. Herman, A.K. De Buysser, A.P. Lommens, A.J. Feys, A.D. Vandeput, A.I. Van Driessche, Sol-gel chemistry of an aqueous precursor solution for YBCO thin films, (n.d.). https://doi.org/10.1007/s10971-009-1987-1.

[61] I. Van Driessche, J. Feys, S.C. Hopkins, P. Lommens, X. Granados, B.A. Glowacki, S. Ricart, B. Holzapfel, M. Vilardell, A. Kirchner, M. Bäcker, Chemical solution deposition using ink-jet

printing for YBCO coated conductors, Supercond. Sci. Technol. 25 (2012) 065017. https://doi.org/10.1088/0953-2048/25/6/065017.

[62] Z. Yin, Y. Huang, N. Bu, X. Wang, Y. Xiong, Inkjet printing for flexible electronics: Materials, processes and equipments, Chinese Sci. Bull. 55 (2010) 3383–3407. https://doi.org/10.1007/s11434-010-3251-y.

[63] X. Ding, J. Liu, T.A.L. Harris, G.W. Woodruff, A Review of the Operating Limits in Slot Die Coating Processes, (n.d.). https://doi.org/10.1002/aic.15268.

[64] V.R. Vlad, A. Usoskin, S. Lee, V. Petrykin, A. Molodyk, E. Bartolome, M. Vilardell, A. Calleja, A. Meledin, X. Obradors, T. Puig, S. Ricart, G. Van Tendeloo, Inkjet Printing Multideposited YBCO on CGO/LMO/MgO/Y2O3/Al2 O3/Hastelloy Tape for 2G-Coated Conductors, IEEE Trans. Appl. Supercond. 28 (2018) 1–5. https://doi.org/10.1109/TASC.2018.2808403.

[65] V. Matias, E.J. Rowley, Y. Coulter, B. Maiorov, T. Holesinger, C. Yung, V. Glyantsev, B. Moeckly, YBCO films grown by reactive co-evaporation on simplified IBAD-MgO coated conductor templates, Supercond. Sci. Technol. 23 (2010) 014018. https://doi.org/10.1088/0953-2048/23/1/014018.

[66] J.-H. Lee, H. Lee, J.-W. Lee, S.-M. Choi, S.-I. Yoo, S.-H. Moon, RCE-DR, a novel process for coated conductor fabrication with high performance, Supercond. Sci. Technol. 27 (2014) 044018. https://doi.org/10.1088/0953-2048/27/4/044018.

[67] S.R. Foltyn, L. Civale, J.L. MacManus-Driscoll, Q.X. Jia, B. Maiorov, H. Wang, M. Maley, Materials science challenges for high-temperature superconducting wire, Nat. Mater. 6 (2007) 631–642. https://doi.org/10.1038/nmat1989.

[68] J.D. Jorgensen, Defects and Superconductivity in the Copper Oxides, Phys. Today. 44 (1991) 34–40. https://doi.org/10.1063/1.881304.

[69] N.F. Heinig, R.D. Redwing, I.F. Tsu, A. Gurevich, J.E. Nordman, S.E. Babcock, D.C. Larbalestier, Evidence for channel conduction in low misorientation angle [001] tilt YBa 2 Cu 3 O 7− x bicrystal films, Appl. Phys. Lett. 69 (1996) 577–579. https://doi.org/10.1063/1.117758.

[70] J.P.F. Feighan, A. Kursumovic, J.L. MacManus-Driscoll, Materials design for artificial pinning centres in superconductor PLD coated conductors, Supercond. Sci. Technol. 30 (2017) 123001. https://doi.org/10.1088/1361-6668/aa90d1.

[71] L. Dusoulier, R. Cloots, B. Vertruyen, J.L. Garcia-Fierro, R. Moreno, B. Ferrari, Interactions in YBa2Cu3O7−x aqueous suspensions, Mater. Chem. Phys. 116 (2009) 368–375. https://doi.org/10.1016/j.matchemphys.2009.03.038.

[72] J. Ekin, Experimental Techniques for Low-Temperature Measurements, Oxford University Press, 2006. https://doi.org/10.1093/acprof:oso/9780198570547.001.0001.

[73] J.W. Ekin, C.C. Clickner, S.E. Russek, S.C. Sanders, Oxygen annealing of ex-situ YBCO/Ag thin-film interfaces, IEEE Trans. Appiled Supercond. 5 (1995) 2400–2403. https://doi.org/10.1109/77.403073.

[74] J.W. Ekin, T.M. Larson, N.F. Bergren, A.J. Nelson, A.B. Swartzlander, L.L. Kazmerski, A.J. Panson, B.A. Blankenship, High-Tc superconductor/noble-metal contacts with surface resistivities in the 10e-10 Ω cm2 range, Appl. Phys. Lett. 52 (1988) 1819–1821. https://doi.org/10.1063/1.99725.

[75] T.B. Lindemer, J.F. Hunley, J.E. Gates, A.L. Sutton, J. Brynestad, C.R. Hubbard, P.K. Gallagher, Experimental and Thermodynamic Study of Nonstoichiometry in YBa2Cu3O7-x;, J. Am.

Ceram. Soc. 72 (1989) 1775–1788. https://doi.org/10.1111/j.1151-2916.1989.tb05978.x.

[76] J. Shimoyama, S. Horii, K. Otzschi, K. Kishio, How to Optimize Critical Current Performance of RE123 Materials by Controlling Oxygen Content, MRS Proc. 689 (2001) E8.18. https://doi.org/10.1557/PROC-689-E8.18.

[77] A. Knizhnik, G.M. Reisner, O. Shafir, Y. Elisha, L. Patlagan, B. Fisher, G. Bazalitsky, Y. Direktovich, A.N. Men, Y. Eckstein, Equilibrium and non-equilibrium states of the YBCO–O 2 system, Supercond. Sci. Technol. 17 (2004) 448–458. https://doi.org/10.1088/0953-2048/17/3/025.

[78] B. Lorenz, C.W. Chu, High Pressure Effects on Superconductivity, in: Front. Supercond. Mater., Springer-Verlag, Berlin/Heidelberg, n.d.: pp. 459–497. https://doi.org/10.1007/3-540-27294-1_12.

[79] J. Crank, The mathematics of diffusion, Second Edition, Oxford Univ. Press. (1975) 414. https://books.google.com/books/about/The_Mathematics_of_Diffusion.html?id=eHANhZwVouYC (accessed July 31, 2021).

[80] P. Cayado, C.F. Sánchez-Valdés, A. Stangl, M. Coll, P. Roura, A. Palau, T. Puig, X. Obradors, Untangling surface oxygen exchange effects in YBa 2 Cu 3 O 6+x thin films by electrical conductivity relaxation, Phys. Chem. Chem. Phys. 19 (2017) 14129–14140. https://doi.org/10.1039/C7CP01855J.

[81] S.J. Rothman, J.L. Routbort, J.E. Baker, Tracer diffusion of oxygen in YBa2Cu3O7−δ, Phys. Rev. B. 40 (1989) 8852–8860. https://doi.org/10.1103/PhysRevB.40.8852.

[82] S.J. Rothman, J.L. Routbort, U. Welp, J.E. Baker, Anisotropy of oxygen tracer diffusion in single-crystal YBa2Cu3O7−y, Phys. Rev. B. 44 (1991) 2326–2333. https://doi.org/10.1103/PhysRevB.44.2326.

[83] S.I. Bredikhin, G.A. Emel'chenko, V.S. Shechtman, A.A. Zhokhov, S. Carter, R.J. Chater, J.A. Kilner, B.C.H. Steele, Anisotropy of oxygen self-diffusion in YBa2Cu3O7−δ single crystals, Phys. C Supercond. 179 (1991) 286–290. https://doi.org/10.1016/0921-4534(91)92173-9.

[84] S.H. Lee, S.C. Bae, J.K. Ku, H.J. Shin, Oxygen diffusion in epitaxial YBCO thin films, Phys. Rev. B. 46 (1992) 9142–9146. https://doi.org/10.1103/PhysRevB.46.9142.

[85] S. Kittelberger, U. Bolz, R.P.P. Huebener, B. Holzapfel, L. Mex, Oxygen diffusion in YBa2Cu3O7−δ films with different microstructures, Phys. C Supercond. 302 (1998) 93–101. https://doi.org/10.1016/S0921-4534(98)00207-X.

[86] G. Sageev Grader, P.K. Gallagher, J. Thomson, M. Gurvitch, Rates of change in high temperature electrical resistivity and oxygen diffusion coefficient in Ba2YCu3Ox, Appl. Phys. A Solids Surfaces. 45 (1988) 179–183. https://doi.org/10.1007/BF00615001.

[87] T.B. Tang, W. Lo, Oxygen diffusion in YBCO: an isothermal thermogravimetric study, Phys. C Supercond. 174 (1991) 463–466. https://doi.org/10.1016/0921-4534(91)91584-Q.

[88] S. Tsukui, R.E. Koritala, M. Li, K.C. Goretta, M. Adachi, J.E. Baker, J.L. Routbort, Oxygen and cation diffusion in YBCO coated conductors, Phys. C Supercond. 392–396 (2003) 841–846. https://doi.org/10.1016/S0921-4534(03)01132-8.

[89] M. Kläser, J. Kaiser, F. Stock, G. Müller-Vogt, A. Erb, Comparative study of oxygen diffusion in rare earth REBa2Cu3O7−δ single crystals (RE=Y, Er, Dy) with different impurity levels, Phys. C Supercond. 306 (1998) 188–198. https://doi.org/10.1016/S0921-4534(98)00371-2.

[90] G. Young, R.E. Funderlic, On the grain boundary diffusion theory of Fisher and Whipple, J.

Appl. Phys. 44 (1973) 5151–5154. https://doi.org/10.1063/1.1662107.

[91] Inderjeet Kaur., Y. Mishin, W. Gust, Fundamentals of grain and interphase boundary diffusion, (1995) 512.

[92] H.S. Kim, J.B. Song, N.Y. Kwon, K.L. Kim, H.G. Lee, The influence of heat-treatment and oxygenation annealing on the superconducting properties of YBCO coated conductors, Supercond. Sci. Technol. 22 (2009) 125016. https://doi.org/10.1088/0953-2048/22/12/125016.

[93] Yeonjoo Park, Hyun-Jin Shin, Young-Gyun Kim, Young Kun Oh, Haigun Lee, Effects of Melting Diffusion and Annealing in Oxygen on Superconducting Characteristics of GdBCO Coated Conductors: Preliminary Results, IEEE Trans. Appl. Supercond. 23 (2013) 6600804–6600804. https://doi.org/10.1109/TASC.2012.2236815.

[94] Jörg Handke, Einfluss einer Silberkontaktschicht auf das Belade - und Quenchverhalten von HTS-Bandleitern, TECHNISCHE UNIVERSITÄT MÜNCHEN, 2009.

[95] M.M. Kuklja, E.A. Kotomin, R. Merkle, Y.A. Mastrikov, J. Maier, Combined theoretical and experimental analysis of processes determining cathode performance in solid oxide fuel cells, Phys. Chem. Chem. Phys. 15 (2013) 5443. https://doi.org/10.1039/c3cp44363a.

[96] S.X. Dou, H.K. Liu, A.J. Bourdillon, N. Savvides, J.P. Zhou, C.C. Sorrell, Labile Cu3+ ions correlated with superconducting properties in YBa2Cu3O7−x, Solid State Commun. 68 (1988) 221–225. https://doi.org/10.1016/0038-1098(88)91104-0.

[97] I.N. Shabanova, S.I. Kurganskii, V.I. Kukuev, O. V. Popova, N.M. Nebogatikov, V.I. Kormilets, Electronic structure and chemical bonding of superconductor YBa2Cu3O7−x, J. Electron Spectros. Relat. Phenomena. 76 (1995) 715–718. https://doi.org/10.1016/0368-2048(95)02509-X.

[98] S. Seiffert, J. Sprakel, Physical chemistry of supramolecular polymer networks, Chem. Soc. Rev. 41 (2012) 909–930. https://doi.org/10.1039/C1CS15191F.

[99] Alexander Stangl, Oxygen kinetics and charge doping for high critical current YBCO films, Universitat Autònoma de Barcelona, 2019. https://hdl.handle.net/10803/667212.

[100] K. Conder, Oxygen diffusion in the superconductors of the YBaCuO family: isotope exchange measurements and models, Mater. Sci. Eng. R Reports. 32 (2001) 41–102. https://doi.org/10.1016/S0927-796X(00)00030-9.

[101] S.B. Adler, Factors Governing Oxygen Reduction in Solid Oxide Fuel Cell Cathodes†, Chem. Rev. 104 (2004) 4791–4843. https://doi.org/10.1021/CR020724O.

[102] M. Ausloos, A. Pękalski, Oxygen diffusion in 123-YBCO, in: Diffus. Process. Exp. Theory, Simulations, Springer-Verlag, Berlin/Heidelberg, 1994: pp. 221–233. https://doi.org/10.1007/BFb0031129.

[103] L. Chen, C.L. Chen, A.J. Jacobson, Electrical conductivity relaxation studies of oxygen transport in epitaxial YBa2Cu3O7-δ thin films, IEEE Trans. Appl. Supercond. 13 (2003) 2882–2885. https://doi.org/10.1109/TASC.2003.812032.

[104] A.R. van C. Warrington, Protective Relays: Their Theory and Practice Volume One, John Wiley & Sons, Boston, MA, 1968. https://doi.org/10.1007/978-1-4684-6459-7.

[105] J.J. Shea, Numerical distance protection - principles and applications [Book Review], IEEE Electr. Insul. Mag. 18 (2002) 46–47. https://doi.org/10.1109/MEI.2002.981327.

[106] B. Snyder, M.J. Kaiser, Ecological and economic cost-benefit analysis of offshore wind energy, Renew. Energy. 34 (2009) 1567–1578. https://doi.org/10.1016/j.renene.2008.11.015.

[107] C. Perpiña Castillo, F. Batista e Silva, C. Lavalle, An assessment of the regional potential for solar power generation in EU-28, Energy Policy. 88 (2016) 86–99. https://doi.org/10.1016/j.enpol.2015.10.004.

[108] T. Anderski, F. Careri, G. Migliavacca, N. Grisey, G. Sanchis, M. Gronau, K. Strunz, E. Peirano, A. Vafeas, R. Pestana, e-Highway2050: Planning the European transmission grid for 2050, in: 2016 IEEE Int. Energy Conf., IEEE, 2016: pp. 1–6. https://doi.org/10.1109/ENERGYCON.2016.7513882.

[109] G.P.A. Anne-Marie Denis, Olivier Despouys, Samuel Nguefeu, Jean-Pierre Taisne, Lucas Violleau, Jean-Baptiste Curis, Wolfgang Grieshaber, Diego Cirio, Andrea Pitto, Gianluigi Migliavacca, Roberto Calisti, Carlos Moreira, Bernardo Silva, Chen-Ching Liu, Lina He, K, DC Grids : Motivation, Feasibility and Outstanding Issues: Status Report for the European Commission Deliverable : D5.4, Brussels, 2013.

[110] A. Ballarino, C.E. Bruzek, N. Dittmar, S. Giannelli, W. Goldacker, G. Grasso, F. Grilli, C. Haberstroh, S. Hole, F. Lesur, A. Marian, J.M. Martinez-Val, L. Martini, C. Rubbia, D. Salmieri, F. Schmidt, M. Tropeano, The BEST PATHS Project on MgB 2 Superconducting Cables for Very High Power Transmission, IEEE Trans. Appl. Supercond. 26 (2016) 1–6. https://doi.org/10.1109/TASC.2016.2545116.

[111] J. Muñoz-Antón, A. Marian, F. Lesur, C.-E. Bruzek, Dichotomic Decision Optimization for the Design of HVDC Superconducting Links, (n.d.). https://doi.org/10.3390/e22121413.

[112] M. Parker, S. Finney, D. Holliday, DC protection of a multi-terminal HVDC network featuring offshore wind farms, Energy Procedia. 142 (2017) 2195–2201. https://doi.org/10.1016/J.EGYPRO.2017.12.588.

[113] G. Ebner, D. Doring, F. Schettler, K. Wurflinger, M. Zeller, Fault Handling at Hybrid High-Voltage AC/DC Transmission Lines With VSC Converters, IEEE Trans. Power Deliv. 33 (2018) 901–908. https://doi.org/10.1109/TPWRD.2017.2748163.

[114] P. Tixador, Superconducting Fault Current Limiter, WORLD SCIENTIFIC, 2018. https://doi.org/10.1142/11062.

[115] W. Pucher, Fundamentals of HVDC interruption, Electra (Paris); (France). 5 (1968).

[116] N.A. Belda, C.A. Plet, R.P.P. Smeets, Analysis of Faults in Multiterminal HVDC Grid for Definition of Test Requirements of HVDC Circuit Breakers, IEEE Trans. Power Deliv. 33 (2018) 403–411. https://doi.org/10.1109/TPWRD.2017.2716369.

[117] W. Leterme, I. Jahn, P. Ruffing, K. Sharifabadi, D. Van Hertem, Designing for High-Voltage dc Grid Protection: Fault Clearing Strategies and Protection Algorithms, IEEE Power Energy Mag. 17 (2019) 73–81. https://doi.org/10.1109/MPE.2019.2897188.

[118] C.M. Franck, HVDC Circuit Breakers: A Review Identifying Future Research Needs, IEEE Trans. Power Deliv. 26 (2011) 998–1007. https://doi.org/10.1109/TPWRD.2010.2095889.

[119] B.J. M. Callavik, A. Blomberg, J. Häfner, The Hybrid HVDC Breaker - an innovation breakthrough enabling reliable HVDC grid, ABB Grid Syst. (2012).

[120] W. Grieshaber, C.C. Davidson, R.S. Whitehouse, J.-P. Dupraz, C.D. Barker, A new ultra-fast HVDC Circuit breaker for meshed DC networks, in: 11th IET Int. Conf. AC DC Power Transm., Institution of Engineering and Technology, 2015: pp. 047 (7 .)-047 (7 .).

https://doi.org/10.1049/cp.2015.0021.

[121] J.P. Despouys, O and Denis, A.-M and Cirio, Diego and Bell, Keith and Moreira, C. and Liu, Clare and Grieshaber, W and Dupraz, TWENTIES: Conclusions of a major R&D Demonstration Project on Offshore DC Grids, in: Cigré, 2014.

[122] C.M. Rey, Superconductors in the Power Grid: Materials and Applications, Supercond. Power Grid Mater. Appl. (2015) 1–438. https://doi.org/10.1016/C2013-0-16436-7.

[123] O.B. Hyun, Brief review of the field test and application of a superconducting fault current limiter, Prog. Supercond. Cryog. 19 (2017) 1–11. https://doi.org/10.9714/PSAC.2017.19.4.001.

[124] M. Noe, M. Steurer, High-temperature superconductor fault current limiters: concepts, applications, anddevelopment status, Supercond. Sci. Technol. 20 (2007) R15. https://doi.org/10.1088/0953-2048/20/3/R01.

[125] C.J. Hawley, F. Darmann, T.P. Beales, Performance of a 1 MV A high temperature superconductors-enabled saturable magneticcore-type fault current limiter, Supercond. Sci. Technol. 18 (2004) 255. https://doi.org/10.1088/0953-2048/18/3/008.

[126] N. Vilhena, P. Arsénio, J. Murta-Pina, A. Pronto, A. Álvarez, A Methodology for Modeling and Simulation of Saturated Cores Fault Current Limiters, IEEE Trans. Appl. Supercond. 25 (2015) 5600704. https://doi.org/10.1109/TASC.2014.2374179.

[127] T. Yazawa, E. Yoneda, J. Matsuzaki, M. Shimada, T. Kuriyama, S. Nomura, T. Ohkuma, Y. Sato, Y. Takahashi, Design and test results of 6.6 kV high-Tc superconducting fault current limiter, IEEE Trans. Appl. Supercond. 11 (2001) 2511–2514. https://doi.org/10.1109/77.920376.

[128] M.C. Ahn, D.K. Bae, S.E. Yang, D.K. Park, T.K. Ko, C. Lee, B.Y. Seok, H.M. Chang, Manufacture and test of small-scale superconducting fault current limiter by using the bifilar winding of coated conductor, IEEE Trans. Appl. Supercond. 16 (2006) 646–649. https://doi.org/10.1109/TASC.2006.870522.

[129] B. Gromoll, G. Ries, W. Schmidt, H.P. Kraemer, B. Seebacher, B. Utz, R. Nies, H.W. Neumueller, E. Baltzer, S. Fischer, B. Heismann, Resistive fault current limiters with YBCO films 100 kVA functional model, IEEE Trans. Appl. Supercond. 9 (1999) 656–659. https://doi.org/10.1109/77.783381.

[130] J. Bock, F. Breuer, H. Walter, S. Elschner, M. Kleimaier, R. Kreutz, M. Noe, CURL 10: Development and Field-Test of a 10 kV/10 MVA Resistive Current Limiter Based on Bulk MCP-BSCCO 2212, IEEE Trans. Appiled Supercond. 15 (2005) 1955–1960. https://doi.org/10.1109/TASC.2005.849344.

[131] X. Yuan, K. Tekletsadik, L. Kovalsky, J. Bock, F. Breuer, S. Elschner, Proof-of-concept prototype test results of a superconducting fault current limiter for transmission-level applications, IEEE Trans. Appl. Supercond. 15 (2005) 1982–1985. https://doi.org/10.1109/TASC.2005.849432.

[132] H.-P. Kraemer, W. Schmidt, M. Wohlfart, H.-W. Neumueller, A. Otto, D. Verebelyi, U. Schoop, A.P. Malozemoff, Test of a 2 MVA medium voltage HTS fault current limiter module made of YBCO coated conductors, J. Phys. Conf. Ser. 97 (2008) 012091. https://doi.org/10.1088/1742-6596/97/1/012091.

[133] V.E. Keilin, V. V. Lobyntsev, M.S. Novikov, S.J. Novikov, V.I. Shcherbakov, Design and Test Results of a 1 MVA Resistive Type Fault Current Limiter, Phys. Procedia. 36 (2012) 1215–1218. https://doi.org/10.1016/J.PHPRO.2012.06.278.

[134] L. Martini, M. Bocchi, G. Angeli, M. Ascade, V. Rossi, A. Valzasina, C. Ravetta, S. Fratti, E. Martino, Live grid field-testing final results of the first italian superconducting fault current limiter and severe 3-phase fault experience, IEEE Trans. Appl. Supercond. 25 (2015). https://doi.org/10.1109/TASC.2014.2371917.

[135] M. Song, C. Sheng, T. Ma, Y. Huang, C. Yang, Y. Xin, H. Jin, T. Yang, J. Xiong, C. Li, Q. Li, C. Wang, B. Li, L. Xiao, P. Luo, Current limiting tests of a prototype 160 kV/1 kA resistive DC superconducting fault current limiter, Supercond. Sci. Technol. 34 (2020). https://doi.org/10.1088/1361-6668/ABC2B1.

[136] R. Dommerque, S. Krämer, A. Hobl, R. Böhm, M. Bludau, J. Bock, D. Klaus, H. Piereder, A. Wilson, T. Krüger, G. Pfeiffer, K. Pfeiffer, S. Elschner, First commercial medium voltage superconducting fault-current limiters: production, test and installation, Supercond. Sci. Technol. 23 (2010) 034020. https://doi.org/10.1088/0953-2048/23/3/034020.

[137] A. Heidary, H. Radmanesh, K. Rouzbehi, A. Mehrizi-Sani, G.B. Gharehpetian, Inductive fault current limiters: A review, Electr. Power Syst. Res. 187 (2020) 106499. https://doi.org/10.1016/J.EPSR.2020.106499.

[138] O. Naeckel, M. Noe, Design and Test of an Air Coil Superconducting Fault Current Limiter Demonstrator, IEEE Trans. Appl. Supercond. 24 (2014). https://doi.org/10.1109/TASC.2013.2286294.

[139] X. Granados, T. Puig, X. Obradors, E. Mendoza, J. Teva, A. Calleja, I.G. Searradilla, M. Segarra, J. Calero, L. García-Tabarés, E. Oyarbide, R. Iturbe, L. Peral, Design, building up and testing of a 400 kVA hybrid FCL, Phys. C Supercond. 372–376 (2002) 1680–1683. https://doi.org/10.1016/S0921-4534(02)01100-0.

[140] M. Steurer, K. Fröhlich, W. Holaus, K. Kaltenegger, A novel hybrid current-limiting circuit breaker for medium voltage: Principle and test results, IEEE Trans. Power Deliv. 18 (2003) 460–467. https://doi.org/10.1109/TPWRD.2003.809614.

[141] Y.S. Cho, N.Y. Lee, H.S. Choi, D.C. Chung, S.H. Lim, Operational characteristics of hybrid-type SFCL with closed and open cores, Phys. C Supercond. Its Appl. Complete (2007) 1204–1208. https://doi.org/10.1016/J.PHYSC.2007.03.459.

[142] J. Magnusson, J.A. Martinez-Velasco, A. Bissal, G. Engdahl, L. Liljestrand, Optimal design of a medium voltage hybrid fault current limiter, ENERGYCON 2014 - IEEE Int. Energy Conf. (2014) 431–438. https://doi.org/10.1109/ENERGYCON.2014.6850463.

[143] Woo-Jae Park, Byung Chul Sung, Jung-Wook Park, The Effect of SFCL on Electric Power Grid With Wind-Turbine Generation System, IEEE Trans. Appl. Supercond. 20 (2010) 1177–1181. https://doi.org/10.1109/TASC.2010.2040918.

[144] J. Bock, E. Preisler, Preparation of single phase 2212 bismuth strontium calcium cuprate by melt processing, Solid State Commun. 72 (1989) 453–458. https://doi.org/10.1016/0038-1098(89)90597-8.

[145] S. Elschner, F. Breuer, A. Wolf, M. Noe, L. Cowey, J. Bock, Characterization of BSCCO 2212 bulk material for resistive current limiters, IEEE Trans. Appiled Supercond. 11 (2001) 2507–2510. https://doi.org/10.1109/77.920375.

[146] S. Elschner, F. Breuer, M. Noe, T. Rettelbach, H. Walter, J. Bock, Manufacturing and testing of MCP 2212 bifilar coils for a 10 MVA fault current limiter, IEEE Trans. Appiled Supercond. 13 (2003) 1980–1983. https://doi.org/10.1109/TASC.2003.812954.

[147] J. Bock, F. Breuer, H. Walter, S. Elschner, M. Kleimaier, R. Kreutz, M. Noe, CURL 10:

Development and Field-Test of a 10 kV/10 MVA Resistive Current Limiter Based on Bulk MCP-BSCCO 2212, IEEE Trans. Appiled Supercond. 15 (2005) 1955–1960. https://doi.org/10.1109/TASC.2005.849344.

[148] R. Kreutz, J. Bock, F. Breuer, K.-P. Juengst, M. Kleimaier, H.-U. Klein, D. Krischel, M. Noe, R. Steingass, K.-H. Weck, System Technology and Test of CURL 10, a 10 kV, 10 MVA Resistive High-Tc Superconducting Fault Current Limiter, IEEE Trans. Appiled Supercond. 15 (2005) 1961–1964. https://doi.org/10.1109/TASC.2005.849345.

[149] S. Elschner, F. Breuer, H. Walter, J. Bock, Magnetic Field Assisted Quench Propagation as a New Concept for Resistive Current Limiting Devices, J. Phys. Conf. Ser. 43 (2006) 224. https://doi.org/10.1088/1742-6596/43/1/224.

[150] N. Vilalta, F. Sandiumenge, S. Piñol, X. Obradors, Precipitate size refinement by CeO 2 and Y 2 BaCuO 5 additions in directionally solidified YBa 2 Cu 3 O 7, J. Mater. Res. 12 (1997) 38–46. https://doi.org/10.1557/JMR.1997.0008.

[151] X. Chaud, D. Isfort, E. Beaugnon, R. Tournier, Isothermal growth of large YBa2Cu3O7−x single domains up to 93 mm, Phys. C Supercond. 341–348 (2000) 2413–2416. https://doi.org/10.1016/S0921-4534(00)01294-6.

[152] R. Tournier, E. Beaugnon, O. Belmont, X. Chaud, D. Bourgault, D. Isfort, L. Porcar, P. Tixador, Processing of large Y1Ba2Cu3O7- x single domains for current-limiting applications, Supercond. Sci. Technol. 13 (2000) 886–895. https://doi.org/10.1088/0953-2048/13/6/354.

[153] X. Obradors, T. Puig, E. Mendoza, J. Plain, J. Figueras, X. Granados, A.E. Carrillo, E. Varesi, F. Sandiumenge, P. Tixador, Tuning the critical currents in bulk MTG YBCO for current limiting devices, Supercond. Sci. Technol. 13 (2000) 879–885. https://doi.org/10.1088/0953-2048/13/6/353.

[154] P. Tixador, X. Obradors, R. Tournier, T. Puig, D. Bourgault, X. Granados, J.M. Duval, E. Mendoza, X. Chaud, E. Varesi, E. Beaugnon, D. Isfort, Quench in bulk HTS materials - application to the fault current limiter, Supercond. Sci. Technol. 13 (2000) 493. https://doi.org/10.1088/0953-2048/13/5/312.

[155] E. Mendoza, T. Puig, X. Granados, X. Obradors, L. Porcar, D. Bourgault, P. Tixador, Extremely high current-limitation capability of underdoped YBa2Cu3O7−x superconductor, Appl. Phys. Lett. 83 (2003) 4809–4811. https://doi.org/10.1063/1.1632543.

[156] Y.Y. Xie, K. Tekletsadik, D. Hazelton, V. Selvamanickam, Second Generation High-Temperature Superconducting Wires for Fault Current Limiter Applications, IEEE Trans. Appl. Supercond. 17 (2007) 1981–1985. https://doi.org/10.1109/TASC.2007.898186.

[157] S. kar, S. Kulkarni, M. Dixit, K.P. Singh, A. Gupta, P.V. Balasubramanyam, S.K. Sarangi, V.V. Rao, Study on Recovery Performance of High Tc Superconducting Tapes for Resistive Type Superconducting Fault Current Limiter Applications, Phys. Procedia. 36 (2012) 1231–1235. https://doi.org/10.1016/j.phpro.2012.06.281.

[158] O. Tsukamoto, AC losses in a type II superconductor strip with inhomogeneous critical current distribution, Supercond. Sci. Technol. 18 (2005) 596–605. https://doi.org/10.1088/0953-2048/18/5/004.

[159] A. Usoskin, H.C. Freyhardt, A. Issaev, J. Knoke, J. Dzick, M. Collet, P. Kirchesch, J. Lehtonen, SUPERPOLI fault-current limiters based on YBCO-coated stainless steel tapes, IEEE Trans. Appiled Supercond. 13 (2003) 1972–1975. https://doi.org/10.1109/TASC.2003.812952.

[160] V. Selvamanickam, Yimin Chen, Xuming Xiong, Y.Y. Xie, M. Martchevski, A. Rar, Yunfei Qiao,

R.M. Schmidt, A. Knoll, K.P. Lenseth, C.S. Weber, High Performance 2G Wires: From R&D to Pilot-Scale Manufacturing, IEEE Trans. Appl. Supercond. 19 (2009) 3225–3230. https://doi.org/10.1109/TASC.2009.2018792.

[161] S. Elschner, A. Kudymow, S. Fink, W. Goldacker, F. Grilli, C. Schacherer, A. Hobl, J. Bock, M. Noe, ENSYSTROB-Resistive Fault Current Limiter Based on Coated Conductors for Medium Voltage Application, IEEE Trans. Appl. Supercond. 21 (2011) 1209–1212. https://doi.org/10.1109/TASC.2010.2100799.

[162] H.-P. Kraemer, W. Schmidt, H. Cai, B. Gamble, D. Madura, T. MacDonald, J. McNamara, W. Romanosky, G. Snitchler, N. Lallouet, F. Schmidt, S. Ahmed, Superconducting Fault Current Limiter for Transmission Voltage, Phys. Procedia. 36 (2012) 921–926. https://doi.org/10.1016/j.phpro.2012.06.230.

[163] A. Hobl, W. Goldacker, B. Dutoit, L. Martini, A. Petermann, P. Tixador, Design and Production of the ECCOFLOW Resistive Fault Current Limiter, IEEE Trans. Appl. Supercond. 23 (2013) 5601804–5601804. https://doi.org/10.1109/TASC.2013.2238288.

[164] P. Tixador, M. Bauer, C.-E. Bruzek, A. Calleja, G. Deutscher, B. Dutoit, F. Gomory, L. Martini, M. Noe, X. Obradors, M. Pekarcikova, F. Sirois, Status of the European Union Project FASTGRID, IEEE Trans. Appl. Supercond. 29 (2019) 1–5. https://doi.org/10.1109/TASC.2019.2908586.

[165] V. Meerovich, V. Sokolovsky, High-temperature superconducting fault current limiters (FCLs) for power grid applications, in: Supercond. Power Grid, Elsevier, 2015: pp. 283–324. https://doi.org/10.1016/B978-1-78242-029-3.00009-1.

[166] O.-B.B. Hyun, Brief review of the field test and application of a superconducting fault current limiter, Prog. Supercond. Cryog. 19 (2017) 1–11. https://doi.org/10.9714/PSAC.2017.19.4.001.

[167] H.-R. Lim, I.-S. Kim\, D.H. Kim, Y.K. Park\, J.-C. Park, Preparation of YBa2Cu307 films on sapphire substrate by pulsed laser deposition, (1999).

[168] H. Kinder, P. Berberich, W. Prusseit, S. Rieder-Zecha, R. Semerad, B. Utz, YBCO film deposition on very large areas up to 20×20 cm2, Phys. C Supercond. 282–287 (1997) 107–110. https://doi.org/10.1016/S0921-4534(97)00230-X.

[169] H.-P. Kraemer, W. Schmidt, B. Utz, H.-W. Neumueller, Switching behavior of YBCO thin film conductors in resistive fault current limiters, IEEE Trans. Appiled Supercond. 13 (2003) 2044–2047. https://doi.org/10.1109/TASC.2003.812980.

[170] H.-P. Kraemer, W. Schmidt, B. Utz, B. Wacker, H.-W. Neumueller, G. Ahlf, R. Hartig, Test of a 1 kA Superconducting Fault Current Limiter for DC Applications, IEEE Trans. Appiled Supercond. 15 (2005) 1986–1989. https://doi.org/10.1109/TASC.2005.849433.

[171] L. Antognazza, M. Decroux, M. Therasse, M. Abplanalp, O. Fischer, Test of YBCO Thin Films Based Fault Current Limiters With a Newly Designed Meander, IEEE Trans. Appiled Supercond. 15 (2005) 1990–1993. https://doi.org/10.1109/TASC.2005.849434.

[172] Z. Gui, Y. Wang, L. Chen, L. Liang, X. Gong, Quench and Recovery Characteristics of SFCL Based on Double-Sided YBCO Thin Films, IEEE Trans. Appl. Supercond. 30 (2020) 1–7. https://doi.org/10.1109/TASC.2019.2963395.

[173] L. Soler, J. Jareño, J. Banchewski, S. Rasi, N. Chamorro, R. Guzman, R. Yáñez, C. Mocuta, S. Ricart, J. Farjas, P. Roura-Grabulosa, X. Obradors, T. Puig, Ultrafast transient liquid assisted growth of high current density superconducting films, Nat. Commun. 11 (2020) 344.

https://doi.org/10.1038/s41467-019-13791-1.

[174] V.N. Kurlov, Sapphire: Properties, Growth, and Applications, Ref. Modul. Mater. Sci. Mater. Eng. (2016). https://doi.org/10.1016/B978-0-12-803581-8.03681-X.

[175] R. Gyuráki, Fluorescent thermal imaging method for investigating transient effects in high-temperature superconductor tapes and coils, Karlsruher Instituts für Technologie (KIT), 2019.

[176] Yukikazu Iwasa, Case Studies in Superconducting Magnets, Springer US, Boston, MA, 2009. https://doi.org/10.1007/b112047.

[177] P. Tixador, N.T. Nguyen, Design of ReBaCuO-coated conductors for FCL, Supercond. Sci. Technol. 25 (2012) 014009. https://doi.org/10.1088/0953-2048/25/1/014009.

[178] P. Tixador, A. Badel, Superconducting Fault Current Limiter optimized design, Phys. C Supercond. Its Appl. 518 (2015) 130–133. https://doi.org/10.1016/j.physc.2015.06.007.

[179] P. Tixador, J. Vialle, A. Badel, Operation of an SCFCL at 65 K, IEEE Trans. Appl. Supercond. 28 (2018) 1–5. https://doi.org/10.1109/TASC.2018.2797303.

[180] K. Nam, B.-Y. Seok, J. Joo Byun, H.-M. Chang, Suppression of bubbles in subcooled liquid nitrogen under heat impulse, Cryogenics (Guildf). 47 (2007) 442–449. https://doi.org/10.1016/j.cryogenics.2007.04.012.

[181] M. Schwarz, C. Schacherer, K.-P. Weiss, A. Jung, Thermodynamic behaviour of a coated conductor for currents above I c, Supercond. Sci. Technol. 21 (2008) 054008. https://doi.org/10.1088/0953-2048/21/5/054008.

[182] J. Lu, E.S. Choi, H.D. Zhou, Physical properties of Hastelloy ® C-276™ at cryogenic temperatures ARTICLES YOU MAY BE INTERESTED IN, J. Appl. Phys. 103 (2008) 64908. https://doi.org/10.1063/1.2899058.

[183] A. Ballarino, Prospects for the use of HTS in high field magnets for future accelerator facilities, in: Cern LHC, CERN-ACC-2014-0273, Dresden, Germany, 2014. https://cds.cern.ch/record/1968557.

[184] J.-X. Lin, X.-M. Liu, C.-W. Cui, C.-Y. Bai, Y.-M. Lu, F. Fan, Y.-Q. Guo, Z.-Y. Liu, C.-B. Cai, A review of thickness-induced evolutions of microstructure and superconducting performance of REBa2Cu3O7−δ coated conductor, Adv. Manuf. 5 (2017) 165–176. https://doi.org/10.1007/s40436-017-0173-x.

[185] A. Sundaram, Y. Zhang, A.R. Knoll, D. Abraimov, P. Brownsey, M. Kasahara, G.M. Carota, R. Nakasaki, J.B. Cameron, G. Schwab, L. V Hope, R.M. Schmidt, H. Kuraseko, T. Fukushima, D.W. Hazelton, 2G HTS wires made on 30 µ m thick Hastelloy substrate, Supercond. Sci. Technol. 29 (2016) 104007. https://doi.org/10.1088/0953-2048/29/10/104007.

[186] G. Majkic, R. Pratap, A. Xu, E. Galstyan, H.C. Higley, S.O. Prestemon, X. Wang, D. Abraimov, J. Jaroszynski, V. Selvamanickam, Engineering current density over 5 kA mm −2 at 4.2 K, 14 T in thick film REBCO tapes, Supercond. Sci. Technol. 31 (2018) 10LT01. https://doi.org/10.1088/1361-6668/aad844.

[187] A. Xu, Y. Zhang, M.H. Gharahcheshmeh, Y. Yao, E. Galstyan, D. Abraimov, F. Kametani, A. Polyanskii, J. Jaroszynski, V. Griffin, G. Majkic, D.C. Larbalestier, V. Selvamanickam, J e (4.2 K, 31.2 T) beyond 1 kA/mm2 of a ~3.2 µm thick, 20 mol% Zr-added MOCVD REBCO coated conductor, Sci. Rep. 7 (2017) 6853. https://doi.org/10.1038/s41598-017-06881-x.

[188] A. Molodyk, S. Samoilenkov, A. Markelov, P. Degtyarenko, S. Lee, V. Petrykin, M. Gaifullin, A. Mankevich, A. Vavilov, B. Sorbom, J. Cheng, S. Garberg, L. Kesler, Z. Hartwig, S. Gavrilkin, A.

Tsvetkov, T. Okada, S. Awaji, D. Abraimov, A. Francis, G. Bradford, D. Larbalestier, C. Senatore, M. Bonura, A.E. Pantoja, S.C. Wimbush, N.M. Strickland, A. Vasiliev, Development and large volume production of extremely high current density YBa2Cu3O7 superconducting wires for fusion, Sci. Rep. 11 (2021) 2084. https://doi.org/10.1038/s41598-021-81559-z.

[189] C. Lacroix, O. Lavergne, T. Leduc, F. Dupuis-Desloges, L. Moret, F. Sirois, G. Escamez, C.É. Bruzek, P. Tixador, V. Grosse, M. Bauer, Successful DC current limitation above 100 Vm−1 for 50 ms using HTS tapes with critical currents exceeding 750 A/cm-width, Supercond. Sci. Technol. 34 (2021). https://doi.org/10.1088/1361-6668/abceb2.

[190] M. Pekarčíková, M. Drienovsky, J. Krajčovič, J. Mišík, E. Cuninková, T. ˇ Hú lan, O. Bošá, M. Vojenčiak, Analysis of thermo-physical properties of materials suitable for thermal stabilization of superconducting tapes for high-voltage superconducting fault current limiters, J. Therm. Anal. Calorim. 138 (n.d.). https://doi.org/10.1007/s10973-019-08309-2.

[191] M. Pekarčíková, J. Mišík, M. Drienovský, J. Krajčovič, M. Vojenčiak, M. Búran, M. Mošaťˇ, T. Húlan, M. Skarba, E. Cuninková, F. Gömöry, Composite Heat Sink Material for Superconducting Tape in Fault Current Limiter Applications, Materials (Basel). 13 (2020) 1832. https://doi.org/10.3390/ma13081832.

[192] E. Cuninková, M. Pekarčíková, M. Skarba, J. Krajčovič, M. Pašák, Experimental and Numerical Analysis of High-Temperature Superconducting Tapes Modified by Composite Thermal Stabilization Subjected to Thermomechanical Loading, Materials (Basel). 14 (2021) 3579. https://doi.org/10.3390/ma14133579.

[193] G. Deutscher, High-Voltage Superconducting Fault Current Limiters Based on High-Diffusivity Dielectric Substrates, J. Supercond. Nov. Magn. 31 (2018) 1961–1963. https://doi.org/10.1007/s10948-018-4633-8.

[194] B. Almog, M. Azoulay, G. Deutscher, Homogenous Crack-Free Large Size YBCO/YSZ/Sapphire Films for Application, in: AIP Conf. Proc., AIP, 2006: pp. 471–472. https://doi.org/10.1063/1.2354789.

[195] M. Bonura, C. Senatore, An equation for the quench propagation velocity valid for high field magnet use of REBCO coated conductors, Appl. Phys. Lett. 108 (2016) 242602. https://doi.org/10.1063/1.4954165.

[196] M. Bonura, C. Senatore, Temperature and Field Dependence of the Quench Propagation Velocity in Industrial REBCO Coated Conductors, IEEE Trans. Appl. Supercond. 27 (2017) 1–5. https://doi.org/10.1109/TASC.2016.2632298.

[197] F. Trillaud, F. Ayela, A. Devred, M. Fratini, D. Leboeuf, P. Tixador, Quench Propagation Ignition Using Single-Mode Diode Laser, IEEE Trans. Appiled Supercond. 15 (2005) 3648–3651. https://doi.org/10.1109/TASC.2005.849381.

[198] J. Pelegrin, E. Martinez, L.A. Angurel, Y.-Y. Xie, V. Selvamanickam, Numerical and Experimental Analysis of Normal Zone Propagation on 2G HTS Wires, IEEE Trans. Appl. Supercond. 21 (2011) 3041–3044. https://doi.org/10.1109/TASC.2010.2084982.

[199] W.J. Lu, J. Fang, D. Li, C.Y. Wu, L.J. Guo, The experimental research and analysis on the quench propagation of YBCO coated conductor and coil, Phys. C Supercond. 484 (2013) 153–158. https://doi.org/10.1016/j.physc.2012.03.062.

[200] D. Colangelo, B. Dutoit, Analysis of the influence of the normal zone propagation velocity on the design of resistive fault current limiters, Supercond. Sci. Technol. 27 (2014). https://doi.org/10.1088/0953-2048/27/12/124005.

[201] T. Naito, H. Fujishiro, YasuhisaYamamura, K. Saito, H. Okamoto, H. Hayashi, Y. Gosho, T. Ohkuma, Y. Shiohara, Specific Heat and Thermal Diffusivity of YBCO Coated Conductors, Phys. Procedia. 36 (2012) 1609–1613. https://doi.org/10.1016/j.phpro.2012.06.316.

[202] X. Wang, A.R. Caruso, M. Breschi, G. Zhang, U.P. Trociewitz, H.W. Weijers, J. Schwartz, Normal Zone Initiation and Propagation in Y-Ba-Cu-O Coated Conductors With Cu Stabilizer, IEEE Trans. Appiled Supercond. 15 (2005) 2586–2589. https://doi.org/10.1109/TASC.2005.847661.

[203] G.A. Levin, P.N. Barnes, The normal zone in YBa 2 Cu 3 O 6+ x -coated conductors, Supercond. Sci. Technol. 20 (2007) 1101–1107. https://doi.org/10.1088/0953-2048/20/12/003.

[204] G.A. Levin, K.A. Novak, P.N. Barnes, The effects of superconductor–stabilizer interfacial resistance on the quench of a current-carrying coated conductor, Supercond. Sci. Technol. 23 (2010) 014021. https://doi.org/10.1088/0953-2048/23/1/014021.

[205] M. Polak, P.N. Barnes, G.A. Levin, YBCO/Ag boundary resistivity in YBCO tapes with metallic substrates, Supercond. Sci. Technol. 19 (2006) 817–820. https://doi.org/10.1088/0953-2048/19/8/022.

[206] C. Lacroix, F. Sirois, Corrigendum: Concept of a current flow diverter for accelerating the normal zone propagation velocity in 2G HTS coated conductors (2014 Supercond. Sci. Technol. 27 035003), Supercond. Sci. Technol. 27 (2014) 129501. https://doi.org/10.1088/0953-2048/27/12/129501.

[207] C. Lacroix, Y. Lapierre, J. Coulombe, F. Sirois, High normal zone propagation velocity in second generation high-temperature superconductor coated conductors with a current flow diverter architecture, Supercond. Sci. Technol. 27 (2014). https://doi.org/10.1088/0953-2048/27/5/055013.

[208] C. Lacroix, F. Sirois, M.R. Wertheimer, INCREASED NORMAL ZONE PROPAGATION VELOCITY IN SUPERCONDUCTING SEGMENTS, US 20150.045231A1, n.d. https://patents.google.com/patent/US20150045231A1/en.

[209] S.E. Russek, S.C. Sanders, A. Roshko, J.W. Ekin, Surface degradation of superconducting YBa 2 Cu 3 O 7−δ thin films, Appl. Phys. Lett. 64 (1994) 3649–3651. https://doi.org/10.1063/1.111192.

[210] J.H. Fournier-Lupien, C. Lacroix, S. Hellmann, J. Huh, K. Pfeiffer, F. Sirois, Use of the buffer layers as a current flow diverter in 2G HTS coated conductors, Supercond. Sci. Technol. 31 (2018). https://doi.org/10.1088/1361-6668/aae2cd.

[211] C. Lacroix, F. Sirois, J.-H.F. Lupien, Engineering of second generation HTS coated conductor architecture to enhance the normal zone propagation velocity in various operating conditions, Supercond. Sci. Technol. 30 (2017) 064004. https://doi.org/10.1088/1361-6668/aa684f.

[212] S. Awaji, Y. Hou, H. Oguro, K. Watanabe, I. Inoue, H. Sakamoto, S. Yasunaga, J. Ryu, Hot Spot Behavior of Y123 Coated Conductors, IEEE Trans. Appl. Supercond. 22 (2012) 6601004–6601004. https://doi.org/10.1109/TASC.2011.2176710.

[213] P. Jacquet, R. Podor, J. Ravaux, J. Teisseire, I. Gozhyk, J. Jupille, R. Lazzari, Grain growth: The key to understand solid-state dewetting of silver thin films, Scr. Mater. 115 (2016) 128–132. https://doi.org/10.1016/j.scriptamat.2016.01.005.

[214] J. Danglad-Flores, S. Eickelmann, H. Riegler, Deposition of polymer films by spin casting: A quantitative analysis, Chem. Eng. Sci. 179 (2018) 257–264.

https://doi.org/10.1016/j.ces.2018.01.012.

[215] H. Minemawari, T. Yamada, H. Matsui, J. Tsutsumi, S. Haas, R. Chiba, R. Kumai, T. Hasegawa, Inkjet printing of single-crystal films, Nature. 475 (2011) 364–367. https://doi.org/10.1038/nature10313.

[216] M. Vilardell, J. Fornell, J. Sort, R. Vlad, J. Fernández, J. Puig, A. Usoskin, A. Palau, T. Puig, X. Obradors, A. Calleja, Inkjet-Printed Chemical Solution Y2O3 Layers for Planarization of Technical Substrates, Coatings. 7 (2017) 227. https://doi.org/10.3390/coatings7120227.

[217] Fumio Okamoto, Ethching Solution for Silver, 05/391358, 1975. https://patents.google.com/patent/US3860423A/en.

[218] S. Ebnesajjad, Plasma Treatment of Polymeric Materials, in: Surf. Treat. Mater. Adhes. Bond., Elsevier, 2014: pp. 227–269. https://doi.org/10.1016/B978-0-323-26435-8.00009-5.

[219] R.A. Wolf, Atmospheric Pressure Plasma for Surface Modification, John Wiley & Sons, Inc., Hoboken, NJ, USA, 2012. https://doi.org/10.1002/9781118547519.

[220] S. Korzec, Dariusz; Burger, Dominik; Nettesheim, Plasma activation from roll to roll, Manuf. Compos. Mater. Packag. (2015) 26–31.

[221] https://www.relyon-plasma.com, (n.d.).

[222] Tutorial on Powder X-ray Diffraction for Characterizing Nanoscale Materials, ACS Nano. 13 (2019). https://doi.org/10.1021/acsnano.9b05157.

[223] E. BETZIG, J.K. TRAUTMAN, T.D. HARRIS, J.S. WEINER, R.L. KOSTELAK, Breaking the Diffraction Barrier: Optical Microscopy on a Nanometric Scale, Science (80-.). 251 (1991) 1468–1470. https://doi.org/10.1126/science.251.5000.1468.

[224] H.L. Ariel Lipson, Stephen G. Lipson, Optical Physics, 4th ed., Cambridge University Press, 2010.

[225] J. Domínguez-Montes, E.L. Eisman, Representative model of particle–wave duality and entanglement based on De Broglie's interpretation, Phys. Essays. 25 (2012) 215–220. https://doi.org/10.4006/0836-1398-25.2.215.

[226] Z. Sobat; S. Sadegh Hassani; M. Ghalbi Ahangari; S. Kiani; A. Mehdizadeh, SCANNING HALL PROBE MICROSCOPY TECHNIQUE FOR INVESTIGATION OF MAGNETIC PROPERTIES, Int. J. Nano Dimens. 6 (2015) 329–337. https://doi.org/10.7508/ijnd.2015.04.001.

[227] X. Granados, S. Iliescu, B. Bozzo, E. Bartolome, T. Puig, X. Obradors, J. Amorós, M. Carrera, Magnetic Mapping - A Way to Test and Understand Current Flows in Thin and Bulk Superconductors, Adv. Sci. Technol. 47 (2006) 1–6. https://doi.org/10.4028/www.scientific.net/ast.47.1.

[228] A.D. Gonzàlez, Càlcul de corrents crítics en materials superconductors via SSA i inversió de Fourier, Universitat Politècnica de Catalunya, 2017.

[229] R.J. Wijngaarden, K. Heeck, H.J.W. Spoelder, R. Surdeanu, R. Griessen, Fast determination of 2D current patterns in flat conductors from measurement of their magnetic field, Phys. C Supercond. 295 (1998) 177–185. https://doi.org/10.1016/S0921-4534(97)01799-1.

[230] Y. Yeshurun, A.P. Malozemoff, A. Shaulov, Magnetic relaxation in high-temperature superconductors, Rev. Mod. Phys. 68 (1996) 911–949. https://doi.org/10.1103/RevModPhys.68.911.

[231] L.J. van der PAUW, A METHOD OF MEASURING SPECIFIC RESISTIVITY AND HALL EFFECT OF DISCS OF ARBITRARY SHAPE, Semicond. Devices Pioneer. Pap. (1991) 174–182. https://doi.org/10.1142/9789814503464_0017.

[232] M. Chudy, Z. Zhong, M. Eisterer, T. Coombs, n-Values of commercial YBCO tapes before and after irradiation by fast neutrons, Supercond. Sci. Technol. 28 (2015) 035008. https://doi.org/10.1088/0953-2048/28/3/035008.

[233] A.K. Ghosh, V–I transition and n-value of multifilamentary LTS and HTS wires and cables, Phys. C Supercond. 401 (2004) 15–21. https://doi.org/10.1016/J.PHYSC.2003.09.006.

[234] J.H. Fournier-Lupien, P. Del Vecchio, C. Lacroix, F. Sirois, Analytical model of 2D electric potential and current transfer in superconducting tapes with a current flow diverter architecture, Supercond. Sci. Technol. 33 (2020). https://doi.org/10.1088/1361-6668/aba543.

[235] J.-H. Fournier-Lupien, F. Sirois, C. Lacroix, Concepts of static vs. dynamic current transfer length in 2G HTS coated conductors with a current flow diverter architecture, Supercond. Sci. Technol. 34 (2021) 085001. https://doi.org/10.1088/1361-6668/abf985.

[236] R. Gyuráki, F. Sirois, F. Grilli, High-speed fluorescent thermal imaging of quench propagation in high temperature superconductor tapes, Supercond. Sci. Technol. 31 (2018) 034003. https://doi.org/10.1088/1361-6668/aaa703.

[237] R. Gyuráki, T. Benkel, F. Schreiner, F. Sirois, F. Grilli, Fluorescent thermal imaging of a non-insulated pancake coil wound from high temperature superconductor tape, Supercond. Sci. Technol. 32 (2019) 105006. https://doi.org/10.1088/1361-6668/ab38f2.

[238] K. Develos-Bagarinao, H. Yamasaki, Y. Nakagawa, K. Endo, Pore formation in YBCO films deposited by a large-area pulsed laser deposition system, Supercond. Sci. Technol. 17 (2004) 1253–1260. https://doi.org/10.1088/0953-2048/17/11/005.

[239] M.I. Faley, S.B. Mi, A. Petraru, C.L. Jia, U. Poppe, K. Urban, Multilayer buffer for high-temperature superconductor devices on MgO, Appl. Phys. Lett. 89 (2006) 082507. https://doi.org/10.1063/1.2338564.

[240] R. Lange, H.J. Clemens, W. Mönch, Surface and interface properties of cleaned and Ag-covered YBa2Cu3O7−x films, J. Alloys Compd. 195 (1993) 247–250. https://doi.org/10.1016/0925-8388(93)90731-2.

[241] J.P. Gong, M. Kawasaki, K. Fujito, R. Tsuchiya, M. Yoshimoto, H. Koinuma, Investigation of precipitate formation on laser-ablatated YBCO thin films, Phys. Rev. B. 50 (1994) 3280–3287. https://doi.org/10.1103/PhysRevB.50.3280.

[242] M. Truchlý, T. Plecenik, O. Krško, M. Gregor, L. Satrapinskyy, T. Roch, B. Grančič, M. Mikula, A. Dujavová, Š. Chromik, P. Kúš, A. Plecenik, Studies of YBa2Cu3O6+x degradation and surface conductivity properties by Scanning Spreading Resistance Microscopy, Phys. C Supercond. 483 (2012) 61–66. https://doi.org/10.1016/J.PHYSC.2012.07.004.

[243] S. Hwang, C. Mao, Failure of Delaminated Carbon/Epoxy Composite Plates under Compression, J. Compos. Mater. 35 (2001) 1634–1653. https://doi.org/10.1177/002199801772661560.

[244] F. Rondeaux, Thermal conductivity measurements of epoxy systems at low temperature, in: AIP Conf. Proc., AIP, 2002: pp. 197–203. https://doi.org/10.1063/1.1472543.

[245] No Title, (n.d.). https://kayakuam.com.

[246] J. Wang, C. Sun, L. Cong, X. Zhang, Y. Zhou, Delamination strength of HTS tape under

transverse tensile stress and its enhancement by using different Ag layer depositing temperatures, Theor. Appl. Mech. Lett. 9 (2019) 147–151. https://doi.org/10.1016/J.TAML.2019.03.002.

[247] T.C. Mokhena, M.J. Mochane, J.S. Sefadi, S.V. Motloung, D.M. Andala, Thermal Conductivity of Graphite-Based Polymer Composites, in: Impact Therm. Conduct. Energy Technol., InTech, 2018. https://doi.org/10.5772/intechopen.75676.

[248] A. Di Bartolomeo, L. Iemmo, F. Urban, M. Palomba, G. Carotenuto, A. Longo, A. Sorrentino, F. Giubileo, G. Barucca, M. Rovere, A. Tagliaferro, G. Ambrosone, U. Coscia, Graphite platelet films deposited by spray technique on low density polyethylene substrates, Mater. Today Proc. 20 (2020) 87–90. https://doi.org/10.1016/J.MATPR.2019.09.086.

[249] M. Palomba, G. Carotenuto, A. Longo, A. Sorrentino, A. Di Bartolomeo, L. Iemmo, F. Urban, F. Giubileo, G. Barucca, M. Rovere, A. Tagliaferro, G. Ambrosone, U. Coscia, Thermoresistive Properties of Graphite Platelet Films Supported by Different Substrates, Materials (Basel). 12 (2019). https://doi.org/10.3390/MA12213638.

[250] I.A. Parinov, Microstructure and Properties of High-Temperature Superconductors, Springer Berlin Heidelberg, Berlin, Heidelberg, 2012. https://doi.org/10.1007/978-3-642-34441-1.

[251] Çiçek, K. Yakinci, Enhanced superconducting properties of multi-wall carbon nanotubes added YBCO-123 Superconducting System, J. Mol. Struct. 1211 (2020) 128089. https://doi.org/10.1016/J.MOLSTRUC.2020.128089.

[252] B. Sahoo, S.R. Mohapatra, A.K. Singh, D. Samal, D. Behera, Effects of CNTs blending on the superconducting parameters of YBCO superconductor, Ceram. Int. 45 (2019) 7709–7716. https://doi.org/10.1016/J.CERAMINT.2019.01.072.

[253] M. Vilardell, X. Granados, S. Ricart, I. Van Driessche, A. Palau, T. Puig, X. Obradors, Flexible manufacturing of functional ceramic coatings by inkjet printing, Thin Solid Films. 548 (2013) 489–497. https://doi.org/10.1016/j.tsf.2013.09.012.

[254] K. Ando, Y. Oishi, Oxygen Self-Diffusion in Y2O3 and Y2O3-ZrO2 Solid Solution, in: 1985: pp. 203–215. https://doi.org/10.1007/978-1-4613-2519-2_16.

[255] M.F. Berard, Diffusion in polycrystalline Y2O3 and Er2O3, Iowa State University, 1968.

[256] S. Dwivedi, Solid oxide fuel cell: Materials for anode, cathode and electrolyte, Int. J. Hydrogen Energy. 45 (2020) 23988–24013. https://doi.org/10.1016/j.ijhydene.2019.11.234.

[257] J. RUPP, L. GAUCKLER, Microstructures and electrical conductivity of nanocrystalline ceria-based thin films, Solid State Ionics. 177 (2006) 2513–2518. https://doi.org/10.1016/j.ssi.2006.07.033.

[258] H.L. Tuller, Ionic conduction in nanocrystalline materials, Solid State Ionics. 131 (2000) 143–157. https://doi.org/10.1016/S0167-2738(00)00629-9.

[259] P. Heitjans, S. Indris, Diffusion and ionic conduction in nanocrystalline ceramics, J. Phys. Condens. Matter. 15 (2003).

[260] Y. Ikuma, Oxygen Diffusion in Powder and Polycrystal of Advanced Metal Oxides, J. Japan Soc. Powder Powder Metall. 53 (2006) 3–10. https://doi.org/10.2497/jjspm.53.3.

[261] W. Komatsu, Y. Ikuma, The Surface Layer Thickness and the Near-Surface Diffusion of Oxygen in Metal Oxides, Mater. Sci. Forum. 29 (1988) 199–218. https://doi.org/10.4028/www.scientific.net/MSF.29.199.

[262] H. Tomonaga, T. Morimoto, Flexographic Printing, in: Sol-Gel Technol. Glas. Prod. Users, Springer US, Boston, MA, 2004: pp. 131–135. https://doi.org/10.1007/978-0-387-88953-5_17.

[263] No Title, (n.d.). https://inktsa.sunchemical.com/flexographic/.

[264] M. Lao, J. Hecher, M. Sieger, P. Pahlke, M. Bauer, R. Hühne, M. Eisterer, Planar current anisotropy and field dependence of Jc in coated conductors assessed by scanning Hall probe microscopy, Supercond. Sci. Technol. 30 (2016) 024004. https://doi.org/10.1088/1361-6668/30/2/024004.

[265] K.R. Nemade, S.A. Waghuley, Synthesis of MgO Nanoparticles by Solvent Mixed Spray Pyrolysis Technique for Optical Investigation, Int. J. Met. 2014 (2014) 1–4. https://doi.org/10.1155/2014/389416.

[266] X.-X. Ye, H. Ai, Z. Guo, H. Huang, L. Jiang, J. Wang, Z. Li, X. Zhou, The high-temperature corrosion of Hastelloy N alloy (UNS N10003) in molten fluoride salts analysed by STXM, XAS, XRD, SEM, EPMA, TEM/EDS, Corros. Sci. 106 (2016) 249–259. https://doi.org/10.1016/j.corsci.2016.02.010.

[267] J. Farjas, J. Camps, P. Roura, S. Ricart, T. Puig, X. Obradors, Thermoanalytical study of the formation mechanism of yttria from yttrium acetate, Thermochim. Acta. 521 (2011) 84–89. https://doi.org/10.1016/j.tca.2011.04.009.

[268] A.R. Wazzan, P. Tung, L.B. Robinson, Diffusion of Silver into Nickel Single Crystals, J. Appl. Phys. 42 (1971) 5316–5320. https://doi.org/10.1063/1.1659942.

[269] A.W. Adamson, Advanced Inorganic Chemistry. By F. A. Cotton and G. Wilkinson, Inorg. Chem. 2 (1963) 665–665. https://doi.org/10.1021/ic50007a079.

[270] T. Palomar, B. Ramírez Barat, E. García, E. Cano, A comparative study of cleaning methods for tarnished silver, J. Cult. Herit. 17 (2016) 20–26. https://doi.org/10.1016/j.culher.2015.07.012.

[271] E.G. Ioanid, A. Ioanid, D.E. Rusu, F. Doroftei, Surface investigation of some medieval silver coins cleaned in high-frequency cold plasma, J. Cult. Herit. 12 (2011) 220–226. https://doi.org/10.1016/j.culher.2010.09.004.

[272] M.H. Hebb, Electrical Conductivity of Silver Sulfide, J. Chem. Phys. 20 (1952) 185–190. https://doi.org/10.1063/1.1700165.

[273] Platers' Guide: With which is Combined Brass World, 17th ed., Brass world publishing Company, Incorporated, 1921. https://books.google.es/books?id=-K3mAAAAMAAJ.

[274] T. Blanton, S. Misture, N. Dontula, S. Zdzieszynski, In situ high-temperature X-ray diffraction characterization of silver sulfide, Ag 2 S, Powder Diffr. 26 (2011) 114–118. https://doi.org/10.1154/1.3583564.

[275] Lyndsie Selwyn, Metals and corrosion : a handbook for the conservation professional, 1st ed., Canadian Conservation Institute, Ottawa, 2004. https://www.worldcat.org/title/metals-and-corrosion-a-handbook-for-the-conservation-professional/oclc/56420148.

[276] A.D. Costa, J. M. ; Mercer, Progress in the understanding and prevention of corrosion, in: Institute of Materials, London (United Kingdom), 1993. https://inis.iaea.org/search/searchsinglerecord.aspx?recordsFor=SingleRecord&RN=25008679.

[277] J. Jiang, A. Chan, S. Ali, A. Saha, K.J. Haushalter, W.-L.M. Lam, M. Glasheen, J. Parker, M. Brenner, S.B. Mahon, H.H. Patel, R. Ambasudhan, S.A. Lipton, R.B. Pilz, G.R. Boss, Hydrogen

Sulfide—Mechanisms of Toxicity and Development of an Antidote, Sci. Rep. 6 (2016) 20831. https://doi.org/10.1038/srep20831.

[278] J.R. Lyons, An estimate of the equilibrium speciation of sulfur vapor over solid sulfur and implications for planetary atmospheres, J. Sulfur Chem. 29 (2008) 269–279. https://doi.org/10.1080/17415990802195615.

[279] T. Theivasanthi, M. Alagar, Electrolytic Synthesis and Characterization of Silver Nanopowder, Nano Biomed. Eng. 4 (2012). https://doi.org/10.5101/nbe.v4i2.p58-65.

[280] A. Fridman, Plasma Chemistry, Cambridge University Press, Cambridge, 2008. https://doi.org/10.1017/CBO9780511546075.

[281] F. Habashi, R. Dugdale, The reduction of sulfide minerals by hydrogen in the presence of lime, Metall. Trans. 4 (1973) 1865–1871. https://doi.org/10.1007/BF02665414.

[282] W. Petasch, B. Kegel, H. Schmid, K. Lendenmann, H.. Keller, Low-pressure plasma cleaning: a process for precision cleaning applications, Surf. Coatings Technol. 97 (1997) 176–181. https://doi.org/10.1016/S0257-8972(97)00143-6.

[283] M.C. Kim, S.H. Yang, J.-H. Boo, J.G. Han, Surface treatment of metals using an atmospheric pressure plasma jet and their surface characteristics, Surf. Coatings Technol. 174–175 (2003) 839–844. https://doi.org/10.1016/S0257-8972(03)00560-7.

[284] J. Lee, T.S. Williams, R.F. Hicks, Atmospheric pressure plasma reduction of copper oxide to copper metal, J. Vac. Sci. Technol. A. 39 (2021) 023001. https://doi.org/10.1116/6.0000704.

[285] Donny L Hamilton, Methods of conserving archaeological material from underwater sites, Texas A&M Univ. 110 (1999). https://citeseerx.ist.psu.edu/viewdoc/download?doi=10.1.1.691.4074&rep=rep1&type=pdf.

[286] V. Costa, The deterioration of silver alloys and some aspects of their conservation, Stud. Conserv. 46 (2001) 18–34. https://doi.org/10.1179/sic.2001.46.Supplement-1.18.

[287] E. Cano, D. Lafuente, D.M. Bastidas, Use of EIS for the evaluation of the protective properties of coatings for metallic cultural heritage: a review, J. Solid State Electrochem. 14 (2010) 381–391. https://doi.org/10.1007/s10008-009-0902-6.

[288] M.C. Bernard, E. Dauvergne, M. Evesque, M. Keddam, H. Takenouti, Reduction of silver tarnishing and protection against subsequent corrosion, Corros. Sci. 47 (2005) 663–679. https://doi.org/10.1016/j.corsci.2004.07.015.

[289] D. Charalambous, W.A. Oddy, THE 'CONSOLIDATIVE' REDUCTION OF SILVER, Stud. Conserv. 20 (1975) 219–227. https://doi.org/10.1179/sic.1975.s1.037.

[290] C. Huang, X. Qian, R. Yang, Thermal conductivity of polymers and polymer nanocomposites, Mater. Sci. Eng. R Reports. 132 (2018) 1–22. https://doi.org/10.1016/J.MSER.2018.06.002.

[291] H.-B. Cho, T. Nakayama, H. Suematsu, T. Suzuki, W. Jiang, K. Niihara, E. Song, N.S.A. Eom, S. Kim, Y.-H. Choa, Insulating polymer nanocomposites with high-thermal-conduction routes via linear densely packed boron nitride nanosheets, Compos. Sci. Technol. 129 (2016) 205–213. https://doi.org/10.1016/j.compscitech.2016.04.033.

[292] T. Evgin, H.D. Koca, N. Horny, A. Turgut, I.H. Tavman, M. Chirtoc, M. Omastová, I. Novak, Effect of aspect ratio on thermal conductivity of high density polyethylene/multi-walled carbon nanotubes nanocomposites, Compos. Part A Appl. Sci. Manuf. 82 (2016) 208–213. https://doi.org/10.1016/J.COMPOSITESA.2015.12.013.

[293] A. Tessema, D. Zhao, J. Moll, S. Xu, R. Yang, C. Li, S.K. Kumar, A. Kidane, Effect of filler loading, geometry, dispersion and temperature on thermal conductivity of polymer nanocomposites, Polym. Test. 57 (2017) 101–106. https://doi.org/10.1016/j.polymertesting.2016.11.015.

[294] M. Mionić, K. Pataky, R. Gaal, A. Magrez, J. Brugger, L. Forró, Carbon nanotubes–SU8 composite for flexible conductive inkjet printable applications, J. Mater. Chem. 22 (2012) 14030. https://doi.org/10.1039/c2jm16547c.

[295] T. Vinod Kumar, M. Chandrasekaran, P. Mohanraj, R. Balasubramanian, R. Muraliraja, V. S. Shaisundaram, Fillers preparation for polymer composite and its properties – a review, Int. J. Eng. Technol. 7 (2018) 212. https://doi.org/10.14419/ijet.v7i2.33.13889.

[296] J.O. Nilsson, M. Leetmaa, O.Y. Vekilova, S.I. Simak, N. V. Skorodumova, Oxygen diffusion in ceria doped with rare-earth elements, Phys. Chem. Chem. Phys. 19 (2017) 13723–13730. https://doi.org/10.1039/C6CP06460D.

[297] B.C.H. Steele, A. Heinzel, Materials for fuel-cell technologies, Nat. 2001 4146861. 414 (2001) 345–352. https://doi.org/10.1038/35104620.

[298] E.O. Oh, C.M. Whang, Y.R. Lee, J.H. Lee, K.J. Yoon, B.K. Kim, J.W. Son, J.H. Lee, H.W. Lee, Thin film yttria-stabilized zirconia electrolyte for intermediate-temperature solid oxide fuel cells (IT-SOFCs) by chemical solution deposition, J. Eur. Ceram. Soc. 32 (2012) 1733–1741. https://doi.org/10.1016/J.JEURCERAMSOC.2012.01.021.

[299] F. Taïr, L. Carreras, J. Camps, J. Farjas, P. Roura, A. Calleja, T. Puig, X. Obradors, Melting temperature of YBa2Cu3O7−x and GdBa2Cu3O7−x at subatmospheric partial pressure, J. Alloys Compd. 692 (2017) 787–792. https://doi.org/10.1016/j.jallcom.2016.08.072.

[300] A. Sawka, A. Kwatera, P. Andreasik, Deposition and characterization of ceria layers using the MOCVD method, Mater. Lett. 204 (2017) 39–41. https://doi.org/10.1016/j.matlet.2017.06.012.

[301] A. Sawka, A. Kwatera, Deposition of gadolinia-doped ceria layers by MOCVD at low temperatures, Ceram. Int. 44 (2018) 6257–6264. https://doi.org/10.1016/j.ceramint.2018.01.012.

[302] K. Kowalski, Oxygen Diffusion and Surface Exchange in Yttria-Stabilized Zirconia and Gadolinia-Doped Ceria Ceramics at Low Temperatures, Defect Diffus. Forum. 289–292 (2009) 769–774. https://doi.org/10.4028/www.scientific.net/DDF.289-292.769.

[303] M. Kilo, C. Argirusis, G. Borchardt, R.A. Jackson, Oxygen diffusion in yttria stabilised zirconia—experimental results and molecular dynamics calculations, Phys. Chem. Chem. Phys. 5 (2003) 2219–2224. https://doi.org/10.1039/B300151M.

[304] G. Saleh, C. Xu, S. Sanvito, Silver Tarnishing Mechanism Revealed by Molecular Dynamics Simulations, Angew. Chemie Int. Ed. 58 (2019) 6017–6021. https://doi.org/10.1002/anie.201901630.

Appendix A. Physical properties of the 2G HTS tape materials

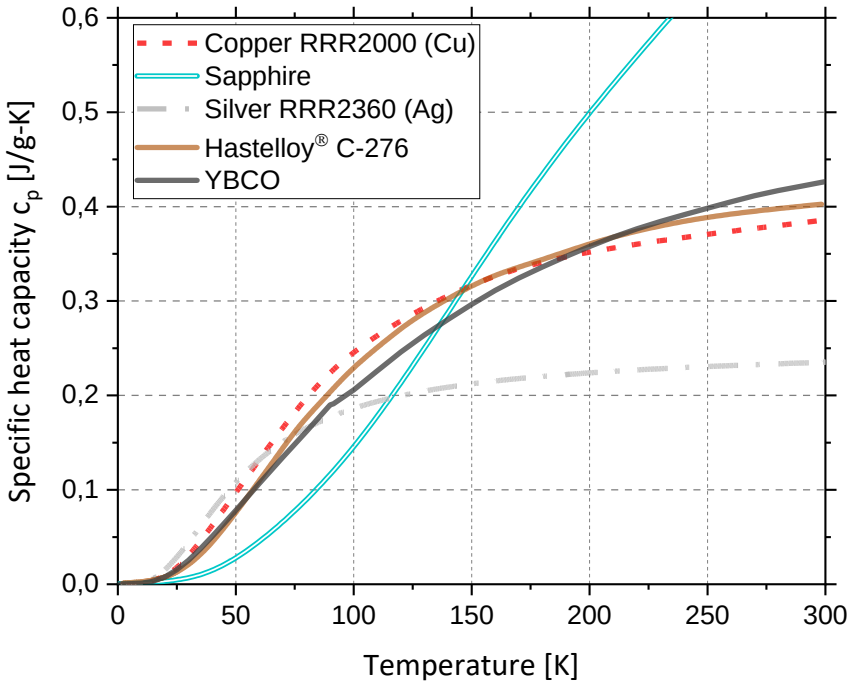

Appendix Figure A-1: Specific heat capacity versus temperature for the different materials used in the Second Generation (2G) of High Temperature Superconductors (HTS) tapes. The legend of this figure corresponds to the curves in the following images.

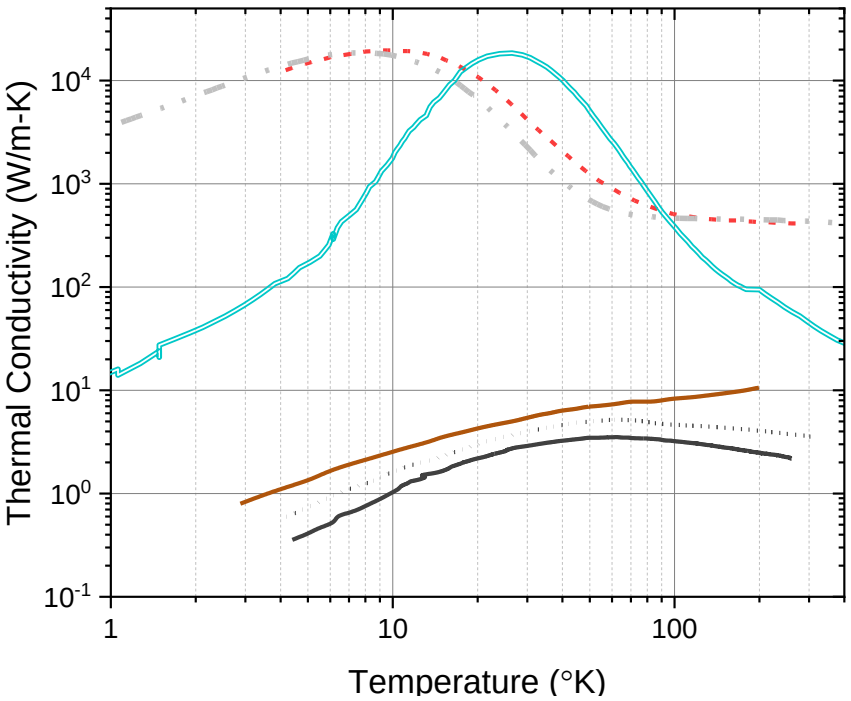

Appendix Figure A-2: Thermal Conductivity (W/m-K) versus temperature (K) for the different materials used in the Second Generation (2G) of High Temperature Superconductors (HTS) tapes. Legend of the curves is the same as in Figure A-1.

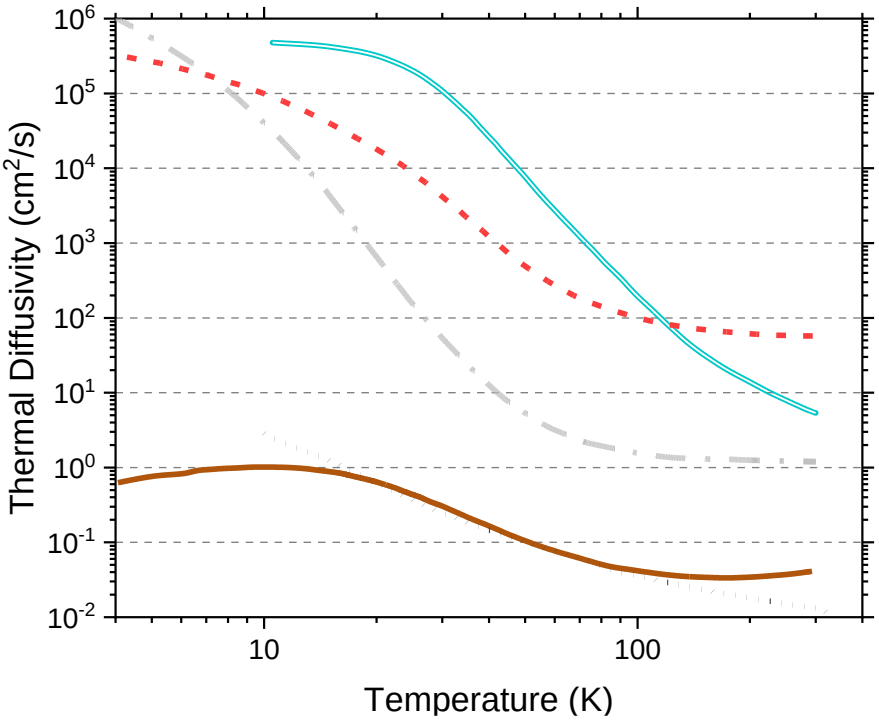

Appendix Figure A-3: Thermal diffusivity (cm^2/s) versus temperature (K) for the different materials used in the Second Generation (2G) of High Temperature Superconductors (HTS) tapes. Legend of the curves is the same as in Figure A-1.

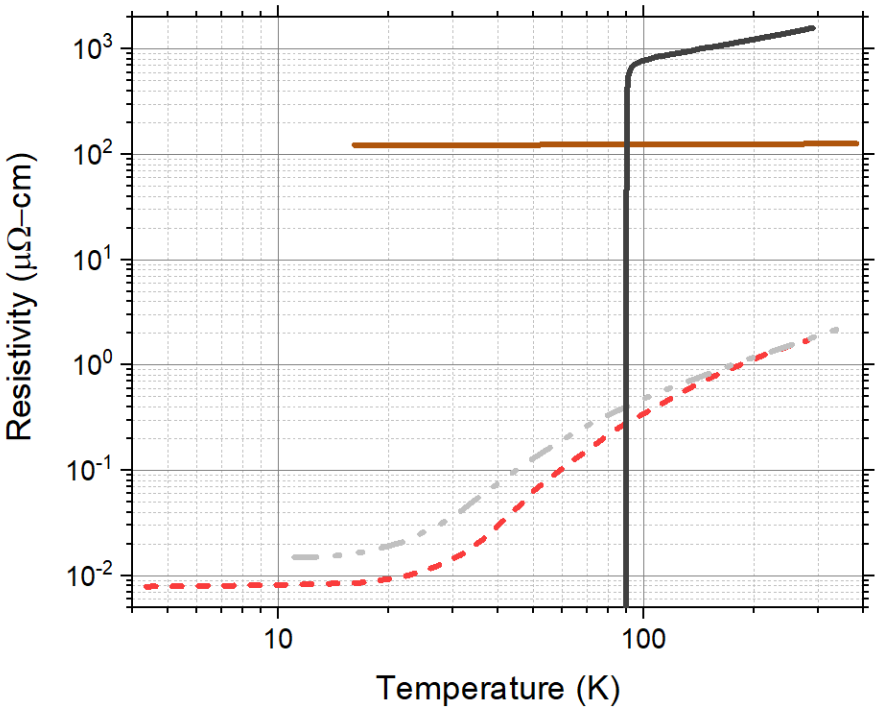

Appendix Figure A-4: Electric Resistivity (Ω-cm) versus temperature (K) for the different materials used in the Second Generation (2G) of High Temperature Superconductors (HTS) tapes. Legend of the curves is the same as in Figure A-1.

Appendix B. Optimum parameters of the tape

In the clear-fault scenario the resistance of the HTS tape is much great than the impedance of the grid thus making the grid behave like a voltage source on the HTS tape. Considering adiabatic conditions and a tape with length a L_{SC} and cross-section A_{cond}, the joule heating happening in tape's volume will translate to an increase in temperature T according to thermal equation bellow:

$$\frac{v_{SC}^2}{R_{cond}} = c_p A_{cond} L_{SC} \frac{dT}{dt}$$

Where R_{cond} is the resistance Ω and c_p the volumetric heat capacity J/m^3-K. Being c_p a variable depended on the temperature T and $R_{cond} = \rho L_{SC}/A_{cond}$:

$$A_{cond} \frac{v_{SC}(t)^2}{\rho(T)\, L_{SC}} = c_p(T) A_{cond} L_{SC} \frac{dT}{dt}$$

Where $\rho(T)$ is the temperature depend resistivity Ω-m. And so, the right side of the equation is integrated over the temperate range $T_{op} - T_{max}$ and the left side over time delay t for the circuit breaker to open and eliminate the fault:

$$\frac{A_{cond}}{L_{SC}} \int_0^t v_{SC}(t)^2 \, dt = A_{cond} L_{SC} \int_{T_{op}}^{T_{max}} \rho(T) c_p(T) \, dT$$

Since grid is basically behaving as a voltage source the variable $v_{SC}(t)$ can be substituted by a constant V_{SC} and the length L_{SC} is determined as:

$$L_{SC} = V_{SC} \sqrt{\left(\frac{1}{\Delta t} \int_{T_{op}}^{T_{max}} \rho(T) c_p(T) \, dT \right)^{-1}}$$

In the hot-spot scenario, the initial resistance of the HTS tape is much smaller than the impedance of the grid thus making the grid behave like a current source. Considering adiabatic conditions and the tape with length a L_{SC} and cross-section A_{cond}, the joule heating happening in tape's volume will translate to an increase in temperature T according to thermal equation bellow:

$$\rho(T) \frac{L_{SC}}{A_{cond}} i_{sc}(t)^2 = c_p(T) L_{SC} A_{cond} \frac{dT}{dt}$$

Following the same procedure described for the clear-fault scenario

$$\int_0^t i_{sc}(t)^2 \, dt = A_{cond} \int_{T_{op}}^{T_{max}} \frac{c_p(T)}{\rho(T)} \, dT$$

Since grid is basically behaving as a current source delivering a current $I \approx I_c$, $i_{sc}(t)$ can be substituted by a constant I_c and the cross-section area A_{cond} is determined as:

$$A_{cond} = I_c \sqrt{\Delta t \left(\int_{T_c}^{T_{max}} \frac{c_p(T)}{\rho(T)} dT \right)^{-1}}$$

Appendix C. Array of Voltage probes

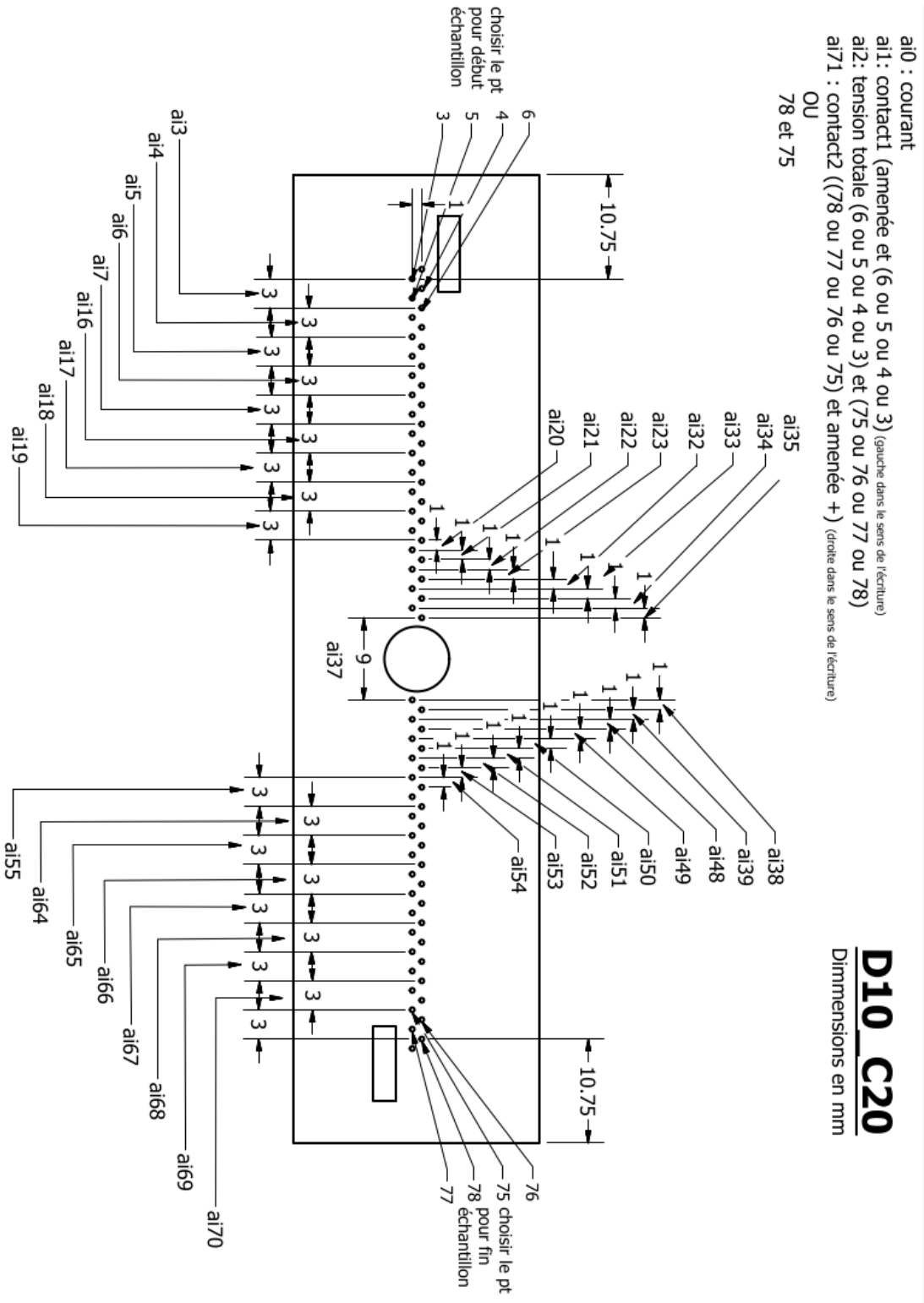

Appendix Figure C-1: Schematic drawing of the array of voltage probes used for transport current tests in Ecolé Polytehcnique of Montreal. This piece is attached to the upper stabilizer layer on the HTS tape for both NZPV and DC limitation tests. Figure provided as a courtesy from EPM collaborators.

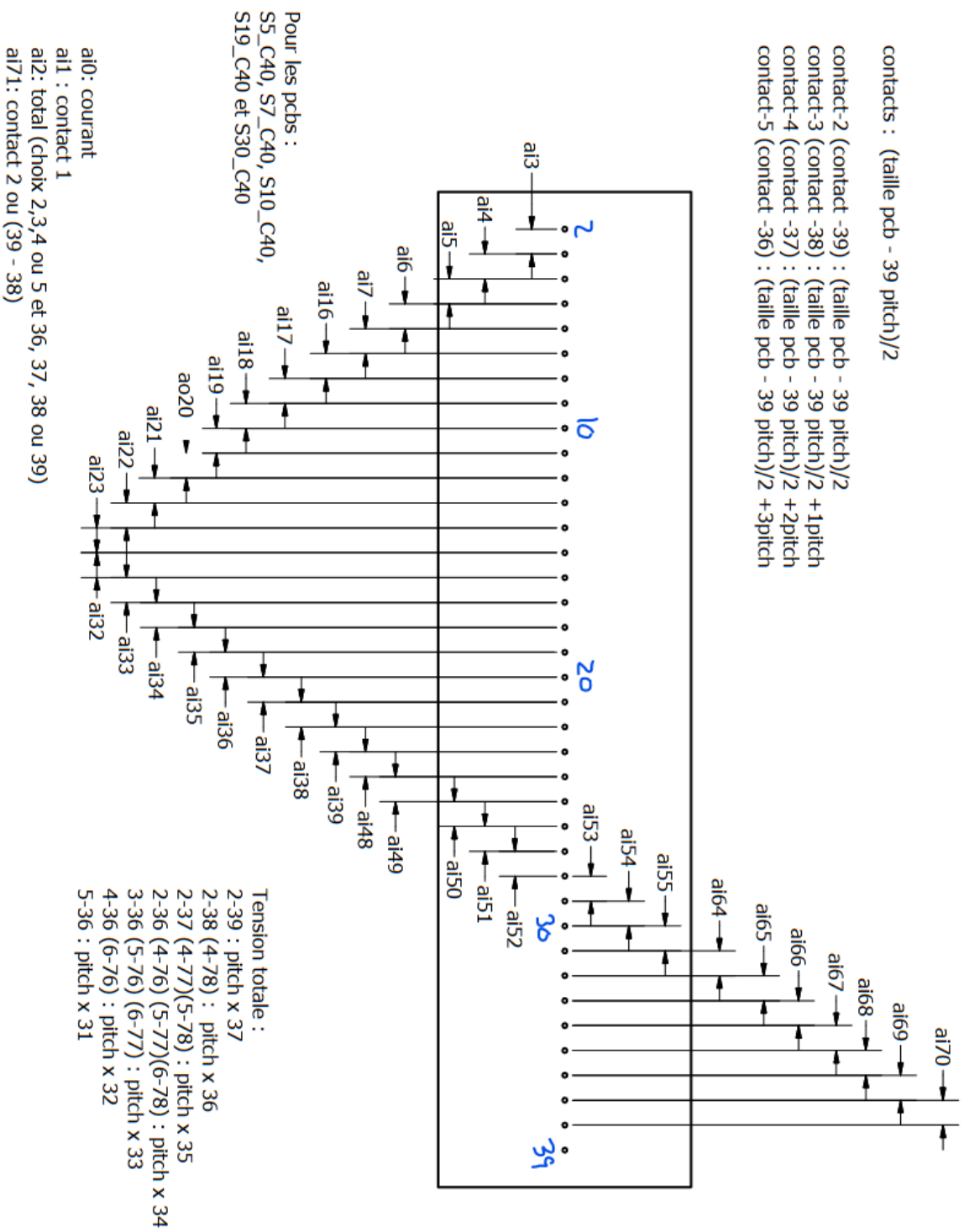

Appendix Figure C-2: Schematic drawing of another array of voltage probes used for transport current tests in Ecolé Polytehcnique of Montreal. This piece is attached to the upper stabilizer layer on the HTS tape for both NZPV and DC limitation tests. Figure provided as a courtesy from EPM collaborators.

Appendix D. Technical information of THEVA tapes

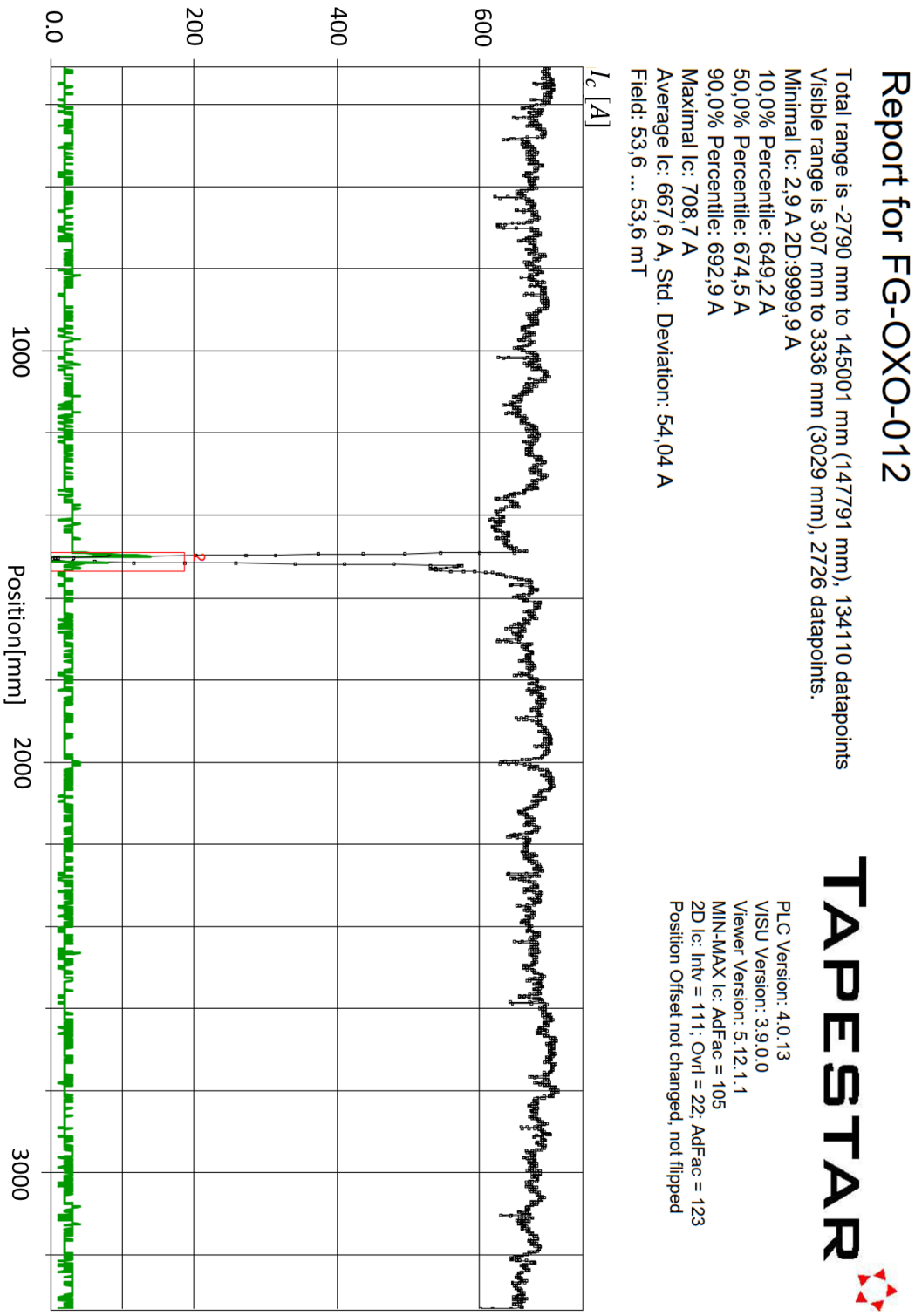

Appendix Figure D-1: critical current evaluation of a reel of THEVA tape code FG-OXO-012 done with the Tapestar system.

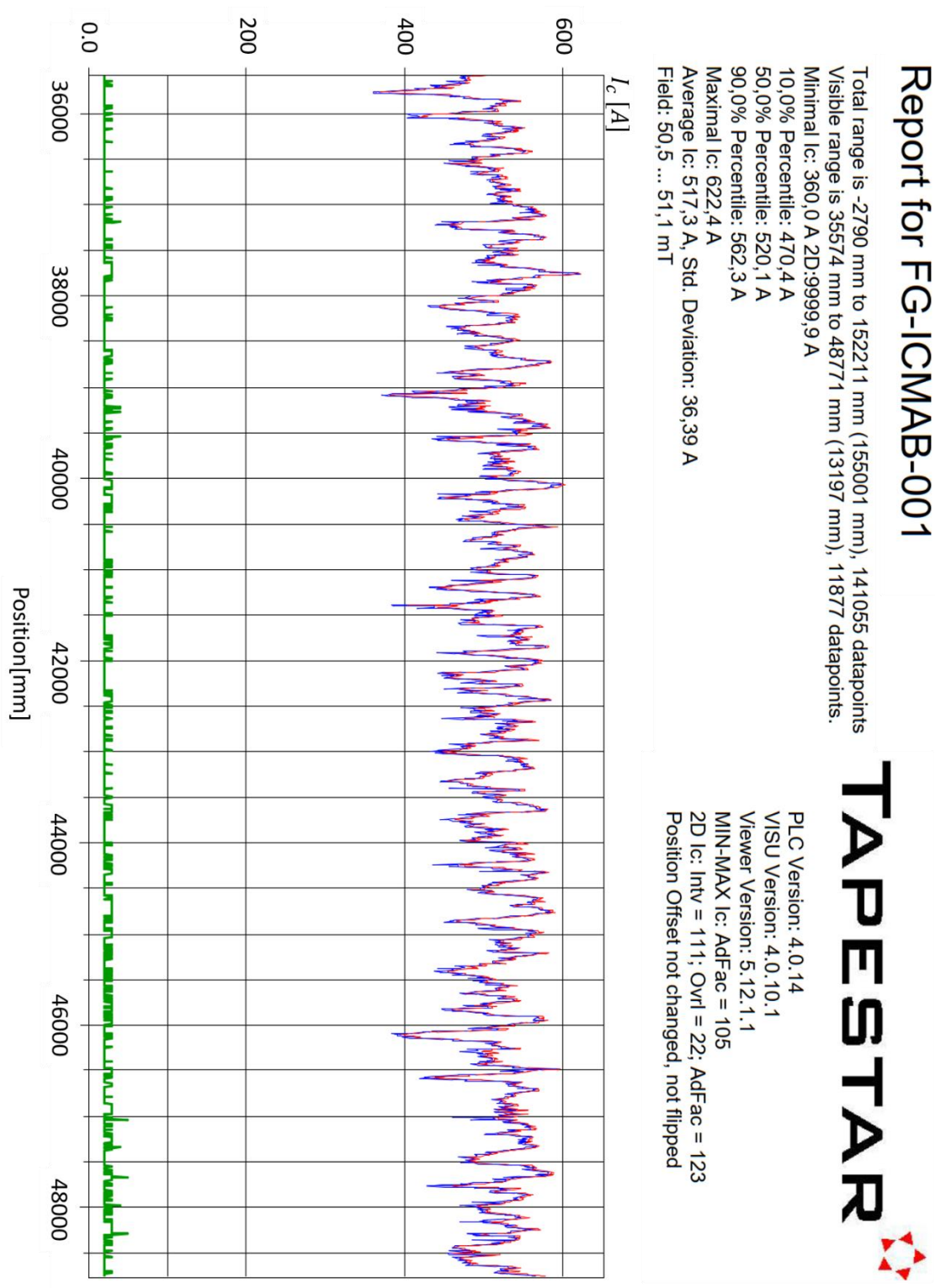

Appendix Figure D-2: critical current evaluation of a reel of THEVA tape code FG-ICMAB-001 done with the Tapestar system.